Innovative piezoelectric materials elaborated by Pulsed Laser Deposition (PLD)

Ihor Pershukov

N° d'ordre NNT : 2024ECDL0014

THESE de DOCTORAT DE **L'ECOLE** CENTRALE DE LYON
membre de **l'Université** de Lyon

École Doctorale N°34 : ED Matériaux de Lyon

Spécialité de doctorat : Matériaux

Soutenue le 28/03/2024 par :

Ihor PERSHUKOV

INNOVATIVE PIEZOELECTRIC MATERIALS ELABORATED BY PULSED LASER DEPOSITION (PLD)

Devant le jury composé de :

Mme Laurence MECHIN, Directrice de recherche CNRS Laboratoire GREYC – ENSICAEN	Rapporteur
M. Alain SYLVESTRE, Professeur Univ. Grenoble Alpes G2Elab	Rapporteur
Mme Valérie DEMANGES, Directrice de recherche CNRS Institut des Sciences Chimiques de Rennes (ISCR)	Examinatrice
Mme Marie BOUSQUET, Chercheuse CEA Univ. Grenoble Alpes, CEA-LETI	Examinatrice
M. Bertrand Vilquin, Maitre de conférences Ecole centrale de Lyon Institut des nanotechnologies de Lyon	Directeur de thèse
M. Florian DUPONT, Chercheur CEA Univ. Grenoble Alpes, CEA-LETI	Co-directeur

Thèse préparée au sein du CEA-LETI

Abbreviations

4G, 5G: 4th et 5th generation of mobile application

ALD: Atomic Layer Deposition

CTE: Thermal Expansion Coefficients

CVD: Chemical Vapor Deposition

FBAR: Film Bulk Acoustic Resonator

FWHM: Full Width at Half Maximum

HRXRD: High Resolution XRD

IAD: Ion-Assisted Deposition

IDT: Interdigitated Transducer

IoT: Internet of Things

LGD: Landau–Ginzburg–Devonshire Formulation

Li-DPM: Lithium Dipivaloylmethane

LNOI: Lithium Niobate on Insulator

LPE: Liquid Phase Epitaxy

MBE: Molecular Beam Epitaxy

MEMS: Microelectromechanical System

MOCVD: Metal-Organic Chemical Vapor Deposition

P-E: Polarization-Electric Field Measurement

PLD: Pulsed Laser Deposition

POI: Piezoelectric on Insulator

PVD: Physical Vapor Deposition

RF: Radiofrequency

RC: Rocking Curves

RMS: Root Mean Square

RT: Room Temperature

SAW: Surface Acoustic Wave

SEM: Scanning Electron Microscopy

SIMS: Secondary Ion Mass Spectrometry

SMR: Solidly Mounted Resonator

TOF-SIMS: Time-of-Flight Secondary Ion Mass Spectrometry

TS: Target-substrate (distance)

TC-SAW: Temperature Compensated SAW (device)

TF-SAW: Thin Film SAW (device)

UHV: Ultrahigh Vacuum

XRD: X-ray diffraction

General Introduction

From the beginning of 2010s, there has been significant growth in the market for smart devices, spanning various applications such as home automation, geolocation, transportation, data transfer, and telecommunications. This interconnected network of devices is commonly known as the Internet of Things (IoT). Due to the increasing number of connected devices and data exchanges, there is a need for updates to networks and electronic components.

In response, the global development of the fifth generation of mobile networks, known as 5G, is underway. 5G aims for scalability through ongoing international standardization efforts and specifications, with key goals including improving speed, network reliability, and accommodating the growing number of connected objects to support IoT deployment.

Radiofrequency (RF) filters are crucial electronic components within interconnected devices, selectively filtering exchanged data among users. The introduction of 5G requires recalibration of these filters to accommodate new frequency bands, such as the 700 MHz and 3.5 GHz spectrums. Looking ahead, the development and deployment of 6G networks are projected for the late 2020s, with potential advancements in utilizing millimeter waves and terahertz radiation to enhance network capabilities.

Two RF filter technologies, surface acoustic wave and bulk acoustic wave resonators, are currently utilized. Bulk acoustic wave filters presently employ aluminum nitride (AlN) as a piezoelectric material, providing them with resonance capabilities. However, the evolving needs of 5G, such as the requirement for higher resonance frequency and increased bandwidth, may lead to potential inadequacy of AlN-based filters in the future.

This thesis constitutes an integral component within the broader framework of 5G development, focusing on the consequential adjustments required in the performance criteria of RF filters. A noteworthy alternative material under investigation is lithium niobate, considered as a potential substitute for aluminum nitride. The theoretical piezoelectric and acoustic characteristics of $LiNbO_3$ position it as a credible candidate for replacing AlN, particularly when utilized in the form of monocrystalline slices, a feat attainable through Smart-Cut™ technology. Filters fabricated from $LiNbO_3$ exhibit promising attributes to fulfill the evolving demands of 5G.

Lithium niobate can be employed to produce RF filters as thin layers, presenting the possibility of enhanced performance with higher resonance frequency and increased bandwidth. However, achieving single-phased and stoichiometric $LiNbO_3$ through conventional deposition techniques is challenging. To optimize filter performance, the piezoelectric layer must meet strict criteria, including high crystallinity, a defect-free structure, and minimal surface roughness.

To explore the deposition of lithium niobate layers, Pulsed Laser Deposition (PLD) is utilized — a recently developed technique gaining industrial importance. The physicochemical properties of the synthesized layers will undergo thorough analysis employing various characterization techniques, such as X-ray diffraction, atomic force microscopy, scanning electron microscopy, Raman spectroscopy, and secondary ion mass spectrometry. These analyses will be systematically compared against predefined criteria for thin films.

The first chapter comprises three main sections. Initially, foundational aspects of piezo- and ferroelectric materials will be explored, providing an understanding of the unique properties and behavior of lithium niobate. The presentation then shifts to RF filters, including a discussion on acoustic filters and modifications necessary for 5G. The final part discusses thin film elaboration techniques, emphasizing challenges associated with the deposition of $LiNbO_3$.

In the second chapter, the focus is on the deposition of thin $LiNbO_3$ layers, utilizing monocrystalline substrates. The investigation specifically delves into the homoepitaxial growth of $LiNbO_3$ on $LiNbO_3$ substrates with different orientations by PLD.

Chapter 3 employs PLD to grow thin films on sapphire, aiming for the production of heteroepitaxial layers. The investigation covers the study of crystalline quality and surface roughness of the layers. Similar to the examination of layers deposited on $LiNbO_3$ substrates, the influence of the cutting plane of the Al_2O_3 substrate on layer growth is explored.

In Chapter 4, the focus is on depositing thin layers, specifically using silicon-based substrates. The research is centered around growing $LiNbO_3$ on silicon substrates, incorporating different buffer layers for use as an electrode. The main goal is studying the alignment, crystallographic characteristics, and surface properties of these layers.

Table of Contents

Chapter 1: State of the art and objectives of the thesis

Table of Contents

1.1 Material

Ferroelectric materials are characterized as polar substances that exhibit at least two stable orientations of the spontaneous polarization vector in the absence of an external electric field. These materials possess the remarkable ability to switch between these orientations when subjected to an electric field [1]. In this section of the chapter, we will delve into the foundational aspects of ferroelectric materials and provide a more comprehensive understanding of the unique properties and behavior of $LiNbO_3$.

1.1.1 Ferroelectricity and piezoelectricity

The piezoelectric effect, which is a fundamental phenomenon in materials science, can be elucidated through the use of a simplistic model as depicted in Figure 1.1. This model serves as a conceptual tool to illustrate the underlying principles and mechanisms behind the generation of electric charges in response to mechanical stress.

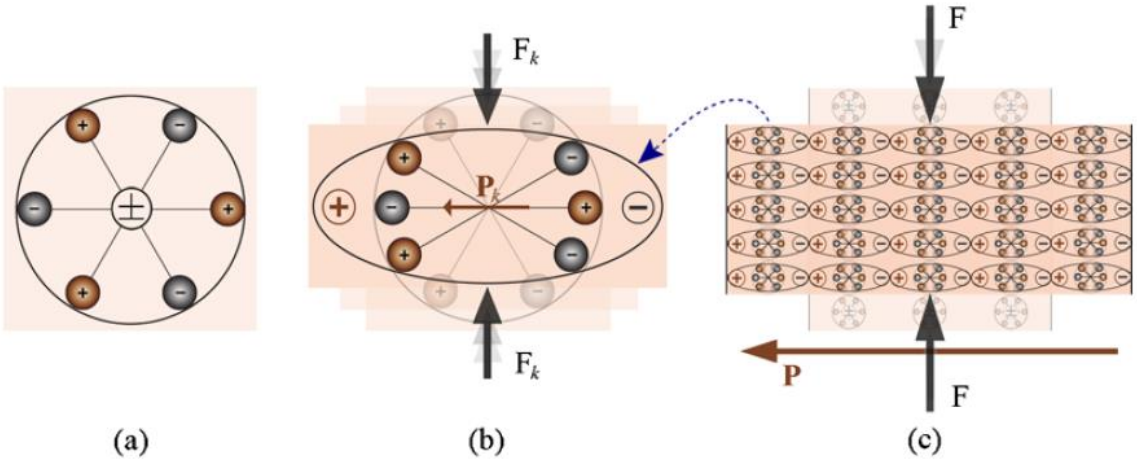

FIGURE 1.1 PIEZOELECTRIC EFFECT EXPLAINED WITH A SIMPLE MOLECULAR MODEL: (A) AN UNPERTURBED MOLECULE WITH NO PIEZOELECTRIC POLARIZATION; (B) THE MOLECULE SUBJECTED TO AN EXTERNAL FORCE (F_K); (C) THE POLARIZING EFFECT ON THE SURFACE [2].

Before the application of external stress, the molecule was electrically neutral with the positive and negative charges balanced (Figure 1(a)). Under external forces like mechanical stress, the molecule's internal structure deforms, causing a separation of positive and negative charges, creating an electric dipole (Figure 1(b)). Within the material, the dipoles cancel each other out, maintaining overall neutrality. However, at the surface, the absence of neighboring dipoles leads to the accumulation of surface charges, creating an electric field(Figure 1(c)).

This phenomenon is the basis for the piezoelectric effect, converting mechanical energy into electrical energy [2].

1.1.1.1 Fundamental Principles of Ferroelectricity and Piezoelectricity

In 1880, Pierre and Jacques Curie made a significant discovery regarding certain materials such as quartz and topaz. They observed that the application of mechanical stress to these materials resulted in the emergence of macroscopic polarization, which indicated the generation of electric surface charges [3]. They observed that mechanical stress could induce macroscopic polarization and generate electric surface charges in certain materials which was the first description of the *direct piezoelectric effect*. Subsequently, Gabriel Lippmann made a significant prediction based on thermodynamic considerations. He proposed that an applied voltage could lead to mechanical deformations or strains in a material, which is now recognized as the *reverse piezoelectric effect* [4]. Lippmann's prediction established the reciprocal nature of the piezoelectric effect, highlighting the interplay between electrical and mechanical phenomena in these materials.

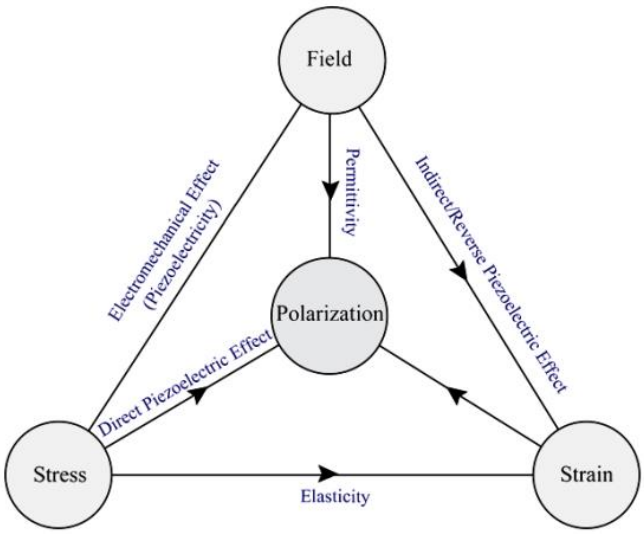

FIGURE 1.2 PIEZOELECTRICITY—AN INTERMINGLING OF ELECTRIC AND ELASTIC PHENOMENA [2].

In summary, piezoelectric materials belong to a special class of dielectric materials that possess the unique ability to be polarized not only by an electric field but also by the application of mechanical stress. This remarkable property, known as piezoelectricity or "pressure electricity," distinguishes these materials from other dielectrics. [2]. The phenomenon of

piezoelectricity and the relationship between mechanical stress and electric polarization can be visually explained and understood by referring to Figure 1.2.

1.1.1.2 Hysteresis Loops

According to the linear theory of piezoelectricity, the density of charge generated in a piezoelectric material is directly proportional to the applied external stress [5]. Ferroelectric materials exhibit spontaneous polarization below the Curie temperature (T_C). The dielectric permittivity (ε) of ferroelectric materials follows a Curie-Weiss law above T_C. To minimize depolarizing fields, ferroelectric materials form ferroelectric domains with uniform polarization. The dependence of dielectric displacement (D) on electric field strength (E) in ferroelectric materials is highly nonlinear and exhibits a characteristic hysteresis loop [6].

In their book [7], Volk and Wöhlecke provide a comprehensive exploration of the fundamentals of ferroelectricity of $LiNbO_3$. They discuss the behavior of congruent $LiNbO_3$, which undergoes a second-order phase transition at Tc ≈ 1190°C from a centrosymmetric paraelectric phase to a noncentrosymmetric ferroelectric phase. The free energy of $LiNbO_3$ can be described using a generalized Landau–Ginzburg–Devonshire (LGD) formulation, which includes the Landau–Ginzburg energy, the elastic energy, and the electrostrictive energy. The Landau–Ginzburg energy captures the thermodynamic behavior of the material and is related to the spontaneous polarization and its higher-order terms. The elastic energy accounts for the strain and deformation within the material due to mechanical stress. The electrostrictive energy arises from the coupling between the applied electric field and the resulting strain in the material [7].

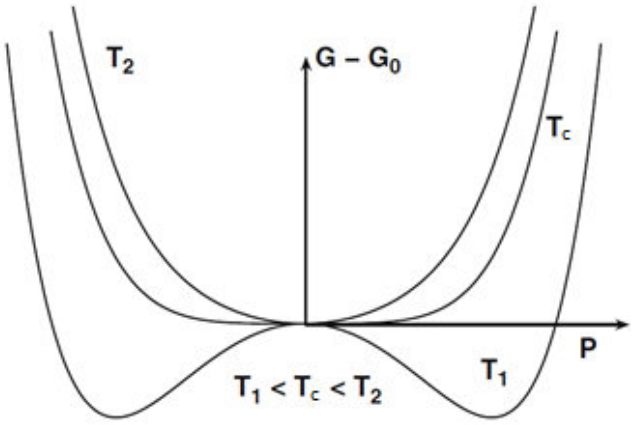

FIGURE 1.3 FREE ENERGY $G - G_0$ AS A FUNCTION OF THE POLARIZATION P FOR THREE TEMPERATURES $T_1 < T_C < T_2$ [7]

In Figure 1.3 [7], the free energy (G) is plotted against polarization (P_s) for various temperatures in a ferroelectric material. Above the Curie temperature (T_C), in the paraelectric phase ($T_C < T_2$), there is a single minimum in the free energy curve, indicating only one stable polarization state. As the temperature approaches T_C, a transition to the ferroelectric phase (T_1 < C) occurs, with two minima representing two stable polarization states with opposite polarities ($\pm P_s$) [7]. At a constant temperature T, the differential of the free energy G with respect to polarization P can be expressed as $E = \frac{dG}{dP}$. This relationship allows us to analyze the behavior of the system and understand the hysteresis loop shown in Figure 1.4 [7].

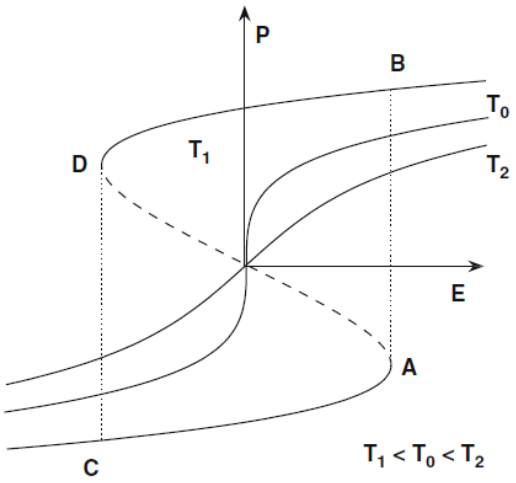

FIGURE 1.4 POLARIZATION P VS. ELECTRIC FIELD E FOR TEMPERATURES $T_1 < T_C = T_0 < T_2$, USING THE SAME PARAMETERS AS FIGURE 1.3 [7].

In the ferroelectric phase, the hysteresis loop represents the response of the material to an applied electric field. The curve between the two states A and C corresponds to unstable states, meaning that the material cannot maintain those polarization states indefinitely. Instead, the system undergoes a spontaneous transition from state A to state B and from state C to state D, following a path within the hysteresis loop. The corresponding electric field in states A or C, which is required to induce the transition to the stable states B or D, is known as the coercive field (E_c). The coercive field represents the minimum strength of the electric field required to reverse the polarization of the material and bring it from one stable state to another. It characterizes the resistance of the material to changes in polarization and is an important parameter in understanding and engineering ferroelectric materials [7].

1.1.1.3 Ferroelectric Domains

During a phase transition to a ferroelectric state, the crystal forms separate regions called domains, each with uniform polarization but different directions ($+P_s$ or $-P_s$). These domains are created to minimize the crystal's free energy [6]. When domains with opposite polarizations exist adjacent to each other, they are separated by structures known as domain walls [8]. In ferroelectric materials, domain walls act as interfaces where the polarization gradually changes between adjacent domains. To reverse the polarization, an external electric field stronger than the coercive field (E_c) is applied [7]. This field induces the switch from the material's original polarization state to the opposite state.

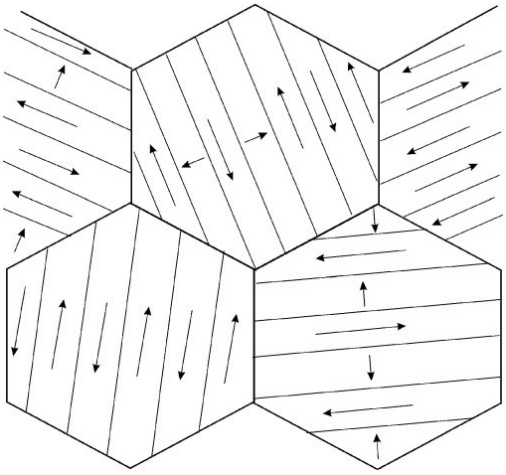

FIGURE 1.5 SCHEMATIC DRAWING OF HEXAGONAL POLYCRYSTALLINE STRUCTURES WHICH ARE DIVIDED INTO DOMAINS [9].

Figure 1.5 depicts hexagonal polycrystalline structures divided into distinct domains, showing the orientations of spontaneous polarization with arrows. In tetragonal systems like this, two types of domain walls are observed: 90° domain walls and 180° domain walls [9]. At a 180° domain wall, adjacent domains have opposite polarization arrangements, while at a 90° domain wall, adjacent domains have perpendicular polarization orientations. The presence and properties of these domain walls significantly influence the characteristics of ferroelectric materials. The arrangement and behavior of ferroelectric domains play a vital role in determining various material properties, including electrical, optical, acoustic, pyroelectric, and mechanical aspects [6].

1.1.2 Lithium Niobate

In the late 1960s, researchers initiated the deposition of lithium niobate ($LiNbO_3$) as a significant development, primarily targeting signal processing chips for television and video recorders [10]. This pivotal moment marked the commencement of experimental endeavors to exploit $LiNbO_3$ as a material to enhance the performance and functionality of electronic devices. Concurrently, multiple projects were underway, focusing on harnessing the distinctive properties of $LiNbO_3$ for applications in the field of optics. Specifically, these projects aimed to leverage $LiNbO_3$'s capabilities in optical dispersion compensators, optical wavelength converters, and optical parametric amplifiers. A noteworthy approach involved the utilization of periodically poled lithium niobate proton-exchanged waveguides, which exhibited improved performance and versatility in these optical devices [10].

1.1.2.1 Lithium Niobate crystal structure

Abrahams et al. conducted a comprehensive investigation into the crystal structure of single crystal lithium niobate using both X-ray diffraction and neutron diffraction techniques [12]. Their research aimed to gain a detailed understanding of the atomic arrangement and symmetry of $LiNbO_3$. Lithium niobate is classified as a ferroelectric oxide and possesses a trigonal paraelectric crystal structure. This structure exhibits a non-centrosymmetric arrangement.

The paraelectric-to-ferroelectric phase transition in $LiNbO_3$ occurs at a relatively high temperature of 1483°C. At room temperature, material maintains its ferroelectric state, exhibiting a spontaneous polarization of approximately 71 $\mu C/cm^2$ [11]. This spontaneous polarization represents the presence of a net electric dipole moment per unit area in the crystal, which arises from the alignment of electric dipoles within the material.

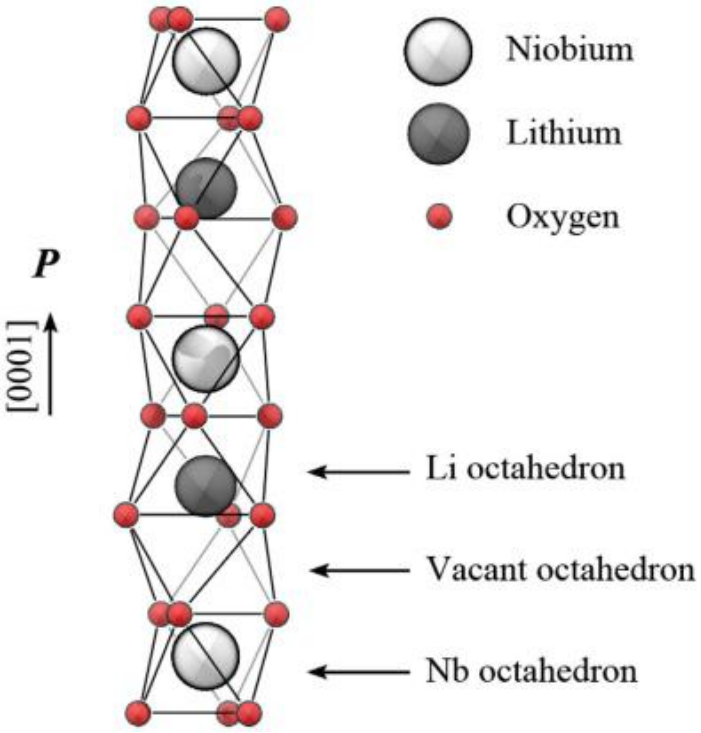

FIGURE 6. SCHEMATIC REPRESENTATION OF THE FERROELECTRIC $LiNbO_3$ CRYSTAL STRUCTURE HIGHLIGHTING THE CATIONIC POSITIONS WITH RESPECT TO THE OXYGEN OCTAHEDRA [12].

At room temperature (RT), $LiNbO_3$ possesses a crystal structure that belongs to the rhombohedral (trigonal) space group R3c, characterized by a point group of 3m. Above the phase transition temperature, the crystal undergoes a structural transformation, adopting the centrosymmetric space group R3m [7]. The crystal structure of $LiNbO_3$ can be described in terms of hexagonal unit cells, highlighting its underlying symmetry and arrangement [13].

In the stoichiometric composition of $LiNbO_3$, the interstitial positions of the oxygen octahedra along the *c*-axis are occupied by Li ions (one-third), Nb ions (one-third), and remain vacant (one-third), forming a repetitive sequence denoted as -Li-Nb-vacancy-Li-Nb- [14]. This arrangement elucidates the structural pattern within the crystal lattice.

Sanna et al. presented a schematic representation of the ferroelectric lithium niobate crystal structure, emphasizing the positions of the cations [12]. It is worth noting that the positively charged cations do not align precisely at the centers of the negatively charged oxygen cages or within an oxygen plane; instead, they undergo a slight shift along the z-axis. This subtle displacement of the cationic sublattice in relation to the oxygen octahedra leads to a separation of charges, resulting in the exhibition of spontaneous polarization in $LiNbO_3$. Importantly, the direction of the spontaneous polarization aligns with the orientation of the cationic shift [12].

The lattice parameters of $LiNbO_3$, described within the hexagonal coordinate system, are conventionally given as a = 5.1483 Å and c = 13.863 Å [15]. These lattice parameters define the dimensions and symmetry of the hexagonal unit cell, providing key insights into the crystal structure of $LiNbO_3$.

1.1.2.2 Ferroelectricity of $LiNbO_3$

Jie Zhu conducted a study where the actual results of the P-E (polarization-electric field) measurement were presented, as depicted in Figure 7. In this particular experiment, a thin film layer with a robust (0 0 6) crystalline orientation was deposited onto a p-type silicon substrate using RF magnetron sputtering [16]. The thickness of the thin film layer was measured to be 400 nm. It is noteworthy to mention that the P-E curve obtained from this measurement did not reach saturation. From the P-E curve obtained in this experiment, the coercive field Ec, which represents the electric field required to reverse the polarization, was determined to be ±420 kV/cm [16]. This value indicates the strength of the electric field needed to induce a complete reversal of the polarization direction in the thin film.

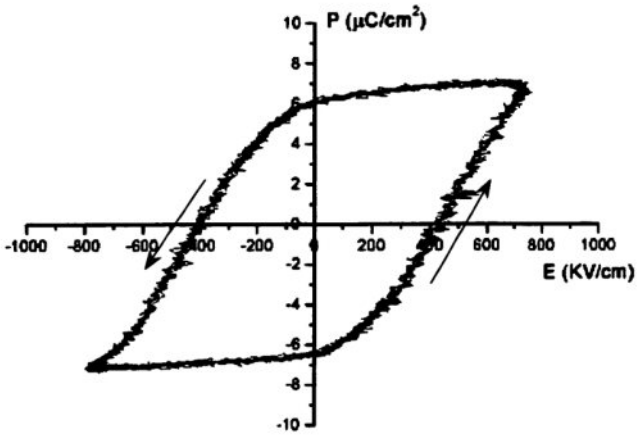

FIGURE 7. P-E HYSTERESIS LOOP OF $LiNbO_3$ THIN FILM DEPOSITED ON A P-TYPE SI (1 1 1) SUBSTRATE BY RF MAGNETRON SPUTTERING [16].

The conductivity of $LiNbO_3$ can be categorized into three distinct parts, each governed by different dominant conduction mechanisms [10]. At temperatures exceeding 1000°C, the conduction is primarily intrinsic in nature, meaning it arises from the inherent properties of the material itself. Between 1000°C and 400°C, which is close to room temperature, the main contributors to the conductivity are mobile protons. These protons are able to move through the crystal lattice, facilitating the flow of electric current. At lower temperatures, a different conduction mechanism comes into play. In this regime, the conductivity is attributed to a

hopping mechanism involving small electrons or small polarons. These entities exhibit a characteristic behavior, enabling the transfer of charge and contributing to the overall conductivity of the material [10].

1.1.2.3 Thermal Expansion Coefficient In Lithium Niobate

Thermal expansion coefficients are an important property of materials as they describe how the dimensions of a material change with temperature. In the case of lithium niobate single crystals with congruent composition, their thermal expansion coefficients have been studied in the temperature range of 50 to 1000°C by J. C. Vyas and S. G. Singh [17]. The thermal expansion coefficients of $LiNbO_3$ single crystals exhibit anisotropy, meaning that they vary depending on the direction in which the crystal is measured. Specifically, in the x or y directions (in-plane directions), $LiNbO_3$ crystals have positive thermal expansion coefficients. This means that as the temperature increases, the crystal expands in these directions [17]. However, the thermal expansion coefficient along the z direction (out-of-plane direction) of $LiNbO_3$ crystals behaves differently. As the temperature increases, the thermal expansion coefficient along the z direction decreases. At higher temperatures, it reaches a point where it becomes negative [17]. This implies that along the z direction, the crystal contracts with increasing temperature.

The thermal expansion coefficients of lithium niobate ($LiNbO_3$) single crystals were measured along the x, y, and z axes in the temperature range studied [17]. According to J. C. Vyas and S. G. Singh findings, the measured value of the thermal expansion coefficient α_x along the x-axis, as shown in Figure 1.8, exhibits a small decrease in magnitude with an increase in temperature. The variation of the thermal expansion coefficient along the y-axis was found to be similar to that along the x-axis. Interestingly, the researchers observed that the thermal expansion coefficient α_z along the z-axis, which corresponds to the out-of-plane direction, is much smaller compared to α_x. In fact, it is noted that α_z is approximately one-sixth of the magnitude of α_x near room temperature. Furthermore, as the temperature increases, α_z decreases further. At around 650°C, it reaches a point where it becomes almost zero [17].

These observations highlight the anisotropic nature of the thermal expansion behavior in $LiNbO_3$ single crystals. The differences in the thermal expansion coefficients along the x, y, and z axes indicate that the crystal undergoes distinct dimensional changes in different directions as the temperature varies. The significant difference between α_z and α_x suggests that $LiNbO_3$ crystals exhibit a notable contraction along the z-axis as the temperature increases.

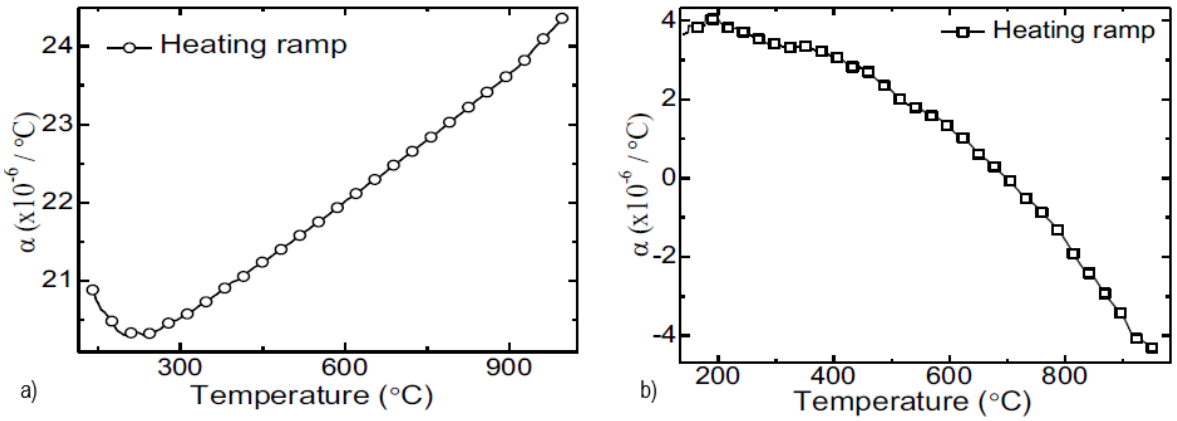

FIGURE 1.8 THERMAL EXPANSION COEFFICIENTS (A) A_X ALONG THE CRYSTALLINE X-AXIS OF $LiNbO_3$ WITH RESPECT TO TEMPERATURE (B) A_Z ALONG THE CRYSTALLINE Z-AXIS OF $LiNbO_3$ WITH RESPECT TO TEMPERATURE. [17].

Understanding the variation of thermal expansion coefficients is essential for applications involving $LiNbO_3$ crystals, as it enables engineers and researchers to account for the dimensional changes that may occur due to temperature fluctuations. It also provides insights into the structural behavior and stability of $LiNbO_3$ crystals under different thermal conditions during and after growth.

1.1.2.4 Stoichiometry

The growth of large, high-quality single crystals of materials like lithium niobate ($LiNbO_3$) can be challenging due to their complex phase transitions [18]. The phase diagram of the Li_2O–Nb_2O_5 system, as depicted in Figure 1.9, provides valuable insights into the composition and phase behavior of $LiNbO_3$.

According to the phase diagram (Figure 9), $LiNbO_3$ is a material with a variable composition, meaning that its chemical composition can vary within a certain range. Specifically, it exhibits a large solid solution range of approximately 6 mol% at temperatures above 1150°C [7]. This indicates that $LiNbO_3$ can accommodate the substitution of certain amounts of other elements within its crystal lattice without undergoing significant phase changes. The presence of a solid solution range in the Li_2O–Nb_2O_5 system is significant for crystal growth processes and material engineering. It allows for the incorporation of dopants or the control of chemical composition to tailor the properties of $LiNbO_3$ crystals, such as their optical, electrical, and piezoelectric characteristics. However, it also adds complexity to crystal growth methods and requires careful control of the growth conditions to achieve high-quality crystals with the desired properties.

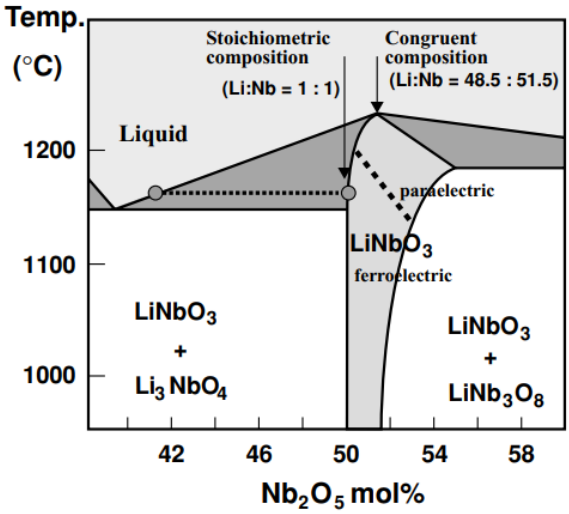

FIGURE 9. SCHEMATIC PHASE DIAGRAM OF Li_2O-Nb_2O_5 PSEUDOBINARY SYSTEM IN THE VICINITY OF $LiNbO_3$ [18].

Solid solutions of lithium niobate can be characterized by the ratio R = {Li}/{Nb}, where {Li} and {Nb} denote the concentrations of lithium and niobium, respectively, in mol%. In the case of single crystals, deviations from the stoichiometric point (R = 1) are inherent, meaning that the actual composition of the crystal deviates from the ideal ratio. Among the different compositions within the solid solution range, the congruent point, characterized by R = 0.944, is of particular importance [18]. At this composition, an inflection point occurs on the liquidus–solidus curve, indicating the transition from the Li_2O:Nb_2O_5 melt to the growth of the $LiNbO_3$ crystal. It is at this congruent point that the highest uniformity of properties is typically achieved.

However, it's worth noting that the formation of LiNbO3 single phase is limited by the presence of two secondary phases: Li_3NbO_4 and $LiNb_3O_8$. These secondary phases, often referred to as "parasitical" phases, have inferior physical properties compared to $LiNbO_3$ and can negatively impact the desired properties of the crystal [19]. Therefore, efforts are made to minimize the presence of these secondary phases during crystal growth processes.

In stoichiometric crystals, the unit cell is free from defects, meaning that the composition of the crystal precisely corresponds to the ideal chemical formula. However, in the case of congruent crystals, which have a composition slightly deviating from stoichiometry, the presence of defect clusters can occur. The formation of these defect clusters depends on the cooling process of the crystal [8]. In the case of slow cooling from high temperatures, stable defect clusters can form in congruent crystal. These stable defect clusters are established during

the cooling process and can persist in the crystal structure at lower temperatures. On the other hand, frustrated defect clusters can be obtained in congruent crystals after domain reversal at room temperature. These defect clusters arise due to the reorientation of domains and the associated strain in the crystal structure [8].

	Congruent $LiNbO_3$ [20]	Near-stoichiometric $LiNbO_3$ [21]
Li_2O composition (mol %)	0.485	0.489 [21]
Curie Temperature	1138°C [22]	1198°C [22]
Coercive fields at 296°K, $kVcm^{-1}$	E_f~206.7 [23] E_r~168.5 [23]	E_f~40.5 [22] E_r~33.1 [21]
Internal field, E_{int} $kVcm^{-1}$	20-30 [24]	3.7 [24]
Thermal expansion coefficient, ($\times 10^{-6}$)	α_c=2.7 α_a=19.2 [25]	α_c=2.8 α_a=17.2 [26]

TABLE 1.1 EFFECT OF NON-STOICHIOMETRY OF LI_2O ON PROPERTIES OF $LINBO_3$ SINGLE CRYSTAL

The non-stoichiometry of Li_2O in $LiNbO_3$ has a significant influence on the structural properties of the crystal. This influence is illustrated in Table 1.1, which provides information about how variations in the Li_2O content affect various structural parameters of $LiNbO_3$. Understanding the impact of non-stoichiometry on the crystal structure is crucial for characterizing and controlling the properties of $LiNbO_3$ crystals, as well as for tailoring their performance for specific applications. In the case of stoichiometric crystals, the unit cell has no defects. In congruent crystals, the defect cluster can be in stable (obtained when the crystals is cooling down slowly from high temperature) or frustrated (obtained after domain reversal at room temperature) [8].

Table 1.1 presents the important characteristics of single crystals of $LiNbO_3$, highlighting the significant differences that can arise even with small variations in composition. One such variation is the increase in the amount of Nb atoms, which has been observed to result in an increase in the Curie temperature of $LiNbO_3$ [21]. The Curie temperature is the temperature at which the ferroelectric-to-paraelectric phase transition occurs, and it is an important parameter that determines the material's behavior.

Another notable difference is the decrease in coercive fields with near-stoichiometric lithium niobate. Coercive fields represent the strength of the external electric field required to reverse the polarization of the material. It is interesting to note that the coercive fields are reduced by almost five times in near-stoichiometric lithium niobate compared to other

compositions [21]. This indicates that near-stoichiometric crystals exhibit a higher susceptibility to polarization reversal, which can be advantageous for certain applications.

Additionally, the thermal expansion coefficient of $LiNbO_3$ is influenced by the composition. The thermal expansion coefficient is a measure of how the material expands or contracts with changes in temperature. Near-stoichiometric lithium niobate exhibits a lower thermal expansion coefficient compared to other compositions, indicating that it is less prone to significant dimensional changes with temperature variations [25], [26]. This can be important for maintaining the stability and reliability of devices and structures incorporating $LiNbO_3$.

These differences in important characteristics emphasize the sensitivity of $LiNbO_3$ properties to even minor changes in composition. It highlights the need for precise control and characterization of the material's composition for specific applications, as these variations can have a significant impact on its behavior and performance.

1.2 Filters and acoustic devices

$LiNbO_3$ is extensively used as a piezoelectric substrate and layer in acoustic devices. As a stable and reliable material, $LiNbO_3$ enables efficient transduction of acoustic waves in various devices such as SAW devices, resonators, filters, and delay lines [27], [28]. Additionally, thin films of $LiNbO_3$ can be deposited as functional layers to enhance device performance by improving sensitivity, bandwidth, and efficiency. With its unique combination of properties, including high piezoelectric coefficient, dielectric constant, and chemical stability, LiNbO3 contributes to advancements in telecommunications, sensing technology, and other fields reliant on precise acoustic wave manipulation [27], [29]. In this section of the chapter, we will delve into the different filters and acoustic devices based on of $LiNbO_3$.

1.2.1 Acoustic waves: different kinds

Acoustic devices are categorized based on the type of wave they use, leading to designations like Surface Acoustic Wave (SAW) and Bulk Acoustic Wave (BAW) devices. This classification considers the physical characteristics and propagation paths of waves. Some waves, like Lamb waves, exhibit features from both SAW and BAW devices.

SAW devices primarily utilize surface acoustic waves that propagate along the material's surface, allowing precise wave control and manipulation. They are advantageous for high-frequency applications like telecommunications and sensing systems. BAW devices, on the other hand, use bulk acoustic waves that propagate through the material's volume, enabling broader acoustic interactions. They are commonly used in frequency control components, filters, and resonators.

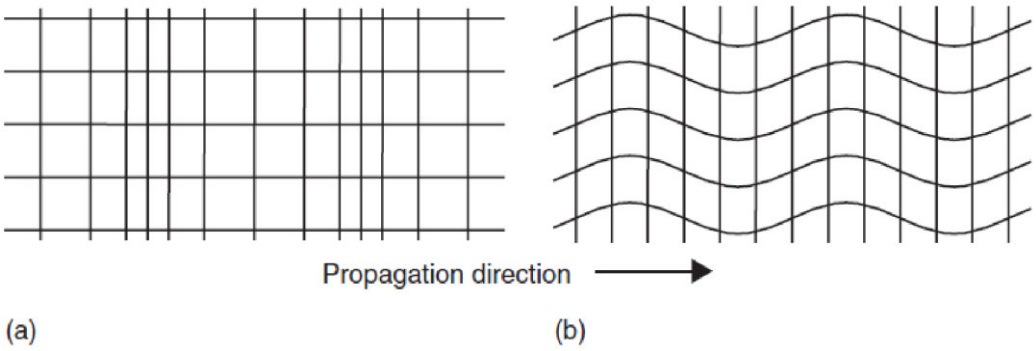

FIGURE 1.10 REPRESENTATION OF THE LONGITUDINAL (A) AND TRANSVERSE (B) MODES OF A BULK ACOUSTIC WAVE [30].

Bulk Acoustic Waves (BAWs) exhibit propagation within a confined medium and can be classified as longitudinal or transverse, depending on the direction of particle displacement in relation to the wave propagation. Longitudinal waves are characterized by particle displacement that occurs parallel to the direction of wave propagation (Figure 1.10 (a)), while transverse (shear) waves involve particle displacement perpendicular to the wave propagation direction (Figure 1.10 (b)) [30].

Surface Acoustic Waves (SAWs) propagate along the surface of a material. Among the different types of surface acoustic waves, Rayleigh waves are commonly used in practical applications. Rayleigh waves consist of two components, causing displacements both parallel and perpendicular to the surface [31]. This results in a particle displacement pattern that forms an elliptical shape [32], as illustrated in Figure 11.

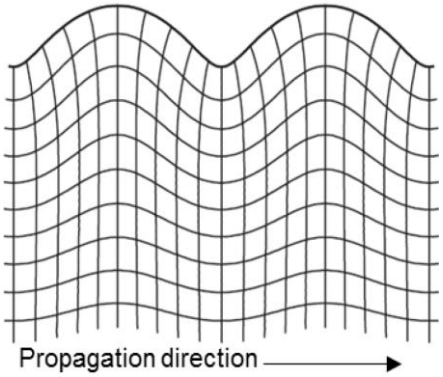

FIGURE 1.11. REPRESENTATION OF THE STRAIN OF A MEDIUM IN WHICH A RAYLEIGH WAVE IS PROPAGATING [32].

It is worth noting that Surface Acoustic Wave (SAW) devices typically operate within the frequency range of 0.5-3.5 GHz [33]. On the other hand, Bulk Acoustic Wave (BAW) devices operate at higher frequencies, typically in the range of 3-8 GHz [33]. The choice between SAW and BAW devices depends on the specific requirements of the application, including the desired frequency range, power consumption, and performance characteristics.

1.2.2 SAW devices

After the discovery of the Interdigitated Transducer (IDT), the first surface acoustic wave (SAW) devices were introduced in 1965 [34]. This marked a significant milestone, revolutionizing acoustic device technology and leading to advancements in telecommunications, sensing, and signal processing.

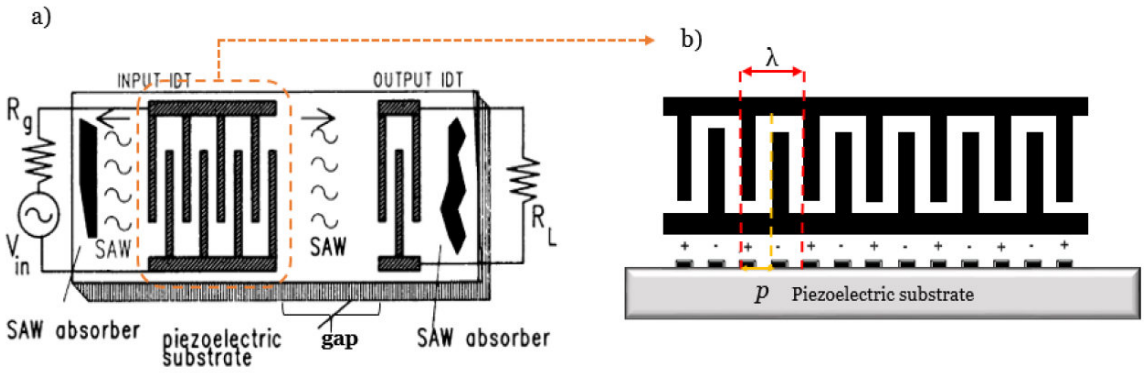

FIGURE 1.12. SCHEMATIC REPRESENTATION OF A BASIC SAW DELAY LINE (A). THE PROPAGATION OF SAW [31].

A typical SAW device, such as a delay line shown in Figure 1.12 [31] , consists of periodically spaced metal electrodes connected to two larger electrodes. When a voltage is applied across the electrodes, an electric field is generated, causing compression and expansion within the piezoelectric substrate and resulting in the propagation of a surface acoustic wave along its surface. This allows efficient conversion and transformation of mechanical energy into electrical energy and vice versa [31].

The mechanical period (p) of the device corresponds to the distance between two electrodes, and the wavelength (λ) of the propagating acoustic wave is equal to twice the mechanical period (λ=2p), as illustrated in Figure 1.12, b. The number of electrodes (N_p) directly influences the bandwidth of the device. A lower value of Np results in a wider bandwidth (Δf) for a constant central frequency (f_c), which can be expressed as: $N_p = \frac{f_c}{\Delta f}$. These relationships are crucial for designing and optimizing the performance of SAW devices.

1.2.2.1 TF-SAW

The thin film surface acoustic wave (SAW) devices consist of a layered structure where a piezoelectric film is deposited onto a non-piezoelectric substrate, as shown in Figure 13 [35]. To ensure optimal performance of thin film surface acoustic wave (SAW) devices, the thickness of the piezoelectric film is typically kept below one SAW wavelength [35]. This requirement helps to maintain the desired acoustic wave propagation characteristics and avoids interference effects. In addition to the thickness considerations, transducer quality films for SAW devices should exhibit certain key characteristics. One important attribute is high electrical resistivity, which minimizes unwanted electrical losses and ensures efficient signal transmission.

Furthermore, an oriented crystalline structure is desirable in the piezoelectric film. This orientation enhances the piezoelectric effect [35].

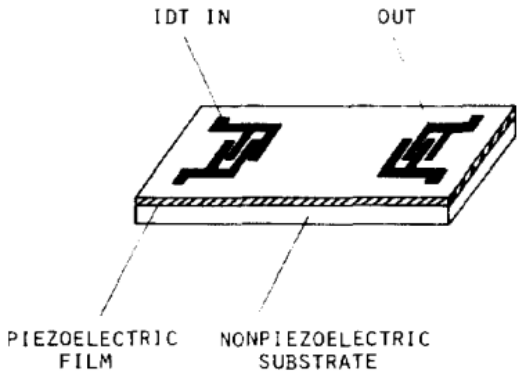

FIGURE 1.13. SHEMATIC REPRESENTATION OF THIN FILM SAW DEVICES [37].

The thickness of the piezoelectric film should be less than one SAW wavelength. Transducer quality films should have the basic characteristics of high electrical resistivity and an oriented crystalline structure, which yields a strong piezoelectric effect [35]. The frequency response of thin film surface acoustic wave (SAW) devices is typically represented as $f_0 = \frac{v}{\lambda}$, where v is the phase velocity and λ is the wavelength of the acoustic wave propagating [35].

In the hypothetical scenario where an ideal conductor is placed on the surface of the device, the electromechanical coupling factor (k_{eff}) can be determined using the following relation: $k_{eff}^2 = \frac{2\Delta v}{v}$. Here, Δv represents the change in velocity of the acoustic wave compared to the device without the presence of the ideal conductor [35]. This coupling factor is an important parameter that quantifies the efficiency of energy transfer between electrical and mechanical domains in the device [37].

Thin film surface acoustic wave (TF-SAW) devices often utilize piezoelectric ZnO layers as the active material [37], [38]. Thin film surface acoustic wave (TF-SAW) devices often utilize piezoelectric ZnO layers as the active material [35], [36].

1.2.3 BAW devices

The BAW (Bulk Acoustic Wave) resonator is a layered structure comprising a piezoelectric film positioned between two metallic electrodes. The region where the upper and lower electrodes overlap with the piezoelectric layer in the vertical direction is referred to as the active area of the resonator [33]. This active area plays a crucial role in the generation and propagation of acoustic waves within the resonator.

The thin film resonating material is a critical component of BAW (Bulk Acoustic Wave) devices. It consists of a piezoelectric film positioned between two metallic electrodes, as illustrated in Figure 1.14, a [37]. The piezoelectric film serves as the active element responsible for converting electrical signals into mechanical vibrations. From a physics perspective, the BAW resonator can be likened to a simple capacitor, as shown in Figure 1.14, b. When a differential voltage is applied across the two electrodes, an acoustic wave is generated within the piezoelectric film. This wave propagates through the thickness direction of the film, leading to acoustic reflections at the film surfaces. The resonance of the BAW device occurs when the acoustic wave is excited in the thickness direction and is determined by the properties of the piezoelectric film and the electrodes [39]- [38]. In BAW devices, materials such as Aluminum Nitride (AlN) and ZnO are commonly used as the piezoelectric film. These materials are selected for their balanced performance, manufacturability, and reliability [38].

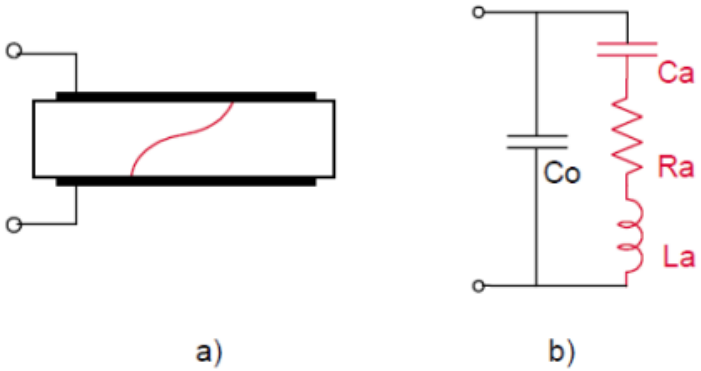

FIGURE 14. FIG. 2. (A) A BASIC BAW RESONATOR (B) THE ELECTRICAL EQUIVALENT MODEL OF A BAW RESONATOR [37]

In BAW (Bulk Acoustic Wave) devices, the resonance phenomenon occurs when the reflected waves align with the incident waves, leading to constructive interference. This can be mathematically described by the equation:

$$f = \frac{nV}{2h},$$

where f represents the resonance frequency, n is an integer representing the number of the standing wave (typically n = 1 for the fundamental mode), V is the velocity of the acoustic wave, and h is the thickness of the piezoelectric layer [39].

1.2.3.1 FBAR devices

The FBAR (Film Bulk Acoustic Resonator) device consists of a thin piezoelectric film positioned between two electrodes, utilizing the fundamental concept of having free surfaces

on both sides of the BAW resonator [40]. The design and fabrication of the FBAR resonator can be achieved through two common methods, as illustrated in Figure 1.15. In the first variant, a sacrificial support layer is placed below the resonator during the device fabrication process. This support layer is later removed, leaving the resonator suspended (Figure 1.15, a). The second approach involves etching the substrate from the back of the wafer towards the front surface, creating a cavity under the resonator (Figure 15, b) [40].

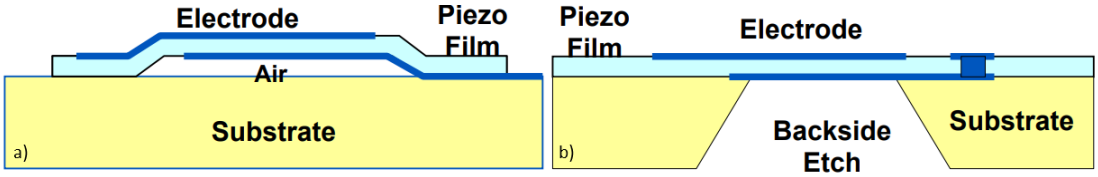

FIGURE 15. FBAR CROSS-SECTION. A) SACRIFICIAL SUPPORT LAYER B) BACKSIDE SUBSTRATE ETCH [40].

As previously mentioned, the thickness of the film and the mass of the electrodes play a critical role in determining the resonant frequencies of the FBAR devices [37]. These parameters directly affect the mechanical properties of the resonator, such as its stiffness and mass, which in turn influence the resonant frequency. By carefully controlling the thickness of the piezoelectric film and the mass of the electrodes, the resonant frequencies of the FBAR devices can be tailored to meet specific application requirements.

1.2.3.2 SMR devices

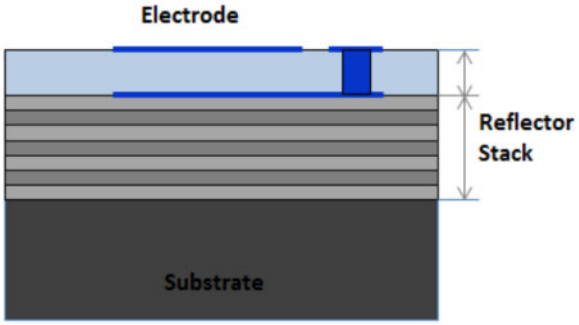

FIGURE 16. CROSS SECTION VIEW OF A SOLIDLY MOUNTED RESONATOR (SMR) [41].

Another BAW topology is the Solidly Mounted Resonator (SMR), which shares a similar architecture to the FBAR device, but with a distinct difference in the design of the acoustic cavity. In the SMR, instead of an air gap, a Bragg reflector is employed [41]. The Bragg reflector, also known as a Bragg mirror, is a multilayer structure that consists of alternating layers with different acoustic impedances. This arrangement creates a periodic

variation in the acoustic impedance, resulting in a high reflectivity for acoustic waves within a specific frequency range.

The Bragg reflector is positioned between the Si wafer and the resonator to minimize losses in the substrate, as depicted in Figure 1.16. This reflector is composed of multiple layers, each with a thickness equal to one-quarter of the wavelength, and with alternating high and low values of acoustic velocity. The design of the reflector depends on the acoustic impedance of the substrate. The first layer of the reflector is chosen to have an opposite impedance to that of the substrate, and subsequent layers alternate in impedance with each other [41]. Common materials used for the low impedance layers of the Bragg reflector include SiO_2, AlN, and ZnO, while high impedance layers often consist of Molybdenum (M) and Tungsten (W). The Bragg reflector serves as a means to enhance the reflectance of the resonator. By increasing the number of layers in the stack, a higher reflection coefficient can be achieved, thereby improving the performance of the resonator [41], [42].

1.2.4 Frequency bands and filter types

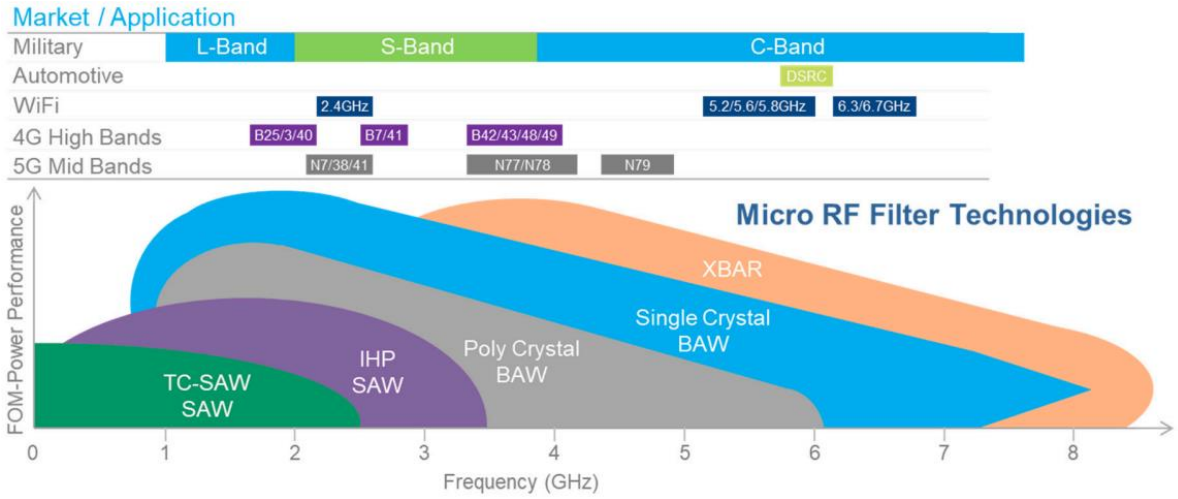

FIGURE 1.17. MARKET APPLICATION AND BAND ALLOCATION OF RADIO FREQUENCY (RF) FILTER TECHNOLOGIES [33], [43].

RF filters play a crucial role in various applications, and currently, the dominant technologies in this field are surface acoustic wave (SAW) filters and bulk acoustic wave (BAW) filters, as mentioned earlier. These micro RF filter technologies are widely employed in a range of applications, as depicted at the top of Figure 1.17.

BAW filters, in particular, have gained significant recognition due to their advantages in terms of high operating frequency and power capacity when compared to SAW filters [33],

[43]. As the demand for higher frequencies increases, there is a notable shift in user preference from the implementation of thin film SAW (TF-SAW) devices to BAW devices. This transition is driven by the need for enhanced performance at higher operating frequencies. For a more detailed understanding of the technology crossover in mobile commercial applications, Figure 1.18 provides a comprehensive depiction. This graph illustrates the general landscape of mobile commercial applications and highlights the points of transition as SAW technology evolves into temperature compensated SAW (TC-SAW) technology and eventually progresses towards BAW devices [40]. This visual representation offers valuable insights into the specific areas where different technologies find their optimal use within the mobile application space.

Over time, Surface Acoustic Wave (SAW) technology has proven to be highly effective in delivering RF filters with compact sizes and cost-efficient manufacturing processes. It has been widely adopted due to its reliable performance and decreasing cost structure. However, as the demand for higher frequencies in mobile handsets has grown, conventional SAW structures face limitations in meeting these increased requirements.

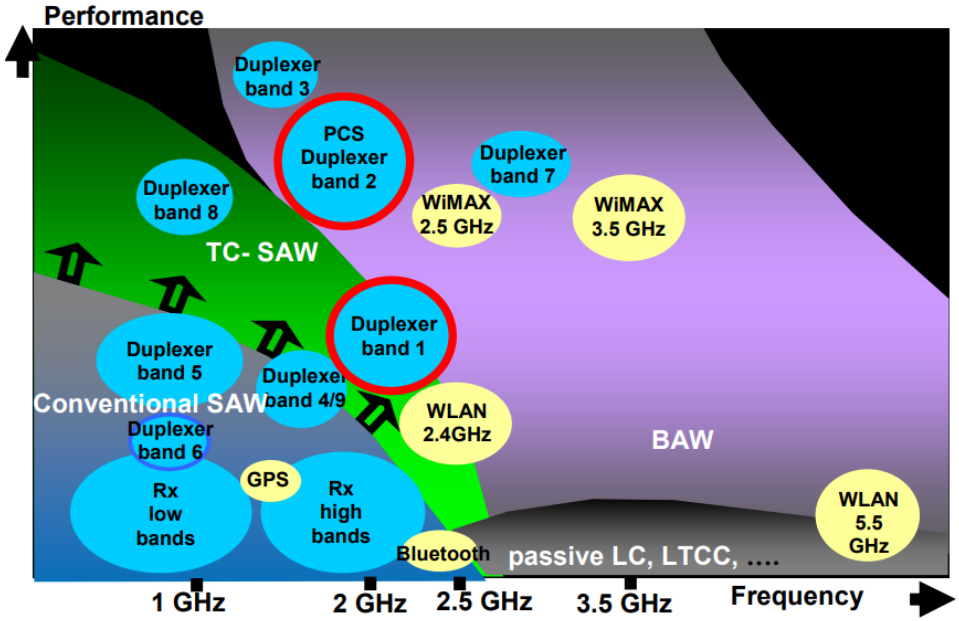

FIGURE 1.18. MOBILE COMMERCIAL APPLICATIONS MAPPED TO SAW, TEMPERATURE COMPENSATED SAW AND BAW TECHNOLOGIES [40].

To address these challenges, Bulk Acoustic Wave (BAW) devices have emerged as a viable solution. BAW devices offer the capability to operate at frequencies starting from 1.8 GHz and above, effectively surpassing the limitations of conventional SAW technology. Additionally, BAW technology shows promise in terms of achieving a low-cost structure that can compete with SAW devices, thus further enhancing its attractiveness [40].

The integration of BAW devices in RF filters for higher handset frequencies not only enables improved performance but also indicates the potential for cost-effective solutions. As a result, BAW technology has gained traction in the industry as a viable alternative to address the evolving demands of high-frequency applications in mobile communication systems.

1.3 Thin film elaboration techniques

1.3.1 Thin film requirements

The growth of homogeneous stoichiometric crystals poses significant challenges, which have been addressed by employing a modified Czochralski method in a Li_2O-rich atmosphere [44]. Consequently, the production of $LiNbO_3$ stoichiometric crystals is costly and their availability remains highly limited. In order to ensure high performance when applying thin films of $LiNbO_3$ in electrically active acoustic and optical devices, several specific requirements must be met, as indicated by reference [45]:

- Well Crystallized Films: The thin films should exhibit a well-developed crystalline structure to achieve the desired functionality.
- Pure $LiNbO_3$ Phase: Attaining a pure $LiNbO_3$ phase is essential for optimal performance of the thin films.
- Smooth Surface: The surface of the films needs to be smooth to avoid any adverse effects on their optical and electrical properties.
- Twin-Free and Domain-Free Crystals: High-quality thin films necessitate the absence of crystal twins and domains.
- High Texture Quality: The thin films should possess a high-quality texture to ensure proper alignment of the crystal lattice.

Epitaxy refers to the growth of a crystal on a crystalline substrate in a manner where the orientations of the two crystals exhibit a specific relationship defined by the interface between them. This results in a distinctive relationship between the lattice and lattice parameters of the substrate and the deposited film. A thin film is considered to be coherently strained to the substrate when it adopts the same in-plane lattice parameters as the substrate throughout its thickness. In simpler terms, one can envision this as the film being subjected to biaxial strain. While these are general examples, other forms of epitaxy are also possible. By using different substrate orientations, it becomes possible to control the surface orientation of the film [46].

The crystallinity of the grown films depends on the temperature and is influenced by various factors [45]:

- Growth Method: The specific technique employed for thin film growth significantly impacts the resulting crystallinity.
- Geometry of the Growth Chamber: The design and configuration of the growth chamber play a crucial role in the crystallization process and subsequent film quality.
- Energy of Adatoms: The energy level of the adatoms, which deposit on the film surface during growth, affects the crystallization outcome.
- Substrate Surface: The quality, crystallinity, and energy of the substrate surface are critical factors influencing the crystallization process of the thin films.

Epitaxial growth, which requires high surface mobility of adatoms, necessitates significantly higher temperatures compared to those utilized for crystallization of amorphous layers or the growth of mono- and polycrystalline films [44].

In cases where the lattice mismatch between the film and substrate is significant, partially or fully relaxed films can be achieved. In such instances, above a certain critical thickness, the film adopts the energetically preferred lattice parameters of the bulk material. This relaxation occurs due to the formation of dislocations at the interface between the film and substrate. Strain and surface orientation are crucial factors in controlling ferroelectric thin films. However, epitaxial deposition techniques are also associated with high quality, enabling precise control over thickness and layering. This allows for the production of heterostructures and superlattices, where atomic-scale control is achievable with great precision [46].

1.3.2 Transfer techniques

To create heterogeneous thin film systems by combining multiple materials, techniques such as transfer, wafer bonding, and silicon-based methods are employed [47] - [48]. For silicon-based microelectromechanical system (MEMS) packaging, wafer bonding is a common choice [47], [49]. This involves joining wafers directly or with minimal pressure, electric fields, or intermediate layers, meeting the stringent demands of MEMS devices for airtightness and bonding strength [47].

Smart Cut^{TM} technology (Soitec, Bernin, France) is widely used for the fabrication of high-quality single-crystal thin film onto different substrates [47], [50]. The standard Smart Cut process for the thin film fabrication is shown in Figure 1.19. The first step in it is the oxidation of the surface. Then, by application of hydrogen ion (H^+), a destroyed layer on the subsurface implantation is created. With the help of the control of the implantation energy of the H^+ ions

thickness of the layer is determined. After that, the oxidized wafers are bonded together (active bonding). Finally, an annealing process is performed, and, depending on the material, the annealing temperature differs a lot [47]. Important to mention is that the donor wafers and substrates can be refreshed and reused after each layer transfer operation [47].

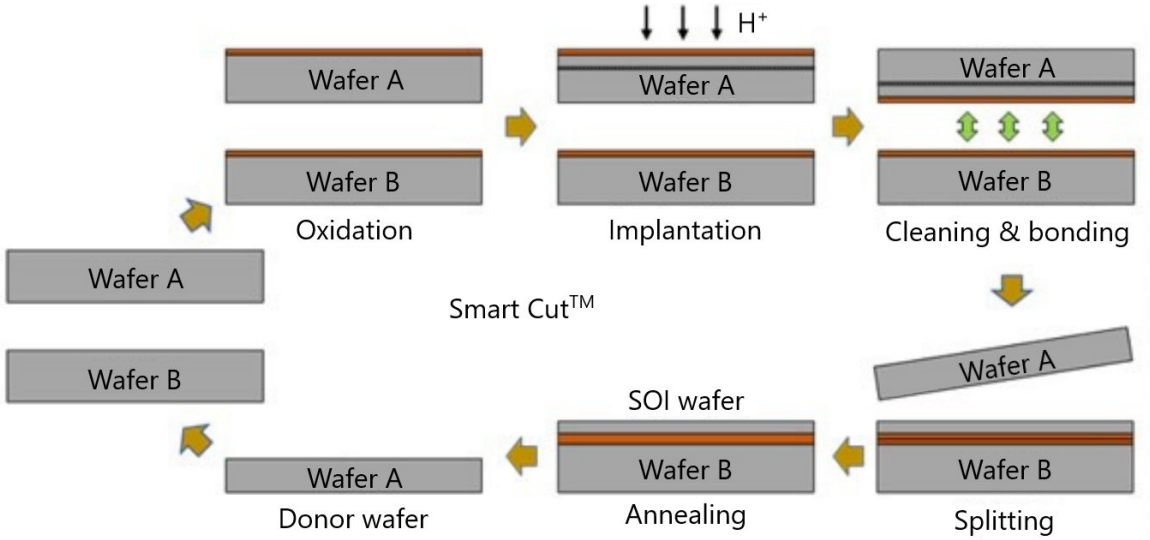

FIGURE 1.19. FLOW CHART OF THE SMART CUT™ PROCESS FOR THE THIN-FILM TRANSFER [47].

Piezoelectric on insulator (POI), or in our case, lithium niobate on insulator (LNOI) are sub-micron thick, single-crystalline $LiNbO_3$ films that stand on top of a transparent and lower refractive index substrate, typically silica (SiO_2) [51]. The LNOI wafers are fabricated using an ion-slicing process, similar to Smart Cut™, shown in Figure 1.20 [51]. Same, as in Smart Cut™, He^+ ions are implanted into a bulk $LiNbO_3$, to create a damaged layer (Figure 1.20, a). Then the ion-implanted lithium niobate is then flipped over and bonded to the substrate (Si, SiO_2, Al_2O_3, etc.) (Figure 1.20, b). After that, the bonded substrates are subsequently annealed to thermally induce stress in the damaged layer, resulting in the splitting of bulk $LiNbO_3$ at the damaged layer (Figure 1.20, c). Finally, polishing to remove the residual damage layer and to create a smooth surface is done (Figure 1.20, d) [51].

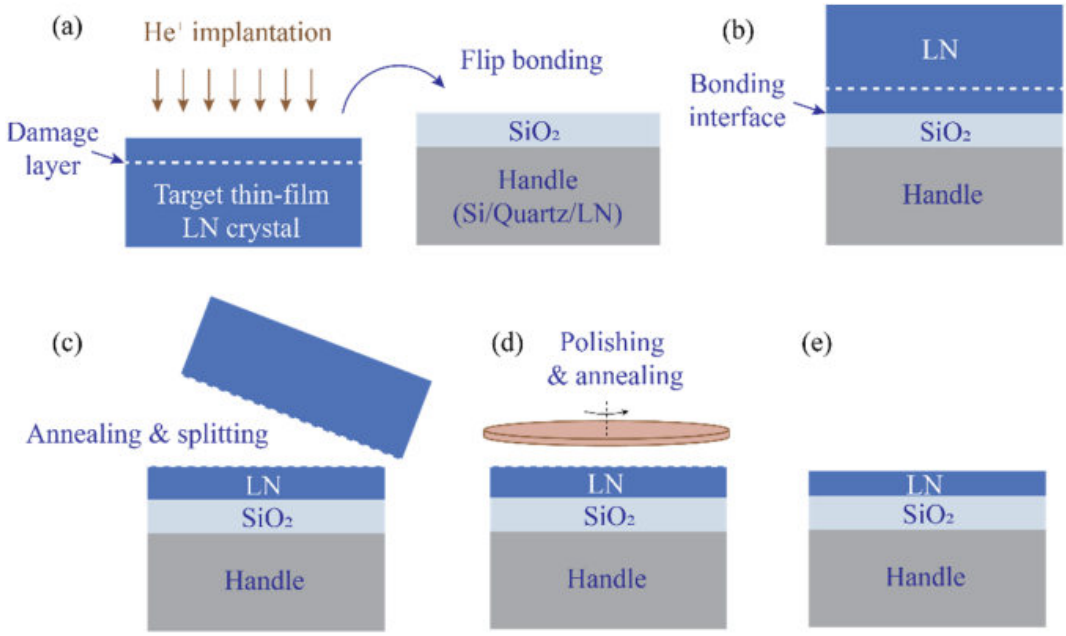

FIGURE 1.20. SCHEMATIC OF LNOI (POI) WAFER PRODUCTION [51].

Nowadays, LNOI wafers are commercially available in sizes up to 4 inches, with different choices of crystal orientations and bottom handles (with silicon or quartz substrates, pre-embedded bottom metal electrode layers, etc.). There are two major choices of $LiNbO_3$ crystal orientations – z-cut and x-cut, but other ones are also available [51]. Smart-cut technique allows bonding $LiNbO_3$ to metal electrodes or various other materials, harnessing its piezoelectric properties to enable lower voltage and lower loss operation. However, it still requires a significant minimum thickness (>300 nm) for successful implementation [25], [52]. During wafer bonding and the transfer of thin films, the thickness of the transferred film is typically limited to a few microns. This limitation arises from constraints in implant energies, which can cause damage due to straggle effects. Consequently, treatments are necessary to address the resulting rough surface [53]. High-temperature thermal annealing is often employed to restore the optoelectrical properties of the transferred film. This process helps mitigate the damage and optimize the overall performance of the thin film [25], [53].

Smart-cut $LiNbO_3$ technology offers comparable wafer quality to bulk LN. However, the available thickness range may not be ideal for efficient light coupling between the chip and external components such as large core fibers or nanoscale integrated optics [25]. To address this limitation, researchers have made significant progress in directly etching LN to fabricate compact optical devices. By utilizing a dry etch process to pattern a 600 nm smart-cut film, they have achieved a thin LN slab with a thickness of 250 nm, demonstrating optical propagation losses as low as 0.027 dB/cm [54].

1.3.3 Chemical Vapor Deposition and MOCVD

Chemical vapor deposition (CVD) encompasses diverse techniques involving the deposition of solid substances from vapor phases via chemical reactions near heated surfaces [55]. In each CVD process, a key step is introducing gaseous reactants into a reactor. Within, these reactants chemically transform on or near a heated substrate, converting gaseous reactants into solid material while generating gaseous byproducts [55].

Successful growth of single crystal films of $LiNbO_3$ on $LiTaO_3$ substrates with a (1 0 0) orientation using chemical vapor deposition (CVD) was achieved. The volatile complex of Li with 2,2,6,6-tetramethylheptane-3,5-dione served as the lithium source, while Nb pentamethylate was utilized as the niobium source. Deposition occurred at 450°C, with an argon carrier gas and oxygen (O_2) used to oxidize the organometallic compounds. Subsequently, the layer was heated at 1000°C in an oxygen atmosphere to convert it into a single crystal of $LiNbO_3$. The resulting structure served as an optical waveguide, but it exhibited high losses of approximately 40 dB/cm [56]. Another approach is direct liquid injection CVD, which involves injecting liquid precursors into a vaporization chamber equipped with injectors (similar to car injectors). The resulting precursor vapors are then transported to the substrate, following a similar mechanism as traditional CVD processes. Microwave-assisted CVD utilizes microwave energy to enhance the chemical reaction rates of the precursors, allowing for deposition at lower temperatures. Remote plasma-assisted CVD employs a plasma to accelerate chemical reactions of the precursors, enabling deposition at even lower temperatures [55].

Metal-organic chemical vapor deposition (MOCVD) processes involve both the chemical decomposition of precursor gases and the vaporization of a solid source. This technique is commonly used for depositing thin films of materials, especially semiconductors, and is widely employed in the production of electronic devices [55]. In a simplified explanation of the MOCVD growth process, two primary steps emerge. The initial step entails transporting molecules to the gas-solid interface. The subsequent step involves reactions at or near the interface, resulting in the creation of crystalline materiall [57].

Wernberg and co-researchers employed metalorganic chemical vapor deposition (MOCVD) to deposit lithium niobate thin films on (0001) sapphire substrates. They combined lithium dipivaloylmethane and niobium ethoxide to create a single-source precursor. This approach yielded films with a c-axis orientation, transparency, and a specular appearance. However, film smoothness was an issue observed during their study [58]. To improve this, they

switched from Li-DPM to a different precursor, $LiNb(OEt)_6$ [59]. This change reduced ligand-exchange reactions, enhancing X-ray diffraction (XRD) rocking curve quality in single-crystal films, notably lowering the full width at half maximum (FWHM) to 1368 arcseconds. This indicates better crystalline quality, and the new precursor also led to a minimal twinning rate of around 1%, underscoring film quality [59].

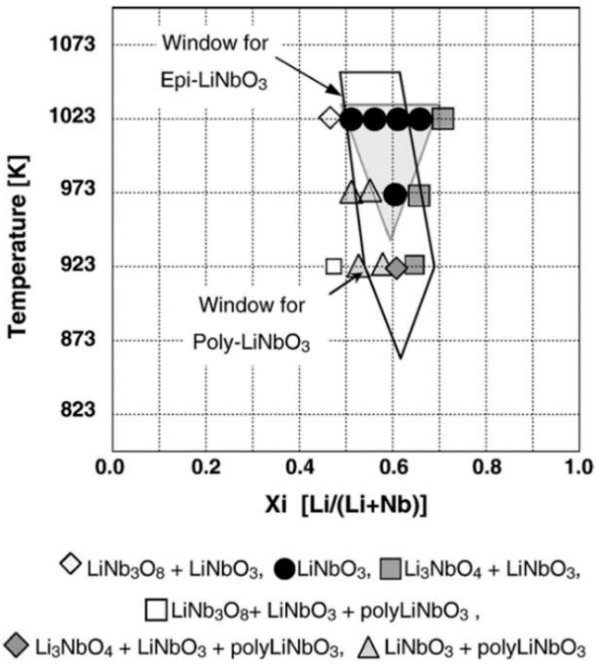

FIGURE 1.21. A PSEUDO-PHASE DIAGRAM VARYING THE LI AND NB COMPOSITION WITH GROWTH TEMPERATURE THAT SHOWS GROWTH WINDOWS FOR SINGLE AND MULTIPLE PHASE $LiNbO_3$ EPITAXY VIA MOCVD BY AKIYAMA ET AL. [60].

Feigelson et al. followed a similar approach in their study, using a mixture of Li(THD) and Nb(THD)4 in varying proportions for lithium niobate growth experiments. Their single-phase films with a c-axis orientation demonstrated remarkable outcomes, featuring a full width at half maximum (FWHM) of 156 arcseconds on Al_2O_3 substrates and 36 arcseconds on $LiTaO_3$ substrates, underscoring excellent crystalline quality [61], [62]. Furthermore, Feigelson et al. noted intriguing differences based on substrate choice. When growing $LiNbO_3$ on $LiTaO_3$ substrates, they observed no twinning, suggesting a favorable epitaxial relationship between the film and substrate [62]. Conversely, sapphire substrates led to twinning in $LiNbO_3$ films, which could be mitigated through high-temperature annealing [61], [63].

Akiyama and colleagues (referred to as Akiyama et al.) effectively regulated Li and Nb composition in their growth experiments by precisely managing precursor material flow. They also investigated the impact of substrate temperature on the Li-to-Nb ratio to find a growth window for single-phase $LiNbO_3$ film formation, shown in Figure 21. However, they observed

polycrystals within the epitaxial film during their study. [60]. Ongoing research focuses on the epitaxial growth of high-quality lithium niobate through metalorganic chemical vapor deposition (MOCVD). Recently, novel techniques like direct liquid injection MOCVD have been developed as alternative approaches in this area of study [64].

1.3.4 Atomic Layer Deposition

Atomic layer deposition (ALD) is an advanced technique used for depositing ultra-thin films on an industrial scale, providing precise control over film thickness and composition [65]. This deposition process involves the sequential injection of two or more precursors into a chamber containing a substrate, which is maintained at specific temperature and pressure conditions. Through a series of alternating reactions, these precursors chemically react on the substrate's surface, enabling the layer-by-layer deposition of materials [66], [67]. While ALD shares some similarities with chemical vapor deposition (CVD), the key distinction lies in the pulsing sequence of the precursors. Unlike CVD, where precursors are pumped simultaneously, ALD employs sequential pulsing, allowing precise control over the deposition process [54]. ALD has several advantages over other thin film deposition techniques, including the ability to produce high-quality ultra-thin films even at low temperatures, the flexibility to control the deposition process based on specific requirements, and the precise control of film thickness. However, ALD can be time-consuming and relatively high in terms of material and energy consumption [67].

Wang et al. used ALD to deposit thin films of lithium niobium oxide (LNO) with a Li/Nb subcycle ratio of 1:4. The resulting films had a remarkable Li+ conductivity at room temperature, making them promising candidates for solid-state electrolytes and materials for interfacial engineering [68]. Furthermore, Østreng et al. used ALD to deposit epitaxial thin films of ferroelectric $LiNbO_3$ on Al_2O_3 substrates. The process required more than 600 cycles to achieve a thickness of 190nm, but the resulting films displayed a pronounced inclination to arrange themselves in an epitaxial manner when grown on substrates like $LaAlO_3$ and Al_2O_3 [69]. In another study conducted by Atosuo et al., a combination of ALD and solid-state reactions (transformations caused by subsequent annealing) to produce high-quality films of LiNbO3 that possessed crystalline structures and were close to being stoichiometric [70].

1.3.5 Liquid Phase Epitaxy

Liquid phase epitaxy (LPE) involves depositing a thin, single-crystalline layer with the same structure as the substrate using a liquid phase, like a solution or melt [71]. LPE aims to grow a crystalline layer identical to the substrate's structure, leading to highly ordered and structurally coherent layers that integrate seamlessly with the substrate crystal [71] , [72].

LPE is often carried out using a solution as the liquid phase, offering advantages over melts:

- Achieving epitaxy at lower temperatures, reducing energy needs and facilitating growth.
- Precise control over the amount of crystalline phase grown or dissolved, allowing fine-tuning of layer thickness and composition.
- Reduced defect densities in layers grown from solutions, leading to improved crystallization and structural integrity [71]- [72].

Susumu Kondo et al. presented their preliminary findings on growing single-crystal $LiNbO_3$ thin films using the liquid-phase epitaxy (LPE) technique back in 1975 [73]. They found that $LiV0_3$ is an effective flux material for LPE growth, achieving epitaxial thin films (3-6 μm thick) on a $LiTaO_3$ substrate [73]. In their study, Ballman et al. examined various crystallographic orientations and employed an annealing process to improve film quality, resulting in smoother films. Moreover, they successfully demonstrated optical waveguiding in LPE-produced $LiNbO_3$ films, with minimal optical losses of 1–5 dB/cm at a wavelength of 632.8 nm [74]. In 1991, Tamada et al. utilized the Li_2O-V_2O_5 flux system to grow thin films on MgO-doped $LiNbO_3$ substrates with a slight lattice mismatch (0.08%). They achieved high-quality films, as indicated by an XRD rocking curve of 11 arcseconds [75]. By employing liquid phase epitaxy with K_2O flux and introducing Yb and Zn dopants, Yi Lu et al. have successfully grown single crystal thin films of $LiNbO_3$ on $LiNbO_3$ substrates [76].

In the process of obtaining lithium niobate films on pure congruent single-domain $LiNbO_3$ substrates (homoepitaxial growth), the liquid phase epitaxy technique has been employed. To facilitate the growth of these films, a Li-rich flux containing $LiVO_3$ has been utilized [77]. Through experimental investigations, it has been determined that the optimal temperature for film preparation is 860°C [77].

1.3.6 Physical Vapor Deposition Processes

Physical vapor deposition techniques involve depositing material at an atomic or molecular level by vaporizing it from a solid or liquid source. This vaporized material is then transported through a vacuum or low-pressure gas or plasma environment to a substrate, where it condenses and forms a film. Usually, PVD processes are employed to create films with thicknesses ranging from a few nanometers to thousands of nanometers. However, they can also be utilized to produce multilayer coatings, deposits with graded compositions, thick deposits, and even standalone structures. The deposition rates typically observed in PVD range from 10 to 100Å (1 to 10 nanometers) per second [78].

Vacuum deposition, a type of physical vapor deposition (PVD), involves vaporizing material from a thermal source and directing it to the substrate without interacting much with gas molecules between them. Material travels in a "line of sight" from source to substrate. The vacuum environment reduces gas contamination, maintaining low impurity levels in the deposition system [78]. Sensor structures for hydrogen gas sensing applications were investigated by Jakubik using $LiNbO_3$ as a substrate: a single thin film structure consisting of WO_3 were deposited sequentially onto a $LiNbO_3$ Y-cut substrate using vacuum deposition techniques [79].

Arc vapor deposition is a physical vapor deposition (PVD) technique that involves the use of a high current and low voltage arc to vaporize a cathodic electrode (cathodic arc) or an anodic electrode (anodic arc). The vaporized material is then deposited onto a substrate. In this process, the vaporized material is highly ionized. To enhance the deposition, the substrate is typically biased, meaning it is given an electric potential that accelerates the ions (referred to as "film ions") towards the substrate surface [78].

Ion plating, also known as ion-assisted deposition (IAD) or ion vapor deposition (IVD), involves the simultaneous or periodic bombardment of the film being deposited with atomic-sized energetic particles. This bombardment is employed to modify and control the properties of the deposited film. In ion plating, several processing variables are crucial, including the energy, flux, and mass of the bombarding particles, as well as the ratio of bombarding particles to depositing particles [78]. The ion plating method was utilized to grow $LiNbO_3$ epitaxial layers on various substrates, including Al_2O_3, MgO (111), and ZnO (001) [80]. It was found that $LiNbO_3$ films tend to align with their *c*-axis perpendicular to the smooth surface of the substrate [80].

Sputter deposition, a physical vapor deposition (PVD) technique, involves releasing particles from a surface (the "target") through physical sputtering. This process ejects surface atoms from a solid due to momentum transfer from high-energy particles, usually gaseous ions accelerated from a plasma [78]. The sputter deposition process can be carried out in a vacuum or in a low-pressure plasma. In a vacuum, the sputtered particles are not slowed down by collisions with gas molecules, so they arrive at the substrate with a high energy. This can result in the formation of a dense, uniform film. In a low-pressure plasma, the sputtered particles collide with gas molecules before they reach the substrate. This can help to thermalize the particles, resulting in a less dense and more uniform film. The sputtering source can be any material that can be vaporized by the energetic particles [78].

In 1974, Takada et al. accomplished the growth of a $LiNbO_3$ film onto a sapphire substrate using sputtering techniques [81]. Notably, they demonstrated the propagation of light within the epitaxially grown film, which exhibited a c-axis orientation [81]. Hewig et al. conducted a research investigation focused on the deposition of $LiNbO_3$ films onto amorphous and single-crystal substrates. The resultant film displayed a polycrystalline structure, characterized by a predominant orientation along the (0 1 2) direction [82].

In the pursuit of achieving monocrystalline $LiNbO_3$, Meek et al. during their experimental endeavors, made two significant findings [83]. Firstly, they discovered that all films sputtered from a stoichiometric target exhibited a deficiency of lithium. Secondly, they found that a secondary source rich in lithium, or a Li-rich source, could be utilized to compensate for the lithium deficiency in the films [83]. Fujimura et al. demonstrated the successful fabrication of high-quality c-axis epitaxial films on sapphire substrates using this approach. These films exhibited the absence of measurable rotational domains, although they did exhibit twinned domains [84]. Through the use of sintered targets, Shimizu et al. achieved the production of monocrystalline $LiNbO_3$ films on different crystallographic orientations of Al_2O_3 and $LiTaO_3$ substrates [85]. Additionally, they successfully obtained c-axis oriented films on amorphous substrates by employing ZnO (0 0 1) and Pt (1 1 1) buffer layers [85].

1.3.6.1 Pulsed Laser Deposition

Pulsed Laser Deposition (PLD), also referred to as laser vaporization or laser ablation, is a physical vapor deposition technique that takes place within a vacuum system. This technology involves the use of a pulsed laser that is precisely focused onto a target consisting of the desired deposition material. The high energy density of the laser causes vaporization or ablation of a small amount of material with each laser pulse, generating a plasma plume [86].

Despite its origins in the late 1980s, the technique of Pulsed Laser Deposition (PLD) has undergone substantial advancements and has become extensively adopted as a deposition method for film fabrication. Notably, PLD has found significant application in oxide research, where its distinctive characteristics are most prominently observed [87]. The initial trials of laser deposition were conducted during the 1960s, and although there were limited efforts in the following decades of the 1970s and 1980s, the technique did not gain significant recognition until pulsed-laser deposition emerged as a prominent method for growing oxide films. This recognition came about due to its successful application in the in situ epitaxial growth of high-temperature superconducting films, leading to widespread attention and subsequent developmental efforts [88].

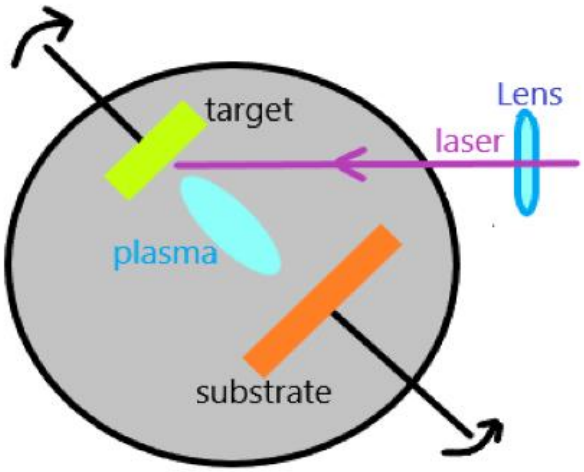

FIGURE 1.22. SCHEMATIC DIAGRAM OF THE PLD PROCESS.

Within the context of PLD, as illustrated in Figure 1.22, the process involves the precise focusing of a pulsed laser onto a target composed of the desired deposition material. When the laser energy density reaches a sufficiently high level, each laser pulse causes vaporization or ablation of a small quantity of the material, thereby generating a plasma plume. The ablated material is ejected from the target in a predominantly forward-directed plume. This ablation plume serves as the source of material flux for the growth of the deposited film [86].

A key and advantageous feature of Pulsed Laser Deposition (PLD) is its capability to achieve stoichiometric transfer of ablated material from multication targets for a wide range of materials. This ability stems from the non-equilibrium nature of the ablation process, which occurs when a small volume of material absorbs high laser energy density [86].

Pulsed laser deposition (PLD) offers several advantageous features for the growth of complex material films. These features include:

- Stoichiometric Transfer: PLD can facilitate the transfer of material from the target in a stoichiometric manner, preserving the desired chemical composition of the film. However, mass differences between ablated species (target elements) can lead to stoichiometry changes as the ablated material interacts with the background gas in the deposition chamber on the way to the substrate.
- Generation of Energetic Species: PLD can generate energetic species during the ablation process, which promotes efficient film growth and enables the deposition of high-quality films. However, the energy of particles reaching the substrate is directly tied to pressure and varies based on laser fluence.
- Hyperthermal Reaction: In the ablation plasma, there is a hyperthermal reaction between the ablated cations and the background gas, facilitating various chemical processes that contribute to the film growth.
- Compatibility with Pressure Range: PLD can be performed under a wide range of background pressures, from ultrahigh vacuum (UHV) conditions to 1 Torr, allowing flexibility in experimental setups [86].

Multication films can be deposited using PLD by employing either single, stoichiometric targets of the desired material or multiple targets for each element. However, it should be noted that the thickness distribution from a stationary plume in PLD is typically nonuniform, as the ablation plume exhibits a highly forward-directed nature. Nevertheless, uniform film coverage over large areas can be achieved by raster scanning the ablation beam over the target and/or by rotating the substrate, thereby compensating for the nonuniform deposition characteristics of the plume.

Achieving the growth of complex oxides necessitates the precise delivery of a growth flux with the accurate stoichiometry within an oxidizing environment that promotes the desired phase formation. The application of pulsed laser deposition has proven effective in reproducing the target stoichiometry for various multication oxides, highlighting its utility in this context. It is important to acknowledge that the mentioned outcome was achieved through the

implementation of a combinatorial synthesis approach. This approach involves simultaneously exploring multiple process parameters, such as composition and temperature, using combinatorial arrays or compositional spread techniques. Pulsed laser deposition has demonstrated its seamless adaptability to combinatorial techniques for thin-film research. The capability to grow epitaxial multication complex inorganic thin films has been and remains a significant advantage of pulsed laser deposition, contributing to its effectiveness and enabling its continued success [86].

1.3.6.2 Impact of Physical Parameters on the Film Growth

By carefully adjusting the experimental parameters, it is possible to exert a certain degree of control over the material properties in PLD. This control encompasses the ability to manipulate the composition of the deposited material, as well as influence crystallographic characteristics such as crystal orientation. Furthermore, it allows for the manipulation of morphological features, including the degree of crystallinity, texture, and average grain size of the deposited film [89], [90].

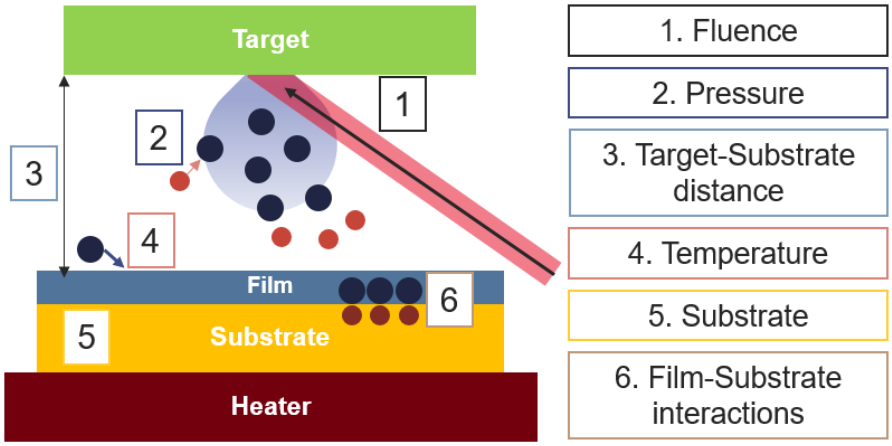

FIGURE 23. SCHEMATIC REPRESENTATION OF MAIN PARAMETERS IN PULSED LASER DEPOSITION.

The precise control over these properties is achieved through the strategic selection and optimization of the PLD process parameters (Figure 1.23), which include:

- laser fluence, which represents the energy per unit area delivered by the laser,
- background gas composition and pressure within the deposition chamber,
- the distance between the target and substrate,
- deposition temperature,
- the properties of the substrate itself,
- the interaction between material of the layer deposited and substrate [89], [90].

While the basic concept of PLD appears straightforward, the actual process is remarkably complex. The stages of ablation, plume expansion, and film deposition often overlap and are intricately interconnected. Moreover, the PLD process involves numerous deposition parameters that can be adjusted, and these parameters have direct consequences on the properties of the resulting thin films [89], [90].

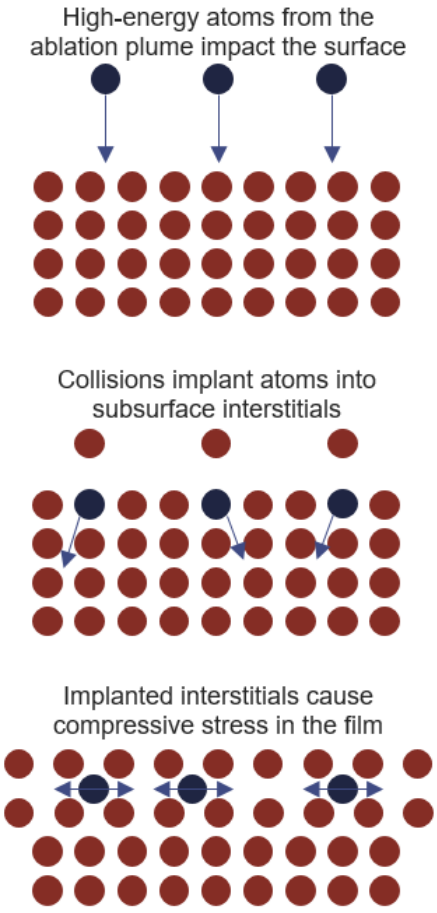

FIGURE 24. DIAGRAM ILLUSTRATING THE STRESS INDUCED BY THE PLUME IN FILMS DEPOSITED BY PLD.

In the process of pulsed laser deposition, the kinetic energies of ions and neutral species within the ablation plume can span a wide range, from a few tenths to several hundred electron volts. These energies are significant enough to induce modifications in the stress state of the deposited films through the formation of defects, as observed in ion-beam-assisted techniques. One of the primary outcomes of allowing deposition from an unabated energetic plume is the introduction of compressive stress in the films. The compressive stress originates from subsurface damage caused by the impact of energetic species, schematically illustrated in Figure 1.24 [86]. The control of kinetic energy in arriving species is crucial for achieving desired film growth, and this control can be attained by adjusting the laser fluence (energy level

at which the species are expelled from the target) and the background gas pressure (serves as a counteracting force impeding plasma expansion) [89].

One potential concern associated with pulsed laser deposition (PLD) is the expulsion of micron-sized particles during the ablation process. This phenomenon is commonly observed when the laser pulse penetrates deeply into the target material. If these particles are deposited onto the substrate, they can cause significant issues in the formation of multilayer device structures. To mitigate this problem, the use of highly dense ablation targets and laser wavelengths that are strongly absorbed by the target material is recommended. These measures tend to reduce or eliminate the formation of particles, thereby improving the quality of the deposited films and ensuring better formation of multilayer device structures. In addition to the particles that are expelled from the ablation targets, the presence of nanoparticles in the gas phase can be observed when the background pressure reaches a sufficiently high level, allowing for heterogeneous particle nucleation. These nanoparticles have the potential to become embedded within the deposited film [86].

In the case of oxide materials, the energetic cations bombarding the surface can selectively dislodge or sputter oxygen atoms, causing the deposited films to have an oxygen deficiency. The kinetic energy of the ablated species is primarily determined by the laser energy and gas-phase collisions. However, this issue can be mitigated by introducing a background gas during the deposition process. The presence of a background gas helps to thermalize the plume, reducing the kinetic energy of the ablated species and preventing the preferential sputtering of oxygen atoms. As a result, the use of a background gas is generally effective in addressing this problem and promoting the deposition of films with the desired oxygen content [86].

In laser ablation, it is important to note that each individual ablation pulse generally supplies enough material to deposit only a submonolayer of the desired phase. The actual amount of film growth per laser pulse is influenced by various factors, including the distance between the target and substrate (target-substrate separation), the pressure of the background gas, the size of the laser spot, and the energy density of the laser. These parameters collectively determine the quantity of material transferred from the target to the substrate during each laser pulse. At lower laser fluence and/or low absorption at the laser wavelength, the laser pulse primarily heats the target, causing the evaporation of target species through thermal processes. In this case, the evaporation rate from a multicomponent target is determined by the vapor pressures of the constituent materials [86]. However, as the laser fluence increases, an ablation threshold is reached, where the laser energy absorption surpasses the threshold required for

simple evaporation. The ablation threshold depends on the absorption coefficient of the material and varies with the laser wavelength [86].

At higher fluences, the absorbed laser energy leads to the formation of a plasma at the target surface, rather than relying solely on vapor pressures for material ejection. This occurs when high-energy densities are absorbed by a small volume of material, enabling vaporization that is not dependent on the vapor pressures of the constituent cations [86]. This phenomenon allows for the stoichiometric transfer of material from multication targets in pulsed laser deposition (PLD) [86]. The laser fluence, representing the energy of the laser per unit area, directly affects the kinetic energy of the species expelled from the target and their expansion toward the substrate. It also influences the expansion profile of the ablation plume [89]. To achieve successful ablation, the fluence must exceed the target's ablation threshold, which is the minimum energy required to eject species from the target [86]. The absorption coefficient determines the volume within the target where the laser energy is absorbed, converting photon energy into thermal energy [89]. By adjusting the fluence, the plasma temperature and kinetic energies can be controlled [91]. Increasing the fluence in PLD leads to the generation of denser plasma plumes during the ablation process [89]. A dense plasma plume is characterized by a higher concentration of energetic electrons in its vicinity. This elevated electron density promotes the ionization of neutral species and increases collision frequency within the plasma. These collisions play a significant role in film growth by facilitating species interactions, nucleation, and growth processes, ultimately influencing the morphology and properties of the deposited film [89].

In a study conducted by Z. Vakulov et al., it was discovered that the nucleation process could be controlled by varying the laser pulse repetition frequency [91]. At a repetition frequency of 4 Hz, the resulting film exhibited a structure composed of local islands and clusters with an average diameter of 118.1 ± 5.9 nm. On the other hand, when the repetition frequency was increased to 10 Hz, nanocrystalline films with a continuous granular structure were obtained, characterized by grains with an average diameter of 235 ± 11.75 nm (which was twice bigger) [91].

The introduction of a background gas in pulsed laser deposition (PLD) serves two primary purposes. Firstly, for the formation of multication thin-film materials, a reactive species are often required as part of the deposition flux. These reactive species, such as molecular oxygen (O_2) for oxide films, are necessary for phase formation based on the thermodynamic stability of the desired phase. The interaction between the ablated species and the background

gas leads to the production of molecular species in the ablation plume, facilitating the formation of multication phases during film growth. Secondly, the background gas is utilized to reduce the kinetic energies of the ablated species. By adjusting the pressure of the background gas, control over the energetic nature of the ablation plume can be achieved, promoting better control over the film growth process and enhancing film quality [86]. The two predominant background gases used in this context are argon (Ar) and molecular oxygen (O_2). These gases assist in the expansion of the ablation plume by participating in momentum transfer with the ablated species. This phenomenon reduces the kinetic energy of the species and decreases their average distance traveled between collisions (mean free path) [89]. The inclusion of an O_2 background gas creates a highly reactive environment localized at the substrate surface, facilitating the growth of reactive films [89], [90]. Additionally, Li ions located in the front part of the ablation plume undergo additional excitations due to collisions, influencing the film growth process [92].

Modifying the distance between the target and substrate, referred to as the target-substrate (TS) distance, has a direct impact on the mass ratio of the species reaching the substrate. By reducing the TS distance, the transfer of momentum from the background gas diminishes. Consequently, the average kinetic energy of the plasma species increases, which exacerbates the undesirable rebound effect. Conversely, increasing the TS distance results in a greater number of scattering events involving both light and heavy species. This allows the species to approach the substrate at a nearly congruent level. Importantly, the TS distance plays a role in determining the number of collisions the species will encounter, thereby influencing their oxidation states. In fact, adjusting the TS distance provides sufficient time for the species to undergo complete oxidation) [89], [93]. However, it should be noted that if the distance between the target and substrate becomes excessively large, the quantity of species reaching the substrate experiences a decrease [90]. As a result, the equilibrium between achieving congruent species transfer and maintaining a satisfactory deposition rate is influenced by the modification of the target-substrate distance.

The selection of the target material in pulsed laser deposition plays a crucial role in determining the properties of the deposited films, including particulate density, epitaxy, phase formation, and deposition rate. A key requirement for successful ablation is choosing a target material with a high optical absorption coefficient at the specific laser wavelength being used. The phase of the target material does not necessarily have to match the desired film phase. Instead, it is the cation stoichiometry that needs to be identical to that of the films, assuming

stoichiometric transfer and minimal evaporation from the film surface. By ensuring the appropriate cation stoichiometry in the target material, the desired film composition can be achieved during deposition through the process of stoichiometric transfer from the target to the substrate surface. This allows for the precise control of film composition and facilitates the growth of high-quality films with the desired properties [86].

In general, two distinct types of substrates are commonly utilized: polycrystalline and single crystals. When a non-textured polycrystalline substrate is employed, it typically results in a polycrystalline film with multiple orientations. In contrast, the use of an oriented single crystal substrate enables the growth of an epitaxial thin film. Epitaxial growth occurs when the substrate possesses a crystal lattice that matches the lattice of the film to be deposited. However, in the case of a single crystal substrate, a mismatch between the crystal lattices of the substrate and the deposited film can give rise to strain and stresses in the film and the growth of a polycrystalline film [89]. Once the ablated species reach the substrate, several processes can occur, including re-evaporation, cluster nucleation, or trapping of the species at defects. The mobility of atoms on the substrate surface is influenced by the temperature, which corresponds to the energy transferred to the atoms. Higher temperatures promote greater surface mobility of atoms, leading to the formation of crystalline films with fewer defects and reduced stresses in the crystal lattice. This improvement in crystalline properties is attributed to the enhanced atomic movement and the ability of atoms to rearrange themselves more effectively at higher temperatures [89], [94].

The utilization of compliant substrates in heteroepitaxial growth has garnered significant interest due to its potential in addressing challenges associated with the growth of pseudomorphic heterostructures involving materials with lattice mismatch. The fundamental concept revolves around employing a thin seed layer that acts as a flexible membrane, capable of absorbing the strain energy generated by a thick deposited layer with a mismatched lattice. This approach aims to prevent the formation of structural defects within the deposited layer, allowing for the growth of high-quality epitaxial films despite the lattice mismatch between the materials involved. By carefully selecting and engineering compliant substrates, it becomes possible to achieve desirable epitaxial growth conditions and mitigate the negative effects of lattice mismatch, enabling the fabrication of functional heterostructures with improved structural integrity [72], [86].

1.3.6.3 Lithium Niobate by Pulsed Laser Deposition

The groundbreaking work by Ogale et al. in 1992 introduced several significant advancements in the field of pulsed laser deposition for the growth of stoichiometric $LiNbO_3$ films [95]. They utilized an excimer laser to ablate a stoichiometric $LiNbO_3$ sintered target and deposited the films onto (1 0 0) Si substrates, resulting in stoichiometric films. This pioneering work also involved the use of a mixed gas ambient consisting of argon and oxygen during the PLD process, which was the first instance of conducting PLD in such a mixed environment. By optimizing the partial pressure ratios of argon and oxygen, Ogale et al. achieved the growth of single-phase $LiNbO_3$ films [95]. However, it should be noted that the films obtained in this study were polycrystalline. Despite the polycrystalline structure, the successful growth of single-phase films demonstrated the effectiveness of the partial pressure optimization in promoting the desired phase formation during the deposition process [95].

Shortly after Shibata et al. conducted further research on the deposition of $LiNbO_3$ thin films using the excimer laser ablation technique using sintered a ceramic target by combining Li_2CO_3 and Nb_2O_5 powders, allowing them to control the Li:Nb ratio in the target material [96]. Shibata et al. focused on the formation of high-quality epitaxial LiNbO3 thin films on sapphire substrates (0 0 1) and (1 1 0) [96], [97]. They investigated the influence of several experimental parameters on the resulting film quality. These parameters included the Li/Nb ratio in the target material, the substrate temperature, and the pressure and composition of the gas used during the deposition process [97]. The $LiNbO_3$ films showed alignment with the substrate orientation, with a rocking curve FWHM of 612 arcseconds. The sapphire substrates had a relatively poor quality, with an FWHM of 540 arcseconds. Despite the substrate limitations, the study demonstrated the potential for achieving high-quality (1 1 0) $LiNbO_3$ films and provided insights into the influence of various parameters on film quality [97].

Efforts to deposit $LiNbO_3$ films using non-Li-enriched targets often resulted in undesired characteristics such as polycrystalline structures, twinned films, or films exhibiting rotational domains [98], [99]. These observations emphasized the criticality of identifying optimal growth conditions for $LiNbO_3$ films through precise control of deposition parameters. It became evident that achieving successful $LiNbO_3$ film growth via PLD necessitates fine-tuning of various factors within a narrow parameter space.

Kakehi et al. conducted a study focusing on the influence of laser fluence on the incorporation of Li into $LiNbO_3$ films [100]. They presented that the interaction between the

incident excimer laser and the oxygen and/or a radical source led to the production of oxygen radicals. These radicals played a significant role in controlling the Li concentration in the deposited films. One of the key effects of the oxygen radicals was the suppression of Li atom reevaporation from the film. The oxidization of Li atoms by the oxygen radicals prevented their evaporation, thereby influencing the overall Li concentration in the film. This mechanism contributed to the successful control of Li incorporation in the deposited films [100].

Son et al. performed a comprehensive parametric investigation, exploring the effects of deposition geometries (waveguides), ambient pressures, target-to-substrate distance, and excess Li in the target [101]. Through their research, the authors were able to identify optimized conditions that suppressed the formation of secondary phases in $LiNbO_3$ films during pulsed laser deposition [101]. The key finding was the existence of an optimized plume strength, which was determined by the position of the substrate relative to the plume. If the substrate was positioned too close to the plume center, a Li-deficient phase would mix in the film, while positioning the substrate too far from the plume resulted in a Li-excess phase. Two main factors were considered to contribute to phase evolution: Li knock-out by the high-energy plume and the differential elemental distribution within the plume. However, the latter was considered more plausible. By using a Li-enriched target, Son et al. were able to maintain the desired film phase while avoiding a significant reduction in plume strength. This allowed them to improve the surface scatter characteristics by reducing the grain size through a higher nucleation density [101]. In continuation of the previous research, Kilburger et al. successfully achieved the epitaxial growth of single-phase (0 0 1) $LiNbO_3$ films along the c-axis on Al_2O_3 substrates [102]. The quality of the films was assessed using X-ray diffraction (XRD), and the rocking curve full width at half maximum (FWHM) was measured to be 0.35° [102].

In recent studies, a nanocomposite seeding method has been utilized to achieve single-domain $LiNbO_3$ thin films by Paldi et al [103]. This method involves creating a seed layer by mixing LN and Au powders prior to the growth process. Epitaxial growth of single-domain films was achieved using both stoichiometric and Li-enriched targets. Microstructural analysis revealed that the incorporation of Au nanoparticles in the seed layer played a significant role in minimizing strain and inhibiting the formation of misfit dislocations, thereby promoting the growth of single domains in the films [103]. High-quality Ag–$LiNbO_3$ nanocomposite thin films were grown by Huang et al. [104], where Ag nanoparticles were embedded within the $LiNbO_3$ matrix. The density and size of the nanoparticles were controlled by adjusting the composition of the target material. Notably, the co-deposition of the metal phase Ag and the

oxide phase $LiNbO_3$ did not result in any deterioration of crystal quality. The Ag–$LiNbO_3$ nanocomposite thin films exhibited intriguing optical properties, including surface plasmon resonance in the visible range, tunable optical constants, and optical anisotropy [104].

1.3.7 Comparison of the growth methods

The deposition of lithium niobate ($LiNbO_3$) can be achieved through various methods. The advantages and disadvantages of these techniques are summarized in Table 1.2, which provides a comparison of their key characteristics and considerations.

Technique	Advantages	Disadvantages
Chemical Vapor Deposition (CVD)	- Economically viable and widely adopted in industrial applications [105]; - High-quality layers with well-defined crystal structures [105]; - Rapid deposition rate [105];	- Frequently employing hazardous precursor materials [105]; - Significant stress induced by elevated temperatures during deposition [105]; - Deposition process conducted at extremely high temperatures (1000°C) [105];
Metal-organic chemical vapor deposition (MOCVD)	- Precise control over stoichiometry, crystallinity, and uniformity [106]; - Versatile composition control [106]; - Capability to coat large surfaces and intricate shapes [107];	- Expensive, with a high cost associated [107]; - Usage of extremely hazardous precursors [107];
Atomic layer Deposition (ALD)	- Production of high-quality films with excellent properties [108]; - Achieving uniform thickness over large areas [108]; - Ability to carry out processing at low temperatures [108]; - Precise control over the stoichiometry of the deposited films [108];	- Low deposition rate, resulting in slow film growth [108]; - High material waste rate during the deposition process [108]; - High energy waste rate due to inefficient utilization [108]; - Generation of nano-particle emissions during deposition [108];
Sputtering	- Suitable for deposition on substrates of any size [105]; - Established technique widely used in the industry [105]; - High deposition rate, enabling efficient production [105];	- Requires substrate heating and can be energetically demanding [105]; - Challenges in achieving precise stoichiometry control [105]; - Target erosion can occur during the deposition process [105];
Liquid Phase Epitaxy (LPE)	- High purity of the layers grown [109]; - low density of defects [109]; - low cost of operation [109];	- Inconsistent film thickness distribution [110]; - Irregular and rough surface morphology [110];

Molecular Beam Epitaxy (MBE)	- Epitaxial growth achievable at temperatures below 1000°C [105]; - Precise control over stoichiometry and thickness [105]; - High-quality crystalline layers obtained [105];	- Slow deposition speed [105]; - Not suitable for large-scale production [105]; - Very low pressure during deposition [105];
Pulsed Laser Deposition (PLD)	Stoichiometric transfer of composition from target to layer [105]; Energetically favorable for promoting crystallization at low temperatures (<500°C) [105]; Capability to grow complex materials [105];	Limited capability for deposition on large substrates [105]; Formation of droplets and particles, often attributed to target erosion [105]; Limited industrial applicability or maturity [105].

TABLE 1.2 ADVANTAGES AND DISADVANTAGES OF THE MAIN DEPOSITION TECHNIQUES USED FOR THE SYNTHESIS OF THIN LAYERS OF LITHIUM NIOBATE.

1.3.8 Reported results

The fabrication of lithium niobate thin films can be accomplished through diverse methodologies, encompassing chemical phase synthesis approaches, physical phase synthesis techniques, and epitaxial methods such as Liquid Phase Epitaxy (LPE) and Molecular Beam Epitaxy (MBE).

Technique	Substrate	Crystallinity	Rocking curve FWHM, °	Surface roughness RMS, nm
CVD	Al_2O_3 (001) [111] Si(100) [112]	Epi: [111] Poly: [112]	0.25 [111] 3.5 [112]	10–15 [112]
MOCVD	Al_2O_3 (001) [113]	Epi: [113]	0.27 [113]	
ALD	Al_2O_3 (001)&(012) [65]	Epi: [65]	1.05, 2.04 [65]	1.3 [65]
MBE	Al_2O_3 [114] $LiTaO_3$ [114]	Epi [114]	0.034 [114]	0.17 [114]
Sputtering	Al_2O_3 [80], [115] MgO (111) [80] ZnO (001) [80] Si (001)&(111) [116]	Epi [80] Poly [116]	0.38 [115]	2.1 [115] 10–25 [116]
PLD	Al_2O_3 [117] Al_2O_3&ZnO [102] SiO_2/Si [118]	Epi [117] Epi [102] Poly [118]	2 [117] 0.046 (Al_2O_3) [102] 0.35 (ZnO) [102] 0.21 [118]	0.52 [117]

TABLE 1.3 REPORTED RESULTS OF THE MAIN DEPOSITION TECHNIQUES USED FOR THE SYNTHESIS OF THIN LAYERS OF LITHIUM NIOBATE.

The majority of thin layers are grown on monocrystalline substrates, such as sapphire or $LiTaO_3$, without buffer layers or electrodes. This facilitates growth due to lattice parameter agreement and congruent stoichiometry. While good-quality layers are obtained, the growth direction is predominantly (0 0 6), influenced by substrate orientation along the crystal plane (0 0 1). PLD yields some of the best results, allowing crystalline deposits at lower temperatures, limiting lithium atom diffusion. MBE (Molecular Beam Epitaxy) produces smaller widths at half maximum in Rocking Curves. On silicon substrates, layers are polycrystalline or textured due to lattice mismatch and significant differences in thermal expansion coefficients (CTE).

1.4 Objectives of the PhD

The focus of this thesis work is situated within the framework of the evolving landscape of 5G technology and its consequential impact on the performance dynamics of acoustic filters. Notable changes associated with 5G, including heightened bandwidth and increased resonance frequency, necessitate a reexamination of acoustic filtering materials. In this context, the primary objective is an in-depth investigation into the deposition processes of lithium niobate, a piezoelectric material extensively employed in acoustic filtering applications.

Lithium niobate ($LiNbO_3$) is recognized as a complex material, and its synthesis poses inherent challenges. The heightened performance requirements mandated by the advancements in 5G technology have profound implications on the physicochemical properties of the deposited layers. Through this research, the aim is to unravel the intricate synthesis processes of $LiNbO_3$ utilizing Pulsed Laser Deposition, shedding light on the nuanced changes in its physicochemical attributes prompted by the heightened performance demands associated with 5G development.

In the course of this research, the physicochemical properties of the deposited layers will be examined through a set of techniques, encompassing:

- Study of Morphological Properties:
    - Atomic Force Microscopy (AFM): Utilized for high-resolution imaging and topographical analysis at the atomic scale.
    - Piezoresponse force microscopy (PFM): Applied for imaging and manipulation of piezoelectric/ferroelectric materials domains.
    - Scanning Electron Microscopy (SEM): Employed to investigate surface morphology and obtain detailed three-dimensional images.
- Study of Structural Properties:
    - X-ray Diffraction (XRD): Applied to characterize crystal structures, offering insights into the structural composition of the layers.
- Study of Chemical Properties:
    - Secondary Ion Mass Spectrometry (SIMS): Utilized to analyze the elemental and isotopic composition of the layers through the sputtering and ionization of secondary ions.

These physicochemical characterization techniques are elucidated in Annex I. The collective application of these methods is designed to yield an understanding of the morphological, structural, and chemical characteristics of the deposited layers. This analysis contributes insights into the behavior of lithium niobate in the context of acoustic filtering applications, particularly in response to the evolving demands of 5G technology.

The heightened performance requirements driven by the development of 5G technology entail specific consequences on the physicochemical properties of the layers, necessitating:

- Crystallization: The layers must exhibit a well-defined crystalline structure to meet the performance demands associated with 5G technology. This involves a systematic and controlled arrangement of atoms to achieve the desired crystalline form.
- Epitaxial or Preferentially Textured Growth: Epitaxial growth or preferential texturing of the layers is imperative. This implies a highly ordered deposition process where the crystallographic orientation of the newly formed layers aligns with that of the substrate, ensuring optimal performance in the context of 5G applications.
- Stoichiometry: Maintaining stoichiometry is crucial for the deposited layers. This ensures a balanced ratio of constituent elements, promoting stability and predictable performance in acoustic filtering applications within the 5G framework.

To effectively address the challenges posed by these requirements, various research areas are being explored. Each area focuses on specific aspects to optimize the physicochemical properties of the layers, ultimately contributing to the successful adaptation of acoustic filters to the evolving landscape of 5G technology.

The Pulsed Laser Deposition technique was implemented using the Solmates 8 in.-wafer-based SIP800 platform for growth of the thin films of $LiNbO_3$. This platform was chosen for its capacity to grow complex materials on large substrates, providing industrial applicability. Additionally, previous applications of PLD have demonstrated superior results in terms of film quality.

The initial phase of this research entails the examination of thin lithium niobate layers deposited on lithium niobate substrates using PLD. Our investigations span a spectrum of substrates, characterized by distinct crystal orientations. The principal aim is to homoepitaxialy grow the $LiNbO_3$ films with exert control over the crystalline orientation. The research methodology encompasses a study of the physical and chemical properties inherent in the as-deposited layers.

In the subsequent phase of our research, we will delve into the deposition of thin layers of $LiNbO_3$ by PLD on monocrystalline sapphire substrates. The selection of sapphire is grounded in their potential application in SAW devices. Our investigation will focus on understanding the impact of deposition parameters and the cutting plane of the substrates on the growth process. The overarching objective is to exercise control over the crystalline orientation of the $LiNbO_3$ films. Furthermore, our research extends to the investigation of specific substrates with the primary goal of uncovering the potential for growing crystallographic planes that have not been previously reported. This exploration opens avenues for novel orientations and properties in the thin $LiNbO_3$ layers, contributing to the diversification of crystallographic possibilities in the realm of acoustic filtering applications.

In the concluding phase of our research, the emphasis shifts to PLD of $LiNbO_3$, with a specific emphasis on utilizing platinized silicon-based substrates. Our investigation is oriented towards the growth on Si substrates, incorporating diverse buffer layers. The choice of buffer layer substrates is informed by their compatibility with RF applications, for their potential utilization as bottom electrodes in BAW devices. The primary focus of this research initiative is a comprehensive study of the crystallographic characteristics, and surface properties of the deposited layers.

Bibliography

[1] Mitsui, T.; Tatsuzaki, I.; Nakamura, E.; Ishibashi, An Introduction to the Physics of Ferroelectrics, vol. 1, New York: Gordon and Breach Science Publishers, 1976.

[2] M. Valle, and R. S. Dahiya , Robotic Tactile Sensing, Dordrecht: Springer, 2013.

[3] P. Curie, J. Curie, Dévelopment, par pression, de l'électricité polaire dans les cristaux hémièdres à faces inclinées, C. R. Acad. Sci., 1880.

[4] G. Lippmann, "Principe de conservation de l'électricité," *Ann. Chim. Phys.*, p. 145–178, 1881.

[5] IEEE, "IEEE Standard on Piezoelectricity".

[6] W. Wersing, W. Heywang, H. Beige, and H. Thomann, "The Role of Ferroelectricity for Piezoelectric Materials," in *Piezoelectricity: evolution and future of a technology*, Berlin Heidelberg, Springer, 2008.

[7] Volk and Wöhlecke, Lithium Niobate Defects, Photorefraction and Ferr, 2008.

[8] V. Gopalan, V. Dierolf, and D. A. Scrymgeour, "Defect–Domain Wall Interactions in Trigonal Ferroelectrics," *Annu. Rev. Mater.*, vol. 37, p. 449–489, 2007.

[9] R. B. Hetnarski, "Piezoelectric Effects and Materials," in *Encyclopedia of Thermal Stresses*, Dordrecht, Springer, 2014.

[10] W. K.K., Properties of lithium niobate, London: Institution of Electrical Engineers, and INSPEC (Information service), Eds., 2002.

[11] Karin M. Rabe, Matthew Dawber, C´eline Lichtensteiger, Charles H. Ahn, Jean-Marc Triscone, "Modern Physics of Ferroelectrics: Essential Background," in *Physics of ferroelectrics: a modern perspective*, Berlin ; New York, Springer, 2007.

[12] S. Sanna and W. G. Schmidt, "LiNbO3 surfaces from a microscopic perspective," *Journal of Physics: Condensed Matter*, vol. 29, pp. 1-7, 2017.

[13] Schmidt, F.; Kozub, A.L.; Biktagirov, T.; Eigner, C.; Silberhorn, C.; Schindlmayr, A.; Schmidt, W.G.; Gerstmann, U., "Free and defect-bound (bi)polarons in LiNbO3: Atomic structure and spectroscopic signatures from ab initio calculations," *Phys. Rev. Res.*, 2020.

[14] Teplyakova, N.A.; Sidorov, N.V.; Palatnikov M.N., " Determination of stoichiometry, concentration of OH groups, and point defects in lithium niobate crystals from their IR absorption spectra," *Opt. Spectrosc.*, p. 1131–1137, 2020.

[15] Boulle A. et al, "Role of nanostructure on the optical waveguiding properties of epitaxial LiNbO3 films," *J. Phys. D: Appl. Phys*, vol. 42, Jul. 2009.

[16] J. Zhu, "Processing and Characterization of LiNbO3 Thin Films for Ferroelectric Nonvolatile Memory Applications," Rice University, 2002.

[17] J. C. Vyas and S. G. Singh, "The negative thermal expansion coefficient in lithium niobate single crystals," in *presented at the SOLID STATE PHYSICS: PROCEEDINGS OF THE 57TH DAE SOLID STATE PHYSICS SYMPOSIUM 2012*, Bombay, 2013.

[18] Günter P. and Huignard J.-P., Photorefractive materials and their applications 2: materials., New York: Springer, 2007.

[19] Sánchez-Dena et al., "Lithium Niobate Single Crystals and Powders Reviewed—Part I," *Crystals 10*, vol. 10, 2020.

[20] Kim S, Gopalan V, Kitamura K, Furukawa, "Domain reversal and nonstoichiometry in lithium tantalate.," *J. Appl. Phys.*, 2001.

[21] Kitamura K, Furukawa Y, Niwa K, Gopalan V, Mitchell TE., "Crystal growth and low coercive field 180° domain switching characteristics of stoistoichiometric LiTaO3.," *Appl. Phys. Lett.*, vol. 73, p. 3073–75, 1998.

[22] Gopalan V, Gupta MC. , "Observation of internal field in LiTaO3 single crystals: its origin and time-temperature dependence," *Appl. Phys. Lett.*, vol. 68, pp. 888-90, 1996.

[23] Gopalan V, Mitchell TE, Furukawa Y, Kitamura K, "The role of nonstoichiometry in 180° domain switching of LiNbO3 crystals," *Appl. Phys. Lett*, vol. 72, p. 1981–83, 1998.

[24] Baumer C, David C, Tunyagi A, Betzler K, Hesse H, et al., "Composition dependence of the UV absorption edge in lithium tantalate," *J. Appl. Phys.*, vol. 93, p. 3102–4, 2003.

[25] A. Bartasyte et al., "Residual stresses and clamped thermal expansion in LiNbO 3 and LiTaO 3 thin films," *Appl. Phys. Lett.*, vol. 101, 2012.

[26] S. Yao, J. Wang, H. Liu, X. Hu, H. Zhang, X. Cheng, and Z. Ling,, "Growth, optical and thermal properties of near-stoichiometric LiNbO3 single crystal," *J. Alloys Compd*, vol. 455, p. 501–505, 2008.

[27] Bo Liu, Xiao Chen, Hualin Cai, Mohammad Mohammad Ali, Xiangguang Tian, Luqi Tao, Yi Yang and Tianling Ren, "Surface acoustic wave devices for sensor applications," *Journal of Semiconductors*, vol. 37, 2016.

[28] K. Chen, Y. Zhu, Z. Liu, and D. Xue, "State of the Art in Crystallization of LiNbO3 and Their Applications," *Molecules*, p. 7044, 2021.

[29] K. Chen, Y. Zhu, Z. Liu, and D. Xue, "State of the Art in Crystallization of LiNbO3 and Their Applications," *Molecules*, vol. 26, no. 22, p. 7044, 2021.

[30] D. Morgan, "Surface Acoustic Wave Filters: With Applications to Electronic Communications and Signal Processing," *Academic Press*, 2010.

[31] C. K. Campbell, Surface Acoustic Wave Devices for Mobile and Wireless Communications, 1 edition. San Diego: Academic Press, 1989.

[32] C. Blog, Piezoelectric Materials: Understanding the Standards.

[33] Liu, Y.; Cai, Y.; Zhang, Y.; Tovstopyat, A.; Liu, S.; Sun, C.L., "Materials, Design, and Characteristics of Bulk Acoustic Wave Resonator: A Review," *Micromachines*, vol. 11, p. 630, 2020.

[34] R. M. White and F. W. Voltmer, "Direct piezoelectric coupling to surface elastic waves," *Appl. Phys. Lett.*, vol. 7, no. 12, pp. 314-316, 1965.

[35] O. Yamazaki, T. Mitsuyu, and K. Wasa, "ZnO Thin-Film SAW Devices," *IEEE Trans. Son. Ultrason.*, vol. 27, no. 6, p. 369–378, 1980.

[36] N. W. Emanetoglu, C. Gorla, Y. Liu, S. Liang, and Y. Lu, , "Epitaxial ZnO piezoelectric thin films for saw devices," *Materials Science in Semiconductor Processing*, 1999.

[37] Z. Chen, "Bulk Acoustic Wave Devices," *RF MEMS Assignment*, 2014.

[38] E. C. Lopez, "Analysis and Design of Bulk Acoustic Wave Filters Based on Acoustically Coupled Resonators," Phd Thesis. Universitat Autonoma de Barcelona, Cerdanyola del Valles, 2011.

[39] M. Gonzalez, "Impact of Li non-stoichiometry on the performance of acoustic devices on LiTaO3 and LiNbO3 single crystals," Phd thesis. Université de Franche-Comté, Chemical Physics, 2016.

[40] S. Mahon and R. Aigner, "Bulk Acoustic Wave Devices – Why, How, and Where They are Going," *Materials Science*, 2007.

[41] M. D. Terzieva, "Overview of bulk acoustic wave technology and its applications," E+E, 2016.

[42] K.-Y. Hashimoto, "Bulk Acoustic Wave Filters for Communications," Norwood, Artech House, 2009.

[43] X. Technology, "Akoustis Technologies".

[44] A. Bartasyte, T. Baron, S. Oliveri, S. Margueron, P. Boulet, "Toward High-Quality Epitaxial LiNbO3 and LiTaO3 Thin Films for Acoustic and Optical Applications," *Adv. Mater. Interfaces,* vol. 4, 2017.

[45] H. Hatano, K. Kitamura and Y. Liu, "Growth and photorefractive properties of stoichiometric LiNbO3 and LiTaO3," *Photorefractive Materials and Their Applications,* 2007.

[46] Fernandez, A., Acharya, M., Lee, H.-G., Schimpf, J., Jiang, Y., Lou, D., Tian, Z., Martin, L. W., "Thin-Film Ferroelectrics," *Advanced Materials,* vol. 34, 2022.

[47] Z. Ren, J. Xu, X. Le, and C. Lee, "Heterogeneous Wafer Bonding Technology and Thin-Film Transfer Technology-Enabling Platform for the Next Generation Applications beyond 5G," *Micromachines,* vol. 12, no. 8, p. 946, 2021.

[48] F. Niklaus, G. Stemme, J.-Q. Lu, and R. J. Gutmann, "Adhesive wafer bonding," *Journal of Applied Physics,* vol. 99, no. 3, p. 031101, 2006.

[49] R. I. Made et al, "Study of Low-Temperature Thermocompression Bonding in Ag-In Solder for Packaging Applications," *Journal of Elec Materi,* vol. 38, no. 2, p. 365–371, 2009.

[50] X.-Q. Feng and Y. Huang, "Mechanics of Smart-Cut® technology," *International Journal of Solids and Structures,* vol. 41, no. 16–17, p. 4299–4320, 2004.

[51] C. Wang, M. Zhang, and M. Lončar, "High- Q Lithium Niobate Microcavities and Their Applications," *Ultra-High-Q Optical Microcavities*, p. 1–35, 2020.

[52] "Thin Films—Partow Technologies," Partow Technologies, [Online]. Available: http://www.partow-tech.com/thinfilms/. [Accessed 13 June 2023].

[53] G. Poberaj, H. Hu, W. Sohler, P. Günter, "Lithium niobate on insulator (LNOI) for micro-photonic devices," *Laser & Photonics Review,* vol. 6, no. 4, p. 488–503, 2012.

[54] Amirmahdi Honardoost, Kamal Abdelsalam, Sasan Fathpour, "Rejuvenating a Versatile Photonic Material: Thin-Film Lithium Niobate," *Laser & Photonics Reviews,* vol. 14, no. 9, p. 2000088, 2020.

[55] J.-O. Carlsson and P. M. Martin, "Chapter 7 - Chemical Vapor Deposition," in *Handbook of Deposition Technologies for Films and Coatings*, William Andrew Publishing, 2010, pp. 314-363.

[56] Curtis, B.; Brunner, H., "The growth of thin films of lithium niobate by chemical vapour de position," *Materials Research Bulletin,* vol. 10, p. 515–520, 1975.

[57] W. Richter, "Physics of metal organic chemical vapour deposition," in *Advances in Solid State Physics*, Berlin, Heidelberg: Springer Berlin Heidelberg, 1986, p. 335–359.

[58] Wernberg, A.A.; Gysling, H.J.; Filo, A.J.; Blanton, T.N., "Epitaxial growth of lithium niobate thin films from a single-source organometallic precursor using metalorganic chemical vapor deposition," *Applied Physics Letters,* vol. 62, p. 946–948, 1993.

[59] Wernberg, A.A.; Gysling, H.J., "MOCVD deposition of epitaxial lithium niobate, LiNbO3, thin films using the single source precursor lithium niobium ethoxide, LiNb(OEt)6," *Chemistry of Materials,* vol. 5, p. 1056–1058, 1993.

[60] Akiyama, Y.; Shitanaka, K.; Murakami, H.; Shin, Y.-S.; Yoshida, M.; Imaishi, N., "Epitaxial growth of lithium niobate film using metalorganic chemical vapor deposition," *Thin Solid Films,* vol. 515, p. 4975–4979, 2007.

[61] Lu, Z.; Hiskes, R.; DiCarolis, S.; Route, R.; Feigelson, R.; Leplingard, F.; Fouquet, J., "Epitaxial LiNbO3 thin films on sapphire substrates grown by solid source MOCVD," *Journal of Materials Research,* vol. 9, p. 2258–2263, 1994.

[62] R. Feigelson, "Epitaxial growth of lithium niobate thin films by the solid source MOCVD method," *Journal of Crystal Growth,* vol. 166, p. 1–16, 1996.

[63] Lee, S.; Feigelson, R., "Reduced optical losses in MOCVD grown lithium niobate thin films on sapphire by controlling nucleation density," *Journal of Crystal Growth,* vol. 186, p. 594–606, 1998.

[64] Astié, V.; Oliveri, S.; Millon, C.; Margueron, S.; Rachetti, M.; Decams, J.; Boulet, P.; Bartasyte, A., "Towards stoichiometric LiNbO3 epitaxial thin films grown by DLI-MOCVD," in *GDR Oxydes Fonctionnels—des Matériaux Aux Dispositifs*, Piriac sur Mer, 2018.

[65] E. Østreng, H. H. Sønsteby, T. Sajavaara, O. Nilsen, and H. Fjellvåg, "Atomic layer deposition of ferroelectric LiNbO3," *J. Mater. Chem. C,*, vol. 1, no. 27, p. 4283–4290, 2013.

[66] D. Pan, L. Ma, Y. Xie, T. C. Jen, and C. Yuan, "On the physical and chemical details of alumina atomic layer deposition: A combined experimental and numerical approach," *Journal of Vacuum Science & Technology A: Vacuum, Surfaces, and Films,* vol. 33, no. 2, p. 021511, 2015.

[67] P. O. Oviroh, R. Akbarzadeh, D. Pan, R. A. M. Coetzee, and T.-C. Jen, "New development of atomic layer deposition: processes, methods and applications," *Science and Technology of Advanced Materials,* vol. 20, no. 1, p. 465–496, 2019.

[68] B. Wang et al., "Atomic Layer Deposition of Lithium Niobium Oxides as Potential Solid-State Electrolytes for Lithium-Ion Batteries," *ACS Appl. Mater. Interfaces,* vol. 10, no. 2, p. 1654–1661, 2018.

[69] E. Østreng, H. H. Sønsteby, T. Sajavaara, O. Nilsen, and H. Fjellvåg, "Atomic layer deposition of ferroelectric LiNbO 3," *J. Mater. Chem,* vol. 1, no. 27, p. 4283–4290, 2013.

[70] Elisa Atosuo, Miia Mäntymäki, Kenichiro Mizohata, Mikko J. Heikkilä, Jyrki Räisänen, Mikko Ritala, and Markku Leskelä, "Preparation of Lithium Containing Oxides by the Solid State Reaction of Atomic Layer Deposited Thin Films," *Chemistry of Materials* , vol. 29, no. 3, pp. 998-1005, 2017.

[71] M.B. Small, E.A. Giess, R Ghez, "Liquid Phase Epitaxy," in *Handbook of Crystal Growth*, Amsterdam, Elsevier, 1994.

[72] M. A. Herman, W. Richter, and H. Sitter, Epitaxy: Physical Principles and Technical Implementation, vol. 62, Berlin, Heidelberg: Springer Berlin Heidelberg, 2004.

[73] S. Kondo, S. Miyazawa, S. Fushimi, and K. Sugii, "Liquid-phase-epitaxial growth of single-crystal LiNbO 3 thin film," *Appl. Phys. Lett.,* vol. 26, no. 9, p. 489–491, 1975.

[74] Ballman, A.; Brown, H.; Tien, P.; Riva-Sanseverino, S, "The growth of LiNbO3 thin films by liquid phase epitaxial techniques," *Journal of Crystal Growth,* vol. 29, no. 3, p. 289–295, 1975.

[75] Tamada, H.; Yamada, A.; Saitoh, M., "LiNbO3 thin-film optical waveguide grown by liquid phase epitaxy and its application to second-harmonic generation," *Journal of Applied Physics,* vol. 70, no. 5, p. 2536–2541, 1991.

[76] Yi Lu, Benjamin Johnston, Peter Dekker, and Judith M. Dawes, "Second Harmonic Generation in Lithium Niobate Planar Waveguides Grown by Liquid Phase Epitaxy," in *Conference on Lasers and Electro-Optics* , Baltimore, 2009.

[77] D. Callejo, S. Manotas, M. D. Serrano, V. Bermúdez, F. Agulló-Rueda, and E. Diéguez, "Compositional study of LiNbO3 thin films grown by liquid phase epitaxy," *Journal of Crystal Growth,* vol. 226, no. 4, p. 488–492, 2001.

[78] [1]T. F. Kuech and T. Nishinaga, "Pt. A: Thin films and epitaxy Basic techniques, Chapter 1," in *Handbook of crystal growth*, Amsterdam, Elsevier, 2015, pp. 1-24.

[79] W. P. Jakubik, "Investigations of thin film structures of WO3 and WO3 with Pd for hydrogen detection in a surface acoustic wave sensor system," *Thin Solid Films,* vol. 515, no. 23, p. 8345–8350, 2007.

[80] H. Matsunaga, H. Ohno, Y. Okamoto, and Y. Nakajima, "Heteroepitaxial growth of LiNbO3 single crystal films by ion plating method," *Journal of Crystal Growth,* vol. 99, no. 1–4, p. 630–633, 1990.

[81] Takada, S.; Ohnishi, M.; Hayakawa, H.; Mikoshiba, N. , "Optical waveguides of single-crystal LiNbO3 film deposited by rf sputtering," *Applied Physics Letters,* vol. 24, p. 490–492, 1974.

[82] Hewig, G.; Jain, K.; Sequeda, F.; Tom, R.; Wang, P.-W., "R.F. Sputtering of LiNbO3 thin films," *Thin Solid Films,* vol. 88, p. 67–74, 1982.

[83] Meek, P.; Holland, L.; Townsend, P., "Sputter deposition of LiNbO3 films," *Thin Solid Films,* vol. 141, p. 251–259, 1986.

[84] Fujimura, N.; Ito, T.; Kakinoki, M., "Heteroepitaxy of LiNbO3 and LiNb3O8 thin films on C-cut sapphire," *Journal of Crystal Growth,* vol. 115, p. 821–825, 1991.

[85] Shimizu, M.; Furushima, Y.; Nishida, T.; Shiosaki, T. , "Preparation and Optical Waveguide Properties of LiNbO3 Thin Films by RF Magnetron Sputtering," *Japanese Journal of Applied Physics,* vol. 32, p. 4111–4114, 1993.

[86] R. Eason, Pulsed Laser Deposition of thin films, Southampton: John Wiley & Sons, Inc., 2007.

[87] D. P. Norton, "Synthesis and properties of epitaxial electronic oxide thin-film materials," *Materials Science and Engineering: R: Reports,* vol. 43, no. 5–6, p. 139–247, 2004.

[88] A. Inam, M.S. Hedge, X.D. Wu, T. Venkatesan, P. England, P.F. Miceli, E.W. Chase, C.C. Chang, J.M. Tarascon, J.B. Wachtman, "As-deposited high Tc and Jc superconducting thin films made at low temperatures," *Applied Physics Letters,* vol. 53, pp. 908-910, 1988.

[89] Luca Indrizzi, Natacha Ohannessian, Daniele Pergolesi, Thomas Lippert, Elisa Gilardi, "Pulsed Laser Deposition as a Tool for the Development of All Solid-State Microbatteries," *Helvetica Chimica Acta,* vol. 104, no. 2, pp. 1-25, 2020.

[90] Alejandro Ojeda-G-P, Max Döbeli, Thomas Lippert, "Influence of Plume Properties on Thin Film Composition in Pulsed Laser Deposition," *Advanced Materials Interfaces,* vol. 5, no. 18, pp. 1-16, 2018.

[91] Z. Vakulov, D. Khakhulin, A. Geldash, R. V. Tominov, V. S. Klimin, V. A. Smirnov, and O. A. Ageev, "Impact of laser pulse repetition frequency on nucleation and growth of LiNbO3 thin films," *Journal of Advanced Dielectrics,* vol. 12, no. 2, p. 2160019, 2022.

[92] S. Canulescu, E. L. Papadopoulou, D. Anglos, T. Lippert, C. W. Schneider, A. Wokaun, "Mechanisms of the laser plume expansion during the ablation of LiMn2O4," *Journal of Applied Physics,* vol. 105, no. 6, p. 063107, 2009.

[93] K. Orsel, R. Groenen, B. Bastiaens, G. Koster, G. Rijnders, K.-J. Boller, "Influence of the oxidation state of SrTiO3 plasmas for stoichiometric growth of pulsed laser

deposition films identified by laser induced fluorescence," *APL Materials*, vol. 3, no. 10, p. 106103, 2015.

[94] E. Hasabeldaim, O. M. Ntwaeaborwa, R. E. Kroon, E. Coetsee, H. C. Swart, "Effect of substrate temperature and post annealing temperature on ZnO:Zn PLD thin film properties," *Optical Materials*, vol. 74, p. 139–149, 2017.

[95] Ogale, S.B.; Nawathey-Dikshit, R.; Dikshit, S.J.; Kanetkar, S.M., "Pulsed laser deposition of stoichiometric LiNbO3 thin films by using O2 and Ar gas mixtures as ambients," *Journal of Applied Physics*, vol. 71, no. 11, p. 5718–5720, 1992.

[96] Yoshihiko Shibata, Kiyoshi Kaya, Kageyasu Akashi, et al., "Epitaxial growth and surface acoustic wave properties of lithium niobate films grown by pulsed laser deposition," *Journal of Applied Physics*, vol. 77, 1995.

[97] Y. Shibata, N. Kuze, M. Matsui, K. Kaya, M. Kanai, and T. Kawai, "SAW properties of LiNbO3 and LiTaO3 films grown by pulsed laser deposition," in *Proceedings of 1996 IEEE International Frequency Control Symposium*, Honolulu, 1996.

[98] A. M. Marsh, S. D. Harkness, F. Qian, and R. K. Singh, "Pulsed laser deposition of high quality LiNbO 3 films on sapphire substrates," *Appl. Phys. Lett.*, vol. 62, no. 9, p. 952–954, 1993.

[99] Veignant, Franck ; Gandais, Madeleine ; Aubert, Pascal ; Garry, Guy, "Structural evolution of lithium niobate deposited on sapphire (0 0 0 1): from early islands to continuous films," *Journal of Crystal Growth*, vol. 196, no. 1, pp. 141-150, 1999.

[100] Kakehi, Y.; Okamoto, A.; Sakurai, Y.; Nishikawa, Y.; Yotsuya, T.; Ogawa, S., "Epitaxial growth of LiNbO3 thin films using pulsed laser deposition," *Applied Surface Science*, vol. 169–170, pp. 560-563, 2001.

[101] Son, J.-W.; Orlov, S.S.; Phillips, B.; Hesselink, L., "Pulsed laser deposition of single phase LiNbO3 thin film waveguides," *Journal of Electroceramics* , vol. 17, no. 2, p. 591–595, 2006.

[102] Kilburger, S.; Millon, E.; Di Bin, P.; Boulle, A.; Guinebretière, R.; Di Bin, C., "Properties of LiNbO3 based heterostructures grown by pulsed-laser deposition for optical waveguiding application," *Thin Solid Films*, vol. 518, no. 16, p. 4654–4657, 2010.

[103] "Nanocomposite-Seeded Epitaxial Growth of Single-Domain Lithium Niobate Thin Films for Surface Acoustic Wave Devices," *Advanced Photonics Research*, vol. 2, no. 6, p. 2000149, 2021.

[104] Jijie Huang, Di Zhang, Zhimin Qi, Bruce Zhangc and Haiyan Wang, "Hybrid Ag–LiNbO3 nanocomposite thin films with tailorable optical properties," *Nanoscale Advances*, vol. 3, no. 4, p. 1121–1126, 2021.

[105] M. Sumets, "Thin films of lithium niobate: potential applications, synthesis methods, structure and properties," in *Lithium Niobate-Based Heterostructures: synthesis, properties and electron phenomena*, IOP Publishing Ltd , 2018, pp. 1-42.

[106] Francesca Lo Presti, Anna L. Pellegrino, Graziella Malandrino, "Metal-Organic Chemical Vapor Deposition of Oxide Perovskite Films: A Facile Route to Complex Functional Systems," *Advanced Materials Interfaces*, vol. 14, no. 9, p. 2102501, 2022.

[107] P. J. Wright, M. J. Crosbie, P. A. Lane, D. J. Williams, A. C. Jones, T. J. Leedham, H. O. Davies, "Metal organic chemical vapor deposition (MOCVD) of oxides and ferroelectric materials," *Journal of Materials Science: Materials in Electronics*, vol. 13, p. 671–678, 2002.

[108] Peter Ozaveshe Oviroh,Rokhsareh Akbarzadeh,Dongqing Pan,Rigardt Alfred Maarten Coetzee, Tien-Chien Jen, "New development of atomic layer deposition: processes,

methods and applications," *Science and Technology of Advanced Materials* , vol. 20, no. 1, pp. 465-496, 2019.

[109] "Liquid Phase Epitaxy," in *Encyclopedia of Materials: Science and Technology*, Elsevier , 2001, pp. 4588-4596.

[110] M. Ohring, "Epitaxy," in *Materials Science of Thin Films (Second Edition)*, Deposition and Structure, 2002, pp. 417-494.

[111] A. Bartasyte et al., "Thickness dependent stresses and thermal expansion of epitaxial LiNbO3 thin films on C-sapphire," *Materials Chemistry and Physics,* vol. 149–150, p. 622–631, 2015.

[112] S. A. Kulinich et al., "Lithium niobate–tantalate thin films on Si by thermal plasma spray CVD," *Thin Solid Films,* vol. 407, no. 1–2, p. 60–66, 2002.

[113] S. Margueron et al., "“Effect of deposition conditions on the stoichiometry and structural properties of LiNbO 3 thin films deposited by MOCVD," in *SPIE OPTO*, San Francisco, 2013.

[114] M. B. Tellekamp, et al., "Molecular Beam Epitaxy Growth of High Crystalline Quality LiNbO3," *Journal of Elec Materi,* vol. 45, no. 12, p. 6292–6299, 2016.

[115] [1]X. Lansiaux, E. Dogheche, D. Remiens, M. Guilloux-viry, A. Perrin, and P. Ruterana, "LiNbO 3 thick films grown on sapphire by using a multistep sputtering process," *Journal of Applied Physics* , vol. 90, no. 10, p. 5274–5277, 2001.

[116] M. Sumets, A. Kostyuchenko, V. Ievlev, S. Kannykin, and V. Dybov, "Sputtering condition effect on structure and properties of LiNbO3 films," *J Mater Sci: Mater Electron,*, vol. 26, no. 6, pp. 4250–4256,, 2015.

[117] S. Kilburger et al., "Growth of LiNbO3 thin films on sapphire by pulsed-laser deposition for electro-optic modulators," *Applied Surface Science,* vol. 253, no. 19, p. 8263–8267, 2007.

[118] X. Wang, Z. Ye and B. Zhao, "Growth and optical properties of completely -axis orientated LiNbO3 films deposited by pulsed laser deposition," *Solid State Communications*, vol. 142, no. 12, pp. 694-697, 2007.

[119] L. Sauze, "Elaboration par PLD de couches de LiNbO3 sur substrats monocristallins," in *Élaboration et caractérisation de couches minces de LiNbO3 obtenues par pulvérisation cathodique et ablation laser pulsée*, Grenoble, Ecole Doctorale Polytechnique Hauts-de-France, 2022, pp. 117-127.

[120] ICDD, "00-004-0802," 2021 International Centre for Diffraction Data, 1954.

[121] R. K. Kirby, "Platinum — A thermal expansion reference material," *Int J Thermophys,* vol. 12, p. 679–685, 1991.

[122] ICDD, "00-038-1420," 2021 International Centre for Diffraction Data, 1988.

[123] Z. H. Cen et al., "Temperature effect on titanium nitride nanometer thin film in air," *J. Phys. D: Appl. Phys,* vol. 50, no. 7, pp. 1-6, 2017.

[124] ICDD, "00-021-1272," 2020 International Centre for Diffraction Data, 1971.

[125] K.V.K. Rao et al., "Thermal Expansion of Rutile and Anatase," *J. Am. Ceram.*, vol. 50, pp. 124-126, 1970.

[126] Wang et al., "Effects of oxygen pressure on the c-axis oriented growth of LiNbO3 thin film SiO2/Si substrate by pulsed laser deposition," *Journal of Materials Science Letters* , vol. 3, pp. 225-227, 2003.

[127] L. C. Sauze et al., "Homo-epitaxial growth of LiNbO3 thin films by Pulsed Laser deposition," *Journal of Crystal Growth,* vol. 601, p. 126950, 2023.

[128] ICDD, "00-020-0631," 2020 International Centre for Diffraction Data, 1970.

[129] ICDD, "00-026-1481," 2021 International Centre for Diffraction Data, 1976.

Chapter 2: Homoepitaxial growth of $LiNbO_3$

Table of Contents

1. Introduction

In the previous chapter, an examination of the challenges associated with the deposition of thin layers of $LiNbO_3$ utilizing various techniques was provided. The objective of obtaining $LiNbO_3$ layers suitable for RF filter applications prompted an investigation into the utilization of pulsed laser ablation (PLD) as a deposition technique.

The current chapter focuses on growing thin layers of $LiNbO_3$ using laser ablation on monocrystalline substrates. Specifically, the research explores growing $LiNbO_3$ on different orientations of $LiNbO_3$ substrates, including X-cut, Y+148°-cut, and Z-cut. This method shows promise in preventing the formation of the undesired paraelectric $LiNb_3O_8$ secondary phase and reducing defects like cracks and porosities caused by thermal stresses.

The choice of X-cut, Y+148°-cut, and Z-cut substrates is based on their compatibility with RF applications, especially those involving surface or bulk acoustic waves. These crystallographic orientations have favorable characteristics that enhance filter performance, making them suitable for investigation in this study. The study aims to advance thin $LiNbO_3$ layer deposition techniques, leading to layers with excellent crystal quality and minimal roughness.

As mentioned in Chapter 1, transfer technologies provide wafer quality comparable to bulk $LiNbO_3$, but they have limitations on thickness (e.g., Smart-cut technique requires a minimum thickness of 300 nm for successful implementation) [1], [2].

1.1 Previous Studies

As previously mentioned in Chapter 1, it is important to note that in $LiNbO_3$, polarization aligns along the *c*-axis, and the material's dielectric, piezoelectric, and ferroelectric properties exhibit significant dependence on crystal orientations. To illustrate, the electromechanical coupling coefficient can vary substantially, ranging from 5.8% for X-cut [3] to 39.2% for Z-cut [4] $LiNbO_3$ Bulk Acoustic Wave (BAW) resonators. The pioneering research conducted at Bell Labs, focusing on the growth of single $LiNbO_3$ monocrystals [5], has led to the availability of lithium niobate wafers, which have found diverse applications in areas such as optical waveguides and Surface Acoustic Wave (SAW) RF filters [6], [7].

The physical properties of $LiNbO_3$, including characteristics like the Curie temperature, remnant polarization, and piezoelectric constants, are profoundly influenced by its

stoichiometry. Unfortunately, during the deposition process, there is a tendency for lithium (Li) atoms to diffuse out of the film. This diffusion results in the formation of a Li-deficient phases known as parasitic, which lack ferroelectric properties [6]. Furthermore, the absence of a well-defined composition line for the $LiNbO_3$ phase diagram presents a significant challenge in achieving stoichiometric growth [8].

These challenges, in addition to several others, have contributed to the absence of a consensus regarding a growth method for producing high-quality $LiNbO_3$ thin films, despite decades of research [8].

Technique	Structure	Crystallinity	Crystal quality, FWHM °	Surface roughness (RMS), nm	Layer orientation
Sol-gel	Epitaxial [9], [10]	single phase [9] coalescence of the crystallites with some defects [10]		1.5 [9]	Z-cut [9]
LPE	Epitaxial [11]	single phase [11]	0.012 [11]	~ 0.83 [11]	Z-cut [11]
PVD	Epitaxial [12]	single phase [12]		~ 10 [12]	Z-cut [12]
PLD	Epitaxial [13]	single phase [13]	0.004 [13]	0.77-3.2 [13]	X-cut [13] Y-cut [13] Z-cut [13]

TABLE 2.1 EXPERIMENTAL FINDINGS FROM VARIOUS DEPOSITION TECHNIQUES FOR LITHIUM NIOBATE HOMOEPITAXIAL THIN FILM GROWTH.

Indeed, it is important to note that there have been reported results regarding the deposition of $LiNbO_3$ onto $LiNbO_3$ substrates with the aim of achieving homoepitaxy. Various deposition techniques have been explored for this purpose, including Sol-gel [9]- [10], Liquid Phase Epitaxy [11], Physical Vapor Deposition [13], and Pulsed Laser Deposition [12]. A compilation of empirical observations derived from diverse deposition methodologies employed in the fabrication of lithium niobate layers on substrates composed of lithium niobate is shown in Table 2.1.

As it is presented in Table 2.1 most of the results reported are based on growth on Z-cut single crystalline substrates. This is related due to the facts that $LiNbO_3$ films tend to align with their c-axis perpendicular to the smooth surface of the substrate [14] and that the thermal expansion coefficient α_z (along the z-axis, which corresponds to the out-of-plane direction), is much smaller compared to α_x and α_y coefficients [15]. The significant suggests that $LiNbO_3$ crystals exhibit a notable contraction along the z-axis as the temperature increases. It's worth noting that the crystallization temperature for $LiNbO_3$ is within the range of 530 to 580 °C [16], but most of the depositions reported were done at 600-700°C [13]- [12].

A 200 nm-thick $LiNbO_3$ film was deposited by PLD by Laura Sauze et al. They employed a stoichiometric $LiNbO_3$ target and used 4-inch $LiNbO_3$ wafers (X-cut, Y-cut, and Z-cut) as substrates [13]. The substrate tempetrature during the deposition was around 400°C with an oxygen pressure of 0.2 mbar inside the chamber [13]. Their research demonstrated that a standard wafer-based Pulsed Laser Deposition method can be effectively employed to grow $LiNbO_3$ thin films with crystalline quality and chemical composition closely resembling that of a monocrystalline substrate. The stoichiometry of their layers closely matched that of the substrate for layers grown on both (110) and (001) oriented substrates [13].

2. Presentation of the study

The primary objective of this study is to conduct a comprehensive investigation of the influence of operational parameters on the quality of the crystalline structure and surface roughness in deposited layers. To achieve this goal, we used the Solmates 8 in.-wafer-based SIP800 platform and employed the Pulsed Laser Deposition technique to homoepitaxially grow $LiNbO_3$ films, with a thickness ranging between 150 to 200 nm, on $LiNbO_3$ substrates.

In the deposition process, we utilized laser ablation with a KrF excimer laser, having a wavelength of 248 nm, operating at a frequency of 100 Hz, and delivering an energy of 450 mJ. Importantly, we maintained a constant distance of 55 mm between the target and substrate throughout the entire deposition process. Table 2.2 categorizes the different modifications in deposition parameters for each sample.

Wafer ID	Crystal cut	Orientation	Pressure (mbar)	Temperature (°C)	Target
X-01	X	(1 1 0)	0.2	500	$LiNbO_3$
X-02	X	(1 1 0)	0.007	500	$LiNbO_3$
X-03	X	(1 1 0)	0.2	600	$LiNbO_3$
X-04	X	(1 1 0)	0.2	600	$Li_{1.1}NbO_{3.05}$
X-05	X	(1 1 0)	0.007	500	$Li_{1.1}NbO_{3.05}$
Y-01	Y+128°	(1 0 4)	0.2	500	$LiNbO_3$
Y-02	Y+128°	(1 0 4)	0.007	500	$LiNbO_3$
Y-03	Y+128°	(1 0 4)	0.2	600	$LiNbO_3$
Y-04	Y+128°	(1 0 4)	0.2	600	$Li_{1.1}NbO_{3.05}$
Y-05	Y+128°	(1 0 4)	0.007	500	$Li_{1.1}NbO_{3.05}$
Z-01	Z	(0 0 1)	0.2	500	$LiNbO_3$
Z-02	Z	(0 0 1)	0.007	500	$LiNbO_3$
Z-03	Z	(0 0 1)	0.2	600	$LiNbO_3$
Z-04	Z	(0 0 1)	0.2	600	$Li_{1.1}NbO_{3.05}$
Z-05	Z	(0 0 1)	0.007	500	$Li_{1.1}NbO_{3.05}$

TABLE 2.2 PRESENTATION OF SAMPLES WITH VARIATIONS IN ASSOCIATED DEPOSITION CONDITIONS.

Unfortunately, during the deposition process, lithium (Li) atoms tend to undergo diffusion away from the film, leading to the creation of a lithium-deficient phase known as $LiNb_3O_8$, which lacks ferroelectric properties. Son et al. concluded that two primary factors

contribute to this phase evolution: the removal of Li by the high-energy plume and variations in elemental distribution within the [17]. To manage this issue, the background gas pressure, acting as a counterforce impeding plasma expansion, was adjusted within the range of 0.007 to 0.2 mbar.

In this study, we incorporated two separate targets, each with distinct compositions, to investigate the resulting influence of the quantity of lithium (Li) atoms in the target on the properties and characteristics of the deposited films. The first target had a stoichiometric composition of $LiNbO_3$, while the second target featured a Li-enriched composition, including 10% Li_2O atoms in $LiNbO_3$. Considering that the crystallization temperature for $LiNbO_3$ falls within the range of 530 to 580 °C [16], the substrate temperature was varied within the range of 500 to 600°C.

To achieve varied crystalline orientations of the thin films after the growth process, we utilized three different crystal cuts of $LiNbO_3$ as substrates: X, Z, and Y+128°. These specific orientations of the substrates provided different lattice parameters, facilitating the controlled deposition of thin films.

Following the deposition of thin films on the samples, transparency measurements were conducted, revealing a spectrum from almost transparent to very dark samples. To assess the crystalline quality of the deposited layers, a specialized methodology employing X-ray diffraction (XRD) techniques was developed. Additionally, precise measurements using Atomic Force Microscopy (AFM) were carried out to investigate the surface morphology of the grown films.

2.1 Study of the influence of the substrate temperature

The effects of substrate temperature on the growth of $LiNbO_3$ thin films by PLD were investigated by Wu et al [1]. Their investigation revealed that the deposition temperature significantly impacted the crystallinity, stoichiometry, and surface morphology of the films. Specifically, lower temperatures led to reduced crystallinity and the presence of secondary phases, while higher temperatures caused overheating and compromised stoichiometry [1].

Several researchers have explored the growth of $LiNbO_3$ using pulsed laser deposition (PLD) at lower temperatures, as documented in studies [1]- [18]. Generally, films grown at 500°C exhibit reduced crystallinity and a higher occurrence of secondary phases compared to those grown at higher temperatures. The slower growth rate at this temperature limits the time

available for ion arrangement into a crystalline structure. Additionally, the lower oxygen pressure at this temperature contributes to the formation of secondary phases. Despite these drawbacks, growing $LiNbO_3$ at 500°C offers notable advantages. Firstly, the films are less susceptible to overheating, minimizing potential damage to their stoichiometry. Secondly, there is an increased possibility of achieving the desired orientation of the films, which is significant for specific applications [1]- [18].

Finally, the deposition temperature in PLD is subject to various factors, including the characteristics of the laser system, oxygen pressure, the properties of the target material, and the desired attributes of the thin films. As a result, the specific values of the deposition temperature will vary depending on these factors. Therefore, optimizing the deposition temperature is important for each PLD system to achieve the desired film properties efficiently. In line with this notion, the substrate deposition temperatures were varied between 500°C and 600°C, as indicated in Table 2.1. By exploring this temperature range, we aimed to identify the most favorable deposition temperature for our PLD machine (Solmates 8 in.-wafer-based SIP800 platform) and films required. Temperature control during the deposition was performed on the ceramic holder under the wafer so that the temperature of the substrate can differ.

2.2 Study of the influence of the oxygen pressure

The oxygen pressure is an important parameter in the growth of $LiNbO_3$ thin films by PLD. It affects the stoichiometry, crystallization, and surface morphology of the films. In general, a higher oxygen pressure will result in a higher deposition rate and a more stoichiometric film. This is because the oxygen pressure helps to stabilize the growth of the $LiNbO_3$ film. However, if the oxygen pressure is too high, it can also lead to the formation of secondary phases [19].

The study investigated the influence of oxygen pressure on the properties of nanocrystalline lithium niobate ($LiNbO_3$) films grown using pulsed laser deposition was done by Vakulov et al. [20]. Their results obtained from the x-ray photoelectron spectroscopy (XPS) study revealed that optimal conditions for the formation of $LiNbO_3$ films were achieved at an oxygen pressure of 1×10^{-2} Torr (0.01 mbar) and 1×10^{-5} Torr (1.3×10^{-5} mbar) [20]. The introduction of an oxygen (O_2) background gas creates a highly reactive environment localized at the substrate's surface [21], [22].

The optimum oxygen pressure for $LiNbO_3$ thin films by PLD depends on the specific laser system and target used:

- Lower oxygen pressures can lead to less crystalline films and rougher surface morphologies [19]. A decrease in pressure implies an increased mean free path for atoms, representing the average distance a particle can travel between successive collisions with other particles. Consequently, heavier Nb atoms are less affected by these collisions compared to lighter Li atoms [21]. As a result, upon reaching the layer, these Nb atoms carry significant kinetic energy, potentially displacing Li atoms (resputtering) and leading to the formation of a low-Li phase. On the contrary, high kinetic energy of atoms can contribute to the creation of higher-quality films, where kinetic energy serves as an energy source for layer formation, akin to thermal energy.
- Higher oxygen pressures can lead to growth with improved stoichiometry, but they can also trigger the formation of secondary phases. [19]. Under such conditions, a lot of collisions will impact both Nb and Li atoms, and resputtering will not happen [23]. Thermal energy will be the primary source of energy in this scenario.

The values of the oxygen pressure will depend on the specific laser system and target used. It is important to optimize the oxygen pressure to achieve the desired film properties. In line with this notion, the deposition pressures were varied between 0.2 and 0.007 mbar, as indicated in Table 2.1. The selection of these values was motivated by the reported homoepitaxial growth experiments conducted by Sauze et al., in which they operated the chamber at an oxygen pressure of 0.2 mbar [13].

2.3 Study of the influence of amount of Li in target

Shibata et al. conducted an investigation to explore the effects of the Li/Nb ratio on the characteristics of $LiNbO_3$ thin films, which were produced through the technique of pulsed laser deposition [24]. To form the targets required for the deposition process, they utilized Li-Nb-O ceramic disks. These disks were created by sintering a mixture of Li_2CO_3 and Nb_2O_5 powders in an air environment at a temperature of 1100°C. The Li/Nb ratios of the targets were systematically varied within the range of 1.0 to 3.0. Finally, their efforts resulted in increased Li content in the deposited layer [24].

As a consequence of this increased Li content, the films exhibited single-phased growth within their experimental system. This result indicated that the change of the Li/Nb ratio played

a critical role in determining the properties of the films [24]. Remarkably, the optimal quality was achieved when the Li/Nb ratio in the target was set to 2, showing the significant influence of this ratio on the characteristics of the deposited thin films [24]. The selection of lithium (Li) content in thin films may require adjustments based on the specific conditions and requirements of individual applications.

In our research, we aimed to explore how the amount of lithium (Li) atoms in the target material affects the properties and characteristics of the deposited films. To do this, we used two ceramic targets with different compositions, as outlined in the study Table 2.1. The first target was having a stoichiometric composition. In contrast, the second target was enriched with an additional 10 mole percent of lithium oxide (Li_2O), resulting in a final composition of $Li_{1.1}NbO_{3.05}$. This particular composition was selected to prevent the formation of a parasitic phase ($LiNb_3O_8$) within the deposited layer, which could occur due to an insufficient amount of Li atoms in the plasma plume. By using these two different targets, we aimed to study how the lithium content influences the properties of the thin films deposited.

3. Characterization and analysis

3.1. Optical properties

3.1.1. Transparency measurement

The visible variations in color among the different samples led us to quantitatively evaluate the transparency of the wafers. Transparency, in this context, refers to the degree of optical clarity, achievable when the refractive index remains uniform throughout the material in the direction of observation. This evaluation included passing light through the samples and comparing the intensity of the transmitted light with the intensity of the incident light. Figure 2.1 shows the results of the measurements together.

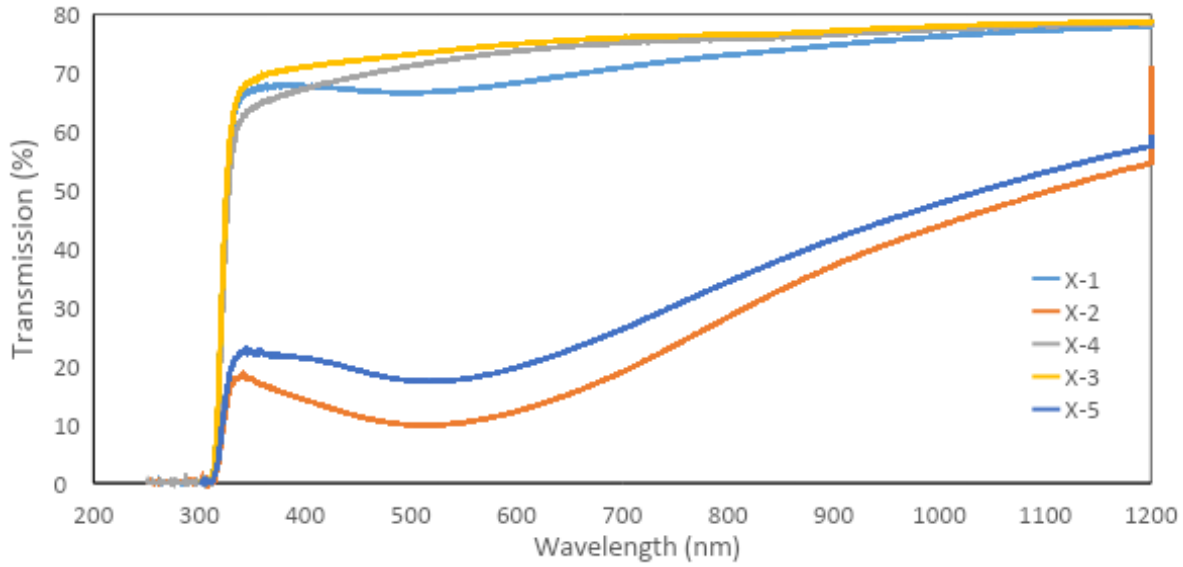

FIGURE 2.1 TRANSPARENCY MEASUREMENTS PROFILES OF THE $LiNbO_3$/ (1 1 0) $LiNbO_3$ DEPOSITED AT VARIOUS CONDITIONS.

Wafers X-2 and X-5 noticeably have less clarity, which is easily visible without special tools. This decrease in transparency has also been confirmed through measurements on the other wafers. Specifically, all wafers with alternative orientations (Z- and Y+128°-cut) deposited at a pressure of 0.007 mbar show similar optical characteristics, with lower transmission compared to growth at 0.2 mbar.

This observation aligns with findings from previous studies conducted by Sugak et al. in 2017 [25]. They observed reversibility in changes to optical properties with the help of annealing procedures in an oxygen atmosphere. This supported the hypothesis that oxygen

diffusion plays a crucial role in the coloration and discoloration processes of $LiNbO_3$. The absorption of the short-wave band is likely due to defects (oxygen loss) within the sublattice that captures electrons. It's also worth noting that the coloration and discoloration processes in these crystals exhibit anisotropic behavior. The maximum diffusion depth was observed along the Z-direction, while minimal diffusion occurred along the X-direction. This can be understood by taking into account the unique structural features of $LiNbO_3$ crystals, where the movement of ions is more simplified along the Z-direction [25].

3.2. Chemical properties

In response to observed changes in optical transparency and knowing that transparency depends on the concentration of oxygen vacancies within $LiNbO_3$ [25], we made an analysis employing Time-of-Flight Secondary Ion Mass Spectrometry (TOF-SIMS). In this method, an ion gun with the ability to deeply ablate samples is used, creating an electric field that can influence the diffusion patterns of atoms, particularly affecting the distribution of lithium.

The TOF-SIMS depth profiles were generated using a TOF SIMS V mass spectrometer provided by IONTOF, employing the following experimental parameters: An analysis beam consisting of Bi3+ ions with an energy level of 25 keV and a current ranging from approximately 0.3 to 0.5 picoamperes was utilized. The field of view was set at 60 µm × 60 µm, and data acquisition involved capturing one shot per pixel, resulting in a total of 128 x 128 pixels. Sputtering was carried out using Cs+ ions with an energy of 1 keV and a current of approximately 80 nanoamperes, resulting in sputter craters measuring 200 µm × 200 µm. Positive secondary ions, including MCs+ and MCs2+ clusters, were detected with a cycle time of 100 microseconds. The analytical procedure was executed in an interlaced mode, comprising 1 frame of analysis followed by 30 frames of sputtering, with a 1-second pause interspersed between them. To mitigate charge-related effects during data acquisition, an electron flood gun was employed.

It's crucial to note that due to the absence of reference samples, quantification and depth calibration of the obtained profiles were not feasible. However, it is still possible to conduct comparative assessments by normalizing the data against signals from the substrate and using samples prepared at 0.2 millibars and 500°C as reference standards.

Depth profiles on Z-, X-, and Y+128°-Cut samples appear almost identical, leading us to analyze them collectively. Films manufactured at 0.2 mbar have a composition close enough

to that of the substrate, unlike those designed at 0.007 mbar. Consequently, it can be told that for X- and Y+128°-cuts depositions (X-2, X-5, Y+128°-2, and Y+128°-5) performed at low pressure, lower levels of oxygen are observed in the films.

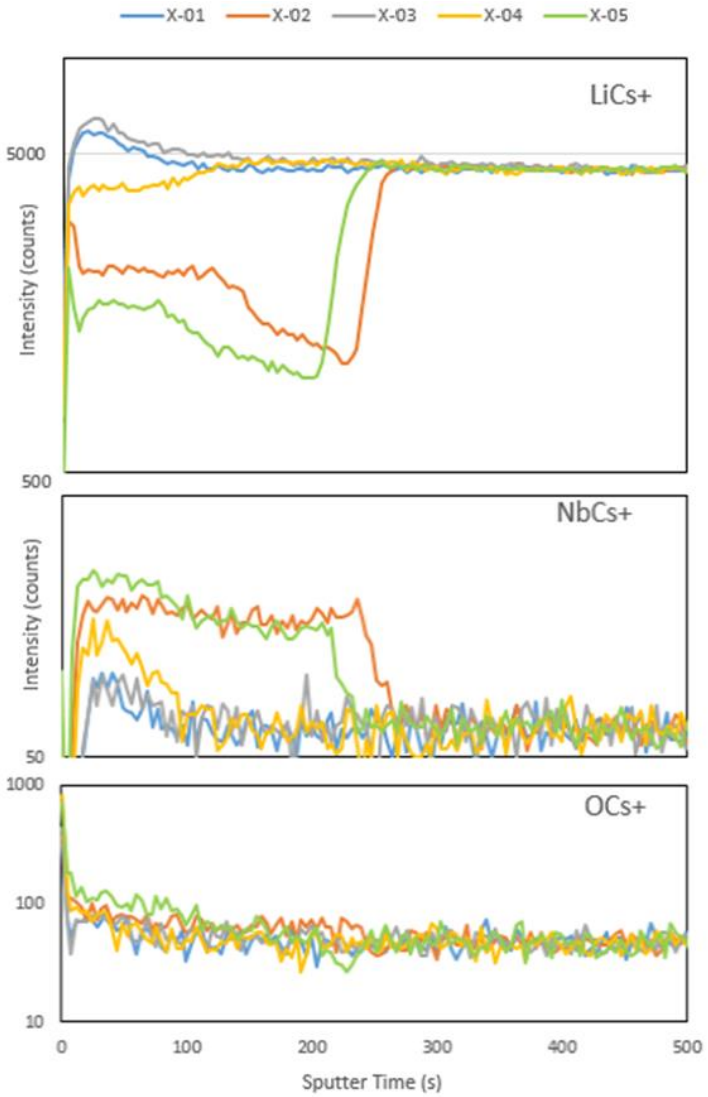

FIGURE 2.2 THE TOF-SIMS DEPTH PROFILES OF THE $LiNbO_3$/ (1 1 0) $LiNbO_3$ DEPOSITED AT VARIOUS CONDITIONS.

When the depositions were done at a pressure of 0.2 mbar for both targets, noticeable differences were observed, with film X-04 (the target enriched with additional Li_2O) showing the most significant variation. This difference becomes evident when comparing the chemical compositions of the grown layers and substrates.

Films produced at 0.2 mbar are similar to the composition of the substrate, unlike films grown at 0.007 mbar. In all films made at the lower pressure, lithium levels were lower compared to those in films deposited at 0.2 millibar. Interestingly, the concentrations at 0.2 millibar are quite like those of the $LiNbO_3$ substrate, while niobium levels are significantly higher than in the substrate. Importantly, it is clear that the pressure during deposition has a

much more significant impact on the chemical composition of the films than factors such as heater temperature and target type.

3.3. Structural properties

3.2.1. XRD analysis

For the purpose of analyzing the quality of the deposited layers in terms of crystalline structure, a specialized methodology employing X-ray diffraction (XRD) techniques was developed. This methodology requires conducting reciprocal space mapping for each sample under investigation. From the obtained mapping data, the Rocking Curve (RC) from symmetrical scan, is extracted and analyzed.

The analysis of the RC yields valuable insights into the quality of the crystal layers. By examining the Full Width at Half Maximum (FWHM) of the diffraction peak associated with the primary crystal plane (which depends on the crystallographic orientations of the substrate), both for the layer and the substrate, the mosaicity of the layer can be evaluated. The FWHM serves as a measure of the extent or perfection of the crystal planes, enabling the assessment of the crystalline quality of the layer.

Fortunately, due to the high quality of almost all the thin films compared to the substrate there were no possibilities to even compare FWHM of the thin films and layers for some of the samples (Figure 2.3 shows the example of such measures) while utilizing high resolution XRD.

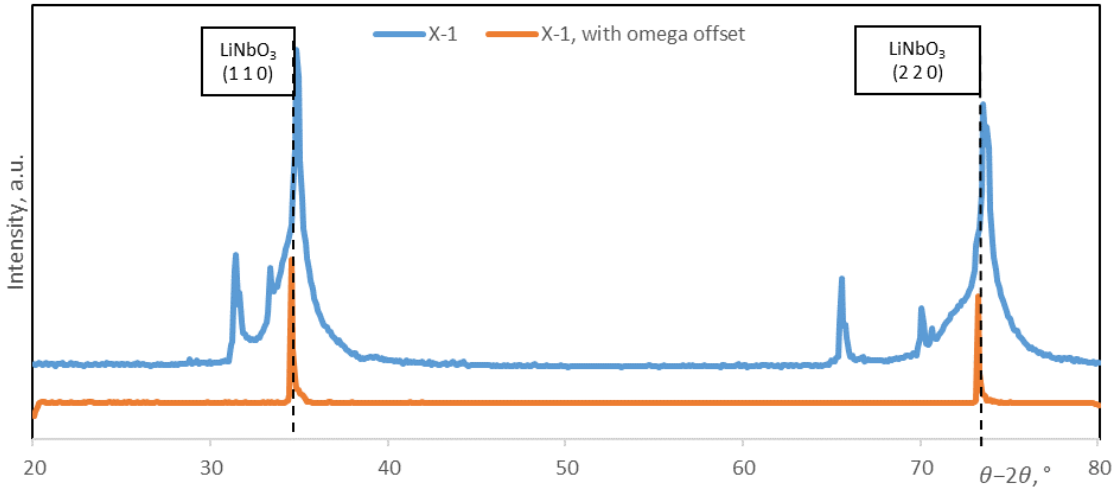

FIGURE 2.3 XRD Θ/2Θ PATTERN OF THE $LiNbO_3$/ (1 1 0) $LiNbO_3$ DEPOSITED AT 0.2 MBAR, 500°C, $LiNbO_3$ TARGET (X-1).

For all the samples, X-ray Diffraction (XRD) φ-scans were conducted, involving the rotation of the sample holder around the axis perpendicular to the sample. These scans confirmed the epitaxial nature of the films. Detailed scans for different samples are provided in the Appendix II for reference. θ/2θ scans were conducted for all the wafers, and below are some examples of such scans (Figure 2.4). Regrettably, for the depositions carried out at low pressure (0.007 millibar) on X-cut wafers (X-2 and X-5), a combination of $LiNbO_3$ and parasitic low-lithium (Li) phase peaks were detected.

In conclusion, the XRD scans have conclusively demonstrated that all depositions carried out on various substrates possess an epitaxial nature. However, it is worth noting that for the depositions conducted at low pressure (0.007 millibar) on X-cut wafers (X-2 and X-5), the presence of a combination of $LiNbO_3$ and parasitic low-lithium (Li) phase peaks was detected. To facilitate a more comprehensive assessment of the crystal quality of the layers, reciprocal space mappings were conducted in high resolution. This approach was chosen as both ω and θ/2θ scans yielded very similar results in terms of the quality of both the substrates and the layers, necessitating a more detailed investigation.

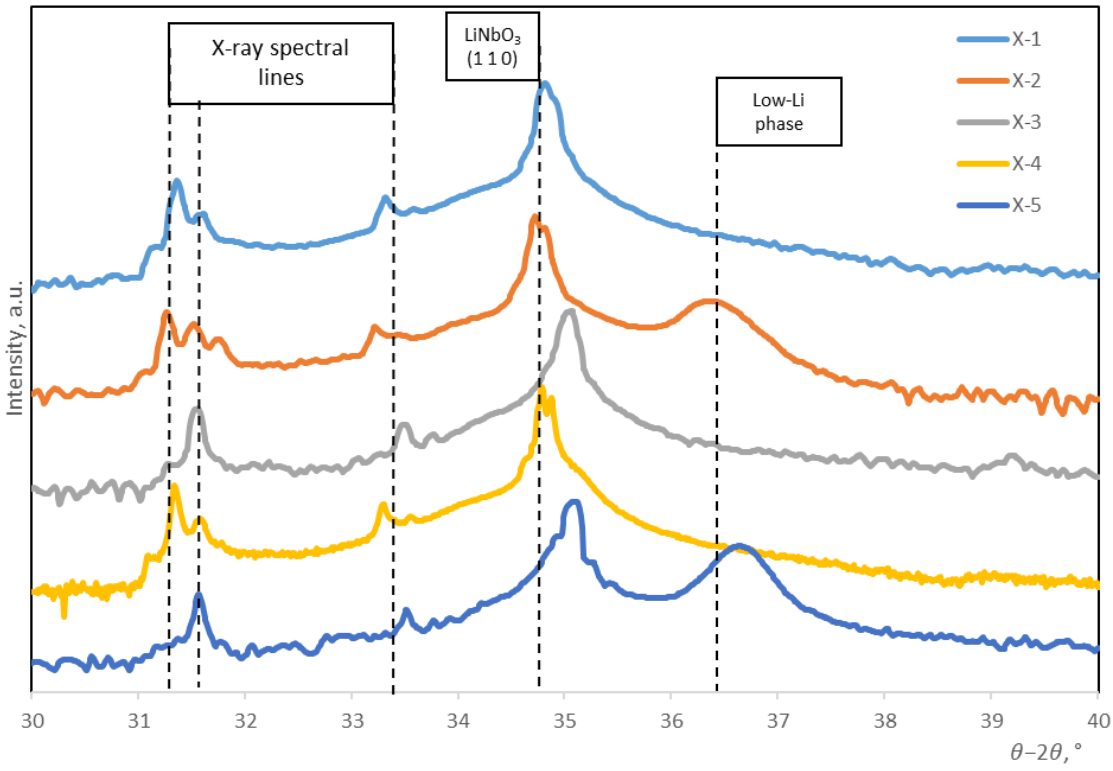

FIGURE 2.4 XRD Θ/2Θ PATTERN OF THE LINBO3/ (1 1 0) $LiNbO_3$ DEPOSITED AT VARIOUS CONDITIONS: (A) 0.2 MBAR, 500°C, $LiNbO_3$ TARGET; (B) 0.007 MBAR, 500°C, $LiNbO_3$ TARGET; (C) 0.2 MBAR, 600°C, $LiNbO_3$ TARGET; (D) 0.2 MBAR, 600°C, $Li_{1.1}NbO_{3.05}$ TARGET; (E) 0.007 MBAR, 500°C, $Li_{1.1}NbO_{3.05}$ TARGET.

3.2.2. High resolution scans and reciprocal space mapping

To assess the crystal quality of the deposited layers, a high-resolution XRD was conducted. Reciprocal Space Maps (RSMs) were measured for specific crystal planes: (1 1 0) for the X-cut substrate, (1 0 4) for the Y+128°-cut substrate, and (0 0 6) for the Z-cut substrate. Following the integration and mathematical analysis of a band in Q_x space, symmetric scans and rocking curves were extracted. The maps for various samples are grouped in Appendix III.

Z-cut

Since no noticeable differences were observed in various scans of the films on Z-cut wafers, especially those created under low-pressure conditions for both target materials, it's reasonable to start our analysis with these scans. The figure below shows the results of a high-resolution reciprocal space map (RSM) on the left and an ω-2θ measurement on the right. These analyses were specifically conducted on the Z-2 wafer at 0.007 mbar and 500°C, using the $LiNbO_3$ target (Figure 2.5). Remarkably, the RSM and ω-2θ measurements have similar features (the corresponding scans for Z-5 are available in the Appendix.

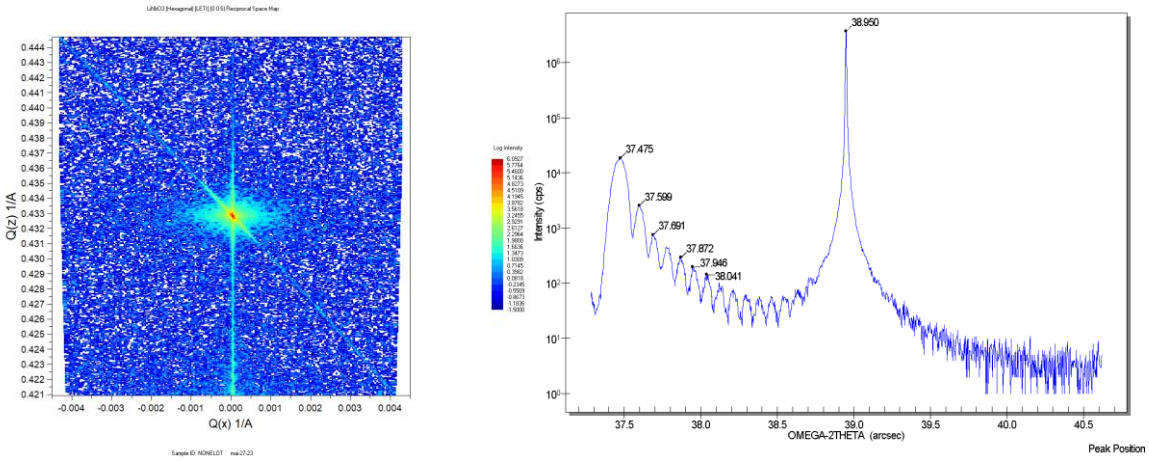

FIGURE 2.5 RECIPROCAL SPACE MAP (RSM) (LEFT) AND Ω-2Θ MEASUREMENT (RIGHT) OF THE Z-2 WAFER $LiNbO_3$/ (0 0 6) $LiNbO_3$ DEPOSITED AT 0.007 MBAR, 500°C, LINBO3 TARGET.

It is imperative to note that, for both wafers deposited at low pressure, the epitaxial peak corresponding to the film is shifted to the left by more than 1°. This shift signifies that the film quality is lower than that of the substrate and may potentially contain low-Li parasitic phases, akin to the observations made with X-cut substrates.

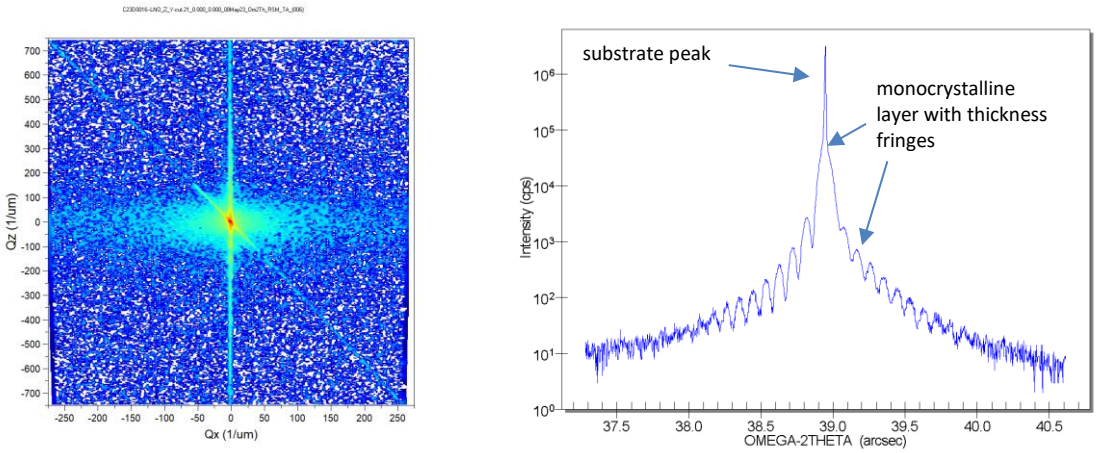

FIGURE 2.6 RECIPROCAL SPACE MAP (RSM) (LEFT) AND Ω-2Θ MEASUREMENT (RIGHT) OF THE Z-2 WAFER $LiNbO_3$/ (0 0 6) $LiNbO_3$ DEPOSITED AT 0.2 MBAR, 600°C, $Li_{1.1}NbO_{3.05}$ TARGET.

On the contrary, when examining the depositions carried out at 0.2 mbar, we observed distinct layers with thickness fringes (shown on Fig. 2.6). We conducted thickness determination by analyzing the spacing of these fringes in the 2θ-ω scans. Upon comparison, these scans exhibit similarity, although the fringes for the deposition conducted at 600°C with the $Li_{1.1}NbO_{3.05}$ target appear more defined (shown on Figure 2.6, another scans can be found in the Appendix III).

The FWHM values consistently remain low and show proximity between the film and the substrate for all Z-cut wafers deposited at 0.2 mbar. These values (of ~0.005°) closely match the instrumental resolution, estimated to be in the range of 0.003°. This result confirms the epitaxial nature of the film. As a result, the deposited layers can be characterized as single-phase and possess a crystalline quality nearly the same as the substrate.

Y+128° and X-cuts

Recognizing the similarities in properties between Y+128° and X-cut wafers, we conducted a collective examination. However, it is important to mention that similar X-cut wafer has previously been analyzed by Sauze et al [13]. Given this, our primary focus will be on the analysis of the Y+128°-cut wafers, as they hold particular significance in the context of SAW device production.

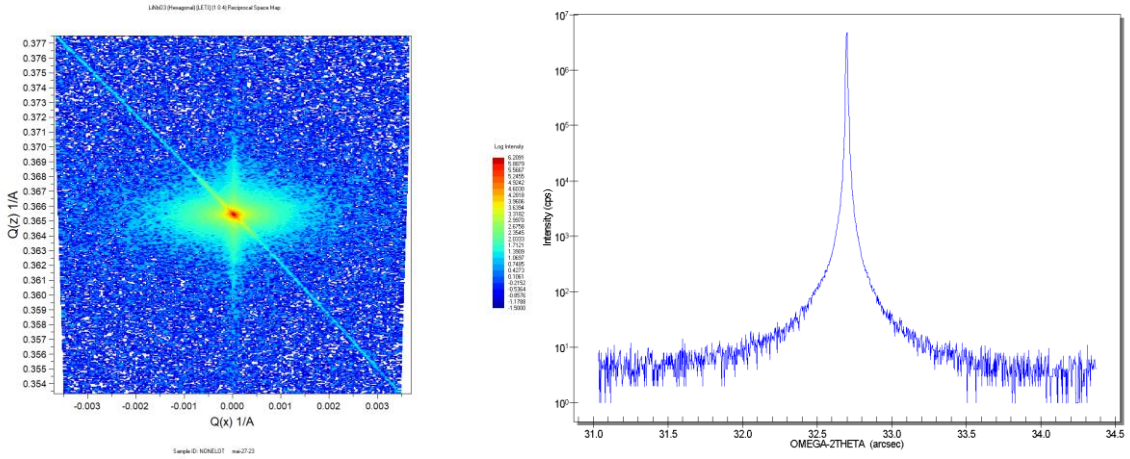

FIGURE 2.7 RECIPROCAL SPACE MAP (RSM) (LEFT) AND Ω-2Θ MEASUREMENT (RIGHT) OF THE Y-2 WAFER $LiNbO_3$/ (0 0 6) $LiNbO_3$ DEPOSITED AT 0.007 MBAR, 500°C, $LiNbO_3$ TARGET.

In the figure presented above (Figure 2.7), the results of a high-resolution RSM analysis are displayed on the left, while an ω-2θ measurement is shown on the right. These analyses were conducted specifically on the Y-02 wafer (deposited under conditions of 0.007 millibar and 500°C, utilizing the $LiNbO_3$ target). Both the RSM and ω-2θ measurements exhibit similar characteristics. For further reference, the corresponding scans for Y-05 are included in the Appendix. It's important to note that neither the RSM nor the ω-2θ measurements reveal any epitaxial layer signal. However, in the RSM, there is an observation of diffuse scattering around the substrate peak. This could be a sign of existence of the low-Li phase, similar to ones observed on X-cut wafers.

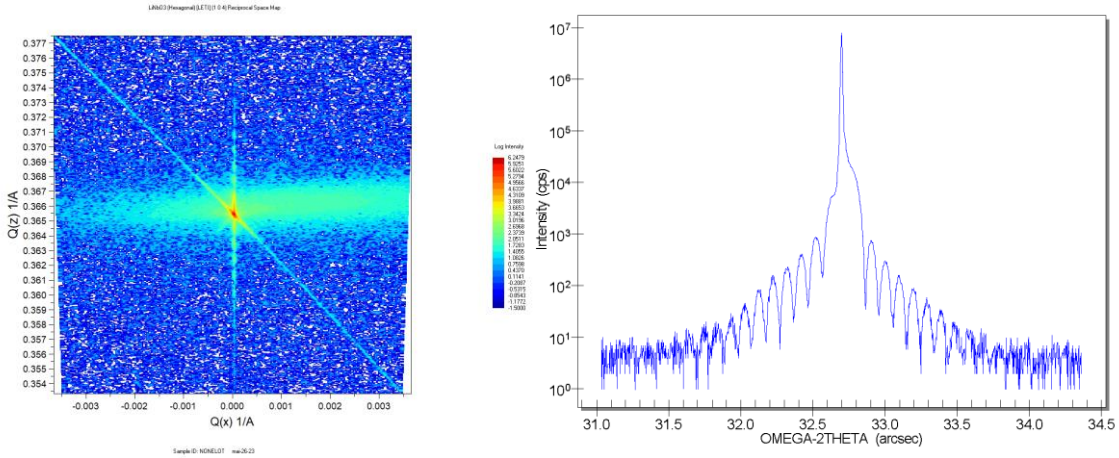

FIGURE 2.8 RECIPROCAL SPACE MAP (RSM) (LEFT) AND Ω-2Θ MEASUREMENT (RIGHT) OF THE Y-1 WAFER $LiNbO_3$/ (0 0 6) $LiNbO_3$ DEPOSITED AT 0.2 MBAR, 500°C, $LiNbO_3$ TARGET.

In contrast, when examining the depositions carried out at 0.2 millibar (Figure 2.8), we observed layers exhibiting thickness fringes. A RSM analysis conducted for the wafer deposited at 0.2 millibar and 500°C using the $LiNbO_3$ target suggests that it is either a textured polycrystalline layer or a highly defective monocrystalline layer with a slight tilt to the right.

Similarly, ω-2θ measurements also indicate the presence of a monocrystalline layer with thickness fringes.

When comparing the RSM and ω-2θ measurements of the wafers deposited at 500°C (above, Figure 2.8) and 600°C (below, Figure 2.9) using the $LiNbO_3$ target, it becomes evident that there are no significant differences, except for a lower quantity of fringes and variations in thickness. These thicknesses were determined by analyzing the spacing between fringes in the 2θ-ω, which measured 95 nm for the 500°C and 120 nm for the 600°C deposition, respectively.

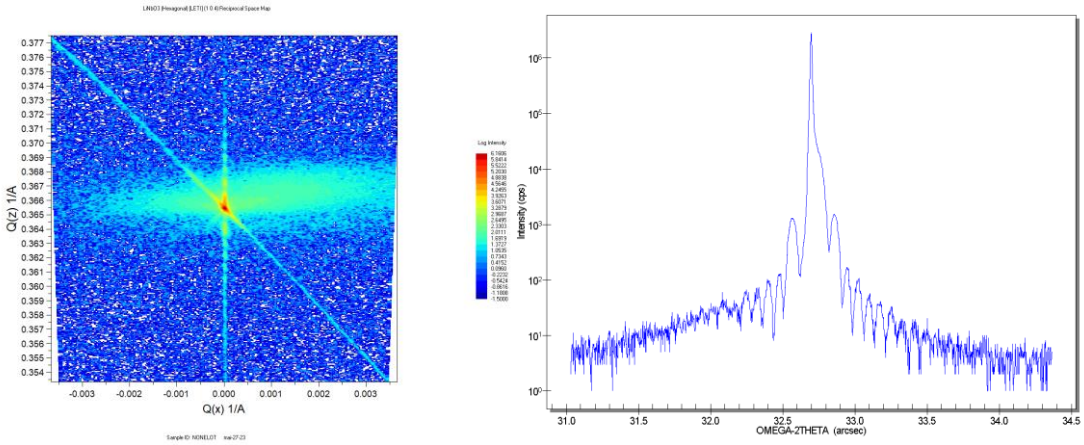

FIGURE 2.9 RECIPROCAL SPACE MAP (RSM) (LEFT) AND Ω-2Θ MEASUREMENT (RIGHT) OF THE Y-3 WAFER $LiNbO_3$/ (0 0 6) $LiNbO_3$ DEPOSITED AT 0.2 MBAR, 600°C, $LiNbO_3$ TARGET.

In summary, for the wafers deposited at 0.2 mbar and 600°C, utilizing a $Li_{1.1}NbO_{3.05}$ target, the RSM reveals no difference compared to the layers deposited at the same temperature and pressure but without the additional Li in the target material. The signals from the fringes exhibit asymmetry in the ω-2θ scans, suggesting lower quality films in comparison to the layers grown at the same conditions but without the additional Li in the target material.

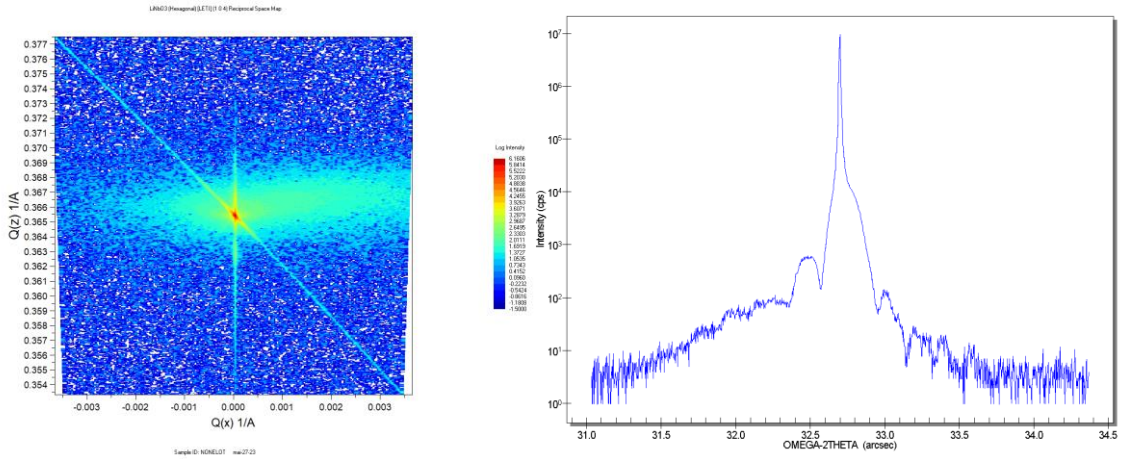

FIGURE 2.10 RECIPROCAL SPACE MAP (RSM) (LEFT) AND Ω-2Θ MEASUREMENT (RIGHT) OF THE Y-4 WAFER $LiNbO_3$/ (0 0 6) $LiNbO_3$ DEPOSITED AT 0.2 MBAR, 600°C, $Li_{1.1}NbO_{3.05}$ TARGET.

Conclusions on XRD measurements

To evaluate the crystalline quality of the deposited layers, Reciprocal Space Maps (RSMs) were measured for different crystal planes: (1 1 0) for the X-cut, (1 0 4) for the Y+128°-cut, and (0 0 6) for the Z-cut substrate. Subsequently, by integrating and applying mathematical analysis to a region in Q_x space, symmetric scans and rocking curves were obtained.

It is important to highlight that, in the case of depositions conducted under low pressure conditions (0.007 millibar) on X-cut wafers (specifically, X-2 and X-5), the analysis revealed the presence of a mixture of $LiNbO_3$ and parasitic low-lithium (Li) phase peaks, which strongly suggests the polycrystalline growth.

In contrast, for depositions carried out at a pressure of 0.2 mbar and temperatures of 500°C and 600°C, using a $LiNbO_3$ target, a finding was the presence of homoepitaxial monocrystalline layers on all types of substrates. Additionally, thickness determination based on fringe spacing produced results in the range of 100-120 nanometers.

Wafer ID	Pressure (mbar)	Temperature (°C)	Target	Low-Li phase	RC, $\times 10^{-3}$ °
X-1	0.2	500	$LiNbO_3$	-	5.3
X-2	0.007	500	$LiNbO_3$	36.6°	-
X-3	0.2	600	$LiNbO_3$	-	5.3
X-4	0.2	600	$Li_{1.1}NbO_{3.05}$	-	4.8
X-5	0.007	500	$Li_{1.1}NbO_{3.05}$	36.6°	-
Y-1	0.2	500	$LiNbO_3$	-	5.3
Y-2	0.007	500	$LiNbO_3$	-	-
Y-3	0.2	600	$LiNbO_3$	-	5.3
Y-4	0.2	600	$Li_{1.1}NbO_{3.05}$	-	5.6
Y-5	0.007	500	$Li_{1.1}NbO_{3.05}$	-	-
Z-1	0.2	500	$LiNbO_3$	-	5.4
Z-2	0.007	500	$LiNbO_3$	-	5.1
Z-3	0.2	600	$LiNbO_3$	-	5.0
Z-4	0.2	600	$Li_{1.1}NbO_{3.05}$	-	5.0
Z-5	0.007	500	$Li_{1.1}NbO_{3.05}$	-	5.3

TABLE 2.3 SUMMARIZATION OF THE CRYSTAL PROPERTIES OF THE THIN FILMS DEPOSITED.

3.4. Surface properties

In order to investigate the surface morphology of the $LiNbO_3$ films, Atomic Force Microscopy (AFM) measurements were carried out for most the samples. Also, important to mention that due to domains formation it was not possible to conduct the measurements on some of the wafers.

Each sample was examined using two different scan sizes: 1 x 1 μm² and 5 x 5 μm². This approach facilitated an evaluation of the roughness of the deposited layers. To accurately assess the surface roughness characteristics of the $LiNbO_3$ films, an analysis of the Root Mean Square (RMS) roughness was performed based on the AFM image.

Acknowledging the similarity in roughness properties between wafers, we suggest conducting a collective examination, using as a basis X-cut wafers.

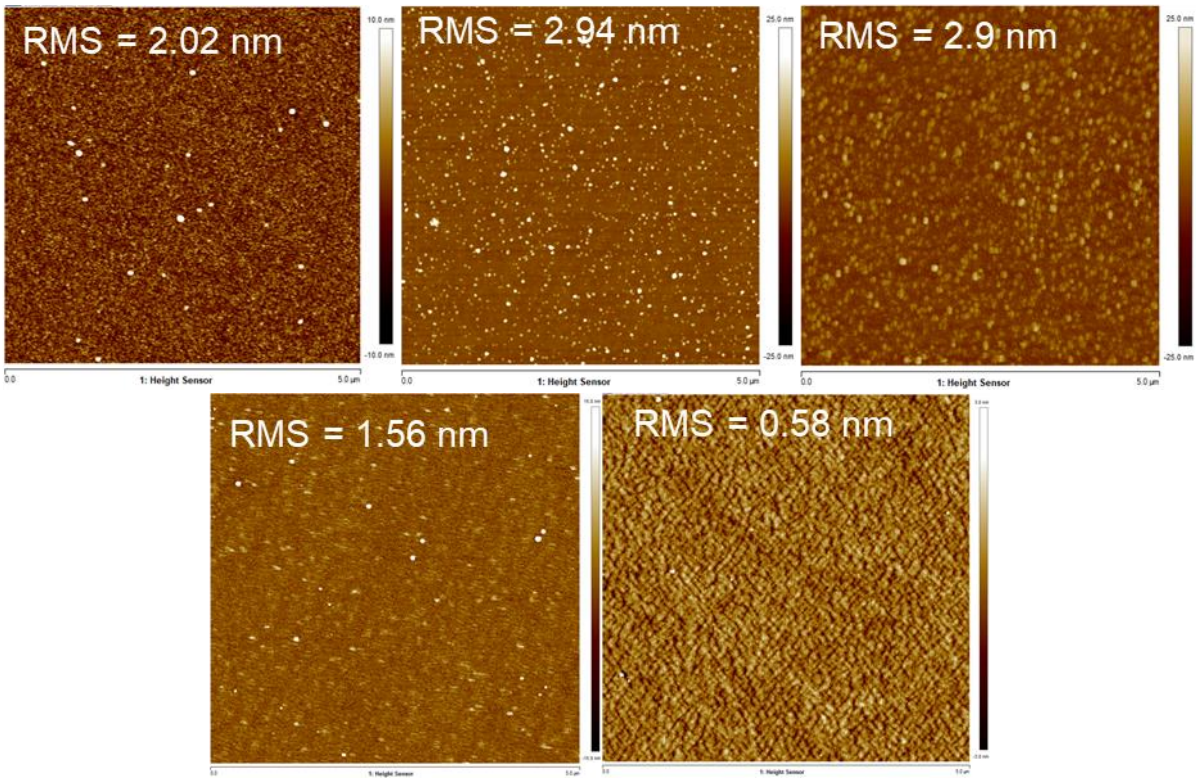

FIGURE 2.11 AFM MICROGRAPHS OF $LiNbO_3$ ON X-CUT $LiNbO_3$: (A) X-1; (B) X-2; (C) X-3; (D) X-4; (E) X-5. SCAN SIZE: (5×5) μM².

The AFM images of the 5 × 5 μm² scans of samples deposited on X-cut wafers are collectively presented in the above figure (Fig 2.11). In all instances of these 5 x 5 μm² scans, the surfaces of the films consist of rounded grains. Additionally, due to the pulsed laser deposition (PLD) process, some grains are also visible. It's important to note that these grains constitute the primary source of surface roughness.

The root mean square (RMS) roughness is highest for the sample grown at 0.2 mbar and 600°C, which is likely due to the presence of large grains on the surface. In contrast, the layer grown 500°C, utilizing a $Li_{1.1}NbO_{3.05}$ target, displays the smoothest surface among the examined samples.

The observations conducted at higher magnification using scan sizes of 1 x 1 μm² (as shown in the figures below) validated the previously obtained results. The grains that compose the layers are clearly noticeable, and the roughness, remains nearly consistent with the lower magnification observations.

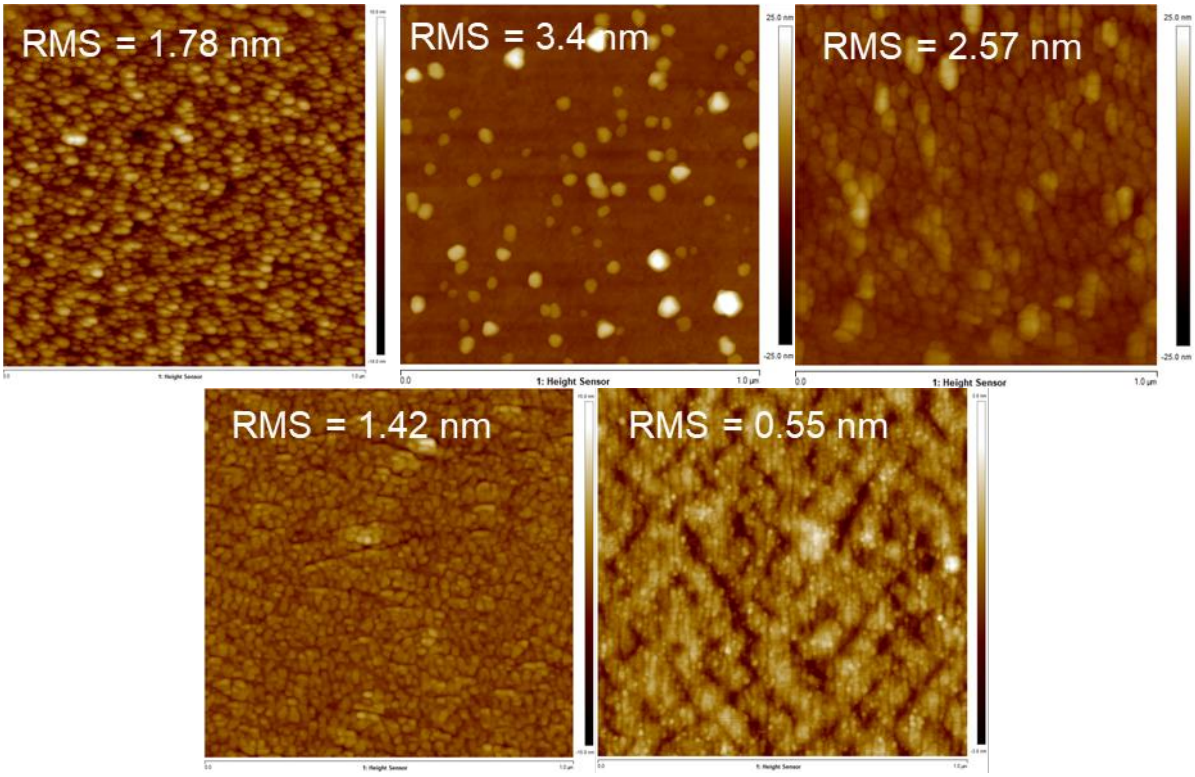

FIGURE 2.12 AFM MICROGRAPHS OF $LiNbO_3$ ON X-CUT $LiNbO_3$: (A) X-1; (B) X-2; (C) X-3; (D) X-4; (E) X-5. SCAN SIZE: (1×1) μM^2.

Notably, epitaxial columns can be observed on the wafer deposited at 0.007 mbar, 500°C, utilizing a $Li_{1.1}NbO_{3.05}$ target. This observation highlights the existence of tiny grains on the film surfaces of other films. These grains greatly influence the overall surface roughness of the deposited layers.

The provided table summarizes the findings related to surface properties observed in all the AFM scans. It provides an overview of how the surface properties are influenced by the diverse deposition conditions (including oxygen pressure, substrate temperature and amount of Li in target) for each crystallographic cut.

Wafer ID	Crystal cut	Pressure (mbar)	Temperature (°C)	Target	RMS 1x1 µm², nm	RMS 5x5 µm², nm
X-1	X	0.2	500	$LiNbO_3$	1.78	2.02
X-2	X	0.007	500	$LiNbO_3$	3.4	2.94
X-3	X	0.2	600	$LiNbO_3$	2.57	2.9
X-4	X	0.2	600	$Li_{1.1}NbO_{3.05}$	1.42	1.56
X-5	X	0.007	500	$Li_{1.1}NbO_{3.05}$	0.547	0.586
Y-1	Y+128°	0.2	500	$LiNbO_3$	2.35	2.51
Y-2	Y+128°	0.007	500	$LiNbO_3$	2.3	1.74
Y-5	Y+128°	0.007	500	$Li_{1.1}NbO_{3.05}$	1.16	1.26
Z-1	Z	0.2	500	$LiNbO_3$	1.46	1.53
Z-4	Z	0.2	600	$Li_{1.1}NbO_{3.05}$	1.41	1.04
Z-5	Z	0.007	500	$Li_{1.1}NbO_{3.05}$	1.39	1.15

TABLE 2.4 SUMMARIZATION OF THE SUREFACE PROPERTIES OF THE THIN FILMS DEPOSITED.

The surfaces of all the films are characterized by the presence of rounded grains. Additionally, due to the pulsed laser deposition process, some grains are also visible. Important is that amount of grains is bigger for the layers deposited at low pressure, which means that these grains can be a consequence of the resputtering. It's noteworthy that these structures constitute the primary source of surface roughness.

The root mean square (RMS) roughness reaches its highest values for the samples grown at 0.2 mbar and 600°C, likely due to the presence of larger grains on the surface. Interestingly, the layers grown at 500°C, using $Li_{1.1}NbO_{3.05}$ target, exhibit the smoothest surface among all the examined samples. However, since the thickness of all the films is around 100nm, the differences in roughness are relatively small.

4. Conclusions on the study

In this study, we utilized Pulsed Laser Deposition to achieve the homo-epitaxial growth of $LiNbO_3$ thin films. We conducted investigations on a range of 4-inch substrates, including those with (0 0 1), (1 1 0), and (1 0 4) crystal orientations, with the primary objective of controlling the crystalline orientation of $LiNbO_3$ films.

To gain control over film crystallinity and chemical composition, we examined growth parameters such as substrate temperature (500 and 600°C), oxygen pressure (0.2 and 0.007mbar), and target composition (stoichiometric $LiNbO_3$ and $Li_{1.1}NbO_{3.05}$). Our research involved the characterization of both the physical and chemical properties of the as-deposited layers, and we correlated these properties with the deposition conditions.

It's essential to emphasize that all wafers, following deposition at low oxygen pressure (0.007 mbar), display a substantial decrease in transparency, a noticeable phenomenon even not using specific tools (they became darker). This decrease in transparency has been further confirmed through quantitative measurements and is consistent with earlier research by Sugak et al. in 2017 [25]. Sugak and colleagues observed reversibility in changes to optical properties after consecutive reducing and oxidizing annealing steps in an oxygen-rich environment. These findings support the hypothesis that oxygen diffusion plays a fundamental role in the processes of coloration and discoloration in $LiNbO_3$ [25].

Time-of-Flight Secondary Ion Mass Spectrometry (TOF-SIMS) was utilized to analyze the composition of the thin films. It is evident that the deposition pressure has a significantly greater influence on the chemical composition of the films compared to factors such as heater temperature and target type. The films deposited at a pressure of 0.2 mbar closely are similar to the composition of the substrate, which is in contrast to the films produced at a pressure of 0.007 mbar.

To evaluate the crystalline quality of the deposited layers, an high-resolution XRD analysis was conducted. Specifically, Reciprocal Space Maps (RSMs) were measured for distinct crystal planes: (1 1 0) for the X-cut substrate, (1 0 4) for the Y+128°-cut substrate, and (0 0 6) for the Z-cut substrate. The films' epitaxial nature was confirmed through ω-2θ measurements, and RSM mappings. It's important to highlight that in the case of depositions conducted under low-pressure (0.007 millibar) the analysis shown the presence of a mixture of $LiNbO_3$ and parasitic low-lithium phase peaks. The formation of parasitic phases can be attributed an increased mean

free path for atoms (average distance a particle can travel between successive collisions with other particles). Consequently, heavier Nb atoms experience less disruption from these collisions compared to lighter Li atoms. Finally, upon reaching the layer, these Nb atoms carry significant kinetic energy, potentially causing the displacement of Li atoms (resputtering) and contributing to the formation of a low-Li phase. Important is that on the surface of these wafers amount of grains is bigger, which means that these structures can be also a consequence of the resputtering.

In contrast, for depositions carried out at a pressure of 0.2 mbar and temperatures of 500°C and 600°C, using a $LiNbO_3$ target, a consistent result was the presence of homoepitaxial monocrystalline layers on all types of substrates.

To explore the surface morphology of the $LiNbO_3$ films deposited using the pulsed laser deposition technique, Atomic Force Microscopy (AFM) measurements were conducted. The AFM analysis revealed that the surfaces of all the films feature rounded grains, with some grains being visible due to the pulsed laser deposition process. However, it's worth noting that since the thickness of all the films is approximately 100 nm, the differences in roughness are relatively small despite the presence of these structures (RMS ~ 0.5 - 2nm).

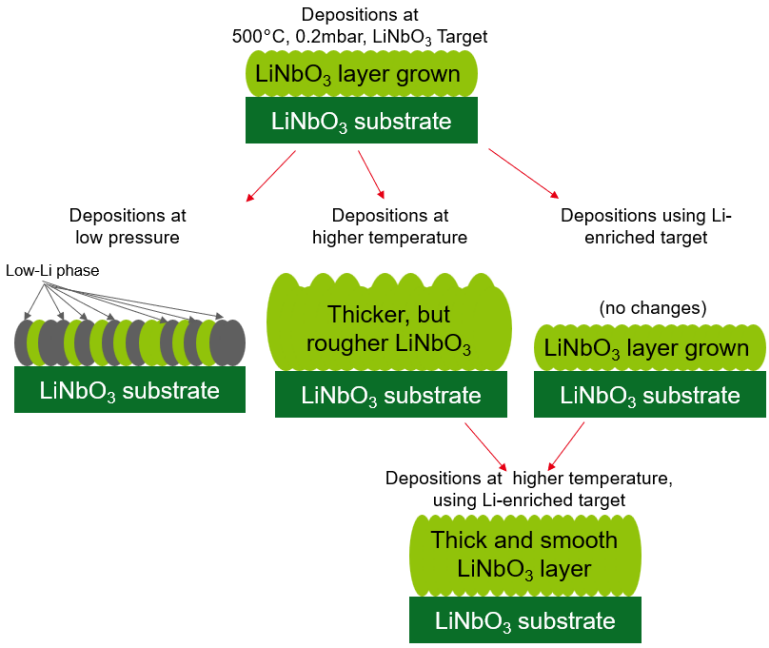

FIGURE 2.13 SCHEMATIZATION OF THE EFFECT OF THE DEPOSITION CONDITIONS FOR $LiNbO_3$ ON $LiNbO_3$ REGROWTH.

Finally, it is possible to summarize the effect of all deposition conditions into a simple scheme (Figure 2.13). This diagram is based on these conclusions:

- Oxygen pressure was the most crucial factor for the process. Wafers, after deposition at low pressure (0.007 mbar), showed reduced transparency and a mixture of $LiNbO_3$ and a parasitic low-lithium phase in the structure. This phenomenon is attributed to resputtering.
- Using temperatures in the range of 500-600°C resulted in the consistent homoepitaxial monocrystalline growth on all types of substrates with almost the same crystal quality. As the temperature increased, there was a slight rise in surface roughness due to the increased formation of nanocrystalline grains on the surface, attributed to a higher amount of material being grown on the substrate.
- Adjusting the amount of Li in the target: At 0.2 mbar pressure for both $LiNbO_3$ and $Li_{1.1}NbO_{3.05}$ targets, we consistently achieved homoepitaxial monocrystalline layers on all substrates with no difference in crystal quality. However, varying the temperature and using the Li-enriched target slightly improved surface morphology, reducing RMS roughness from ~2.5 nm to ~1.5 nm for a 120 nm thick layer.

Laura Sauze et al. employed Pulsed Laser Deposition (PLD) to deposit a 200 nm-thick $LiNbO_3$ film on 4-inch $LiNbO_3$ wafers, specifically X-cut, Y-cut, and Z-cut, at a substrate temperature of 400°C and an oxygen pressure of 0.2 mbar. Their research demonstrated the effectiveness of this method in producing $LiNbO_3$ thin films with quality and composition similar to that of monocrystalline substrates. In our investigation, we extended this research by providing further insights into the conditions for homoepitaxial regrowth through the use of different temperature, pressure, and target parameters for PLD. Moreover, we examined the growth on additional crystallographic cuts of the substrates, including the Y+128°-cut.

It's important to try using targets with more lithium compared to niobium, like Shibata et al did [24]. They got their best result with a Li/Nb ratio of 2, while ours were 1.1 and 1. Integrating such layers into an acoustic device can give the possibility to analyze resonance frequency and coupling coefficient, offering valuable information for optimization. Adding a conductive sublayer might control the diffusion of lithium atoms and facilitate the growth of specific layers. Furthermore, annealing processes could potentially enhance crystal quality and reduce surface roughness, contributing to improved overall performance.

Bibliography

[1] Z. Wu, W. Hu, J. Liu, M. Wang et Z. Liu, «Effects of substrate temperature on the growth of oriented LiNbO3 thin films by pulsed laser deposition,» *Materials Letters,* vol. 34 , n° %13–6, pp. 332-335, 1998.

[2] «Thin Films—Partow Technologies,» Partow Technologies, [En ligne]. Available: http://www.partow-tech.com/thinfilms/. [Accès le 13 June 2023].

[3] M. Gorisse et al., «High Frequency LiNbO3 Bulk Wave Resonator,» chez *IEEE International Frequency Control Symposium & European Frequency Time Forum*, 2019.

[4] Kadota et al., «FBAR using LiNbO3 thin film deposited by CVD,» chez *2010 IEEE International Ultrasonics Symposium*, 2010.

[5] K.H. Nassau et al., «Preparation of single domain crystals,» *J. Phys. Chem. Solids 27,* vol. 27, n° %16-7, pp. 989-996, 1966.

[6] A. Bartasyte, T. Baron, S. Oliveri, S. Margueron, P. Boulet, «Toward High-Quality Epitaxial LiNbO3 and LiTaO3 Thin Films for Acoustic and Optical Applications,» *Adv. Mater. Interfaces,* vol. 4, 2017.

[7] C. Wang, M. Zhang, and M. Lončar, «High- Q Lithium Niobate Microcavities and Their Applications,» *Ultra-High-Q Optical Microcavities,* p. 1–35, 2020.

[8] Zivasatienraj, B.; Tellekamp, M.B.; Doolittle, W.A., «Epitaxy of LiNbO3: Historical Challenges and Recent Success,» *Crystals* , n° %111, p. 397, 2021.

[9] M. Takahashi et al., «Epitaxial growth and characterization of stoichiometric LiNbO3 films prepared by the sol-gel method,» *Journal of Applied Physics,* vol. 96, n° %111, p. 6569–6573, 2004.

[10] K. Terabe et al., «Transmission electron microscopy study on epitaxial growth behaviors of sol-gel-derived LiNbO3 films,» *Journal of Crystal Growth,* vol. 179, pp. 577-584, 1997.

[11] H. J. Lee, T. I. Shin, J. W. Shur, and D. H. Yoon, «Growth and characterisation of Zn:LiNbO3/Mg:LiNbO3 multilayer thin films grown by liquid phase epitaxy,» *Cryst. Res. Technol.,* vol. 41, n° %19, p. 848–852, 2006.

[12] S. Schwyn; H. W. Lehmann; R. Widmer, «Waveguiding epitaxial LiNbO3 layers deposited by radio frequency sputtering,» *J. Appl. Phys.,* vol. 72, p. 1154–1159, 1992.

[13] L. C. Sauze et al., «Homo-epitaxial growth of LiNbO3 thin films by Pulsed Laser deposition,» *Journal of Crystal Growth,* vol. 601, p. 126950, 2023.

[14] H. Matsunaga, H. Ohno, Y. Okamoto, and Y. Nakajima, «Heteroepitaxial growth of LiNbO3 single crystal films by ion plating method,» *Journal of Crystal Growth,* vol. 99, n° %11–4, p. 630–633, 1990.

[15] J. C. Vyas and S. G. Singh, «The negative thermal expansion coefficient in lithium niobate single crystals,» chez *presented at the SOLID STATE PHYSICS: PROCEEDINGS OF THE 57TH DAE SOLID STATE PHYSICS SYMPOSIUM 2012*, Bombay, 2013.

[16] Sánchez-Dena et al., «Lithium Niobate Single Crystals and Powders Reviewed—Part I,» *Crystals 10,* vol. 10, 2020.

[17] Son, J.-W.; Orlov, S.S.; Phillips, B.; Hesselink, L., «Pulsed laser deposition of single phase LiNbO3 thin film waveguides,» *Journal of Electroceramics ,* vol. 17, n° %12, p. 591–595, 2006.

[18] Kilburger, S.; Millon, E.; Di Bin, P.; Boulle, A.; Guinebretière, R.; Di Bin, C., «Properties of LiNbO3 based heterostructures grown by pulsed-laser deposition for optical waveguiding application,» *Thin Solid Films,* vol. 518, n° %116, p. 4654–4657, 2010.

[19] Wang et al., «Effects of oxygen pressure on the c-axis oriented growth of LiNbO3 thin film SiO2/Si substrate by pulsed laser deposition,» *Journal of Materials Science Letters ,* vol. 3, pp. 225-227, 2003.

[20] Z. Vakulov, D. Khakhulin, A. Geldash, R. V. Tominov, V. S. Klimin, V. A. Smirnov, and O. A. Ageev, «Impact of laser pulse repetition frequency on nucleation and growth of LiNbO3 thin films,» *Journal of Advanced Dielectrics,* vol. 12, n° %12, p. 2160019, 2022.

[21] Luca Indrizzi, Natacha Ohannessian, Daniele Pergolesi, Thomas Lippert, Elisa Gilardi, «Pulsed Laser Deposition as a Tool for the Development of All Solid-State Microbatteries,» *Helvetica Chimica Acta,* vol. 104, n° %12, pp. 1-25, 2020.

[22] Alejandro Ojeda-G-P, Max Döbeli, Thomas Lippert, «Influence of Plume Properties on Thin Film Composition in Pulsed Laser Deposition,» *Advanced Materials Interfaces,* vol. 5, n° %118, pp. 1-16, 2018.

[23] S. Canulescu, E. L. Papadopoulou, D. Anglos, T. Lippert, C. W. Schneider, A. Wokaun, «Mechanisms of the laser plume expansion during the ablation of LiMn2O4,» *Journal of Applied Physics,* vol. 105, n° %16, p. 063107, 2009.

[24] Yoshihiko Shibata, Kiyoshi Kaya, Kageyasu Akashi, et al., «Epitaxial growth and surface acoustic wave properties of lithium niobate films grown by pulsed laser deposition,» *Journal of Applied Physics,* vol. 77, 1995.

[25] D Sugak et al., «Spatial distribution of LiNbO3 single crystals optical properties changes after redox high-temperature treatment,» *IOP Conference Series: Materials Science and Engineering,* vol. 169, 2017.

Chapter 3: Growth on sapphire

Table of Contents

1. Introduction

In the previous chapter, we conducted a deposition process to grow thin films of $LiNbO_3$ on $LiNbO_3$ substrates, with the objective of achieving homoepitaxial growth of these thin films. In this context, we addressed challenges related to chemical composition and structural defects, like cracks. In order to control the film crystallinity and chemical composition, growth parameters, such as substrate temperature, oxygen pressure, and target composition, were studied. The physical and chemical properties of the as-deposited $LiNbO_3$ layers were characterized and correlated to the deposition conditions.

However, to make it easier to integrate into the production of Radio Frequency filters, especially Surface Acoustic Wave (SAW) devices, it is crucial to deposit the mentioned thin film on different substrates, such as Al_2O_3 wafers. Even though different cuts of sapphire crystals have been used before as bases for the PLD growth of $LiNbO_3$, further improvements in the properties of the layer are needed for their effective use in acoustic and optical devices.

The present chapter shifts its focus towards the growth of thin $LiNbO_3$ films on Al_2O_3 with the aim of achieving heteroepitaxial layers. Several deposition parameters have been adjusted, including the substrate's heating setpoint temperature, oxygen pressure, and target composition. Our research focuses on examining the quality of crystals and the roughness of surfaces in the layers. Just like how we studied layers deposited on $LiNbO_3$ bases, we are also interested in the influence of the cutting plane of the Al_2O_3 substrate on layer growth. As a result, we will study several crystal orientations, including the *a*-plane (1 1 0), *c*-plane (0 0 1), *m*-plane (1 0 0), *n*-plane (1 1 3), *r*-plane (0 1 2), and *v*-plane (2 2 3).

The aim of this study is to explore the possibility of achieving growth orientation layers different from the (0 0 1) plane. For instance, in the context of waveguide applications, waves propagate along the (1 0 0) direction within a $LiNbO_3$ layer oriented along the (1 1 0) plane, which is known to offer greater thermal stability compared to a Z-cut structure [1].

Controlling the growth orientation along various crystal planes is important to make them suitable for various applications. For BAW and optical applications, layers oriented along the *c*-axis are predominantly utilized [2], [3]. (1 1 0) and (1 0 0) oriented layers find application in surface acoustic wave devices. Additionally, more complex orientations, can also be employed for Surface Acoustic Wave (SAW) resonators [2].

Our research primarily focuses on the orientation, crystalline quality, and surface roughness of the layers, with attention to the cut of the substrate. We'll carefully study the microscopic properties of the as-deposited thin films in relation to deposition conditions.

Reported results of growth of $LiNbO_3$ on Al_2O_3 substrates

As previously discussed in Chapters 1 and 2, the lithium niobate phase diagram doesn't have a well-defined boundary for composition. Additionally, there's a challenge because lithium (Li) atoms tend to move away from the film through diffusion. This makes it difficult to achieve balanced growth of $LiNbO_3$ ([3], [4]). These factors can lead to the formation of secondary non-ferroelectric phases, such as Li_3NbO_4 and $LiNb_3O_8$, which should be prevented [5].

Sapphire has previously served as a substrate for growing layers of lithium niobate, resulting in the successful epitaxial growth of layers in certain crystal orientations. Table 3.1 presents a compilation of empirical observations obtained from PLD techniques employed in the production of lithium niobate thin films on Al_2O_3 substrates.

Authors	Substrate orientation	Substrate size	Crystal quality, FWHM °	Surface roughness (RMS), nm	Layer orientation
Kilburger et al [6]	(0 0 1)	10 × 10 mm^2	0.52	~ 2	(0 0 1)
Shibata et al [7], [8]	(0 0 1), (1 1 0)	10 mm ⌀ disks, 12×7 mm^2	0.17		(0 0 1)
Kakehi et al [9]	(0 0 1)				(0 0 1)
G.-H. Lee et al [10], [11]	(0 0 1)		0.1	~ 0.7 [10] ~ 2 [11]	(0 0 1)
Balestrino et al [12]	(0 0 1)		0.1		(0 0 1)
Gim et al [13]	(1 1 0)		0.3		(1 1 0)
Lam et al [14]	(0 0 1) & (1 1 0)				(0 0 1) & (1 1 0)
S-H Lee et al [15]	(1 1 0)				(0 0 1) & (1 1 0)
Dai et al [16]	(1 1 0)	10 × 10 mm^2 [16]			(0 0 1) & (1 1 0)
Marsh et al [17]	(0 1 2)				(0 1 2)
L. Sauze [2]	(0 0 1)	150 mm ⌀ disks	0.85	3.63	(0 0 1)
	(1 1 0)		6.29	13.44	(0 1 2)
	(1 0 0)		0.75	1.73	(0 0 1)

TABLE 3.1 EXPERIMENTAL FINDINGS FROM PLD FOR LITHIUM NIOBATE THIN FILM GROWTH ON SAPPHIRE

As indicated in Table 3.1, the majority of the reported observations are centered on the growth of films on Z-cut sapphire substrates. This preference is based on the tendency of

$LiNbO_3$ films to align their c-axis perpendicular to the smooth substrate surface [18]. Furthermore, this selection is influenced by the significant variation of the thermal expansion coefficient α_z, directed along the out-of-plane direction (z-axis), when compared to the α_x and α_y coefficients [19].

Conversely, there is a limited amount of research results that describe the formation of layers with crystallographic orientations different from (0 0 1) and are presented for (1 1 0) and (0 1 2) orientations [13]- [17]. It's worth mentioning that there have been cases of (0 0 1)layers, even on X-cut sapphire substrates [8].

2. Presentation of the study

The main goal of this study is to thoroughly investigate how operational factors influence the quality of the crystalline structure and surface roughness in $LiNbO_3$ layers deposited on Al_2O_3. Additionally, the study aims to clarify the conditions for achieving epitaxial growth of layers with different crystallographic orientations on sapphire. To achieve this goal, the Solmates 8 in.-wafer-based SIP800 platform, was used with the Pulsed Laser Deposition technique for the heteroepitaxial growth of $LiNbO_3$ films. The platform and laser ablation characteristics stayed the same with those detailed in Chapter 2 and Annex I.

In our efforts to achieve heteroepitaxy, it is important to determine the lattice parameters and calculate the lattice mismatch between sapphire and lithium niobate. The lattice mismatch is represented in absolute value and is calculated according to the equation:

$$\frac{(Lattice_{Layer} - Lattice_{Substrate})}{Lattice_{Substrate}} \times 100\%$$

The difference in Coefficients of Thermal Expansion (CTEs) is also significant.

Lattice parameter	$LiNbO_3$	Al_2O_3	Lattice mismatch, %	CTE at 300K, $LiNbO_3$, $\times 10^{-6}$ K^{-1}	CTE at 300K, Al_2O_3, $\times 10^{-6}$ K^{-1}
a (Å)	5.17 [20]	4.76 [20]	8.19	3.5 [19]	5.1 [21]
c (Å)	13.8 [20]	12.9 [20]	6.77	20.5 [19]	5.7 [21]

TABLE 3.2 LATTICE PARAMETERS AND MISMATCH BETWEEN SAPPHIRE AND LITHIUM NIOBATE.

A study is conducted to investigate the impact of deposition parameters on the growth of the layers. Three key deposition parameters are being modified: the setpoint temperature for substrate heating, oxygen pressure, and substrate orientation. Consequently, six different cutting planes of Al_2O_3 substrates will be examined, with some orientations matching those in the study on $LiNbO_3$ substrates, while others differ: *c*-cut (0 0 1), *a*-cut (1 1 0), *r*-cut (0 1 2), *m*-cut (1 00), *n*-cut (1 1 3), and *v*-cuts (2 2 3).

2.1 Study of the influence of the substrate temperature

Wu et al. conducted a study on the influence of substrate temperature on the growth of $LiNbO_3$ thin films via PLD [22]. Their research findings demonstrated that the deposition temperature had a significant effect on the crystallinity, stoichiometry, and surface morphology of the films. More specifically, lower temperatures were observed to reduce crystallinity and

cause the appearance of secondary phases, while higher temperatures resulted in overheating and cracks [22].

Several researchers carried out investigations into the growth of $LiNbO_3$ using PLD at different temperatures, from 450 to 800°C [6]- [17]. It's noteworthy that the crystallization temperature for $LiNbO_3$ falls within the range of 530 to 580 °C [5].

In accordance with these facts, the substrate deposition temperatures were systematically varied within the range of 500°C to 600°C, as clarified in Table 3.2. The goal of this temperature exploration was to identify the ideal deposition temperature for our PLD apparatus, in order to meet the specific requirements of the films. Precise temperature control during the deposition process was achieved by regulating the temperature of the ceramic holder beneath the wafer.

For certain trial runs, the deposition process stated at 600°C to establish a seed layer, after which the substrate heating was gradually reduced to lower temperatures, finishing with a final substrate temperature of 200°C for the last stages of deposition.

2.2 Study of the influence of the oxygen pressure

Oxygen pressure represents a crucial parameter in the growth of $LiNbO_3$ thin films by PLD. It has a significant impact on the stoichiometry, crystallization, and surface morphology of the films. Generally, enhancing the oxygen pressure results in a higher deposition rate and the production of films with better stoichiometry. This impact is linked to the stabilizing function of oxygen pressure. However, high pressure can also lead to the formation of secondary phases. [23].

The optimal oxygen pressure for PLD-produced $LiNbO_3$ thin films is contingent upon the specific laser system and target employed:

- Lower oxygen pressures can lead to films with lower crystallinity and rougher surface morphologies [23]. Reducing pressure means that atoms have a longer mean free path. This means that heavier Nb atoms are less influenced by collisions compared to lighter Li atoms. Consequently, when these Nb atoms reach the layer, they carry kinetic energy, which may displace Li atoms (resputtering) and result in the formation of a low-Li phase. On the other hand, high kinetic energy of atoms can contribute to the production

of higher-quality films, where this energy acts as a source for layer formation, similar to thermal energy.

- Higher oxygen pressures tend to yield more stoichiometric films but sometimes are associated with an increased propensity of secondary phase formation [23]. Under such conditions, a lot of collisions will impact both Nb and Li atoms, and resputtering will not happen. Thermal energy will be the primary source of energy in this scenario.

The introduction of an oxygen (O_2) background gas establishes an exceptionally reactive environment localized at the substrate's surface, thereby promoting the growth of films with heightened reactivity, [24]. Additionally, it's worth noting that lithium (Li) ions located in the front part of the ablation plume undergo additional excitations due to collision events, consequently influencing the overall film growth process [25].

Numerous researchers have conducted extensive investigations into the growth of $LiNbO_3$ using PLD at varying oxygen pressures, with reported ranges from 0.001 mbar as reported in [7]- [8], to 1.3 mbar [26]. These findings are consistent with the observations made by Vakulov et al [27]. Their results, derived from an X-ray photoelectron spectroscopy (XPS) study, revealed that the optimal conditions for producing $LiNbO_3$ films were attained at oxygen pressures of 0.01 mbar and 1.3×10^{-5} mbar [27].

In line with these reported results, purposeful adjustments were made to the substrate deposition pressures, ranging from 0.2 to 0.007 mbar, as detailed in Table 3.3. The selection of these specific values was influenced by the homoepitaxial growth experiments previously conducted by Sauze et al., during which they operated the chamber at an oxygen pressure of 0.2 mbar [28].

2.3 Study of the influence of the substrate orientation

The number of results reporting the growth of layers with crystallographic orientations different from (0 0 1) is relatively limited, and they are presented for (1 1 0) and (0 1 2) orientations [13]- [17]. It is worth noting that there have been instances of (0 0 1) layer growth even on X-cut sapphire substrates [8].

Consequently, we intend to investigate six different cutting planes of Al_2O_3, with some orientations aligning with those studied for $LiNbO_3$ substrates, while others are different: *c*-cut (0 0 1), *a*-cut (1 1 0), *r*-cut (0 1 2), *m*-cut (1 00), *n*-cut (1 1 3), and *v*-cuts (2 2 3).

For this purpose, we will use 4-inch (*c*-, *a*- and *r*-Al_2O_3) and 2-inch (*m*-, *n*- and *v*-Al_2O_3) wafers to grow various crystallographic orientations of LiNbO3 and examine the properties of the as-deposited thin films as they relate to deposition parameters. Table 3.3 groups together the various deposition parameter modifications by sample.

ID	Size (inch)	Substrate Orientation	Pressure (mbar)	Temperature (°C)	Target
C-1	4	(0 0 1)	0.2	500	$LiNbO_3$
C-2	4	(0 0 1)	0.007	500	$LiNbO_3$
C-3	4	(0 0 1)	0.2	600	$LiNbO_3$
C-4	4	(0 0 1)	0.2	600	$Li_{1.1}NbO_{3.05}$
C-5	4	(0 0 1)	0.007	500	$Li_{1.1}NbO_{3.05}$
C-6	4	(0 0 1)	0.2	500	$Li_{1.1}NbO_{3.05}$
C-7	4	(0 0 1)	0.007	600	$Li_{1.1}NbO_{3.05}$
C-8	4	(0 0 1)	0.007	600-200	$Li_{1.1}NbO_{3.05}$
A-1	4	(1 1 0)	0.2	500	$LiNbO_3$
A-2	4	(1 1 0)	0.007	500	$LiNbO_3$
A-3	4	(1 1 0)	0.2	600	$LiNbO_3$
A-4	4	(1 1 0)	0.2	600	$Li_{1.1}NbO_{3.05}$
A-5	4	(1 1 0)	0.007	500	$Li_{1.1}NbO_{3.05}$
A-6	4	(1 1 0)	0.2	500	$Li_{1.1}NbO_{3.05}$
A-7	4	(1 1 0)	0.007	600	$Li_{1.1}NbO_{3.05}$
A-8	4	(1 1 0)	0.007	600-200	$Li_{1.1}NbO_{3.05}$
R-1	4	(0 1 2)	0.2	500	$LiNbO_3$
R-2	4	(0 1 2)	0.007	500	$LiNbO_3$
R-3	4	(0 1 2)	0.2	600	$LiNbO_3$
R-4	4	(0 1 2)	0.2	600	$Li_{1.1}NbO_{3.05}$
R-5	4	(0 1 2)	0.007	500	$Li_{1.1}NbO_{3.05}$
R-6	4	(0 1 2)	0.2	500	$Li_{1.1}NbO_{3.05}$
R-7	4	(0 1 2)	0.007	600	$Li_{1.1}NbO_{3.05}$
R-8	4	(0 1 2)	0.007	600-200	$Li_{1.1}NbO_{3.05}$
M-1	2	(1 0 0)	0.007	600	$Li_{1.1}NbO_{3.05}$
N-1	2	(1 1 3)	0.007	600	$Li_{1.1}NbO_{3.05}$
V-1	2	(2 2 3)	0.007	600	$Li_{1.1}NbO_{3.05}$

TABLE 3.3 PRESENTATION OF SAMPLES WITH VARIATIONS IN ASSOCIATED DEPOSITION CONDITIONS.

3. Characterization and analysis

The structural properties of the as-grown $LiNbO_3$ layers have been assessed through X-Ray Diffraction (XRD). The XRD analysis encompassed the following aspects:

- Identification of Phases: A 2θ/ω scan was performed to identify the phases present in the sample.
- Crystallite Disorientation and Layer Quality: The disorientation of crystallites within the layer and the overall layer quality concerning a preferential growth plane were examined through a Rocking Curve analysis (ω scan).
- Epitaxial Relationship: To assess the epitaxial relationship between the layer and the substrate, Azimuth Scans (φ scans) were performed.

The surface morphology of the grown $LiNbO_3$ films was thoroughly examined using Atomic Force Microscopy (AFM). Each sample underwent examination with two scan sizes: 1 x 1 μm² and 5 x 5 μm². This dual-scale approach allowed for a comprehensive assessment of the roughness displayed by the deposited layers. To accurately measure the surface roughness characteristics of the $LiNbO_3$ films, a Root Mean Square (RMS) roughness analysis was carried out, encompassing the entirety of the AFM image.

3.1 Growth on the C-plane

ID	Size (inch)	Substrate Orientation	Pressure (mbar)	Temperature (°C)	Target
C-1	4	(0 0 1)	0.2	500	$LiNbO_3$
C-2	4	(0 0 1)	0.007	500	$LiNbO_3$
C-3	4	(0 0 1)	0.2	600	$LiNbO_3$
C-4	4	(0 0 1)	0.2	600	$Li_{1.1}NbO_{3.05}$
C-5	4	(0 0 1)	0.007	500	$Li_{1.1}NbO_{3.05}$
C-6	4	(0 0 1)	0.2	500	$Li_{1.1}NbO_{3.05}$
C-7	4	(0 0 1)	0.007	600	$Li_{1.1}NbO_{3.05}$
C-8	4	(0 0 1)	0.007	600-200	$Li_{1.1}NbO_{3.05}$

TABLE 3.4. PRESENTATION OF SAMPLES WITH VARIATIONS IN ASSOCIATED DEPOSITION CONDITIONS.

In order to explore the impact of deposition parameters on the growth of lithium niobate layers on sapphire, starting with (0 0 1) layers growth is recommended. This choice is motivated by the preference for the c-axis as the growth orientation for $LiNbO_3$ films. The table 3.4 categorizes the different alterations in deposition parameters by sample for growth on *c*-plane sapphire.

Structural properties

The structural properties of the as-grown $LiNbO_3$ layers have been evaluated XRD analysis. θ-2θ measurements were conducted for all the wafers, both with a 0.5° ω-offset (aimed at minimizing the contribution of sapphire) and without it. The figure below illustrates the difference between the scans obtained.

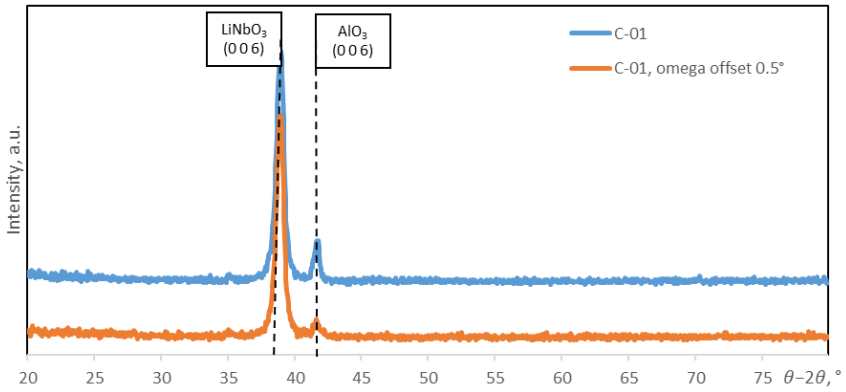

FIGURE 3.1 XRD Θ/2Θ PATTERNS, WITHOUT (UP) AND WITH 0.5° Ω-OFFSET (DOWN) OF THE $LiNbO_3$/ (0 0 6) SAPPHIRE DEPOSITED AT 0.2 MBAR, 500°C, $LiNbO_3$ TARGET

In the diagram below, θ-2θ measurements with a 0.5° ω-offset are presented for all the Z-cut sapphire wafers after the deposition. The orientations of $LiNbO_3$, $LiNb_3O_8$, and Al_2O_3 have been determined with reference to ICDD sheets: 00-020-0631 [29] for LiNbO3 04-013-9445 [30] for LiNb3O8, and 00-046-1212 [31] for Al2O3, as detailed in Appendix II.

The XRD patterns shown below reveal that by fine-tuning the deposition parameters during growth on Z-cut sapphire, only (0 0 6) $LiNbO_3$ crystals were obtained. One of the deposition processes commenced at 600°C to establish a seed layer, following which the substrate heating was gradually reduced to lower temperatures, led to a final substrate temperature of 200°C for the final stages of deposition, resulting in the growth of the low-Li subphase (6 0 0) $LiNb_3O_8$. The presence of this secondary "parasitic" phase alongside $LiNbO_3$

leads to bad physical properties compared to pure $LiNbO_3$ and can have negative impacts on the desired characteristics of the crystal, as discussed in reference [5].

It is noteworthy to mention that $LiNbO_3$ peaks display a slight leftward shift in symmetric scan due to the presence of stress and strain in the film. From the position of the diffraction peak, Bragg's law is used to deduce the interplanar distances (d_{hkl}) of the layer. This information allows for the calculation of the deformation in the crystal structure, which is a measure of the change in the lattice parameter.

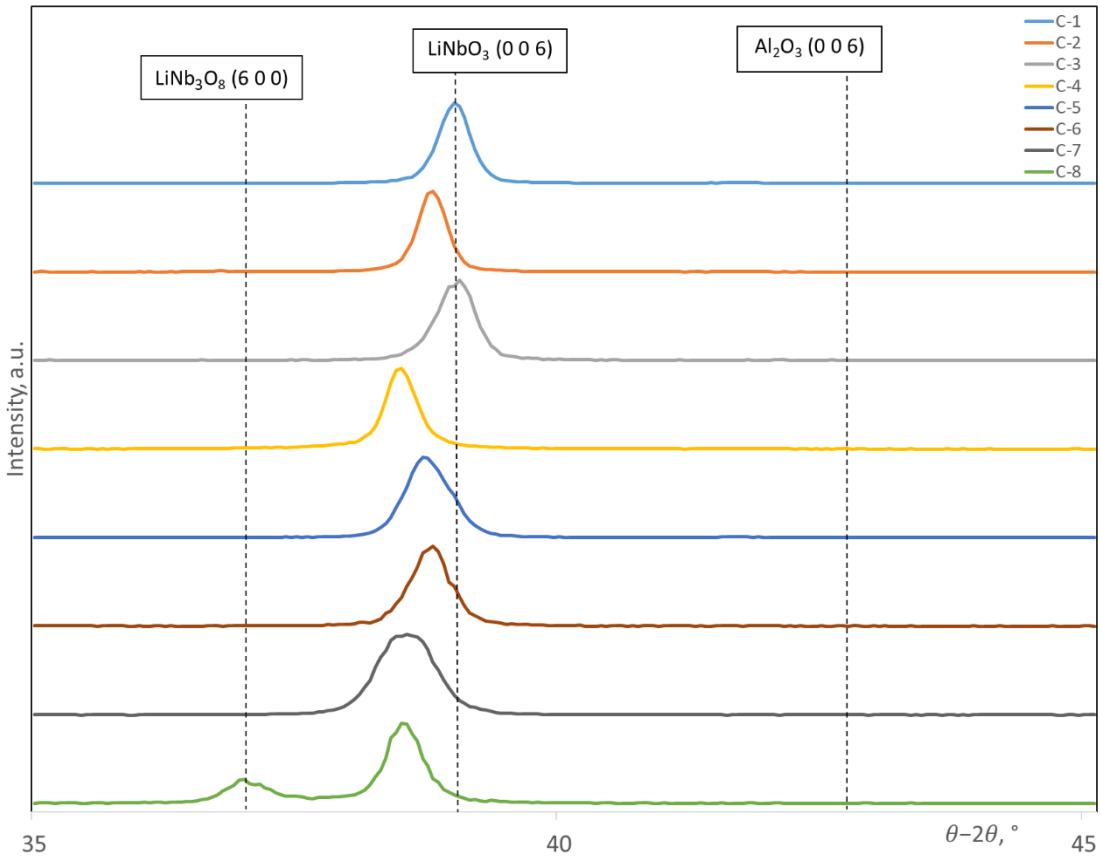

FIGURE 3.2 XRD Θ/2Θ MEASUREMENTS, 0.5° Ω-OFFSET OF THE $LiNbO_3$/ (0 0 6) SAPPHIRE.

Symmetrical ω (Rocking Curve) measurements were conducted to identify the broadening of the diffraction peaks. The broadening of the peaks can be attributed to mosaicity, which signifies the misorientation of crystallites. These measurements enable a quantitative description of XRD peak width through the Full-Width-at-Half-Maximum (FWHM).

An example of a comparison of such measurements is illustrated in the figure below. This diagram presents a comparison of omega scans performed on wafers grown using a $Li_{1.1}NbO_{3.05}$ target, one at 500°C with 0.2 mbar O_2 atmothphere (C-6) and the other at 600°C

with 0.007 mbar (C-7). The mosaicity of the layer, denoting the misorientation of crystallites, is noticeably higher for the C-6 wafer, with a FWHM of 0.99° as opposed to 0.76° for the C-7 wafer. This difference could potentially be attributed to the displacement of certain Li atoms by Nb atoms. These atoms, possessing a big amount of kinetic energy due to their longer mean free path (resulting from a lower number of collisions), may contribute to this observed effect. Other measurements can be found in Appendix II.

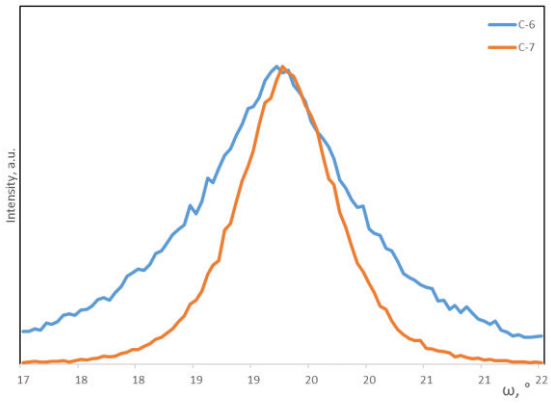

FIGURE 3.3 XRD Ω SYMMETRICAL PATTERNS, $LiNbO_3$/ (0 0 6) SAPPHIRE DEPOSITED USING $Li_{1.1}NbO_{3.05}$ TARGET AT 500°C, 0.2 MBAR (C-6) AND 600°C, 0.007 MBAR (C-7).

All φ measurements conducted for the layers grown on Z-cut sapphire consistently reveal the epitaxial nature of the $LiNbO_3$ growth. These measurements involve the rotation in φ for out-of-plane (0 1 2) $LiNbO_3$ and Al_2O_3 peaks. It's worth emphasizing that all of these measurements consistently reveal a 6-fold structure, indicating the presence of an epitaxial polyscystalline structure with what are known as twins or 2-domains growth. An example of such scans performed on a sapphire heterostructure deposited using a $Li_{1.1}NbO_{3.05}$ target at 600°C and 0.007 mbar (C-7) is depicted in the figure below.

Asymmetrical ω (Rocking Curve) measurements were carried out to assess the broadening of the diffraction peaks observed in φ measurements for (0 1 2) $LiNbO_3$ and Al_2O_3 peaks. The table below provides a summary of all the properties of the as-grown $LiNbO_3$ layers that have been analyzed through XRD (Table 3.5).

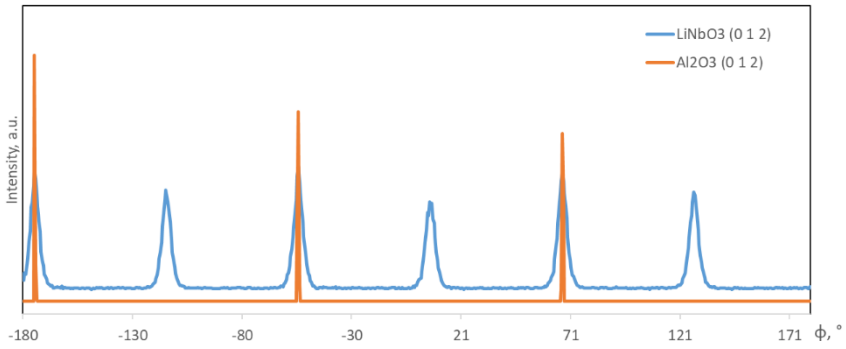

FIGURE 3.4 XRD Φ MEASUREMENTS PATTERNS, $LiNbO_3$/ (0 0 6) SAPPHIRE HETEROSTRUCTURE DEPOSITED USING $Li_{1.1}NbO_{3.05}$ TARGET AT 600°C, 0.007 MBAR (C-7) FOR OUT-OF-PLANE (0 1 2) PEAKS OF $LiNbO_3$ AND Al_2O_3.

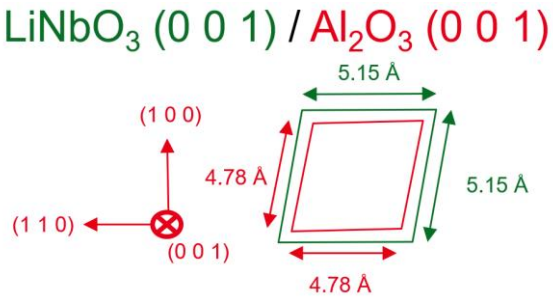

FIGURE 3.5 POSSIBLE EPITAXIAL RELATIONSHIPS LITHIUM NIOBATE THIN FILM ON Z-CUT SAPPHIRE SUBSTRATE.

The symmetry, as observed in φ measurements, consistently exhibits a 6-fold pattern, indicating the presence of an epitaxial polycrystalline structure with twins. Based on the φ measurements the possible crystallographic relationships between the (0 0 1) plane of $LiNbO_3$ are schematized for Al_2O3 Z-cut substrates (Fig.3.5). The lattice mismatch of this possible structure is ~7.7 %.

In the summary Table 3.5, data related to XRD results for layers grown on Z-cut wafers under various deposition conditions is presented. The RC (Rocking Curve) values for symmetrical measurements for most of the layers are all below 1°, with variations ranging from 0.76° to 0.99, depending on the specific sample. The deposition conducted using a $Li_{1.1}NbO_{3.05}$ target at 600°C with 0.007 mbar (C-7) exhibits the lowest FWHM (Full-Width-at-Half-Maximum) for asymmetrical ω measurements. The combination of the lowest FWHM for both symmetrical and asymmetrical scans is achieved through deposition at 500°C with 0.007 mbar using a $LiNbO_3$ target (C-2). Only growth performed at 500°C with 0.2 mbar have symmetrical RC higher than 1° (1.5°) and relatively high asymmetrical one (3.5°).

ID	Pressure (mbar)	Temperature (°C)	Target	RC (symmetrical), °	RC (asymmetrical), °
C-1	0.2	500	$LiNbO_3$	0.913	2.1
C-2	0.007	500	$LiNbO_3$	0.78	1.5
C-3	0.2	600	$LiNbO_3$	0.924	2.1
C-4	0.2	600	$Li_{1.1}NbO_{3.05}$	0.874	2.2
C-5	0.007	500	$Li_{1.1}NbO_{3.05}$	0.913	2.4
C-6	0.2	500	$Li_{1.1}NbO_{3.05}$	1.5	3.5
C-7	0.007	600	$Li_{1.1}NbO_{3.05}$	0.99	1.41
C-8	0.007	600-200	$Li_{1.1}NbO_{3.05}$	0.84	2.12

TABLE 3.5 PRESENTATION OF THE SUMMARY THE XRD RESULTS FOR LAYERS GROWN ON Z-CUT WAFERS WITH VARIATIONS IN ASSOCIATED DEPOSITION CONDITIONS.

It's crucial to highlight that for the majority of deposition conditions, only (0 0 6) $LiNbO_3$ crystals were obtained. The deposition process commenced at 600°C to establish a seed layer, following which the substrate heating was gradually reduced to lower temperatures. This resulted in a final substrate temperature of 200°C for the subsequent stages of deposition, leading to the growth of a combination of the low-Li subphase (6 0 0) $LiNb_3O_8$ and (0 0 6) $LiNbO_3$ crystals.

Surface properties

SEM (Scanning Electron Microscopy) observations were performed to evaluate the surfaces of the layers. This analysis aimed to identify the presence of cracks and particles on the layers. The observations, conducted at various magnifications, are presented in the figure below. Importantly, the SEM examinations did not reveal any cracks, but they did detect the presence of grains on the layers.

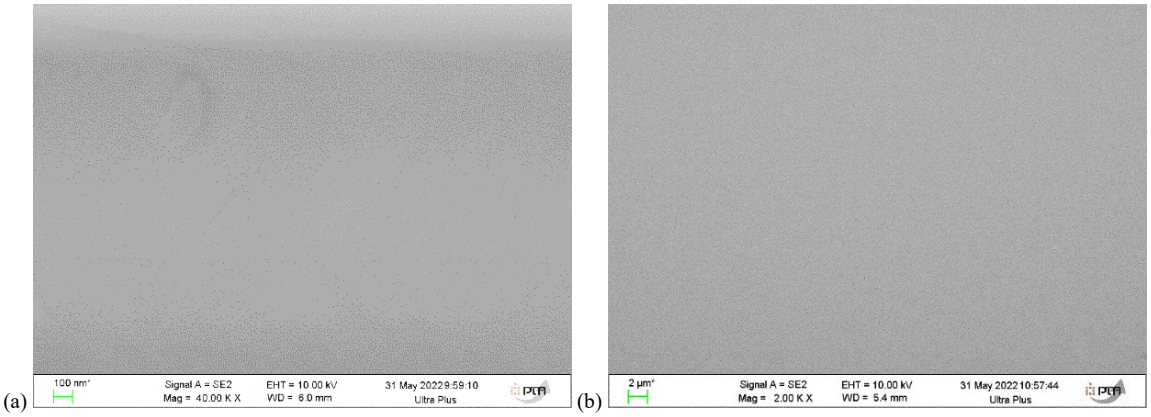

FIGURE 3.6 SEM MICROGRAPHS OF $LiNbO_3$ C-Al_2O_3 HETEROSTRUCTURES GROWN AT: (A) 0.2 MBAR, 500°C, $LiNbO_3$ TARGET; (B) 0.2 MBAR, 600°C, $LiNbO_3$ TARGET.

To explore the surface morphology of the $LiNbO_3$ films deposited on Z-cut Al_2O_3, AFM measurements were conducted for most of the samples. Each sample underwent examination using two scan sizes: 1 x 1 µm² and 5 x 5 µm². This dual-scale approach allowed for a comprehensive assessment of the roughness displayed by the deposited layers. To precisely evaluate the surface roughness characteristics of the $LiNbO_3$ films, an analysis of the Root Mean Square (RMS) roughness was carried out based on the entire AFM image.

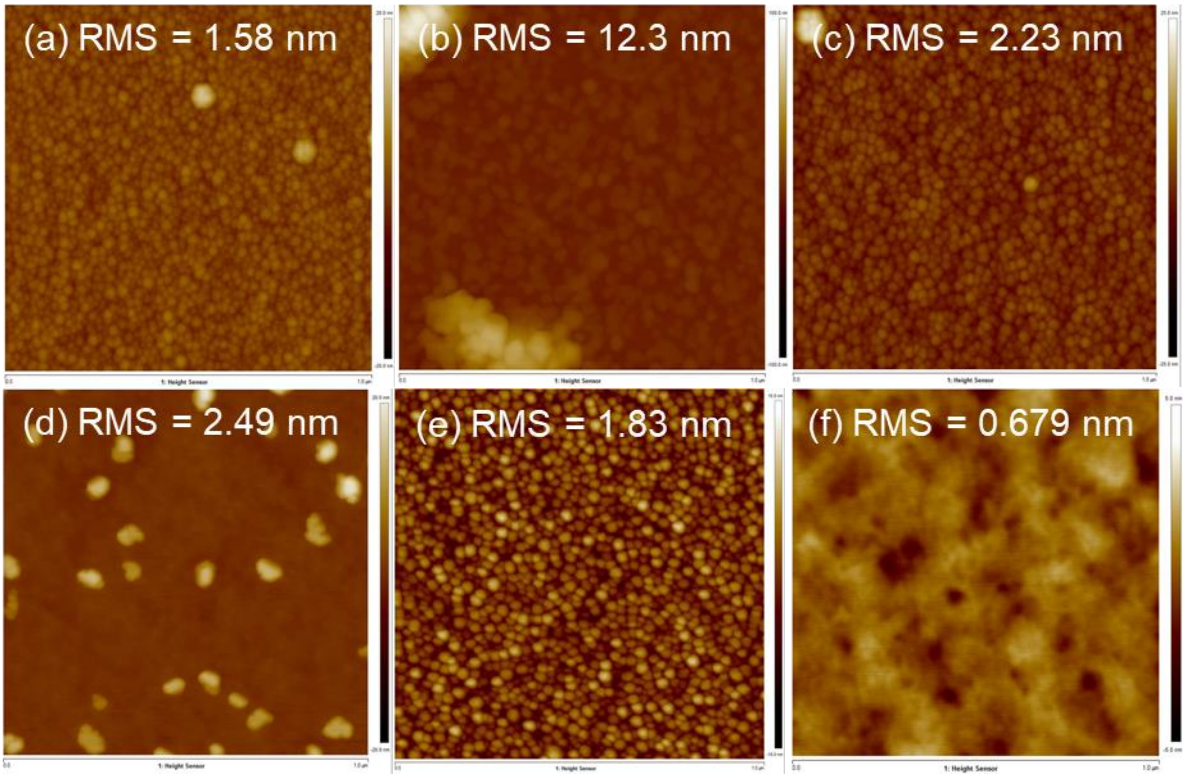

FIGURE 3.7 AFM MICROGRAPHS OF $LiNbO_3$ ON Z-CUT Al_2O_3 GROWN AT: (A) 0.2 MBAR, 500°C, $LiNbO_3$ TARGET; (B) 0.007 MBAR, 500°C, $LiNbO_3$ TARGET; (C) 0.2 MBAR, 600°C, $LiNbO_3$ TARGET; (D) 0.2 MBAR, 600°C, $Li_{1.1}NbO_{3.05}$ TARGET; (E) 0.007 MBAR, 500°C, $Li_{1.1}NbO_{3.05}$ TARGET; (F) (E) 0.007 MBAR, 600°C, $Li_{1.1}NbO_{3.05}$ TARGET;. SCAN SIZE: (1 × 1) μM^2.

The AFM images of the 1 x 1 µm² scans for samples deposited on Z-cut wafers are collectively shown in the figure above. All of the 5 x 5 µm² scans can be found in the Annex IV. In all cases, these scans reveal that the surfaces of the films are composed of rounded grains. Furthermore, due to the PLD process, some grains on the suface are also visible. It's crucial to highlight that these grains are the main source of surface roughness in these samples. Another potential origin of these grains could be resputtering, which refers to the re-emission of the deposited Li during the deposition process as a result of bombardment with Nb atoms (due to their high kinetic energy). This phenomenon has been observed in instances of deposition at

low pressure without additional Li in the target, consequently leading to the possibility of the formation of a low-Li phase.

The provided table summarizes the findings related to surface properties observed in the AFM scans. It provides an overview of how the surface properties are influenced by the diverse deposition conditions (including oxygen pressure, substrate temperature and amount of Li in target) for depositions done on Z-cut sapphire wafers.

The surfaces of all the films exhibit the presence of rounded grains, and some grains are also visible due to the pulsed laser deposition process. It's important to note that these grains are the primary source of surface roughness in these films. The RMS roughness reaches its highest values for the samples grown at 0.007 mbar and 500°C using a $LiNbO_3$ target, where some grains are visible. On the other hand, the surface roughness of the wafer grown at 0.007 mbar and 600°C using a Li-enriched target was the lowest, and it was even less than 1nm. However, since the thickness of all the films is around 200nm, the roughness of most samples is relatively small. This indicates that while surface roughness varies between samples, the overall roughness is limited due to the thin film thickness.

ID	Pressure (mbar)	Temperature (°C)	Target	RMS 1x1 µm², nm	RMS 5x5 µm², nm
C-1	0.2	500	$LiNbO_3$	1.58	1.7
C-2	0.007	500	$LiNbO_3$	12.3	9.76
C-3	0.2	600	$LiNbO_3$	2.23	1.8
C-4	0.2	600	$Li_{1.1}NbO_{3.05}$	2.49	2.74
C-5	0.007	500	$Li_{1.1}NbO_{3.05}$	1.83	1.85
C-7	0.007	600	$Li_{1.1}NbO_{3.05}$	0.68	0.82
C-8	0.007	600-200	$Li_{1.1}NbO_{3.05}$	1.5	1.6

TABLE 3.6 PRESENTATION OF THE SUMMARY ON THE SURFACE CHARACTERIZATION FOR LAYERS GROWN ON Z-CUT WAFERS WITH VARIATIONS IN ASSOCIATED DEPOSITION CONDITIONS.

Summary on the growth on the Z-cut sapphire

In the context of growth on $LiNbO_3$ on sapphire substrates, it's important to note that the morphology and roughness of the layer are influenced by several factors, including the substrate's heating setpoint temperature, oxygen pressure, and target composition. Our investigation encompassed the study of the crystalline quality and surface roughness of these layers, taking into consideration these critical factors. All the results from the characterization have been summarized in the table below.

For all the deposition conditions, it was observed that $LiNbO_3$ films grown on *c*-sapphire exhibited a strong (0 0 1) texture. In one of the deposition processes, the initial phase was carried out at 600°C to establish a seed layer. Subsequently, the substrate heating was gradually reduced to lower temperatures, ultimately reaching a final substrate temperature of 200°C for the subsequent stages of deposition. This process resulted in the growth of the low-Li subphase (6 0 0) $LiNb_3O_8$. In all other deposition processes, single-phased polycrystalline (0 0 6) $LiNbO_3$ layers were obtained.

The deposition process carried out using a $Li_{1.1}NbO_{3.05}$ target at 600°C with 0.007 mbar (C-7) demonstrates the lowest Full-Width-at-Half-Maximum (FWHM) for asymmetrical ω measurements (RC). The combination of the lowest FWHM values for both symmetrical and asymmetrical scans is achieved through deposition at 500°C with 0.007 mbar using a $LiNbO_3$ target (C-2). All φ measurements conducted for the layers grown on Z-cut sapphire consistently reveal the epitaxial nature of the $LiNbO_3$ growth. It's worth emphasizing that all these measurements consistently reveal a 6-fold structure, indicating the presence of an epitaxial polycrystalline structure.

ID	RC (symmetrical), °	RC (asymmetrical), °	RMS 1x1 µm², nm	RMS 5x5 µm², nm
C-1	0.913	2.1	1.58	1.7
C-2	0.78	1.5	12.3	9.76
C-3	0.924	2.1	2.23	1.8
C-4	0.874	2.2	2.49	2.74
C-5	0.913	2.4	1.83	1.85
C-6	1.5	3.5		
C-7	0.99	1.41	0.68	0.82
C-8	0.84	2.12	1.5	1.6

TABLE 3.7 PRESENTATION OF THE SUMMARY THE XRD RESULTS FOR LAYERS GROWN ON Z-CUT WAFERS WITH VARIATIONS IN ASSOCIATED DEPOSITION CONDITIONS.

Both AFM and SEM examinations did not reveal any cracks in the layers. However, they detected the presence of grains on the layers. The surfaces of all the films are characterized by the presence of rounded grains. Additionally, due to the pulsed laser deposition process, some grains are visible. It's noteworthy that these grains constitute the primary source of surface roughness in the samples. The surface roughness of the wafer grown at 0.007 mbar and 600°C

using a Li-enriched target was the lowest, measuring less than 1nm. However, considering that the thickness of all the films is around 200nm, the roughness of most samples is relatively small.

Most of the previously reported results were focused on growing films with the (0 0 1) orientation. This choice is supported by the tendency of $LiNbO_3$ films to align their c-axis perpendicular to the smooth substrate surface [18]. However, it's important to note that we couldn't achieve the same high crystal quality as reported by Lee (with a rocking curve of 0.1°) [11] and by Balestrino (RC of 0.1°) [12]. It could be possible to achieve such crystallinity after further improvement of deposition parameters. Our result (0.78°) was more similar to the one reported by Laura Sauze (0.75°) [2] . On the other hand, the lowest roughness we obtained for this crystal cut was 0.68 nm, which is close to the value reported by G.-H. Lee (0.7nm) [9].

In conclusion, it can be affirmed that 200nm thick $LiNbO_3$ thin films grown on Z-cut Al_2O_3 substrates at 600°C and 0.007mbar exhibit the most favorable combination of both relatively low roughness (with an RMS of 0.8 nm for the 5x5 μm² scan) and good crystalline quality (as indicated by symmetrical and asymmetrical Rocking Curve values of 0.99° and 1.41°, respectively).

3.2. Growth on the A-plane

ID	Substrate Orientation	Pressure (mbar)	Temperature (°C)	Target
A-1	(1 1 0)	0.2	500	$LiNbO_3$
A-2	(1 1 0)	0.007	500	$LiNbO_3$
A-3	(1 1 0)	0.2	600	$LiNbO_3$
A-4	(1 1 0)	0.2	600	$Li_{1.1}NbO_{3.05}$
A-5	(1 1 0)	0.007	500	$Li_{1.1}NbO_{3.05}$
A-6	(1 1 0)	0.2	500	$Li_{1.1}NbO_{3.05}$
A-7	(1 1 0)	0.007	600	$Li_{1.1}NbO_{3.05}$
A-8	(1 1 0)	0.007	600-200	$Li_{1.1}NbO_{3.05}$

TABLE 3.8 PRESENTATION OF SAMPLES WITH VARIATIONS IN ASSOCIATED DEPOSITION CONDITIONS.

To investigate the influence of deposition parameters on the growth of lithium niobate thin films on sapphire substrates with orientations other than (0 0 1), it is advisable to begin with the growth of (1 1 0) layers. This choice is motivated by previous works that have demonstrated the feasibility of growing layers with such an orientation [13]- [14].

The table above organizes the various modifications in deposition parameters by sample for growth on A-plane sapphire.

Structural properties

The structural properties of the as-grown $LiNbO_3$ layers were assessed using XRD analysis (same as for Z-cut wafers). θ-2θ measurements were conducted for all the wafers, both with and without a 0.5° ω-offset (aimed at reducing the contribution of sapphire). In the diagram below, θ-2θ measurements with a 0.5° ω-offset are presented for all the *a*-sapphire wafers after the deposition. The orientations of $LiNbO_3$, $LiNb_3O_8$, and Al_2O_3 were determined with reference to ICDD sheets: 00-020-0631 [29] for $LiNbO_3$, 04-013-9445 [30] for $LiNb_3O_8$, and 00-046-1212 [31] for Al_2O_3, as detailed in Appendix II.

In order to estimate the proportion of grains oriented according to the different crystallographic planes and to determine the preferred orientation of the layer, we employed the following equation [32]:

$$TD_{(hkl)} = \frac{\frac{I_{(hkl)}}{I_{0(hkl)}}}{\frac{\sum \quad I_{(hkl)}}{I_{0(hkl)}}} \times 100$$

Where $I_{(hkl)}$ was the experimental integrated intensity of the plans (hkl) and $I_{0(hkl)}$ was the theoretical intensity [32].

The XRD patterns displayed below indicate that through precise adjustments in the deposition parameters during growth on X-cut sapphire, (1 1 0), (0 0 6) and combination of (1 1 0) and (0 0 6) LiNbO3 orientations were achieved.

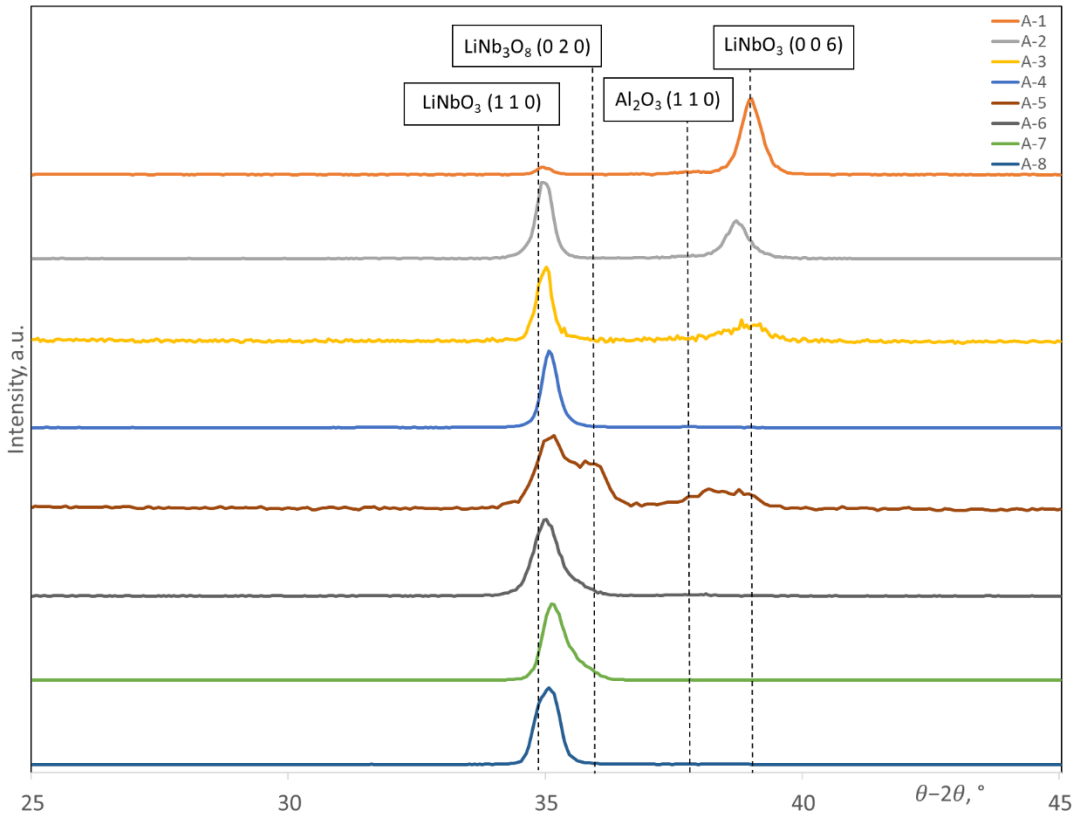

FIGURE 3.8 XRD Θ/2Θ SYMMETRICAL PATTERNS, 0.5° Ω-OFFSET OF THE $LiNbO_3$/ (1 1 0) SAPPHIRE.

In contrast to the previous observations made for $LiNbO_3$ films deposited on *c*-Al_2O_3, there is a consistent competition in growth between the (0 0 6) and (1 1 0) orientations. In one deposition process, the growth began at 600°C to establish a seed layer, and subsequently, the substrate heating was gradually reduced to lower temperatures, ultimately reaching a final substrate temperature of 200°C for the later stages of deposition. This resulted in the growth of a low-Li subphase (0 2 0) $LiNb_3O_8$. The presence of this secondary "parasitic" phase alongside $LiNbO_3$ leads to inferior physical properties compared to pure $LiNbO_3$ and can have adverse effects on the desired characteristics of the crystal, as discussed in reference [5]. The growth of this subphase may have occurred due to low thermal energy in the film during the final stages of the deposition process, given that the final substrate temperature was 200°C.

The XRD patterns reveal that the $LiNbO_3$ films deposited on a-sapphire under a 0.2 mbar O_2 atmosphere, with additional Li_2O in the target, are polycrystalline and exhibit strong (1 1 0) texturation. Notably, a combination of both (0 0 6) and (1 1 0) orientations was grown on x-cut sapphire, also with additional Li in the target, at 500°C with a 0.007 mbar O_2

atmosphere. This suggests that nucleation during the point of solid-phase crystallization does not result in an ideal selection of the (1 1 0) orientation. Although (1 1 0) is the major domain in the initial growth stage, crystallization exhibits selectivity toward the c-axis orientation.

Symmetrical and asymmetrical ω (Rocking Curve) measurements were performed to assess the broadening of the diffraction peaks for the primary layer orientations, similar to the approach used for Z-cut sapphire.

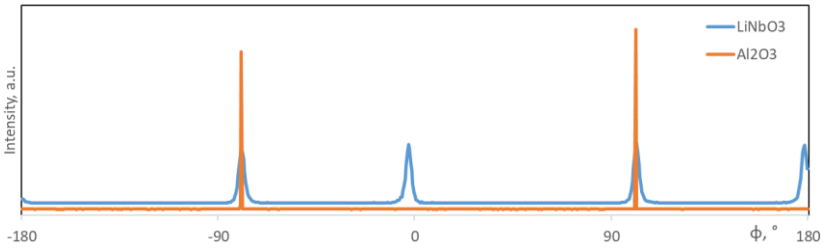

FIGURE 3.9 XRD Φ MEASUREMENTS PATTERNS, $LiNbO_3$/ (1 1 0) SAPPHIRE HETEROSTRUCTURE DEPOSITED USING $Li_{1.1}NbO_{3.05}$ TARGET AT 600°C, 0.2 MBAR (A-4) FOR OUT-OF-PLANE (0 1 2) PEAKS OF $LiNbO_3$ AND Al_2O_3.

The φ measurements conducted for the layers grown on a-sapphire consistently confirm the epitaxial nature of $LiNbO_3$ growth. Similar to those conducted for Z-cut wafers, these measurements consistently revealed 6-fold structures for (0 0 6) layers and 4-fold structures for (1 1 0) layers. These structural patterns indicate the presence of an epitaxial polyscystalline structure with twins. An illustration of such scans conducted on a sapphire heterostructure, deposited using a $Li_{1.1}NbO_{3.05}$ target at 600°C and 0.2 mbar (referred to as A-4), is provided in the figure above. Based on the φ measurements the possible crystallographic relationships between the (1 1 0) and (0 0 1) planes of $LiNbO_3$ are schematized for Al_2O_3 X-cut substrates (Fig.3.10). For the schematized relationships we calculated lattice mismatches:

- For (1 1 0) $LiNbO_3$ they are 8.6% and 7.6%, depending on the direction;
- For (0 0 1)) $LiNbO_3$ they are 25.7% and 8%, depending on the direction;

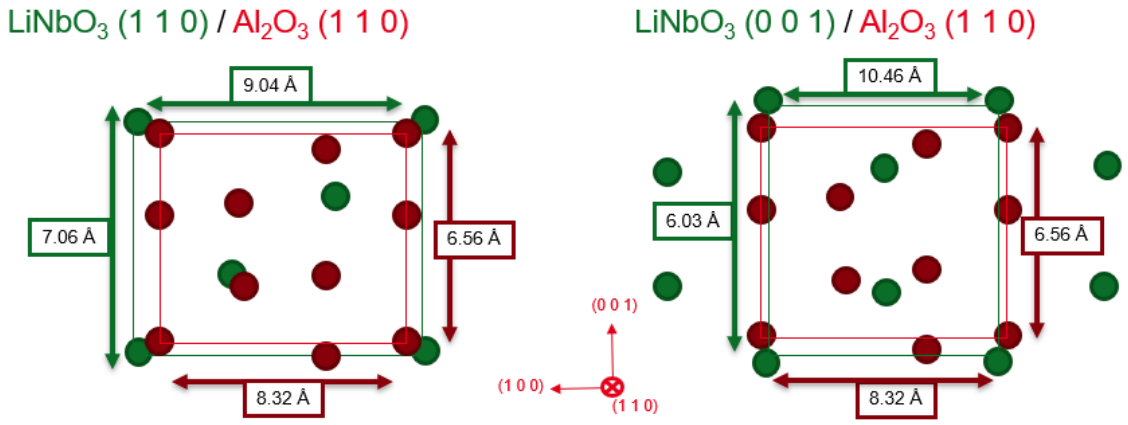

FIGURE 3.10 POSSIBLE EPITAXIAL RELATIONSHIPS LITHIUM NIOBATE THIN FILM ON Z-CUT SAPPHIRE SUBSTRATE.

The Table 3.9 provided summarizes the XRD results for layers grown on X-cut sapphire wafers under various deposition conditions. In the specific deposition process where the growth commenced at 600°C and the substrate heating was gradually reduced to lower temperatures, it resulted in the coexistence of two phases: low-Li (parasitic) $LiNb_3O_8$ (0 2 0) subphase and (1 1 0) $LiNbO_3$. The growth of $LiNb_3O_8$ (0 2 0) may have occurred due to low thermal energy in the film during the final stages of the deposition process, given that the final substrate temperature was 200°C.

ID	Main layer orientation	Texture Degree, %	Symmetry (in phi scan)	RC (symmetrical), °	RC (asymmetrical), °
A-1	(0 0 6)	96.7	6-fold	1.51	2.4
A-2	(0 0 6)	65.8	6-fold	1.691	2.0
A-3	(0 0 6)	97.7	6-fold	0.9	2.6
A-4	(1 1 0)	99.9	4-fold	1.48	1.9
A-5	(0 0 6)	99.6	6-fold	1.21	2.2
A-6	(1 1 0)	99.5	4-fold	0.43	2.24
A-7	(1 1 0)	99.7	4-fold	0.98	1.41
A-8	(1 1 0), but also parasitic phase	96	4-fold	1.12	1.46

TABLE 3.9 PRESENTATION OF SAMPLES WITH VARIATIONS IN ASSOCIATED DEPOSITION CONDITIONS.

At for most of the samples, a coexistence of (1 1 0) and (0 0 6) orientations of $LiNbO_3$ was observed. The main layer orientation for the samples grown using a $LiNbO_3$ target was always (0 0 6). On the other hand, the samples with (1 1 0) $LiNbO_3$ orientation were deposited using a $Li_{1.1}NbO_{3.05}$ target under the following conditions:

- 0.2 mbar, 500°C (A-4);

- 0.2 mbar, 600°C (A-6);
- 0.007 mbar, 600°C (A-7).

It's important to note that the RC values for symmetrical measurements for most of the (1 1 0) layers are close to 1°, indicating a relatively good degree of orientation for these layers. The deposition conducted using a $Li_{1.1}NbO_{3.05}$ target at 500°C with 0.2 mbar (A-6) had the lowest FWHM (Full-Width-at-Half-Maximum) for symmetrical ω measurements (RC) at 0.43°, which suggests a relatively high degree of crystalline quality for this sample.

The combination of the lowest FWHM for both symmetrical and asymmetrical scans of (1 1 0) LiNbO3 was achieved through deposition at 600°C with 0.007 mbar using a $Li_{1.1}NbO_{3.05}$ target (A-7). This indicates that both pressure and temperature can be tailored to achieve optimal crystal quality and orientation for $LiNbO_3$ thin films. It could be very interesting to further enhance the deposition temperature, which was not possible with our equipment.

Surface properties

ID	Pressure (mbar)	Temperature (°C)	Target	RMS 1x1 µm², nm	RMS 5x5 µm², nm
A-1	0.2	500	$LiNbO_3$	4.64	5.17
A-2	0.007	500	$LiNbO_3$	6.83	7.46
A-3	0.2	600	$LiNbO_3$	9.39	9.46
A-4	0.2	600	$Li_{1.1}NbO_{3.05}$	5.07	5.26
A-5	0.007	500	$Li_{1.1}NbO_{3.05}$	6.37	6.20
A-6	0.2	500	$Li_{1.1}NbO_{3.05}$	4.76	4.96
A-7	0.007	600	$Li_{1.1}NbO_{3.05}$	11.6	12.4
A-8	0.007	600-200	$Li_{1.1}NbO_{3.05}$	5	5.53

TABLE 3.10 PRESENTATION OF THE SUMMARY ON THE SURFACE CHARACTERIZATION FOR LAYERS GROWN ON X-CUT WAFERS WITH VARIATIONS IN ASSOCIATED DEPOSITION CONDITIONS.

To explore the surface topography of $LiNbO_3$ thin films deposited on X-cut Al_2O_3 substrates, we conducted AFM measurements. Each individual sample underwent examination using two scanning dimensions, specifically 1 x 1 µm² and 5 x 5 µm². To accurately assess the surface roughness characteristics of the $LiNbO_3$ films, we performed an analysis of the RMS roughness, mirroring the approach used for Z-cut wafers. The provided Table 3.10 summarizes the findings related to surface properties observed in the AFM scans. It provides an overview of how the surface properties are influenced by the diverse deposition conditions (including

oxygen pressure, substrate temperature and amount of Li in target) for depositions done on X-cut sapphire wafers.

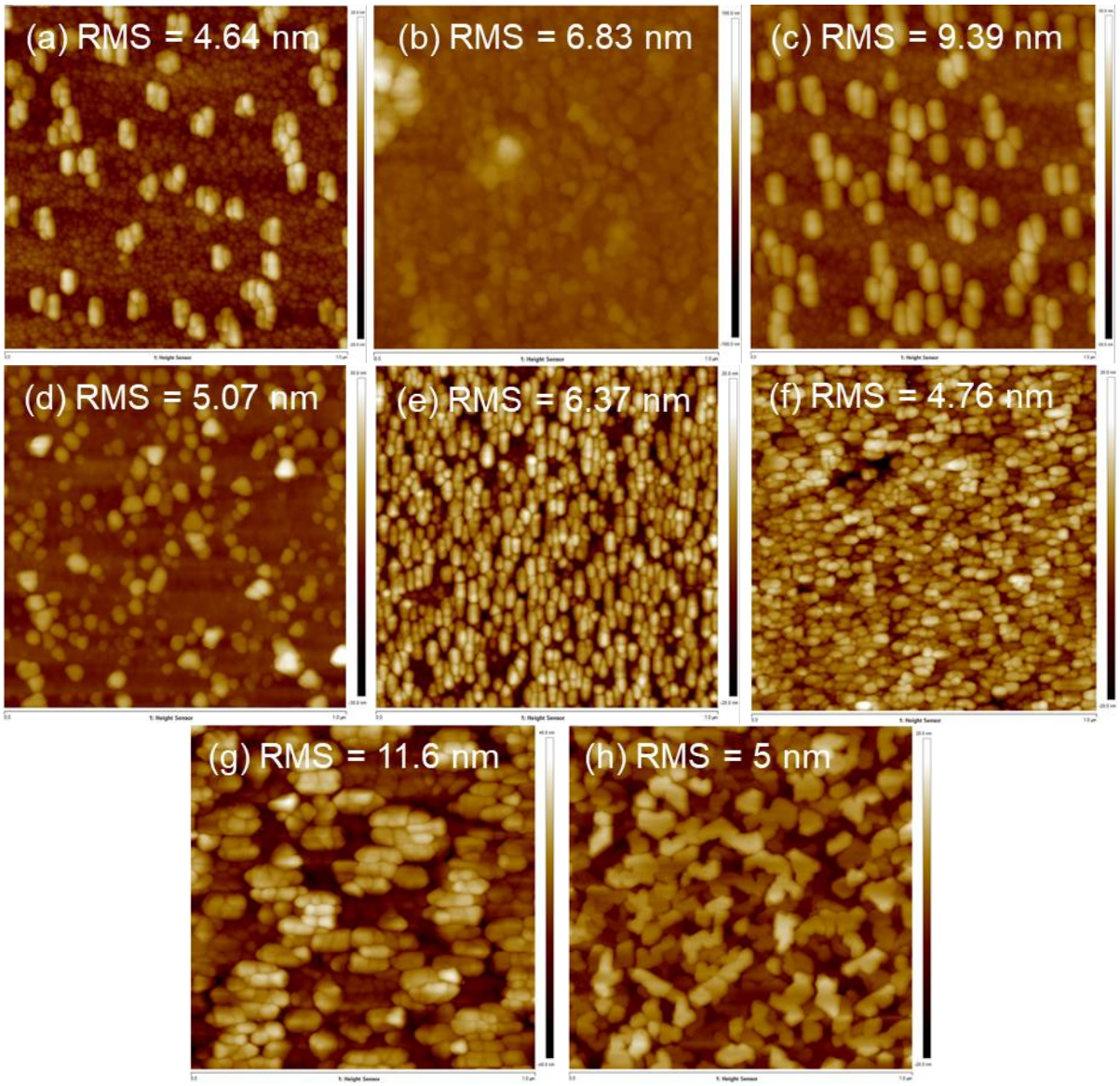

FIGURE 3.11 AFM MICROGRAPHS OF $LiNbO_3$ ON X-CUT Al_2O_3: (A) A-1; (B) A-2; (C) A-3; (D) A-4; (E) A-5; (F) A-6; (G) A-7; (H) A-8; SCAN SIZE: (1 × 1) μM^2.

Figure above presents a compilation of AFM images obtained from 1 x 1 µm² scans for samples deposited on X-cut wafers. All of the 5 x 5 µm² scans are provided in the Annex IV. In all instances, these scans unveil the presence of rounded grain structures on the film surfaces. Additionally, as a consequence of the PLD procedure, observable grains are present. It is imperative to emphasize that these grains serve as the primary contributors to the surface roughness observed in these specimens.

Most of the film surfaces display the presence of grains aligned in a single direction, alongside the visibility of grains resulting from the deposition process. The RMS roughness attains its peak values for the specimens grown under conditions of 0.2 mbar and 600°C, utilizing a $LiNbO_3$ target (A-3). Conversely, the surface roughness of the wafer grown at 0.2 mbar and 500°C, employing a Li-enriched target, exhibits the lowest values (A-6).

Summary on the growth on the X-cut sapphire

In the context of $LiNbO_3$ growth on X-cut sapphire substrates, it is imperative to emphasize that the morphology and roughness of the deposited layer are affected by the specific deposition conditions (atmosphere, substrate temperature and target composition). Our research endeavors encompassed the examination of both the crystalline quality and surface roughness of these layers, with due consideration to these parameters. A summary of all the findings from the characterization has been compiled in the table presented below.

The XRD measurements reveal that by tuning the deposition parameters during the growth process on X-cut sapphire substrates, it was possible to attain distinct $LiNbO_3$ orientations, specifically (1 1 0), (0 0 6), and a combination of (1 1 0) and (0 0 6). In contrast to earlier observations made for $LiNbO_3$ films deposited on *c*-Al_2O_3, a persistent competition in growth is observed between the (0 0 6) and (1 1 0) orientations.

All the deposition processes resulted in heteroepitaxial growth. However, a low-Li parasitic phase was observed in the samples where the deposition began at 600°C and then cooled to 200°C. The samples with a (1 1 0) $LiNbO_3$ orientation were obtained using a $Li_{1.1}NbO_{3.05}$ target under the following conditions:

- 0.2 mbar, 500°C (A-4);
- 0.2 mbar, 600°C (A-6);
- 0.007 mbar, 600°C (A-7).

The RC values for symmetrical measurements for most of the (1 1 0) layers are approximately 1°, indicating a relatively high degree of orientation for these layers. Among these samples, the deposition performed at 500°C with 0.2 mbar (A-6) had the lowest FWHM for symmetrical ω measurements (RC): 0.43°, suggesting a relatively high degree of crystalline quality for this particular sample. The combination of the lowest FWHM values for both symmetrical and

asymmetrical scans of (1 1 0) $LiNbO_3$ was achieved through deposition at 600°C with 0.007 mbar, using a $Li_{1.1}NbO_{3.05}$ target (A-7).

ID	Pressure (mbar)	Temperature (°C)	Target	Main layer orientation	RC (symmetrical), °	RC (asymmetrical), °	RMS 1x1 µm², nm	RMS 5x5 µm², nm
A-1	0.2	500	$LiNbO_3$	(0 0 6)	1.51	2.4	4.64	5.17
A-2	0.007	500	$LiNbO_3$	(0 0 6)	1.691	2.0	6.83	7.46
A-3	0.2	600	$LiNbO_3$	(0 0 6)	0.9	2.6	9.39	9.46
A-4	0.2	600	$Li_{1.1}NbO_{3.05}$	(1 1 0)	1.48	1.9	5.07	5.26
A-5	0.007	500	$Li_{1.1}NbO_{3.05}$	(0 0 6)	1.21	2.2	6.37	6.20
A-6	0.2	500	$Li_{1.1}NbO_{3.05}$	(1 1 0)	0.43	2.24	4.76	4.96
A-7	0.007	600	$Li_{1.1}NbO_{3.05}$	(1 1 0)	0.98	1.41	11.6	12.4
A-8	0.007	600-200	$Li_{1.1}NbO_{3.05}$	(1 1 0), but also parasitic phase	1.12	1.46	5	5.53

TABLE 3.10 PRESENTATION OF THE SUMMARY THE CHARACTERIZATIONS FOR LAYERS GROWN ON X-CUT WAFERS WITH VARIATIONS IN ASSOCIATED DEPOSITION CONDITIONS.

AFM examinations did not reveal any cracks within the layers. Most of the film surfaces exhibit the presence of grains oriented in a singular direction, in conjunction with the visibility of grains originating from the deposition process. The RMS roughness reaches its highest values for the specimens grown under conditions of 0.2 mbar and 600°C, utilizing a $LiNbO_3$ target (A-3). In contrast, the surface roughness of the wafer grown at 0.2 mbar and 500°C, employing a Li-enriched target, demonstrates the lowest values (A-6).

In summary, it can be confidently stated that the deposition of 200nm thick $LiNbO_3$ thin films on X-cut Al_2O_3 substrate at 0.2 mbar and 500°C, utilizing a $Li_{1.1}NbO_{3.05}$ target, yields the most advantageous combination of low roughness (with a Root Mean Square (RMS) value of 4.96 nm for the 5x5 µm² scan) and excellent crystalline quality, as evidenced by the symmetrical Rocking Curve value of 0.43°.

3.3 Growth on the R-plane

ID	Substrate Orientation	Pressure (mbar)	Temperature (°C)	Target
R-1	(0 1 2)	0.2	500	$LiNbO_3$
R-2	(0 1 2)	0.007	500	$LiNbO_3$
R-3	(0 1 2)	0.2	600	$LiNbO_3$
R-4	(0 1 2)	0.2	600	$Li_{1.1}NbO_{3.05}$
R-5	(0 1 2)	0.007	500	$Li_{1.1}NbO_{3.05}$
R-6	(0 1 2)	0.2	500	$Li_{1.1}NbO_{3.05}$
R-7	(0 1 2)	0.007	600	$Li_{1.1}NbO_{3.05}$
R-8	(0 1 2)	0.007	600-200	$Li_{1.1}NbO_{3.05}$

TABLE 3.11 PRESENTATION OF SAMPLES WITH VARIATIONS IN ASSOCIATED DEPOSITION CONDITIONS.

To investigate the influence of deposition parameters on the predominant crystallographic orientation of lithium niobate layers on sapphire, we conducted deposition on (0 1 2) Al_2O_3. The table provided below categorizes the various adjustments in deposition parameters for each sample in the context of growth on *r*-plane sapphire.

Structural properties

The structural properties of the as-grown $LiNbO_3$ layers were evaluated through XRD analysis, following a similar approach to that employed for Z-cut and X-cut wafers. We conducted θ-2θ measurements, both with and without a 0.5° ω-offset, as well as ω and φ measurements for all the wafers. The diagram presented below illustrates the θ-2θ measurements with a 0.5° ω-offset for all the *r*-sapphire wafers after the deposition. The orientations of $LiNbO_3$, $LiNb_3O_8$, and Al_2O_3 were determined by referencing ICDD sheets: 00-020-0631 [29] for $LiNbO_3$ 04-013-9445 [30] for $LiNb_3O_8$, and 00-046-1212 [31] for Al_2O_3, as detailed in Appendix II.

The XRD patterns presented below reveal that by making meticulous adjustments to the deposition parameters during the growth on r-sapphire, a variety of $LiNbO_3$ main crystallographic orientations were obtained. Unlike the previous findings from $LiNbO_3$ film depositions on *c*-Al_2O_3 and *a*-Al_2O_3, the growth of (0 0 6) $LiNbO_3$ is notably absent in these samples. The main layer orientations exhibited variation among different samples, and the

process for determining these orientations was consistent with the methodology used for deposition on X-cut sapphire.

Four orientations were identified:

- (1 1 0);
- (1 0 0), represented by the (3 0 0) peak;
- (1 0 1), indicated by the (2 0 2) peak;
- (0 1 2), characterized by the (0 1 2) and (0 2 4) peaks.

The φ measurements performed on the layers grown on *r*-sapphire consistently demonstrate the epitaxial nature of $LiNbO_3$ growth. These measurements closely mirror those conducted for Z- and X-cut wafers.

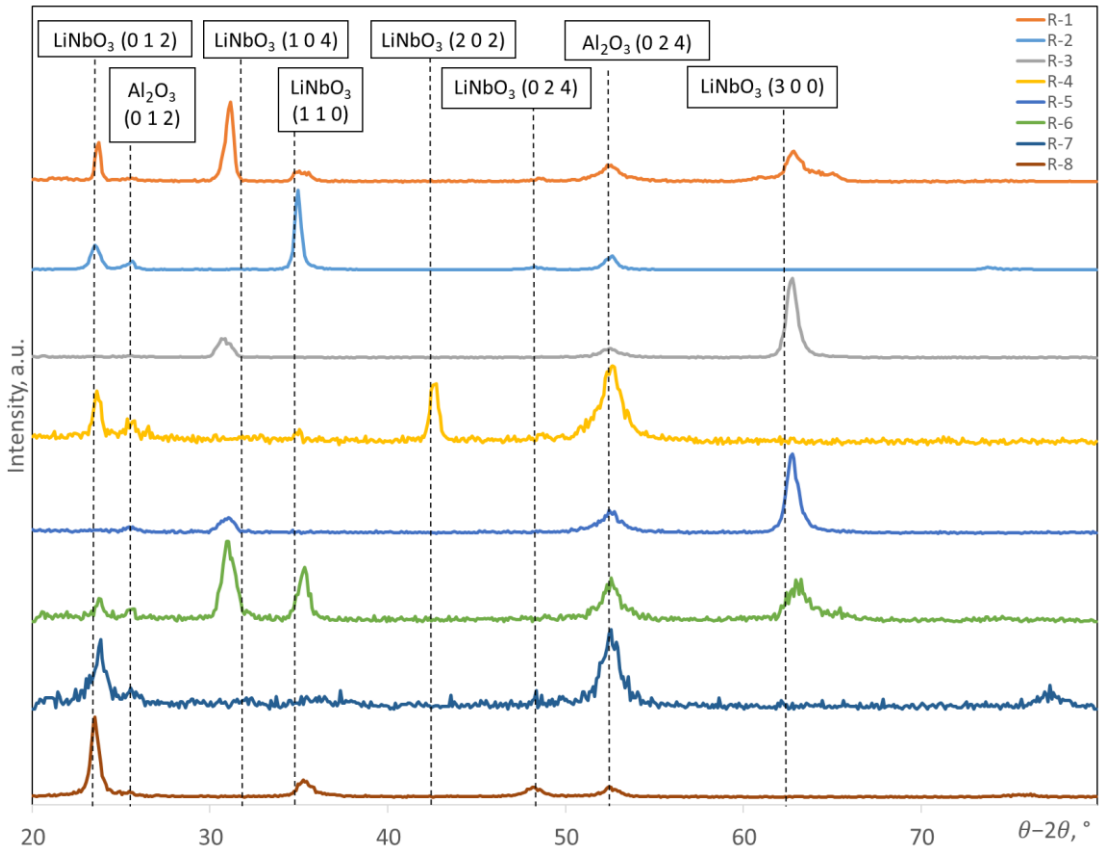

FIG 3.12 XRD Θ/2Θ MEASUREMNTS, 0.5° Ω-OFFSET OF THE $LiNbO_3$/ (0 1 2) SAPPHIRE.

Symmetrical ω (Rocking Curve) and asymmetrical ω measurements were performed subsequent to the identification of the primary crystallographic orientation represented by the peak. These measurements were executed to evaluate the broadening of the diffraction peaks, employing a methodology akin to that used for layers deposited on *c*- and *a*-sapphire.

The summary table (Table 3.12) provides data related to XRD results for layers grown on r-sapphire under various deposition conditions.

ID	Pressure (mbar)	Temperature (°C)	Target	Main layer orientation	Texture Degree, %	Symmetry (in phi scan)	RC (symmetrical), °	RC (asymmetrical), °
R-1	0.2	500	$LiNbO_3$	(3 0 0)	73.8	8-fold	1.8	2.4
R-2	0.007	500	$LiNbO_3$	(1 1 0)	94.2	4-fold	2.7	2.6
R-3	0.2	600	$LiNbO_3$	(3 0 0)	94.5	2-fold	1.3	1.9
R-4	0.2	600	$Li_{1.1}NbO_{3.05}$	(1 0 1)	93.4	3-fold	4.6	8.9
R-5	0.007	500	$Li_{1.1}NbO_{3.05}$	(3 0 0)	95.8	2-fold	2.0	2.3
R-6	0.2	500	$Li_{1.1}NbO_{3.05}$	(3 0 0)	50	4-fold	3.3	5.5
R-7	0.007	600	$Li_{1.1}NbO_{3.05}$	(0 1 2)	100	2-fold	1.5	3.6
R-8	0.007	600-200	$Li_{1.1}NbO_{3.05}$	(0 1 2)	98.5	2-fold	1.7	1.9

TABLE 3.12 PRESENTATION OF THE SUMMARY ON THE SURFACE CHARACTERIZATION FOR LAYERS GROWN ON R-CUT WAFERS WITH VARIATIONS IN ASSOCIATED DEPOSITION CONDITIONS.

Notably, layers with the primary crystallographic orientation of (1 0 0), as represented by the (3 0 0) peak, were observed multiple times. The RC values for these layers consistently fall below 2°, with variations ranging from 1.3° to 3°, depending on the specific sample. The most favorable combination of the lowest FWHM for both symmetrical and asymmetrical scans, along with texturation percent, is achieved through deposition at 600°C with 0.2 mbar using a $LiNbO_3$ target (R-3). The φ measurements performed on the layers can be seen bellow.

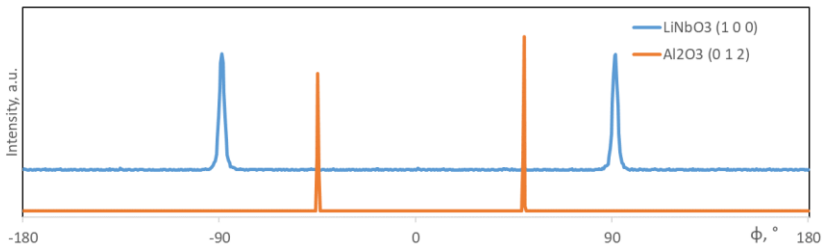

FIG 3.13 XRD Φ MEASUREMENTS PATTERNS, $LiNbO_3$/ (0 1 2) SAPPHIRE HETEROSTRUCTURE DEPOSITED USING $LiNbO_3$ TARGET AT 600°C, 0.2 MBAR (R-3) FOR OUT-OF-PLANE (1 0 4) PEAKS OF $LiNbO_3$ (3 0 0) AND Al_2O_3 (0 1 2).

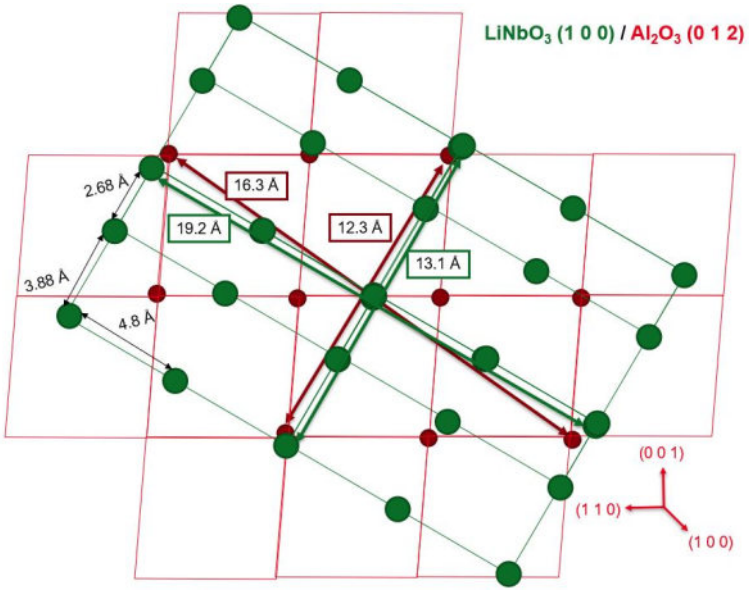

FIGURE 3.14 POSSIBLE EPITAXIAL RELATIONSHIP OF LITHIUM NIOBATE (1 0 0) THIN FILM ON R-CUT SAPPHIRE SUBSTRATE.

Utilizing the φ measurements, a schematic representation of the potential epitaxial relationship for the (1 0 0) planes between $LiNbO_3$ and Al_2O_3 R-cut substrates is depicted (see Fig. 3.14). The lattice mismatches for superlattices were calculated to be 17% and 6%, depending on the direction.

Layer with the main (1 1 0) crystallographic orientation, was observed once. It is achieved through deposition at 500°C with 0.007 mbar using a $LiNbO_3$ target (R-2). The RC values for symmetrical and a symmetrical measurements were 2.7° and 2.6°. If to compare this date with depositions performed on a-sapphire, it is possible to conclude quality of the layer is poor. The φ measurements performed on the thin film and substrate can be seen bellow.

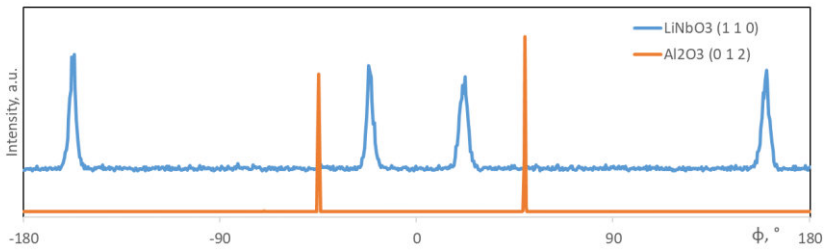

FIGURE 3.15 XRD Φ MEASUREMENTS PATTERNS, $LiNbO_3$/ (0 1 2) SAPPHIRE HETEROSTRUCTURE DEPOSITED USING $LiNbO_3$ TARGET AT 500°C, 0.007 MBAR (R-2) FOR OUT-OF-PLANE (1 0 4) PEAKS OF $LiNbO_3$ (1 1 0) AND Al_2O_3 (0 1 2).

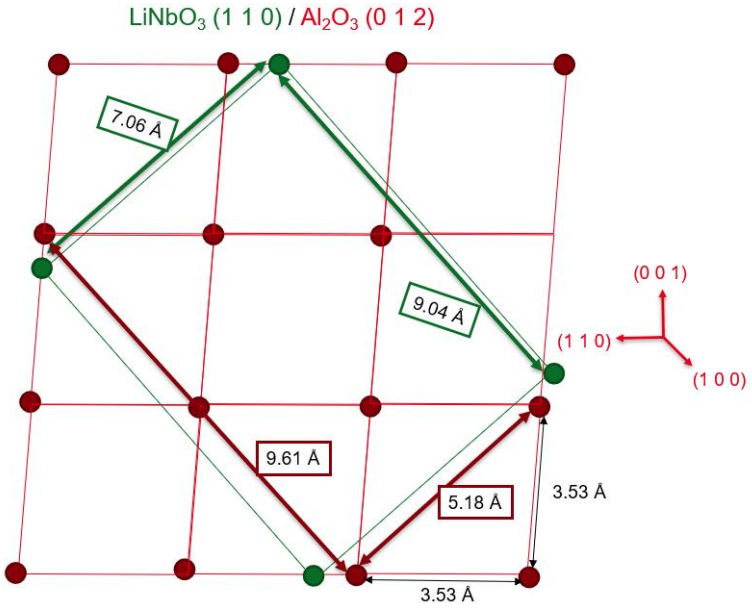

FIGURE 3.16 POSSIBLE EPITAXIAL RELATIONSHIP OF LITHIUM NIOBATE (1 1 0) THIN FILM ON R-CUT SAPPHIRE SUBSTRATE.

Using the φ measurements, a schematic representation of the possible epitaxial relationship for the (1 1 0) planes between $LiNbO_3$ and (0 1 2) Al_2O_3 substrates is presented (Fig. 3.16). The calculated lattice mismatches were also calculated for superlattices and are 35% and 6%, depending on the direction.

Layers with the main (0 1 2) crystallographic orientation were observed twice. Notably, for the layer deposited using a $Li_{1.1}NbO_{3.05}$ target at 600°C with 0.007 mbar (R-7), this orientation was the sole crystallographic orientation. This particular thin film also exhibited low FWHM values for both symmetrical and asymmetrical scans: 0.76° and 1.92°, respectively.

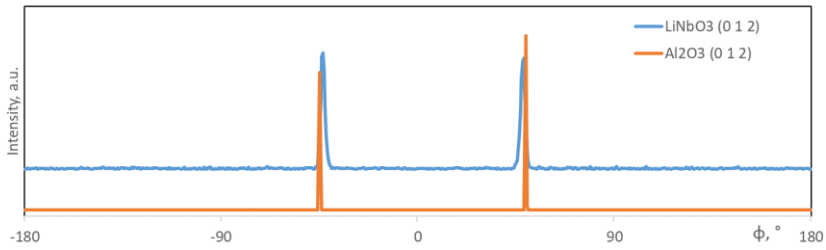

FIGURE 3.17 XRD Φ MEASUREMENTS PATTERNS, $LiNbO_3$/ (0 1 2) SAPPHIRE HETEROSTRUCTURE MBAR (R-7) FOR OUT-OF-PLANE (1 0 4) PEAKS OF $LiNbO_3$ (0 1 2) AND Al_2O_3 (0 1 2).

Based on the φ measurements the possible epitaxial relationship between the *r*-$LiNbO_3$ and *r*-Al_2O_3 is schematized (Fig.3.18). The lattice mismatch of this possible structure is 11 %.

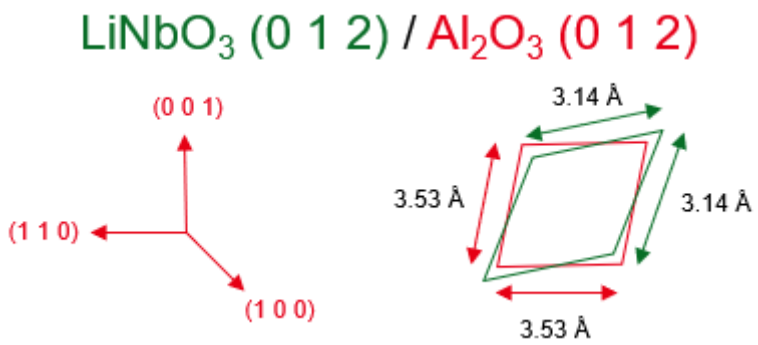

FIGURE 3.18 POSSIBLE EPITAXIAL RELATIONSHIP OF LITHIUM NIOBATE (0 1 2) THIN FILM ON R-CUT SAPPHIRE SUBSTRATE.

Remarkably, during the deposition process conducted using a $Li_{1.1}NbO_{3.05}$ target at 600°C with 0.2 mbar pressure, a primary crystallographic orientation, (1 0 1), represented by the (2 0 2) peak, was observed. This thin film similarly displayed low FWHM values for both symmetrical and asymmetrical scans: 0.76° and 1.92°, respectively. This orientation achieved by PLD process had not been reported previously in the literature.

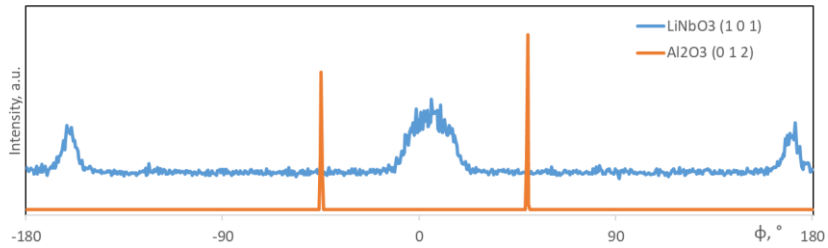

FIGURE 3.19 XRD Φ MEASUREMENTS PATTERNS, $LiNbO_3$/ (0 1 2) SAPPHIRE HETEROSTRUCTURE (R-4) FOR OUT-OF-PLANE (1 0 4) PEAKS OF $LiNbO_3$ (1 0 1) AND AL_2O_3 (0 1 2).

Based on the φ measurements, a schematic illustration of the potential epitaxial relationship for the planes of (1 0 1) $LiNbO_3$ and (0 1 2) Al_2O_3 is provided (refer to Fig. 3.19). The calculated lattice mismatches for superlattices are also determined and are to 2.5%.

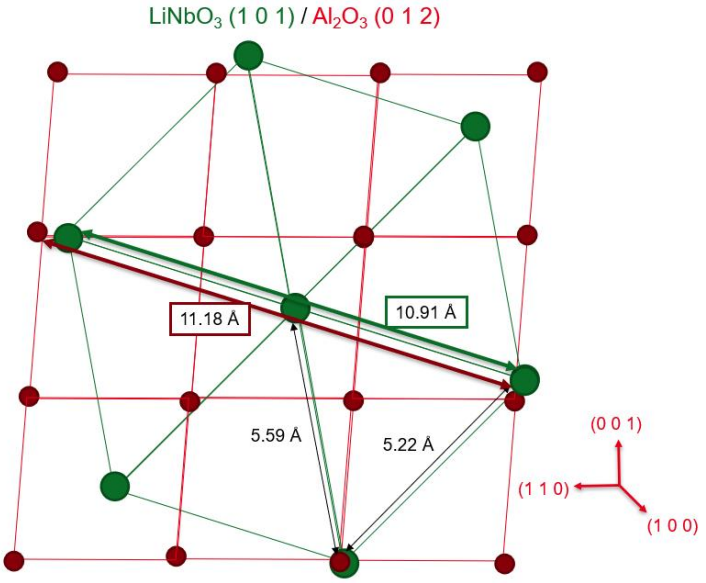

FIGURE 3.20 POSSIBLE EPITAXIAL RELATIONSHIP OF LITHIUM NIOBATE (1 0 1) THIN FILM ON R-CUT SAPPHIRE SUBSTRATE.

The presented image below illustrates X-ray diffraction (XRD) φ measurements focusing on the out-of-plane reflection associated with the primary crystallographic orientations. It displays five signals corresponding to (1 0 4) reflections:

- (0 1 2) orientation of Al_2O_3.
- (0 1 2) orientation of $LiNbO_3$ from R-7 wafer.
- (1 0 0) orientation of $LiNbO_3$ from R-3 wafer.
- (1 1 0) orientation of $LiNbO_3$ from R-2 wafer.
- (1 0 1) orientation of $LiNbO_3$ from R-4 wafer.

These measurements unveil the epitaxial relationships between different layers, as influenced by their predominant crystallographic orientations. Notably, noticeable shifts and additional peaks are evident in the signals emanating from the thin films when compared to the signal originating from the substrate, due to differences in layers deposited.

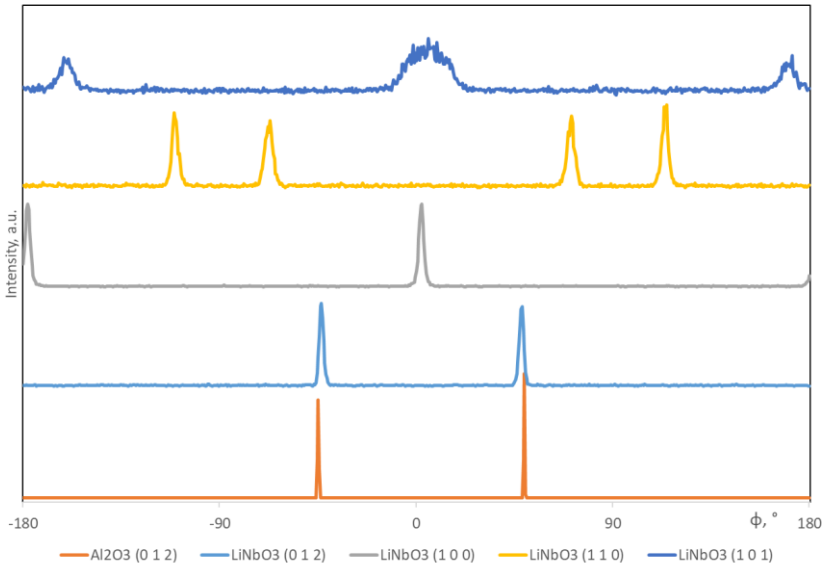

FIGURE 3.21 XRD Φ MEASUREMENTS PATTERNS SHOWING EPITAXIAL RELATIONSHIPS, $LiNbO_3$/(0 1 2) SAPPHIRE HETEROSTRUCTURES FOR OUT-OF-PLANE (1 0 4) PEAKS OF Al_2O_3 (0 1 2) SUBSTRATE AND R-3 $LiNbO_3$ (1 0 0), R-2 $LiNbO_3$ (1 1 0), R-7 $LiNbO_3$ (0 1 2), AND R-4 $LiNbO_3$ (1 0 1).

Surface properties

In order to investigate the surface topography of $LiNbO_3$ thin films deposited on *r*-sapphire substrates, we conducted AFM measurements using the same methodology as applied to Z- and X-cut wafers. An analysis of the RMS roughness of the layers was also carried out. Considering the distinct predominant crystallographic orientations exhibited by the grown films, our analysis was focused on these orientations, with special emphasis on layers demonstrating superior structural properties (in terms of calculated TD and RC measured).

(0 1 2) layers

In the case of the R-7 layer deposited using a $Li_{1.1}NbO_{3.05}$ target at 600°C with 0.007 mbar O_2 pressure, the (0 1 2) orientation was the exclusive crystallographic orientation observed. Consequently, we are presenting the Atomic Force Microscopy (AFM) micrographs for the surface topology analysis of this wafer, which are visible in the images below.

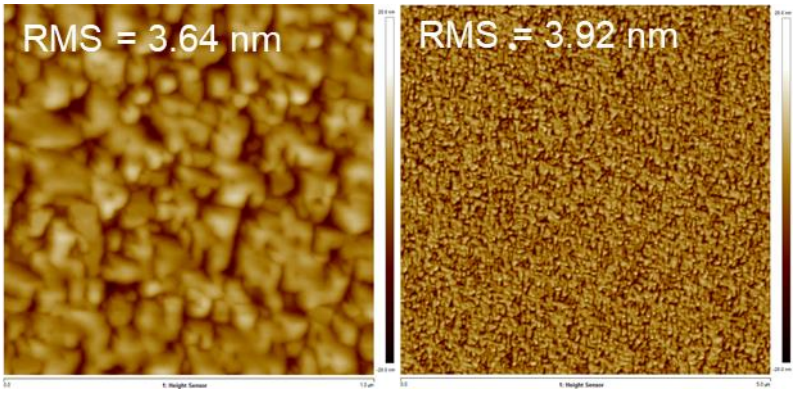

FIGURE 3.22 AFM MICROGRAPHS OF $LiNbO_3$/ (0 1 2) Al_2O_3 STRUCTURE EXHIBITING (0 1 2) MAIN CRYSTALLOGRAPHIC ORIENTATION GROWN AT 0.007 MBAR, 600°C, $Li_{1.1}NbO_{3.05}$ TARGET. SCAN SIZES: (1 × 1) μM^2 (LEFT), (5 × 5) μM^2 (RIGHT).

In this particular case, a significant number of grains are visible on the surface of the layer, mostly attributed to the PLD process. Unfortunately, it is not possible to determine the composition of these rounded grains with the (0 1 2) crystallographic orientation. The Root Mean Square (RMS) roughness values obtained from the measurements are not so high, measuring just below 4 nanometers for both scans, despite the film's thickness being 200 nanometers.

(1 0 0) layers

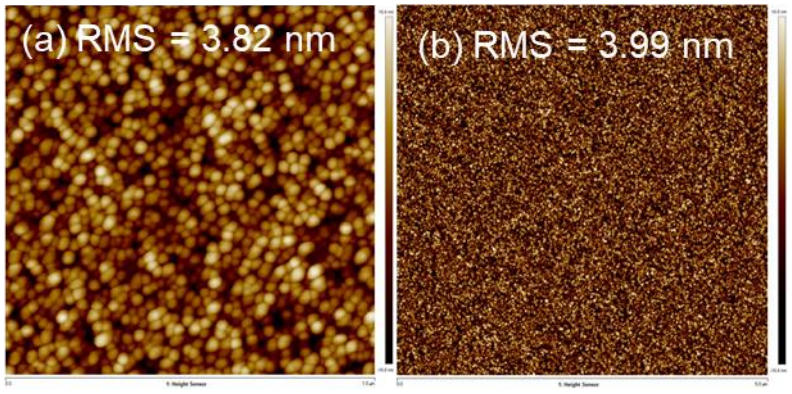

FIGURE 3.23 AFM MICROGRAPHS OF $LiNbO_3$ ON *R*-Al_2O_3 GROWN AT: 0.2 MBAR, 600°C, $LiNbO_3$ TARGET (A-3). SCAN SIZES: (1 × 1) μM^2 (A), (5 × 5) μM^2 (B).

It is worth noting that layers with the main crystallographic orientation of (1 0 0), as indicated by the (3 0 0) peak, were observed on multiple wafers. Therefore, we propose to investigate the surface properties of two heterostructures with the highest Texture Degrees – R-3 (94.5%) and R-5 (95.8%). What makes this even more interesting is that they were deposited under notably different conditions. The R-3 layer was grown using a $LiNbO_3$ target at 600°C

with a pressure of 0.2 mbar (Figures above), whereas the R-5 heterostructure was deposited using a $Li_{1.1}NbO_{3.05}$ target at 500°C and a pressure of 0.007 mbar (Figures below).

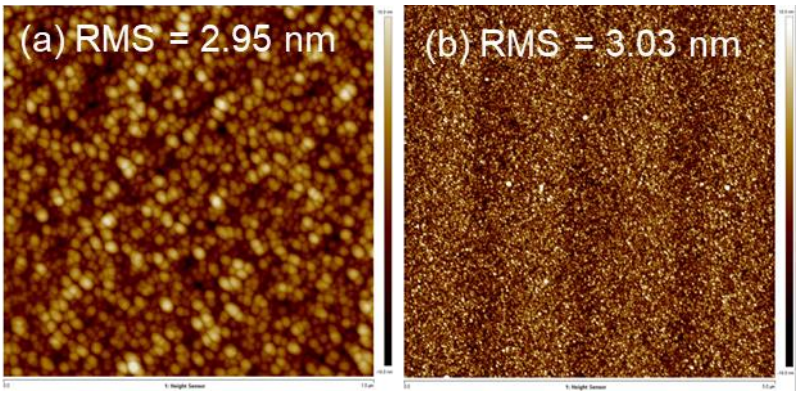

FIGURE 3.24 AFM MICROGRAPHS OF $LiNbO_3$ ON *R*-Al_2O_3 GROWN AT: 0.007 MBAR, 500°C, $Li_{1.1}NbO_{3.05}$ TARGET. SCAN SIZES: (1 × 1) μM^2 (A), (5 × 5) μM^2 (B).

For both wafers, the film surfaces consist of rounded grains, with the additional presence of grains, which can be attributed to the PLD process. The RMS roughness is slightly higher for the sample grown at 0.2 mbar and 600°C, likely due to the grains presence. On the other hand, the RMS roughness values obtained from the measurements are quite similar, measuring just below 4 and 3 nanometers, even though the film's thickness is 200 nm. It's worth noting that the layer grown at 500°C using the $Li_{1.1}NbO_{3.05}$ target exhibits a smoother surface and the presence of epitaxial columns, indicating a distinctive surface morphology.

(1 1 0) layers

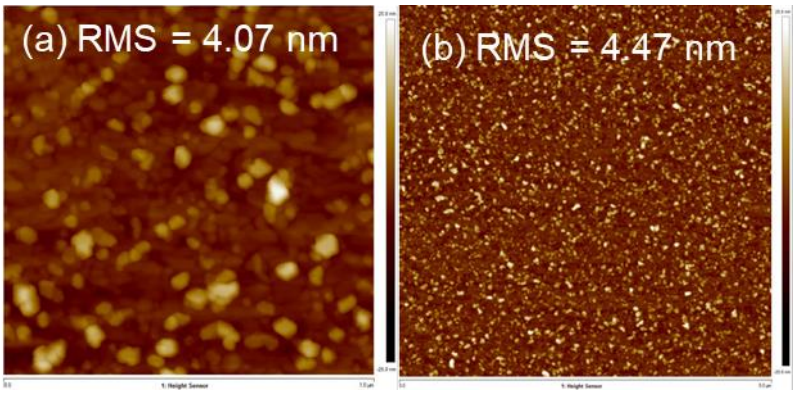

FIGURE 3.25 AFM MICROGRAPHS OF $LiNbO_3$ ON *R*-Al_2O_3 GROWN AT: 0.007 MBAR, 500°C, $LiNbO_3$ TARGET (R-2). SCAN SIZES: (1 × 1) μM^2 (A), (5 × 5) μM^2 (B).

Layer with the main (1 1 0) crystallographic orientation, was observed once after deposition on *r*-sapphire. It is achieved through deposition at 500°C with 0.007 mbar using a $LiNbO_3$ target (R-2). Interesting is that roughness achieved was slightly lower than for (1 1 0) $LiNbO_3$ deposited on (1 1 0) Al_2O_3 discussed before.

(1 0 1) layers

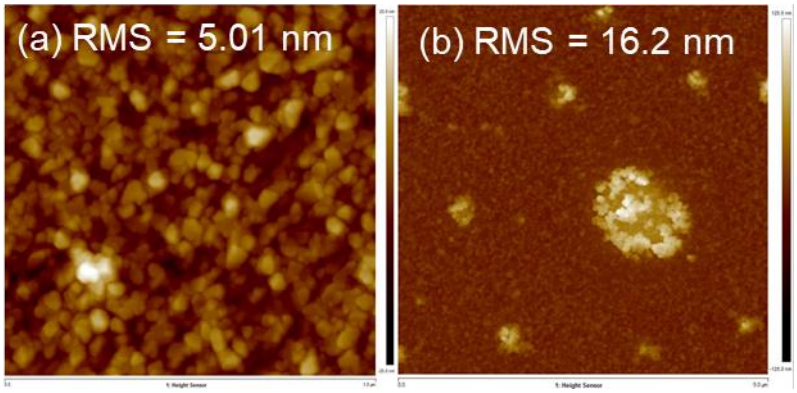

FIGURE 3.25 AFM MICROGRAPHS OF $LiNbO_3$ ON *R*-Al_2O_3 GROWN AT: 0.2 MBAR, 600°C, $Li_{1.1}NbO_{3.05}$ TARGET (R-4). SCAN SIZES: (1 × 1) μM^2 (A), (5 × 5) μM^2 (B).

The layer characterized by the primary (1 0 1) crystallographic orientation was observed only once, after the deposition on *r*-Al_2O_3 at 0.2 mbar, 600°C, $Li_{1.1}NbO_{3.05}$ target. Since this orientation has not been previously reported after deposition PLD, it is not possible to perform a comparative analysis. It is clear that the surface of this layer is described by the presence of large defects, resulting in increased roughness with an RMS value of 16.2 nm, as observed in the (5 × 5) μm^2 scan. Conversely, when examining a smaller region with a (1 × 1) μm^2 scan, the layer is found to be composed of grains, and the roughness is lower at an RMS of 5.01 nm. This scan also shows the absence of the large particles observed in the larger scan.

Summary on surface properties

ID	Pressure (mbar)	Temperature (°C)	Target	Main layer orientation	RMS 1x1 µm², nm	RMS 5x5 µm², nm
R-1	0.2	500	$LiNbO_3$	(3 0 0)	3.16	3.15
R-2	0.007	500	$LiNbO_3$	(1 1 0)	4.07	4.47
R-3	0.2	600	$LiNbO_3$	(3 0 0)	3.82	3.99
R-4	0.2	600	$Li_{1.1}NbO_{3.05}$	(1 0 1)	5.01	16.2
R-5	0.007	500	$Li_{1.1}NbO_{3.05}$	(3 0 0)	2.95	3.03
R-7	0.007	600	$Li_{1.1}NbO_{3.05}$	(0 1 2)	3.64	3.92
R-8	0.007	600-200	$Li_{1.1}NbO_{3.05}$	(0 1 2)	7.27	5.9

TABLE 3.13 PRESENTATION OF THE SUMMARY THE CHARACTERIZATIONS FOR LAYERS GROWN ON X-CUT WAFERS WITH VARIATIONS IN ASSOCIATED DEPOSITION CONDITIONS.

The provided table (Table 3.13) summarizes all of the results related to surface properties observed in the AFM scans. It provides an overview of how the surface properties

are influenced by the diverse deposition conditions (including oxygen pressure, substrate temperature and amount of Li in target) for depositions done on *r*-sapphire wafers.

In all cases, the film surfaces consist of rounded grains, with the presence of grains attributable to the deposition process, as observed similarly in the case of growth on Z- and X-cut sapphire substrates. The highest roughness is observed in the sample grown at 0.2 mbar and 600°C, primarily attributed to the presence of larger grains. In contrast, the layer grown at 500°C using a Li-enriched target exhibits a smoother surface and prominently displays epitaxial columns in the scan. This improvement in surface quality could be attributed to several factors: compensation of Li resputtering by additional Li in the target, the high kinetic energy of atoms (due to low pressure during deposition) serving as an additional source of energy during layer formation, and a lower coefficient of thermal expansion (CTE) difference between $LiNbO_3$ and Al_2O_3 compared to the conditions at 600°C.

3.4 Growth on other planes

To explore the possibility of growing crystallographic planes that have not been previously reported, we carried out deposition experiments on 2-inch Al_2O_3 substrates with various crystal cuts. Given that the layers deposited using a Li-enriched target at 0.007 mbar and 600°C exhibited favorable structural properties on *c*-, *a*-, and *r*-sapphire substrates, we chose to carry out our experiments under these specific conditions. The table provided below summarizes the deposition parameters for each sample.

ID	Size (inch)	Substrate Orientation	Pressure (mbar)	Temperature (°C)	Target
M-1	2	(1 0 0)	0.007	600	$Li_{1.1}NbO_{3.05}$
N-1	2	(1 1 3)	0.007	600	$Li_{1.1}NbO_{3.05}$
V-1	2	(2 2 3)	0.007	600	$Li_{1.1}NbO_{3.05}$

TABLE 3.14 PRESENTATION OF SAMPLES VARIATIONS ASSOCIATED WITH DEPOSITION CONDITIONS.

The structural properties of the as-grown $LiNbO_3$ layers were assessed through XRD analysis, following the same procedure as was conducted for *c*-, *a*-, and *r*-sapphire. θ-2θ measurements were performed for all samples, both with and without a 0.5° ω-offset, aimed for minimizing the contribution of Al_2O_3. The orientations of $LiNbO_3$, $LiNb_3O_8$, and Al_2O_3 were determined with reference to ICDD sheets: 00-020-0631 [29] for $LiNbO_3$ 04-013-9445 [30] for $LiNb_3O_8$, and 00-046-1212 [31] for Al_2O_3, as described in Appendix II. Symmetrical and asymmetrical ω (Rocking Curve) measurements were conducted to identify the broadening of the diffraction peaks. Additionally, φ measurements were carried out to confirm the epitaxial nature of $LiNbO_3$ growth.

To investigate the surface topography of the deposited $LiNbO_3$ thin films, we conducted AFM measurements, employing the same methodology as was applied to *c*-, *a*-, and *r*-sapphire. Each sample was subject to examination in two scanning dimensions, specifically 1 x 1 μm² and 5 x 5 μm². Additionally, we carried out an analysis of the Root Mean Square (RMS) roughness for each sample.

M-plane

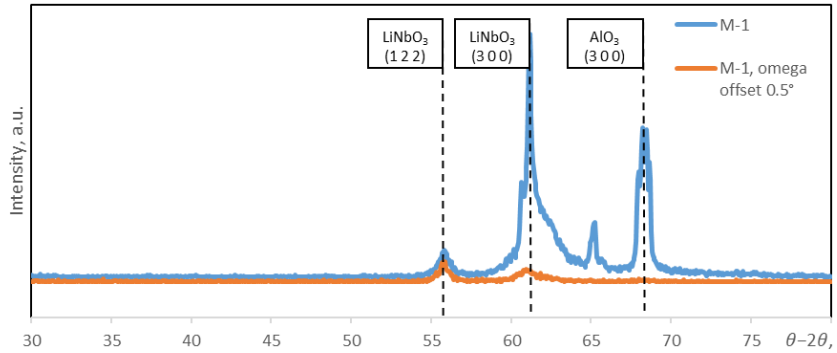

FIGURE 3.26 XRD Θ/2Θ PATTERNS, WITHOUT (UP) AND WITH 0.5° Ω-OFFSET (DOWN) OF THE $LiNbO_3$/ (3 0 0) SAPPHIRE DEPOSITED AT 0.007 MBAR, 600°C, $Li_{1.1}NbO_{3.05}$ TARGET

θ-2θ measurements were carried out with and without a 0.5° ω-offset and the figure below illustrates the contrast between the scans obtained. It is clear that the $LiNbO_3$ layer is composed of crystals with (3 0 0) and (1 2 2) orientations. The degree of texturation calculated indicates a very strong (3 0 0) orientation of the crystals, accounting 99.8 %. This result supports the findings of Laura Sauze et al. [28], suggesting the possibility of growing Y-cut $LiNbO_3$ on Y-cut Al_2O_3, while taking into account the use of a different target composition and distinct deposition conditions in this study. Symmetrical ω measurement has FWHM of 1.27°.

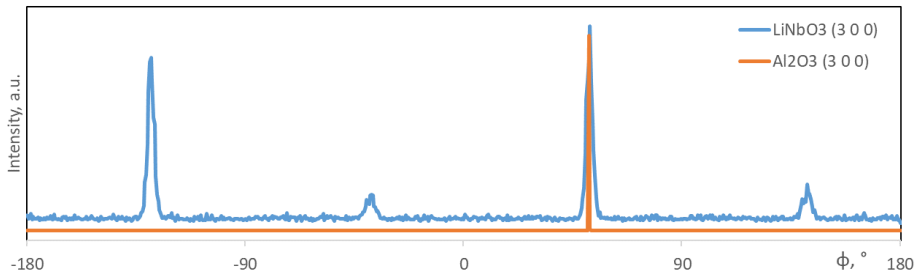

FIGURE 3.27 XRD Φ MEASUREMENTS PATTERNS, $LiNbO_3$/ (3 0 0) SAPPHIRE HETEROSTRUCTURE (M-1) FOR OUT-OF-PLANE (1 0 4) PEAKS OF $LiNbO_3$ (3 0 0) AND Al_2O_3 (3 0 0).

The φ measurements conducted on both the thin film and the substrate are presented below. These measurements were carried out for the out-of-plane (1 0 4) peak of both (3 0 0) Al_2O_3 and (3 0 0) $LiNbO_3$. It is important to highlight that of this measurement demonstrated a 4-fold structural pattern for the thin film deposited, which suggests the existence of an epitaxial polycrystalline structure. Based on the φ measurements the possible epitaxial relationship is schematized (Fig.3.28). The lattice mismatch of this possible structure is 16 % and 7% depending on the direction.

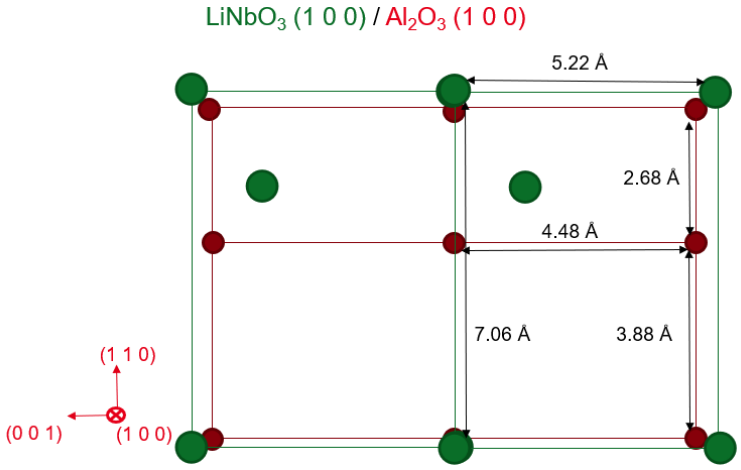

FIGURE 3.28 POSSIBLE EPITAXIAL RELATIONSHIP OF LITHIUM NIOBATE (1 0 0) THIN FILM ON *M*-SAPPHIRE SUBSTRATE.

The film surface is primarily composed of rounded grains, with some grains. The RMS roughness is slightly higher when the sample is measured at lower magnifications due to the presence of several grains. However, when analyzing a smaller region with a (1 × 1) μm^2 scan, the layer is seen to be composed of grains, and the roughness is notably low, with an RMS value of 0.1 nanometers. Both AFM micrographs can be seen below.

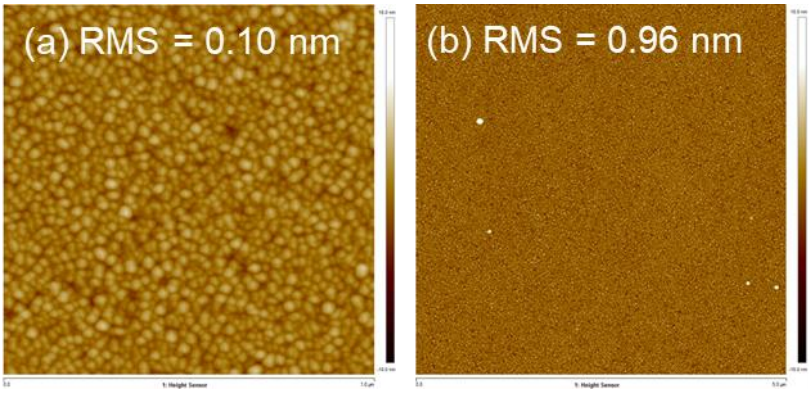

FIGURE 3.29 AFM MICROGRAPHS OF $LiNbO_3$ ON *M*-Al_2O_3 (M-1). SCAN SIZES: (1 × 1) μM^2 (A), (5 × 5) μM^2 (B).

N-plane

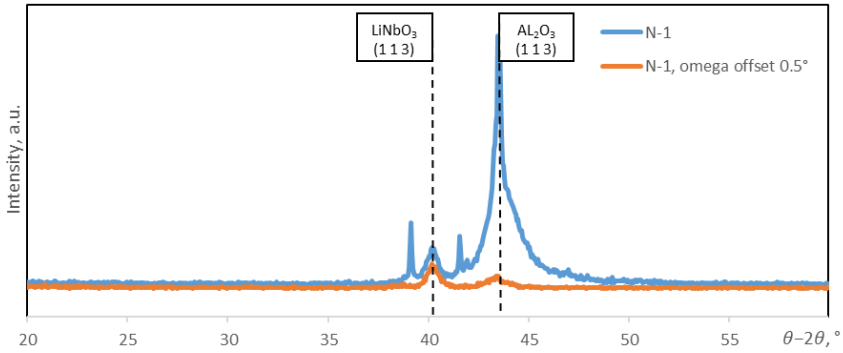

FIGURE 3.30 XRD Θ/2Θ PATTERNS, WITHOUT (UP) AND WITH 0.5° Ω-OFFSET (DOWN) OF THE $LiNbO_3$/ (1 1 3) SAPPHIRE DEPOSITED AT 0.007 MBAR, 600°C, $Li_{1.1}NbO_{3.05}$ TARGET.

θ-2θ measurements show that the $LiNbO_3$ film deposited on the N-plane Al_2O_3 substrate has only (1 1 3) crystallographic orientation. Symmetrical ω (Rocking Curve) measurement has FWHM of 1.23°.

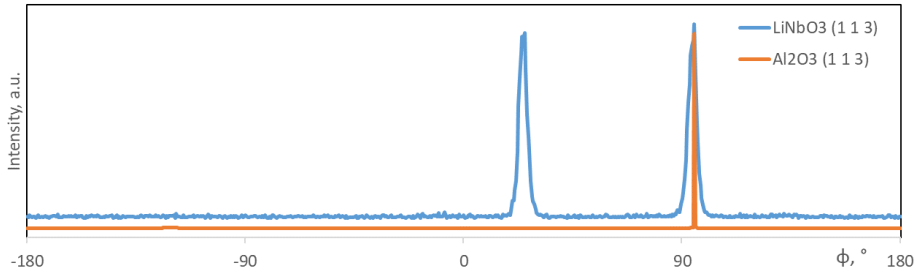

FIGURE 3.31 XRD Φ MEASUREMENTS PATTERNS, $LiNbO_3$/ (1 1 3) SAPPHIRE HETEROSTRUCTURE (N-1) FOR OUT-OF-PLANE (1 0 4) PEAKS OF $LiNbO_3$ (1 1 3) AND Al_2O_3 (1 1 3).

The φ measurements performed on both the thin film and the substrate confirm the epitaxial nature of the deposited film, as shown above. These measurements were taken for the out-of-plane (1 0 4) peak of both (1 1 3) Al_2O_3 and (1 1 3) $LiNbO_3$.

Based on the φ measurements the possible epitaxial relationship is schematized (Fig.3.32). The lattice mismatch of this possible structure is 11 % and 1% depending on the direction.

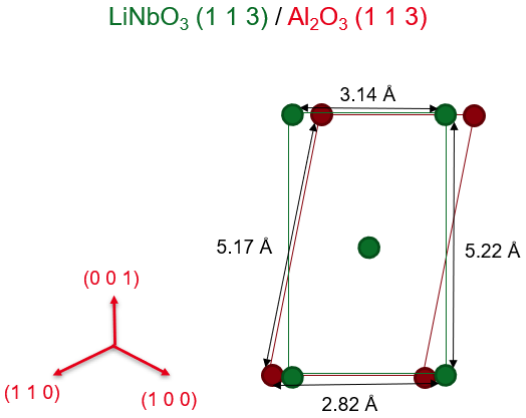

FIGURE 3.32 POSSIBLE EPITAXIAL RELATIONSHIP OF LITHIUM NIOBATE (1 1 3) THIN FILM ON N-SAPPHIRE SUBSTRATE.

While the AFM scans do reveal the presence of some grains and grains (can be seen bellow), the RMS roughness remains relatively low compared to other deposited films, measuring approximately 0.7 nanometers for both scans conducted.

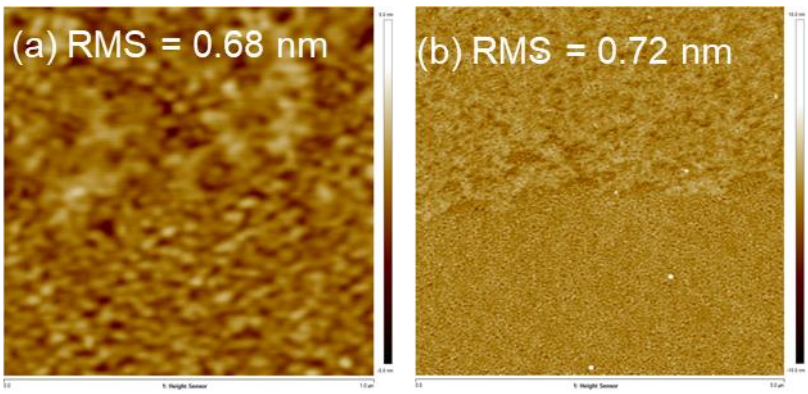

FIGURE 3.33 AFM MICROGRAPHS OF $LiNbO_3$ ON *N*-Al_2O_3 (N-1). SCAN SIZES: (1 × 1) μM^2 (A), (5 × 5) μM^2 (B).

V-plane

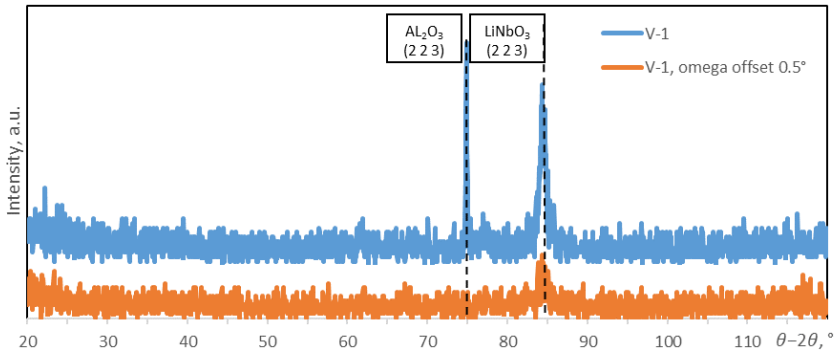

FIGURE 3.34 XRD Θ/2Θ PATTERNS, WITHOUT (UP) AND WITH 0.5° Ω-OFFSET (DOWN) OF THE $LiNbO_3$/ (2 2 3) SAPPHIRE DEPOSITED AT 0.007 MBAR, 600°C, $Li_{1.1}NbO_{3.05}$ TARGET.

The θ-2θ measurements, as displayed below, indicate that the $LiNbO_3$ film deposited on the V-plane Al_2O_3 substrate has only (2 2 3) crystallographic orientation. Additionally, the symmetrical ω (Rocking Curve) measurement exhibits a Full Width at Half Maximum (FWHM) value of 0.7°.

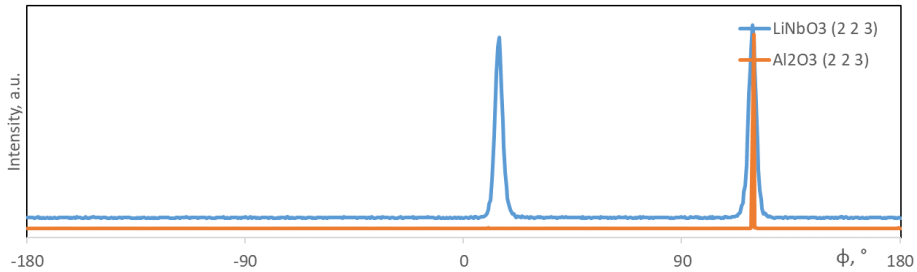

FIGURE 3.34 XRD Φ MEASUREMENTS PATTERNS, $LiNbO_3$/ (2 2 3) SAPPHIRE HETEROSTRUCTURE (V-1) FOR OUT-OF-PLANE (0 1 2) PEAKS OF $LiNbO_3$ (2 2 3) AND Al_2O_3 (2 2 3).

The φ measurements conducted on both the thin film and the substrate validate the epitaxial nature of the deposited film, as shown above. These measurements were carried out for the out-of-plane (0 1 2) peak of both (2 2 3) Al_2O_3 and (2 2 3) $LiNbO_3$. Based on the φ measurements the possible epitaxial relationship is schematized (Fig.3.35). The lattice mismatch of this possible structure is 12 % and 4% depending on the direction.

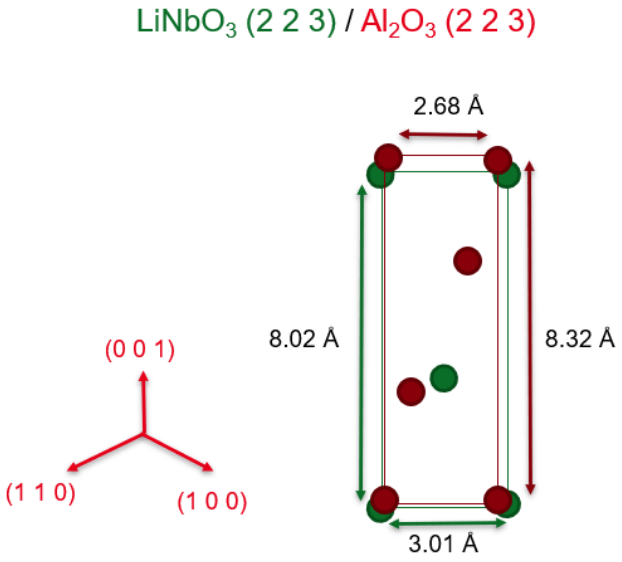

FIGURE 3.35 POSSIBLE EPITAXIAL RELATIONSHIP OF LITHIUM NIOBATE (1 1 3) THIN FILM ON N-SAPPHIRE SUBSTRATE.

The film surface is predominantly characterized by rounded grains with roughness relatively low in comparison to other deposition cases (≈0.85nm).

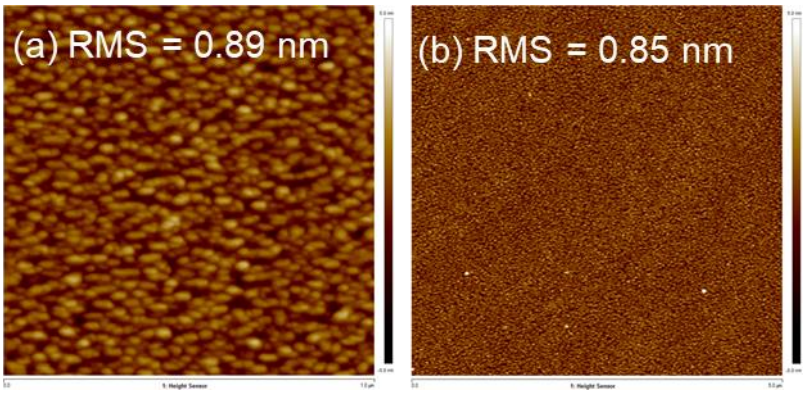

FIGURE 3.36 AFM MICROGRAPHS OF $LiNbO_3$ ON *V*-Al_2O_3 (V-1). SCAN SIZES: (1 × 1) μM^2 (A), (5 × 5) μM^2 (B).

3.5 Summary on the characterizations

The provided table summarizes all the results related to structure and surface properties observed for the layers deposited using a Li-enriched target at 0.007 mbar and 600°C on 2-inch Al_2O_3 substrates with various crystal cuts.

ID	Layer orientation	RC (symmetrical), °	RMS 1x1 µm², nm	RMS 5x5 µm², nm
M-1	(1 0 0)	1.27°	0.1	0.96
N-1	(1 1 3)	1.22°	0.68	0.72
V-1	(2 2 3)	0.66°	0.89	0.85

TABLE 3.15 SUMMARY OF SAMPLES PROPERTIES.

In contrast to prior findings from $LiNbO_3$ film depositions on *c*-Al_2O3 and *a*-$Al2O_3$, the presence of (0 0 6) LiNbO3 orientation is absent in these samples. The primary layer orientations varied among different samples and were dependent on the substrate orientation. Only one layer, grown on the (1 0 0) sapphire, displayed an additional (1 2 2) orientation of the crystals. The method used for determining these orientations was consistent with the approach employed for deposition on X-cut sapphire. The predominant layer orientation was found to be (1 0 0), as represented by the (3 0 0) peak, with a texturation degree of 99 percent. The φ measurements conducted on all of the thin films and substrates demonstrated the existence of an epitaxial polycrystalline structure.

It's worth mentioning that the Rocking Curve values for most of the layers discussed in this section are approximately 1°, suggesting a relatively good degree of orientation for these layers. In the case of the V-1 wafer with the (2 2 3) orientation of the layer, this value is even lower (0.66°), indicating a relatively high degree of orientation for this particular layer.

The AFM examinations did not detect any cracks within the layers. In most cases, the film surfaces display grains aligned in a single direction. Moreover, due to the deposition process, visible grains are present. It is important to note that these grains are the primary contributors to the observed surface roughness in these specimens. The RMS roughness for all of the wafers is less than 1 nanometer, which could be attributed to the presence of a smaller quantity of grains on the surface, in contrast to the wafers with other reported crystallographic orientations in this chapter.

3.6 Fabricated SAW devices characteristics

Surface acoustic wave devices were fabricated and tested on all *c*- (C-1 – C-5) and some *a*-sapphire (A1 – A3) wafers by Emma Borel from CEA-Leti. The fabrication process consisted of 400 nm of Al deposition, lithography, wet etching, and stripping. The CVD growth was also performed by Emma Bore. The key lithography steps included:

- Resin Application: A mixture of VM652 and UV5 resins was applied to the wafer through spin coating during 60 seconds, with a spin rate of 2000 rpm/s.
- Soft Bake: The coated wafer underwent a soft bake process at 130°C for 90 seconds to ensure proper adhesion of the resin to the wafer surface.
- Insolation: Using MJB4 and a vacuum contact method, the wafer was exposed to light for 1.3 seconds to transfer the desired pattern.
- Post Bake: Following insolation, another bake at 130°C for 60 seconds was performed to solidify and finalize the pattern on the wafer.

The wet etching process was employed to selectively remove material from the wafer according to the pattern defined in the lithography step. The final step involved the removal of any remaining layers and residues through a stripping process, including acetone for 3 minutes, IPA (Isopropyl Alcohol) for a 1-minute immersion, and EDI (Electrodeionization) to ensure the complete removal of any remaining material.

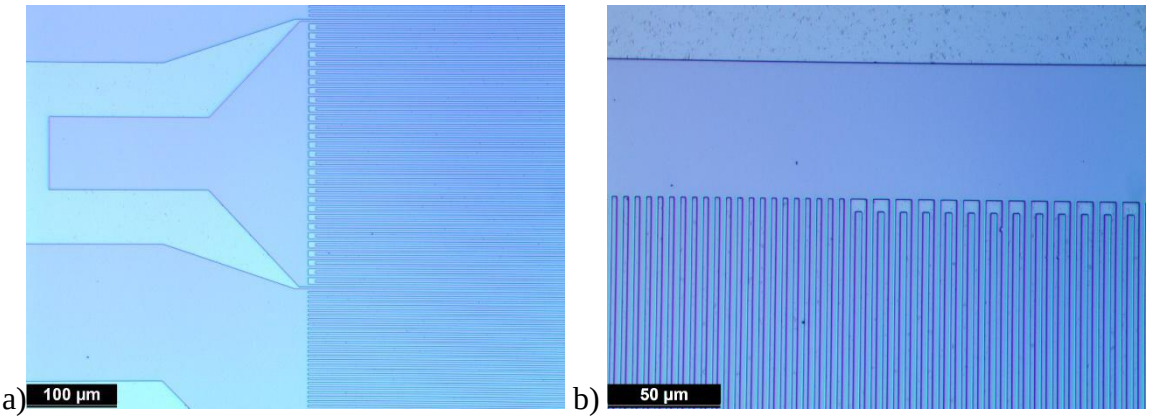

FIGURE 3.37 OPTICAL MICROSCOPIES OF PATTERNS AFTER LITHOGRAPHY ON THE WAFER C-1 WITH DIFFERENT MAGNIFICATIONS: (A) LOWER AND (B) HIGHER.

Following the lithography process, the patterns displayed appeared with clear defined walls in optical microscopy (example can be seen in Figure 3.37), so the overall lithographic procedure was successful and obtained structures can be presented as in Figure 3.38. Important

to mention is that the process and the mask were designed and optimized in CEA-Leti for $LiNbO_3$ layers done by Smart-cut POI technology.

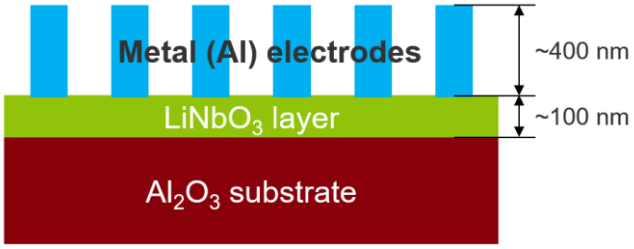

FIGURE 3.38 SCHEME OF THE OBTAINED STRUCTURES.

Unfortunately, none of the obtained structures showed the expected piezoelectric response and transfer characteristics commonly seen in SAW devices. An illustration of the obtained transfer characteristics can be seen in Figure 3.39. This outcome can be attributed to the thin piezoelectric layer deposited, which was approximately 100 nanometers, even prior to the lithography process. When compared to previously documented findings, functional SAW devices were created using a $LiNbO_3$ layer with a thickness of 300 nanometers, produced through sputtering and annealing on a diamond substrate [33]. Jie Zhu measured the thickness of the thin film layer on which polarization-electric field (P-E) measurements were conducted, and it was determined to be 400 nanometers [34]. Finally, it is possible to conclude that deposition of thicker layers is required for the fabrication of the SAW devices.

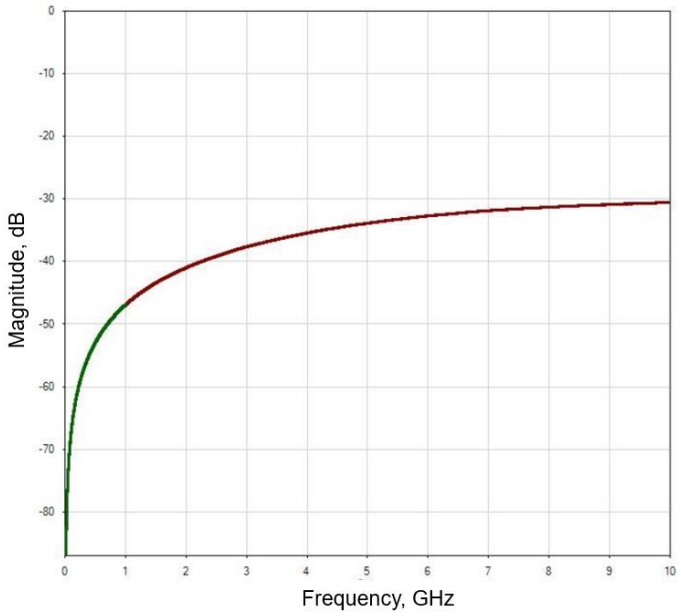

FIGURE 3.39 TRANSFER CHARACTERISTICS OF THE SAW DEVICE FABRICATED ON A-3 WAFER.

4. Conclusions on the study

In this research, we employed Pulsed Laser Deposition to achieve the epitaxial growth of $LiNbO_3$ thin films on Al_2O_3 substrates. Our studies covered a range of 4-inch substrates, including those with (0 0 1), (1 1 0), and (0 1 2) crystal orientations, with the primary aim of controlling the crystalline orientation of $LiNbO_3$ films. Additionally, we conducted research on a range of 2-inch substrates, including those with (1 0 0), (1 1 3), and (2 2 3) crystal orientations, with the primary objective of exploring the possibility of growing crystallographic planes not previously reported.

To achieve precise control over the crystallinity and chemical composition of the films, we systematically investigated various growth parameters. These parameters included substrate temperature, which was maintained at 500°C and 600°C, and a steady reduction of the substrate temperature after an initial stage at 600°C to establish a seed layer. We also examined different oxygen pressures, with values set at 0.2 and 0.007 mbar. Additionally, we explored variations in target composition, utilizing both stoichiometric $LiNbO_3$ and $Li_{1.1}NbO_{3.05}$ targets. Our research encompassed a comprehensive characterization of both the physical and chemical properties of the as-deposited layers, and we established correlations between these properties and the specific deposition conditions employed.

The structural properties of the as-grown $LiNbO_3$ layers were assessed through XRD (X-ray diffraction) analysis. We conducted θ-2θ measurements, both with and without a 0.5° ω-offset, as well as ω and φ measurements for all the wafers.

- θ-2θ measurements were performed to observe the crystal orientations of the grown layers. The orientations of $LiNbO_3$, $LiNb_3O_8$, and Al_2O_3 have been determined with reference to ICDD sheets: 00-020-0631 [29] for $LiNbO_3$ 04-013-9445 [30] for $LiNb_3O_8$, and 00-046-1212 [31] for Al_2O_3, as detailed in Appendix II.
- The disorientation of crystallites within the layer and the overall layer quality, with respect to a preferential growth plane, were examined through Rocking Curve analysis (ω scan).
- All φ measurements conducted for the layers grown on sapphire consistently reveal the epitaxial nature of the $LiNbO_3$ growth.

The surface morphology of the grown $LiNbO_3$ films was extensively analyzed using Atomic Force Microscopy (AFM). Each sample was meticulously examined with two scan sizes: 1 x 1 μm² and 5 x 5 μm². Additionally, Scanning Electron Microscopy (SEM) was employed for some of the wafers in the study.

Both AFM and SEM examinations did not identify any cracks in the layers for all of the wafers. However, they did detect the presence of grains on the layers. The surfaces of all the films are characterized by the presence of rounded grains. Additionally, due to the pulsed laser deposition process, some grains are visible. It's noteworthy that these grains are the primary source of surface roughness in the samples.

For the growth on Al_2O_3 substrates, epitaxial $LiNbO_3$ layers with a variety of main crystallographic orientations were achieved, including (0 0 1), (1 1 0), (1 0 0), (1 0 1), (0 1 2), (1 1 3), and (2 2 3).

Under all deposition conditions, it was observed that $LiNbO_3$ films grown on c-sapphire exhibited a strong (0 0 1) texture. The process involving a gradual reduction of the substrate temperature after an initial stage at 600°C to establish a seed layer resulted in the growth of the combinations of low-Li subphase (6 0 0) $LiNb_3O_8$ and (0 0 6) $LiNbO_3$. The presence of this secondary "parasitic" phase alongside $LiNbO_3$ leads to inferior physical properties compared to pure $LiNbO_3$ [5]. The growth of this subphase may have occurred due to low thermal energy in the film during the final stages of the deposition process, given that the final substrate temperature was 200°C. In all other deposition processes, epitaxial single-phased polyscystalline (0 0 6) $LiNbO_3$ layers were obtained. The deposition process conducted with a $Li_{1.1}NbO_{3.05}$ target at 600°C and 0.007 mbar (C-7) exhibited favorable crystalline properties, with symmetrical and asymmetrical ω measurements of 0.99° and 1.41°, respectively. Furthermore, the surface roughness was relatively low (RMS of 0.8 nm for the 5 x 5 μm² scan). Figure 3.37 provides a schematical illustration of the effects from changes in the deposition conditions on *c*-sapphire.

During the growth process on X-cut sapphire substrates, we observed a competition in growth between the (0 0 6) and (1 1 0) orientations. The process, which involved gradually reducing the substrate temperature after an initial stage at 600°C, resulted in the growth of a low-Li subphase (0 2 0) $LiNb_3O_8$. Achievement of the (1 1 0) main layer orientation, was only possible with $Li_{1.1}NbO_{3.05}$ target and obtained orientations in dependence with orientation are presented in the table below. The most favorable combination of low roughness (with a RMS

of 4.96 nm) and excellent crystalline quality, as demonstrated by the symmetrical RC of 0.43° was achieved using for the deposition made on X-cut Al_2O_3 substrates at 0.2 mbar and 500°C, using a $Li_{1.1}NbO_{3.05}$ target.

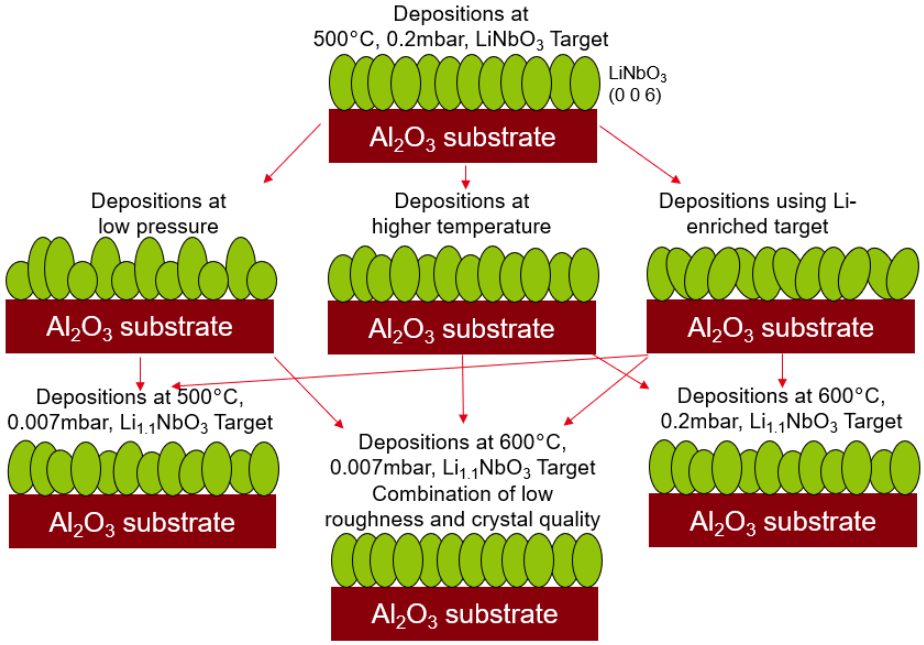

FIGURE 3.37 SCHEME OF THE DEPOSITION CONDITIONS EFFECTS ON GROWTH ON *C*-SAPPHIRE.

For the growth on *r*-sapphire substrates, a variety of $LiNbO_3$ main crystallographic orientations were achieved, including (1 1 0), (1 0 0), (1 0 1), and (0 1 2), as shown in the table above. The variations in main layer orientations observed among different samples indicate that by adjusting the deposition conditions on (0 1 2) Al_2O_3, it is possible to control the orientation of polycrystalline epitaxial thin films grown. The effects of such changes for *a*- and *r*-sapphire are summarized in Table 3.16.

Conditions			**$LiNbO_3$ layer orientation**	
Pressure, mbar	Temperature, °C	Target	Al_2O_3 (1 1 0)	Al_2O_3 (0 1 2)
0.2	500	$LiNbO_3$	(0 0 1)	(3 0 0)
0.007	500	$LiNbO_3$	(0 0 1)	(1 1 0)
0.2	600	$LiNbO_3$	(0 0 1)	(3 0 0)
0.2	600	$Li_{1.1}NbO_{3.05}$	(1 1 0)	(1 0 1)
0.007	500	$Li_{1.1}NbO_{3.05}$	(0 0 6)	(3 0 0)
0.2	500	$Li_{1.1}NbO_{3.05}$	(1 1 0)	(3 0 0)
0.007	600	$Li_{1.1}NbO_{3.05}$	(1 1 0)	(0 1 2)

TABLE 3.16 PRESENTATION OF LAYERS MAIN CRYSTALLOGRAPHIC ORIENTATION OBTAINED IN DEPENDENCE WITH VARIATIONS IN ASSOCIATED DEPOSITION CONDITIONS FOR (1 1 0) AND (0 1 2) AL_2O_3 SUBSTRATES.

Additionally, growth on *m*-, *n*-, and *v*-sapphire substrates resulted in the deposition of (1 0 0), (1 1 3), and (2 2 3) layers on 2-inch substrates. The RC values for these layers were approximately 1°, indicating a relatively good degree of orientation. Furthermore, the RMS roughness for all of the wafers was less than 1 nanometer, signifying relatively smooth surfaces.

SAW devices were fabricated and tested on layers grown on *c*- and *a*-sapphire wafers using a process that involved lithography, wet etching, and stripping. Regrettably, the resulting structures did not demonstrate the expected piezoelectric response and transfer characteristics. This is probably due to the low thickness of the piezoelectric layer deposited, about 100 nanometers, even before lithography. In comparison, successful SAW devices in previous studies used 300 nanometers thick $LiNbO_3$ layer [33]. In conclusion, depositing thicker layers is necessary for making effective SAW devices.

4.1 Comparison with previously reported results

First and foremost, it is crucial to note that we utilized 4-inch substrates for most of the depositions, which are larger than the wafers reported previously. Considering the substantial impact of the main layer orientation on both the surface and structural properties of the thin films, we propose a comparative analysis of these attributes in relation to these orientations. The table below provides such a comparison.

	Previously repoted		**Our result**	
Layer orientation	Crystal quality (RC), °	Roughness (RMS), nm	Crystal quality (RC), °	Roughness (RMS) 5x5 μm², nm
(0 0 1)	0.1 [11], [12]	0.7 [10]	0.78 (C-2)	0.8 (C-7)
(1 1 0)	0.3 [13]	No data	0.4 (A-6)	0.8 (A-6)
(0 1 2)	6.3 [2]	13.4 [2]	1.5 (R-7)	3.9 (R-7)
(1 0 0)	No data	No data	1.3 (R-3)	3.0 (R-5)
(1 0 1)	Growth was not reported before		4.6 (R-6)	16.2 (R-6)
(1 1 3)			1.2 (N-1)	0.72(N-1)
(2 2 3)			0.7 (V-1)	0.85(V-1)

TABLE 3.17 COMPARISON OF PROPERTIES OF LAYERS DEPOSITED BY PLD IN RELATION TO THEIR MAIN CRYSTALLOGRAPHIC ORIENTATION.

The majority of the reported layers were primarily focused on the growth of (0 0 1) films. This preference is justified by the tendency of $LiNbO_3$ films to orient their c-axis perpendicular to the smooth substrate surface [18]. However, it's worth noting that we were unable to attain the same level of crystal quality as reported by Lee (RC of 0.1°) [11] and by Balestrino (RC of 0.1°) [12]. Their better results could be attributed to different factors such as

preannealing of the substrate before deposition and a lower frequency of the laser (15 Hz), resulting in a lower flux for deposition. Our result (0.78°), was closer to the one reported by Laura Sauze (0.75°) [2]. On the other hand, the lowest roughness we achieved for this crystal cut was 0.68 nm, which is close to the value reported by G.-H. Lee (0.7nm) [10].

In the case of the X-cut $LiNbO_3$ layer, it is apparent that Gim et al. achieved slightly better crystal quality (with a Rocking Curve of 0.3°) [13] compared to our layer (0.4°). Regrettably, they did not provide any data concerning the surface properties of the film they deposited. The (0 1 2) layer presented by Laura Sauze [2] exhibited both lower surface and crystal quality compared to the ones reported in our study.

The growth of (1 0 1), (1 1 3), and (2 2 3) layers of $LiNbO_3$ by Pulsed Laser Deposition on sapphire substrates had not been reported before, making it challenging to directly compare these layers with previous studies.

Bibliography

[1] N. Courjal et al., «Lithium Niobate Optical Waveguides and Microwaveguides,» *Emerging Waveguide Technology,* 2018.

[2] L. Sauze, «Elaboration par PLD de couches de LiNbO3 sur substrats monocristallins,» chez *Élaboration et caractérisation de couches minces de LiNbO3 obtenues par pulvérisation cathodique et ablation laser pulsée*, Grenoble, Ecole Doctorale Polytechnique Hauts-de-France, 2022, pp. 117-127.

[3] A. Bartasyte, T. Baron, S. Oliveri, S. Margueron, P. Boulet, «Toward High-Quality Epitaxial LiNbO3 and LiTaO3 Thin Films for Acoustic and Optical Applications,» *Adv. Mater. Interfaces,* vol. 4, 2017.

[4] Zivasatienraj, B.; Tellekamp, M.B.; Doolittle, W.A., «Epitaxy of LiNbO3: Historical Challenges and Recent Success,» *Crystals* , n° %111, p. 397, 2021.

[5] Sánchez-Dena et al., «Lithium Niobate Single Crystals and Powders Reviewed—Part I,» *Crystals 10,* vol. 10, 2020.

[6] S. Kilburger et al., «Growth of LiNbO3 thin films on sapphire by pulsed-laser deposition for electro-optic modulators,» *Applied Surface Science,* vol. 253, n° %119, p. 8263–8267, 2007.

[7] Shibata et al, «Epitaxial growth of LiNbO3 thin films by excimer laser ablation method and their surface acoustic wave properties,» *Appl. Phys. Lett,* n° %161, p. 1000–1002, 1992.

[8] Yoshihiko Shibata, Kiyoshi Kaya, Kageyasu Akashi, et al., «Epitaxial growth and surface acoustic wave properties of lithium niobate films grown by pulsed laser deposition,» *Journal of Applied Physics,* vol. 77, 1995.

[9] Kakehi, Y.; Okamoto, A.; Sakurai, Y.; Nishikawa, Y.; Yotsuya, T.; Ogawa, S., «Epitaxial growth of LiNbO3 thin films using pulsed laser deposition,» *Applied Surface Science,* vol. 169–170, pp. 560-563, 2001.

[10] G.-H. Lee, «Role of substrate step bunches on the growth behavior of LiNbO3 hin film on a-Al2O3 substrate,» *Materials Science and Engineering B* , n° %1138, p. 41–45, 2007.

[11] G.H. Lee et al, «Effect of deposition flux on surface roughness of LiNbO3 thin film,» *Materials Science and Engineering,* n° %195, pp. 137-140, 2002.

[12] G. Balestrino et al., «Epitaxial LiNbO3 thin films grown by pulsed laser deposition for optical waveguides,» *Appl. Phys. Lett,* vol. 78, n° %19, p. 1204–1206, 2001.

[13] Gim et al, «Growth of LiNbO3 films on single crystal sapphire substrates using pulsed laser deposition,» *Integrated Ferroelectrics,* vol. 25, n° %11-4, pp. 91-102, 2006.

[14] H.K Lam et al., «Orientation controllable deposition,» *Journal of Crystal Growth,* vol. 268, n° %11–2, pp. 144-148, 2004.

[15] S-H Lee et al., «Control of epitaxial growth of pulsed laser deposited LiNbO3 films and their electro-optic effects,» *Appl. Phys. Lett.,* vol. 68, p. 472–474 , 1996.

[16] J. Y. Dai, H. K. Lam, Q. Li, J. Wang, H. L. W. Chan, and C. L. Choy, «Structural characterization and electron-energy-loss spectroscopic study of pulsed laser deposited LiNbO3 films on a-sapphire,» *Journal of Applied Physics,* vol. 96, n° %111, pp. 6319-6322, 2004.

[17] A. M. Marsh, S. D. Harkness, F. Qian, and R. K. Singh, «Pulsed laser deposition of high quality LiNbO 3 films on sapphire substrates,» *Appl. Phys. Lett.*, vol. 62, n° %19, p. 952–954, 1993.

[18] H. Matsunaga, H. Ohno, Y. Okamoto, and Y. Nakajima, «Heteroepitaxial growth of LiNbO3 single crystal films by ion plating method,» *Journal of Crystal Growth*, vol. 99, n° %11–4, p. 630–633, 1990.

[19] J. C. Vyas and S. G. Singh, «The negative thermal expansion coefficient in lithium niobate single crystals,» chez *presented at the SOLID STATE PHYSICS: PROCEEDINGS OF THE 57TH DAE SOLID STATE PHYSICS SYMPOSIUM 2012*, Bombay, 2013.

[20] Y. Shibata et al, «Strain Mechanism of LiNbO3/Sapphire Heterostructures Grown by Pulsed Laser Deposition,» *Japanese Journal of Applied Physics*, vol. 36, pp. 7344-7347, 1997.

[21] «Thermal expansion at elevated temperatures : 11. Aluminium oxide: experimental data between 100 and 800 K and their analysis,» *J. Phys. C: Solid State Phys.*, vol. 5, pp. 1046-1058, 1972.

[22] Z. Wu, W. Hu, J. Liu, M. Wang et Z. Liu, «Effects of substrate temperature on the growth of oriented LiNbO3 thin films by pulsed laser deposition,» *Materials Letters*, vol. 34 , n° %13–6, pp. 332-335, 1998.

[23] Wang et al., «Effects of oxygen pressure on the c-axis oriented growth of LiNbO3 thin film SiO2/Si substrate by pulsed laser deposition,» *Journal of Materials Science Letters* , vol. 3, pp. 225-227, 2003.

[24] Luca Indrizzi, Natacha Ohannessian, Daniele Pergolesi, Thomas Lippert, Elisa Gilardi, «Pulsed Laser Deposition as a Tool for the Development of All Solid-State Microbatteries,» *Helvetica Chimica Acta*, vol. 104, n° %12, pp. 1-25, 2020.

[25] S. Canulescu, E. L. Papadopoulou, D. Anglos, T. Lippert, C. W. Schneider, A. Wokaun, «Mechanisms of the laser plume expansion during the ablation of LiMn2O4,» *Journal of Applied Physics*, vol. 105, n° %16, p. 063107, 2009.

[26] Veignant, Franck ; Gandais, Madeleine ; Aubert, Pascal ; Garry, Guy, «Structural evolution of lithium niobate deposited on sapphire (0 0 0 1): from early islands to continuous films,» *Journal of Crystal Growth*, vol. 196, n° %11, pp. 141-150, 1999.

[27] Z. Vakulov, D. Khakhulin, A. Geldash, R. V. Tominov, V. S. Klimin, V. A. Smirnov, and O. A. Ageev, «Impact of laser pulse repetition frequency on nucleation and growth of LiNbO3 thin films,» *Journal of Advanced Dielectrics*, vol. 12, n° %12, p. 2160019, 2022.

[28] L. C. Sauze et al., «Homo-epitaxial growth of LiNbO3 thin films by Pulsed Laser deposition,» *Journal of Crystal Growth*, vol. 601, p. 126950, 2023.

[29] ICDD, «00-020-0631,» International Centre for Diffraction Data, 2020.

[30] ICDD, «04-013-9445,» International Centre for Diffraction Data, 2022.

[31] ICDD, «00-046-1212,» International Centre for Diffraction Data, 2020.

[32] V. Valvoda and M. Järvinen, «On The Harris Texture Index,» *Powder Diffraction*, vol. 5, n° %14, pp. 200-203, 1990.

[33] V. Edon, D. Rèmiens, S. Saada, «Structural, electrical and piezoelectric properties of LiNbO3 thin films for surface acoustic wave resonators applications,» *Applied Surface Science*, vol. 256, n° %15, pp. 1455-1460, 2009.

[34] J. Zhu, «Processing and Characterization of LiNbO3 Thin Films for Ferroelectric Nonvolatile Memory Applications,» Rice University, 2002.

Chapter 4: Growth on platinized silicon

Table of Contents

1. Introduction

In the previous chapters, we conducted a deposition process to grow thin films of $LiNbO_3$ on both $LiNbO_3$ and Al_2O_3 substrates. These layers, lacking a bottom electrode, hold potential utility in surface acoustic wave (SAW) applications. Our primary goal was to achieve homo- and heteroepitaxial growth of these thin films while addressing challenges related to chemical composition and structural defects, particularly cracks. To gain control over the film's crystallinity and chemical composition, we systematically investigated growth parameters such as substrate temperature, oxygen pressure, and target composition.

Surface Acoustic Wave (SAW) resonators are easier to make because they don't need a bottom electrode. This means only one etching step is needed for the top electrode. However, it is crucial to note that their characteristics, like bandwidth and resonant frequency, are not as good as resonators made for bulk acoustic wave (BAW) devices.

Creating a Bulk Acoustic Wave (BAW) resonator involves depositing layers of $LiNbO_3$ on a conductive substrate. Then, the upper electrode is deposited and etched. However, growing $LiNbO_3$ on a conductive metal layer, usually polycrystalline, can pose challenges, especially in controlling the chemical composition (stoichiometry).

The current chapter shifts its focus towards the PLD of thin $LiNbO_3$ layers, with a specific emphasis on using silicon-based substrates. Our research focuses on the growth of $LiNbO_3$ on silicon substrates, incorporating various buffer layers, including combinations of platinum (Pt) with titanium nitride (TiN), and with titanium oxide (TiO_2). The selection of buffer layer substrates is based on their compatibility with RF applications, particularly those involving bulk acoustic waves, and the potential use of specific buffer layers as bottom electrodes for BAW devices. In our initial experiments, we utilized a Pt electrode.

The process of growing thin films of $LiNbO_3$ on polycrystalline substrates is complicated, mainly because lithium atoms easily diffuse, leading to a potential decrease in the final stoichiometry of the layer [1]. This difficulty presents challenges in maintaining precise control over the chemical composition. The diffusion of lithium atoms in a polycrystalline layer is more noticeable compared to a monocrystals, such as sapphire and $LiNbO_3$ substrates [2], [3]. One way to address this issue is to increase the amount of Li ions in the plasma plume to compensate for both resputtering and diffusion into the substrate. Volk and Wöhlecke provided detailed insights into the Li shortage resulting from these factors [4]. A three-dimensional

diffusion mechanism of Li in $LiNbO_3$ was demonstrated in 2013 [5]. It's crucial to note that Li ions can act as charge carriers, so preventing their movement to the substrate is important (due to quite high mobility of Li ions, ionic conductivity is the dominant charge transport mechanism in $LiNbO_3$ films [6], [7]). The potential solution is to use buffer layers. Thin films deposited between the substrate and lithium niobate could be used with the aim of limiting the diffusion of lithium atoms and therefore reducing the proportion of non-stoichiometric phase [3]. The variety of previously reported buffers is limited, but there are still a few valuable results:

- Magnesium oxide (MgO) grown epitaxially on GaAs allowed to grow epitaxially Z-cut of $LiNbO_3$ with crystallographic properties improved compared to growth on GaAs without buffer layer [8];
- Zinc oxide was used several times. For example well crystallized and highly (0 0 1) oriented layer was grown on ZnO/sapphire heterostructure. Even the substrate itself was monocrystalline and no specific reduction of the Li diffusion was needed, conductive ZnO buffer layer was deposited and high conductivity (600 Sm^{-1}) of this layer was achieved [9]. $LiNbO_3$ films with *c*-axis orientation were also grown via RF magnetron sputtering on amorphous SiO_2/Si structure using ZnO buffer layer [10];
- Platinum (Pt) buffer layers were used to achieve (0 0 1) oriented lithium niobate on amorphous SiO_2/Si substrates [10]. Also, TiO_2 and Pt layers combination resulted into growth of textured $LiNbO_3$ layer oriented along (1 1 1) and (0 0 1) crystallographic planes, but the presence of a secondary phase ($LiNb_3O_8$) and random cracks on the surface were observed [3].
- Silica (SiO_2) amorphous buffer layer also allowed highly oriented growth of *c*-$LiNbO_3$ in order to be used in waveguiding applications [11];
- 2D molybdenum disulfide (MoS_2) was reported to be used as protective layer for anodes in Li–S batteries [12];

Also important to mention, that polycrystalline $LiNbO_3$ thin films directly on the Si(111) substrate via pulsed laser deposition were fabricated in order to be used for on-chip microdisk resonators fabrication, but no data about crystal or surface properties and Li-ions diffusion was reported [13].

Based on these structures reported we are going to use in our work combination of Pt electrodes and TiO_2 or TiN layers on the electrode's surface, to possibly limit the diffusion of

lithium on the one side and Li-enriched target ($Li_{1.1}NbO_{3.05}$) to increase the amount of Li ions in the plasma plume to compensate possible resputtering.

Our research primarily focuses on the investigation of the alignment, crystallographic characteristics, and surface properties of the layers. We will methodically analyze the microstructural attributes of the thin films as they are initially deposited, while considering different deposition parameters.

2. Presentation of the study

The primary objective of this study is to conduct a comprehensive investigation of the influence of operational parameters on the quality of the crystalline structure and surface roughness in deposited layers. To achieve this goal, we used the Solmates 8 in.-wafer-based SIP800 platform and employed the Pulsed Laser Deposition technique to grow $LiNbO_3$ films, with a thickness ranging between 150 to 200 nm, on platinized silicon substrates. The platinized layers were intended for use as electrodes.

The various stages involved in manufacturing these electrodes were done on the CEA-Leti platform. The properties of the materials used as buffer layers are grouped in the Table 4.1 bellow.

Material	**Lattice structure**	**Lattice constants, Å**	**Thermal expansion coefficient, × 10^{-6} K^{-1} (at 300°K)**
Pt	Cubic [14]	3.9 [14]	8.9 [15]
TiN	Cubic [16]	4.2 [16]	10.27 [17]
TiO_2	Tetragonal [18]	3.8 & 9.5 [18]	7.8 & 3.8 [19]

TABLE 4.1 PROPERTIES OF MATERIALS USED AS BUFFER LAYER

As in our previous studies described in Chapters 2 and 3, du ring the deposition process, laser ablation was employed, using a KrF excimer laser with a wavelength of 248 nm, operating at a frequency of 100 Hz and imparting an energy of 450 mJ.

In the same way as described in Chapters 2 and 3, we integrated two targets, to explore the consequential impact of the quantity of Li atoms in the target on the properties and characteristics of the deposited films. The first target demonstrated a stoichiometric composition of $LiNbO_3$, while the second target exhibited a Li-enriched composition, incorporating 10% Li_2O atoms in $LiNbO_3$. The investigation of these parameters would be incomplete without accounting for the temperature of the substrate during deposition and the oxygen pressure. As such, the substrate temperature was varied within the range of 500 to 600°C, while the oxygen pressure was adjusted in the range of 0.007 to 0.2 mbar.

2.1 Study of the influence of the substrate temperature and oxygen pressure

Similarly, to the methodology employed in Chapters 2 and 3, we systematically varied the substrate deposition temperatures within the prescribed range of 500°C to 600°C, as detailed in Table 4.1. The primary objective of this temperature investigation was to identify the most suitable deposition temperature for our PLD system, the Solmates 8-inch-wafer-based SIP800 platform, to align with the precise film requirements.

As demonstrated in previous chapters (specifically Chapters 2 and 3), changing the oxygen pressure has been shown to result in an higher deposition rate and the generation of more stoichiometric films. This phenomenon can be attributed to the stabilizing role of oxygen pressure, which facilitates the growth of $LiNbO_3$ films. Reducing pressure means that atoms have a bigger mean free path. This means heavier Nb atoms are less influenced by these collisions compared to lighter Li atoms. When reaching the layer, these Nb atoms carry significant kinetic energy, potentially displacing Li atoms (resputtering) and causing the formation of a low-Li phase. Conversely, the high kinetic energy of atoms can contribute to producing higher-quality films, where kinetic energy acts as an energy source for layer formation, similar to thermal energy. However, it is crucial to note that excessively high levels of oxygen pressure can also lead to the formation of secondary phases [20]. Our findings for depositions on $LiNbO_3$ and Al_2O_3 substrates (Chapters 2 and 3) are in alignment with the findings reported by Vakulov et al [21]. Their results demonstrated that the optimal conditions for the fabrication of LiNbO3 films were achieved at oxygen pressures of 10^{-2} mbar and 10^{-5} mbar [21].

Based on the information from previous research [21], and our experiments (referenced in Chapters 2 and 3), we changed the substrate deposition pressures. These adjustments varied from 0.2 to 0.007 mbar, as outlined in Table 4.1. The specific selection of these pressure values was also influenced by prior growth experiments on platinized silicon and sapphire, as conducted by Sauze et al., who operated the chamber at an oxygen pressure of 0.2 mbar [2], [3].

2.2 Study of the influence of the buffer material

The lithium niobate layers were deposited onto a conductive platinum layer. Platinum electrodes were selected for their ability to withstand high temperatures form the one side, and their lattice parameters closely matched to those of $LiNbO_3$, as described by Laura Sauze [3]. Unfortunately, platinum (Pt) tends to separate from silicon dioxide (SiO_2). To address this issue, either titanium oxide (TiO2) or titanium nitride (TiN) is employed as an adhesion layer between Pt and the oxide in different experiments.

It's worth noting that the growth of the platinum layer might be influenced by the presence of the lower TiN layer, given their mesh compatibility and similar cubic structure. Consequently, this interaction could promote the texture of the platinum layer. The necessity of such layers was also shown by Laura Sauze [3].

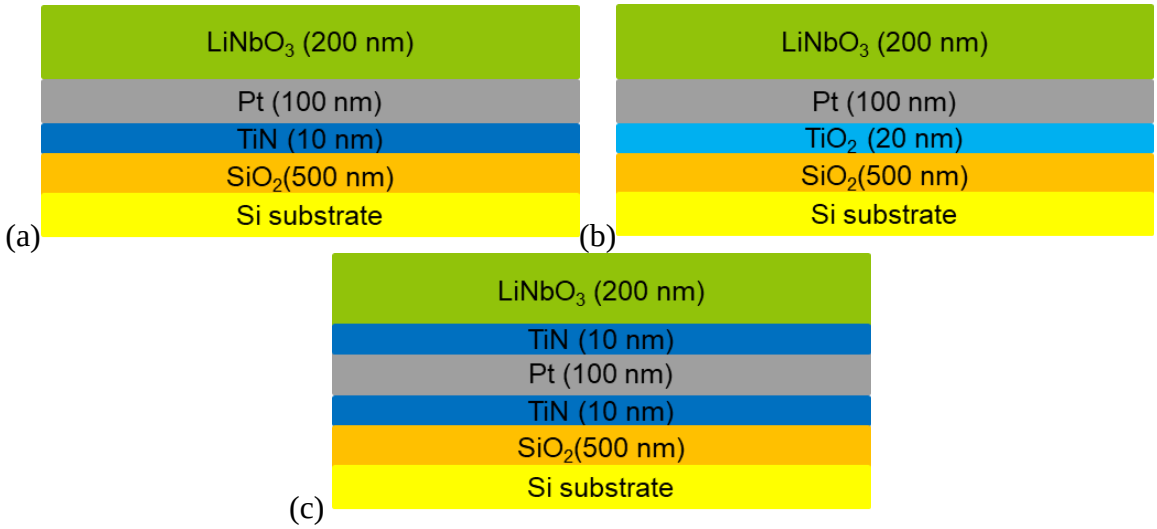

FIGURE 4.1. STACKS EMPLOYED TO INVESTIGATE THE DEPOSITION OF $LiNbO_3$, WITH A FOCUS ON ASSESSING CRYSTALLOGRAPHIC AND SURFACE PROPERTIES.

$LiNbO_3$ layers of 200 nm thickness were deposited by PLD on the Pt electrodes with various buffer layers. Different structures were created:

- $LiNbO_3$ / Pt / TiN / SiO_2/ Si
- $LiNbO_3$ / Pt / TiO_2 / SiO_2/ Si
- $LiNbO_3$ / TiN / Pt / TiN / SiO_2/ Si.

Wafer ID	Buffer layer	Pressure (mbar)	Temperature (°C)	Target
P-1	Pt (100 nm) / TiN (10 nm)	0.2	500	$LiNbO_3$
P-2	Pt (100 nm) / TiN (10 nm)	0.007	500	$LiNbO_3$
P-3	Pt (100 nm) / TiN (10 nm)	0.2	500	$Li_{1.1}NbO_{3.05}$
P-4	Pt (100 nm) / TiN (10 nm)	0.007	500	$Li_{1.1}NbO_{3.05}$
P-5	TiN (10 nm) / Pt (100 nm) / TiN (10 nm)	0.2	500	$LiNbO_3$
P-6	Pt (100 nm) / TiO_2 (20 nm)	0.2	500	$LiNbO_3$
P-7	Pt (100 nm) / TiO_2 (20 nm)	0,2	500	$Li_{1.1}NbO_{3.05}$
P-8	Pt (100 nm) / TiO_2 (20 nm)	0,007	600	$Li_{1.1}NbO_{3.05}$
P-9	Pt (100 nm) / TiO_2 (20 nm)	0,007	500	$Li_{1.1}NbO_{3.05}$
P-10	Pt (100 nm) / TiO_2 (20 nm)	0,2	600	$Li_{1.1}NbO_{3.05}$

TABLE 4.2 PRESENTATION OF SAMPLES WITH VARIATIONS IN ASSOCIATED DEPOSITION CONDITIONS.

The different stages related to the production of these electrodes were carried out on the CEA-Leti platform. In conclusion, through the amalgamation of diverse deposition conditions and buffer layers, it becomes achievable to carefully examine the properties of the as-deposited thin films in relation to the deposition parameters. Table 4.2 compiles the different adjustments made to deposition parameters according to the samples.

3. Characterization and analysis

First and foremost, the measurement of film thickness homogeneity after deposition was carried out utilizing ellipsometry. This analysis showed a remarkable thickness uniformity of 98%, pointing the promising capabilities of PLD for the industrial deposition of $LiNbO_3$ films. Film thickness uniformity in this case refers to the consistency of the thickness of a thin film across its entire surface. In the case of the PLD system employed on Solmates 8 in.-wafer-based SIP800 platform, it can be increased even more.

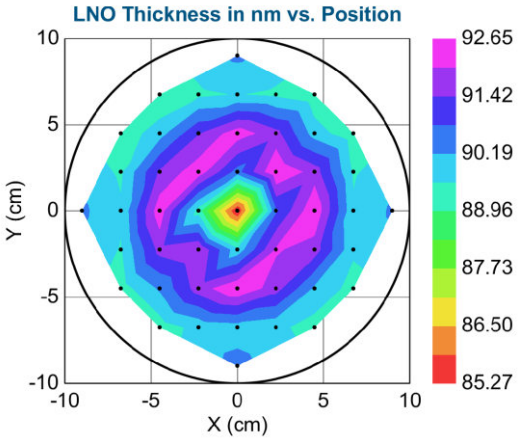

FIGURE 4.2 THICKNESS MAP MEASURED BY ELLIPSOMETRY OF A 300 MM DIAMETER SI WAFER WITH 100NM $LiNbO_3$ FILM DEPOSITED.

The structural properties of the as-grown $LiNbO_3$ layers were evaluated using XRD analysis in the same way for sapphire heterostructures in Chapter 3, which included:

- Out-of-plane texture (growth orientation) and potential presence of secondary phases: A symmetrical scan in the Bragg-Brentano configuration was performed using a PANalytical® EMPYREAN goniometer to investigate the out-of-plane texture and the potential presence of secondary phases. θ-2θ measurements were performed on all wafers with and without a 0.5° ω-offset to minimize the contribution of the substrate and Pt layer. The orientations of the $LiNbO_3$, TiN, TiO_2, Pt, and Si phases were determined using the following ICDD sheets: 00-020-0631 [22] for $LiNbO_3$, 00-038-1420 [16] for TiN, 00-021-1272 [18] for TiO_2, 00-004-0802 [14] for Pt, 00-026-1481 [23] for Si. The texture degree was calculated in the same way as in Chapter 3.
- Crystallite Disorientation and Layer Quality: Rocking curve analysis (ω scan) was performed to examine the disorientation of crystallites within the layer and the overall layer quality, especially regarding preferential growth planes.

- Azimuth Scans (φ scans) were conducted, but no epitaxial layers were identified, as there was an amorphous SiO_2 layer measuring 500 nm within the stack.

The surface morphology of the as-grown $LiNbO_3$ films was investigated using AFM and SEM. AFM measurements were performed to explore the surface morphology of the $LiNbO_3$ films (same as in Chapters 2 and 3). Each sample was scanned at two different sizes: 1 x 1 µm² and 5 x 5 µm². To accurately quantify the surface roughness characteristics of the $LiNbO_3$ films, a root mean square (RMS) roughness analysis was performed over the entire AFM image, as in Chapters 2 and 3. SEM observations were performed to investigate the film thickness, surface morphology, and structure variations in the thickness of the films between different cutting planes. The layers were examined using a ZEISS®-MERLIN instrument with 2 kV secondary electron imaging in both slice view (cross-section) and top view.

Piezoresponse force microscopy (PFM) was used to capture images of domains on the wafers where domains were suspected based on the surface structures observed in AFM and SEM. The primary goal was to identify these domains, and if they were indeed present, to endeavor to manipulate them (switching) by applying a voltage to the sample.

3.1 Growth using TiN buffer layer

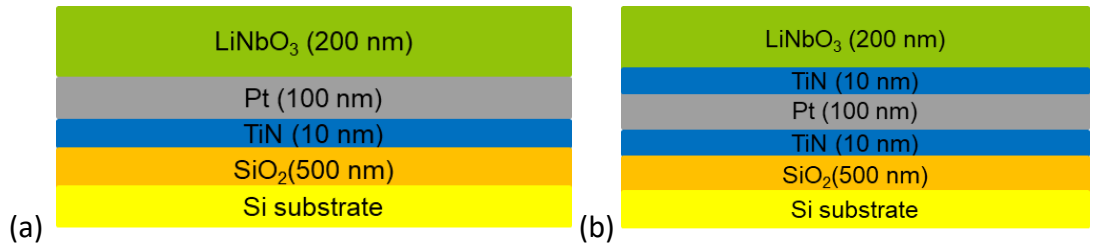

FIGURE 4.3 STACKS EMPLOYED TO INVESTIGATE THE DEPOSITION OF $LiNbO_3$ USING TIN BUFFER LAYERS.

First, $LiNbO_3$ films were deposited on Pt electrodes with TiN buffer layers. The goal was to obtain a layer with a (0 0 1) crystalline orientation, as the *c*-axis has the best piezoelectric properties. The stacks used to study the growth of $LiNbO_3$ on Pt/Si are shown in Figure 4.3. Table 4.3. compiles the adjustments made to deposition parameters according to the samples.

Wafer ID	Buffer layer	Pressure (mbar)	Temperature (°C)	Target
P-1	Pt (100 nm) / TiN (10 nm)	0.2	500	$LiNbO_3$
P-2	Pt (100 nm) / TiN (10 nm)	0.007	500	$LiNbO_3$
P-3	Pt (100 nm) / TiN (10 nm)	0.2	500	$Li_{1.1}NbO_{3.05}$
P-4	Pt (100 nm) / TiN (10 nm)	0.007	500	$Li_{1.1}NbO_{3.05}$
P-5	TiN (10 nm) / Pt (100 nm) / TiN (10 nm)	0.2	500	$LiNbO_3$

TABLE 4.3. PRESENTATION OF SAMPLES WITH VARIATIONS IN ASSOCIATED DEPOSITION CONDITIONS.

X-ray diffraction

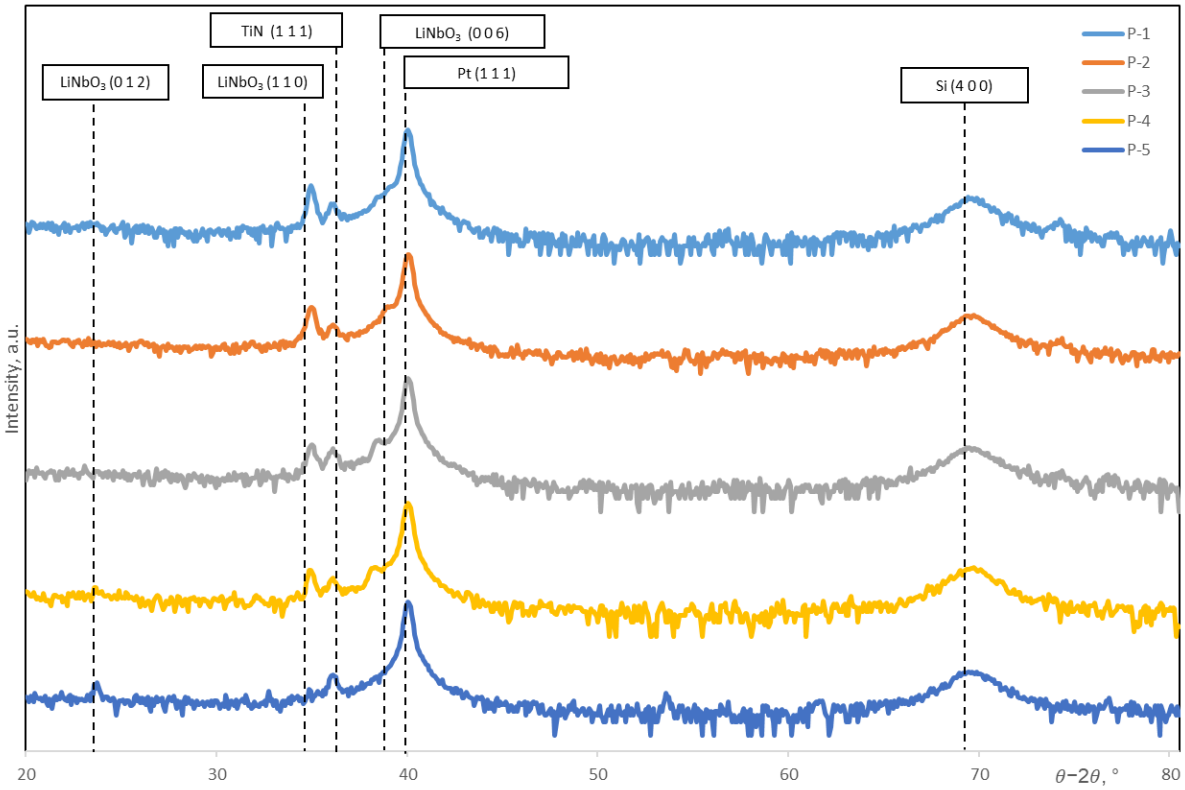

FIGURE 4.4. XRD Θ/2Θ SYMMETRICAL PATTERNS, WITH 0.5° Ω-OFFSET OF THE $LiNbO_3$ ON PLATINIZED SILICON HETEROSTRUCTURES WITH TIN BUFFER.

In the diagram bellow, θ-2θ measurements with a 0.5° ω-offset are presented for all the wafers after the deposition. The orientations of $LiNbO_3$, TiN, TiO_2, Pt and Si have been determined with reference to ICDD sheets: 00-020-0631 [22] for $LiNbO_3$, 00-038-1420 [16] for TiN, 00-004-0802 for [14] Pt, and 00-026-1481 [23] for Si, as detailed in Annex II. Symmetrical ω (rocking curve) measurements were performed to determine the broadening of the diffraction peaks. The broadening of the peaks can be attributed to mosaicity, which is a measure of the misorientation of crystallites within the sample. Azimuth scans (φ scans) were performed, but no epitaxial layers were observed due to a 500 nm amorphous SiO_2 layer in the stack.

The summary table presents XRD data for $LiNbO_3$ layers grown on Pt electrodes with TiN buffer layers under various deposition conditions. The rocking curve (RC) values for symmetrical measurements of most layers are higher than 5°, ranging from 5.7° to 7.6° depending on the sample. However, the RC for the growth performed on the TiN/Pt/TiN wafer (P-5) could not be fitted due to the very low signal intensity. Azimuth scans (φ scans) were performed, but no signal was detected, indicating that there were no epitaxial layers due to a 500 nm amorphous SiO_2 layer in the stack.

Wafer ID	Buffer layer	Pressure (mbar)	Temperature (°C)	Target	Main layer orientation	Texture Degree, %	RC, °
P-1	Pt (100 nm) / TiN (10 nm)	0.2	500	$LiNbO_3$	(0 0 6)	83	7.61
P-2	Pt (100 nm) / TiN (10 nm)	0.007	500	$LiNbO_3$	(0 0 6)	81	6.02
P-3	Pt (100 nm) / TiN (10 nm)	0.2	500	$Li_{1.1}NbO_{3.05}$	(0 0 6)	87	6.24
P-4	Pt (100 nm) / TiN (10 nm)	0.007	500	$Li_{1.1}NbO_{3.05}$	(0 0 6)	87	5.71
P-5	TiN (10 nm) / Pt (100 nm) / TiN (10 nm)	0.2	500	$LiNbO_3$	(0 1 2)	100	No data (signal is low)

TABLE 4.4. PRESENTATION OF THE SUMMARY THE XRD RESULTS FOR LAYERS GROWN ON TIN/PT/SI WAFERS WITH VARIATIONS IN ASSOCIATED DEPOSITION CONDITIONS.

The predominant layer orientation for most deposition conditions was (0 0 6) $LiNbO_3$. For the growth performed directly on TiN, the main crystallographic orientation was (0 1 2). Finally, the best combination of highest texture degree and lowest rocking curve was achieved for the layer grown on the Pt (100 nm)/TiN (10 nm) structure at 0.007 mbar and 500 °C using the Li-rich target (P-4). The texture degree was calculated in the same way as in Chapter 3. These results are in agreement with the tendency of $LiNbO_3$ films to align their c-axis perpendicular to the smooth substrate surface [18], and other reports about deposition on platinized silicon substrates [3], [10].

Atomic force microscopy

In order to investigate the surface topography of $LiNbO_3$ thin films deposited on platinized silicon layers with titanium nitride buffer layer, both AFM and SEM were used. The structural quality of the thin films deposited on Pt with a TiN underlayer is comparable for all four samples, whereas the film deposited on the TiN/Pt/TiN multilayer is markedly distinct. The effects of the underlayer and deposition conditions on the film surface roughness are being explored. AFM images of the deposited films are presented in Figures 4.5. and 4.6.

Figure 4.5 shows a compilation of AFM images obtained from 1 x 1 μm² scans of the deposited samples. All of these images clearly reveal the presence of grain crystal structures on the film surfaces, and these structures constitute the primary contributors to the observed surface roughness.

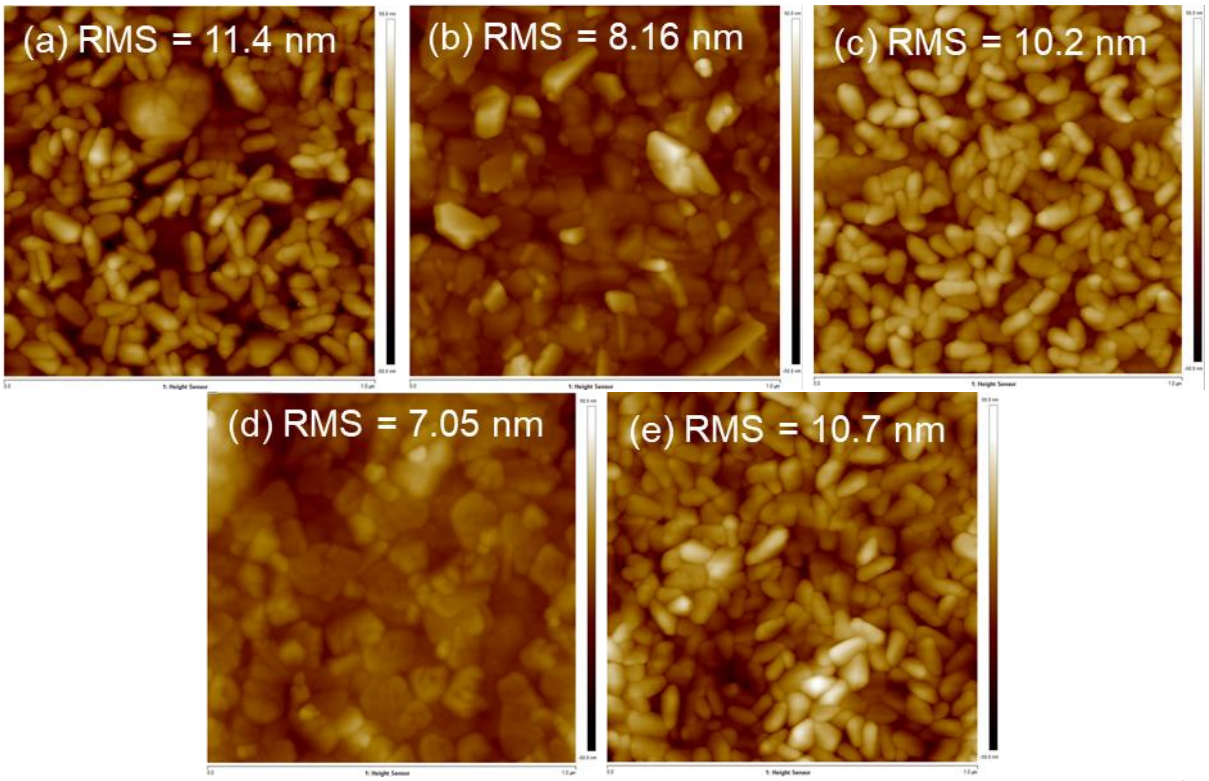

FIGURE 4.5. AFM MICROGRAPHS OF (A) P-1; (B) P-2; (C) P-3; (D) P-4; (E) P-5. SCAN SIZE: (1 × 1) μM^2.

It is notable that most of the film surfaces contain grains that are not oriented in a single direction. The RMS roughness is at its highest for the samples grown at 0.2 mbar and 500°C using a $LiNbO_3$ target (P-1). In contrast, the sample grown at 0.007 mbar and 500°C using a Li-enriched target exhibits the lowest surface roughness (P-4). Importantly, there is no significant difference in surface roughness between the layers deposited on the Pt/TiN and

TiN/Pt/TiN structures under the same conditions (P-1 and P-5), as illustrated in Figures 4.5(a) and (e). Figure 4.6. displays AFM images of the deposited samples obtained from 5 x 5 μm² scans. As with the images obtained from 1 x 1 μm² scans, all of these images also clearly show the presence of crystal structures and large grains on the film surfaces. These structures are the primary factors contributing to the notably high surface roughness, with RMS roughness values exceeding 10 nm. It is important to highlight that there is no significant difference in surface roughness between the thin films deposited on Pt with a TiN underlayer and the samples with a TiN/Pt/TiN multilayer configuration.

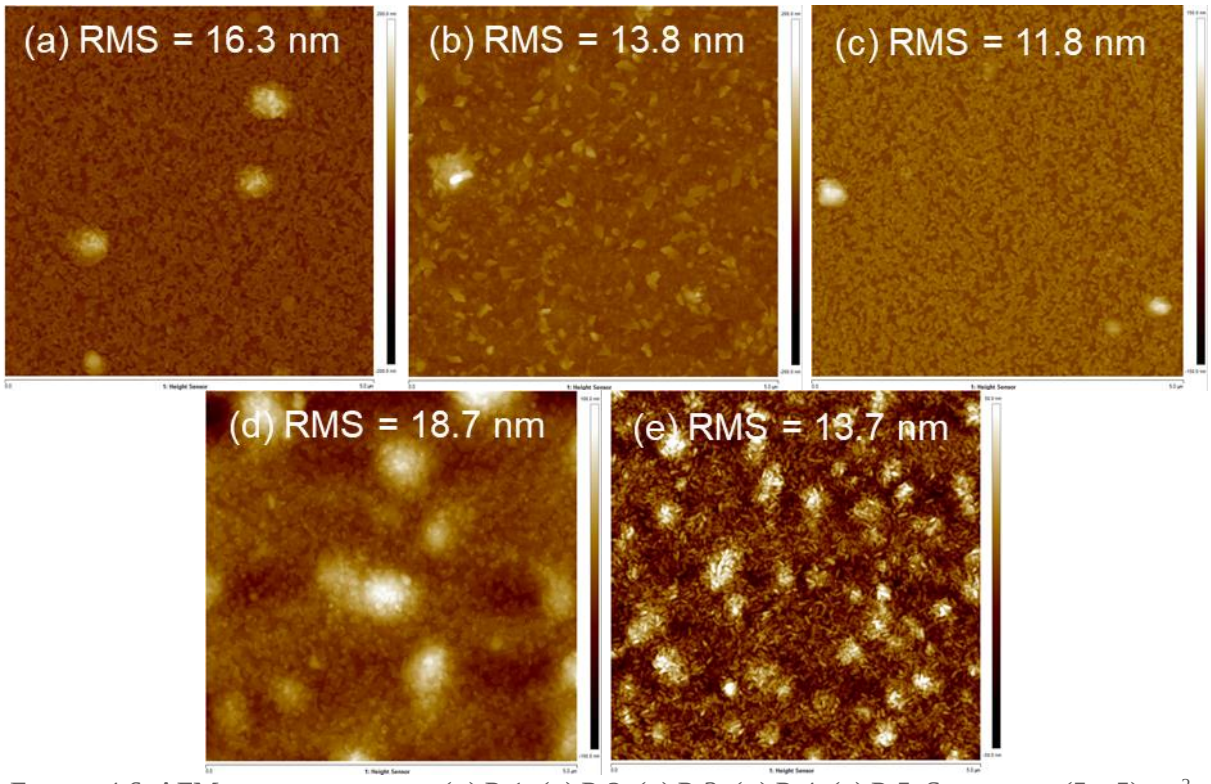

FIGURE 4.6. AFM MICROGRAPHS OF (A) P-1; (B) P-2; (C) P-3; (D) P-4; (E) P-5. SCAN SIZE: (5 × 5) μM^2.

Table 4.4. presents a compilation of results related to the surface properties observed in the AFM scans. It provides an overview of how these surface properties are influenced by various deposition conditions, including parameters such as oxygen pressure, buffer layer, and the quantity of Li in the target, particularly for depositions conducted on Pt/TiN structures. It is noteworthy that the RMS roughness values for all wafers exceed 10 nm, and there is no significant difference in terms of surface roughness among the thin films deposited under various conditions. Given that the film thickness is 200 nm, it is clear that these layers exhibit a high level of roughness.

Wafer ID	Buffer layer	Pressure (mbar)	Temperature (°C)	Target	RMS 1x1 µm², nm	RMS 5x5 µm², nm
P-1	Pt (100 nm) / TiN (10 nm)	0.2	500	$LiNbO_3$	11.4	16.3
P-2	Pt (100 nm) / TiN (10 nm)	0.007	500	$LiNbO_3$	8.16	13.8
P-3	Pt (100 nm) / TiN (10 nm)	0.2	500	$Li_{1.1}NbO_{3.05}$	10.2	11.8
P-4	Pt (100 nm) / TiN (10 nm)	0.007	500	$Li_{1.1}NbO_{3.05}$	7.05	18.7
P-5	TiN (10 nm) / Pt (100 nm) / TiN (10 nm)	0.2	500	$LiNbO_3$	10.7	13.7

TABLE 4.4. PRESENTATION OF THE SUMMARY THE AFM MEASUREMENTS FOR LAYERS GROWN ON PT/TIN/SI WAFERS WITH VARIATIONS IN ASSOCIATED DEPOSITION CONDITIONS.

Scanning electron microscopy

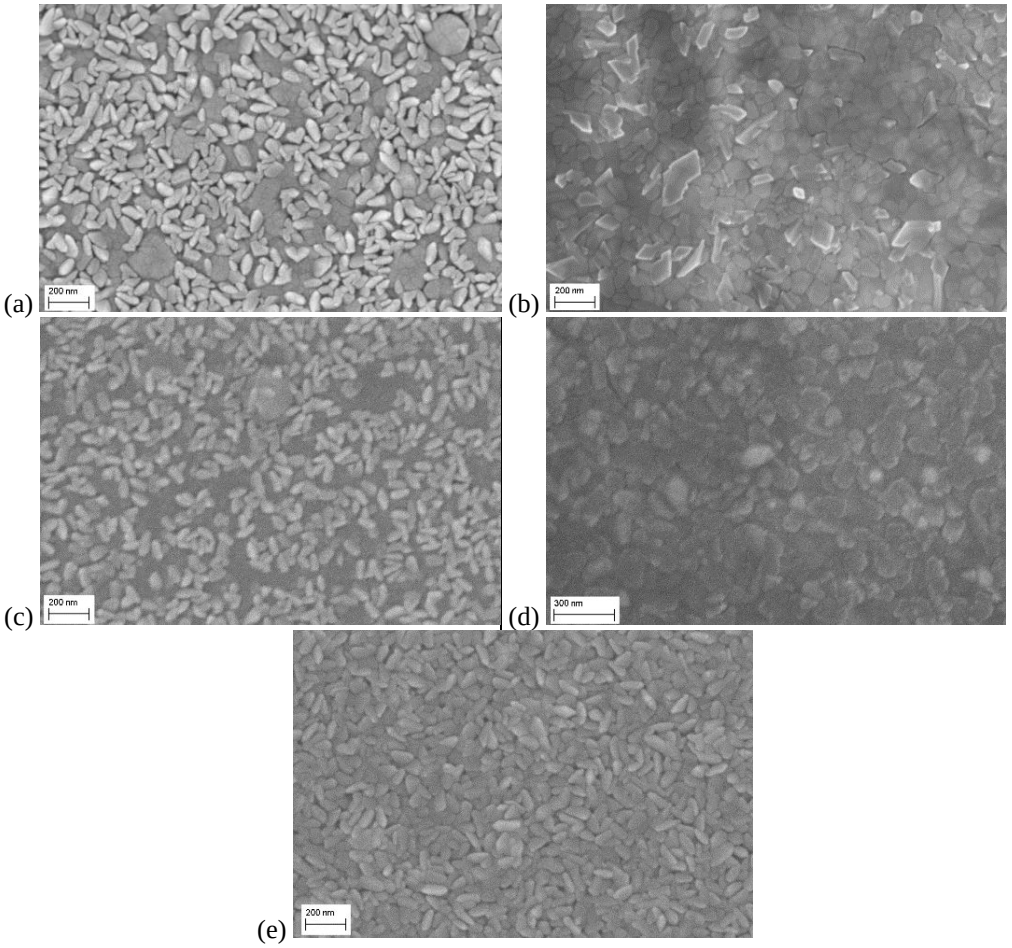

FIGURE 4.7. SEM OBSERVATION IN TOP-VIEW OF LAYERS OF $LiNbO_3$: (A) P-1; (B) P-2; (C) P-3; (D) P-4; (E) P-5.

SEM observations are conducted to investigate the layers in its thicknesses. The surface is coated with a 7.7 nm layer of carbon, and the layer is observed first from a top view and then at a 15° tilt for a more comprehensive analysis.

The surface state of the layers observed from a top view aligns with the findings from the AFM analysis. No cracks are evident, and the layers appear dense, composed of visible grains. Notably, two types of structures are observed: one type consists of "rice" grains (P-1, P-3, and P-5, all from wafers deposited at 0.2 mbar), while the other type is composed of larger crystals (P-2 and P-4, from wafers deposited at lower pressures). From the other side, these structural differences do not result in a significant enhancement of surface roughness.

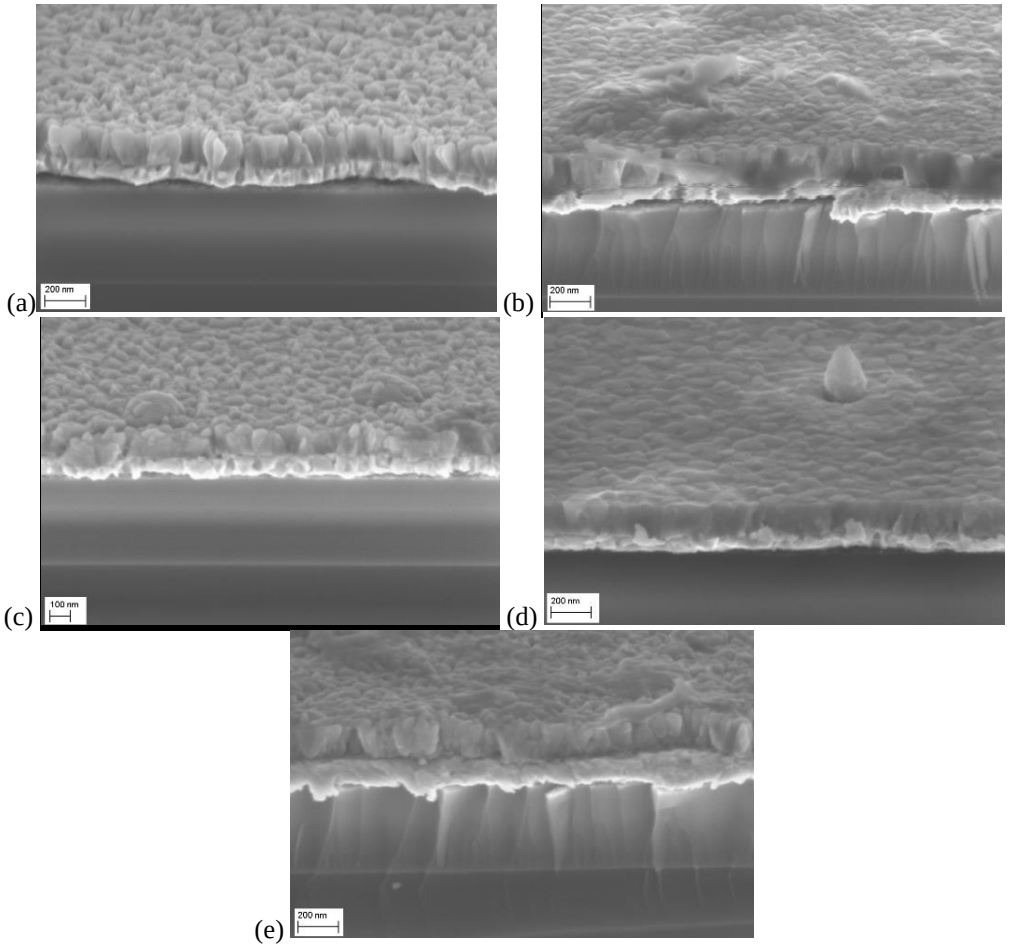

FIGURE 4.8. SEM OBSERVATION IN CROSS-SECTION INCLINED AT 15° OF LAYERS OF $LiNbO_3$: (A) P-1; (B) P-2; (C) P-3; (D) P-4; (E) P-5.

The surface grains are lined up in columns, and the layer looks dense near the substrate. However, it's difficult to see the layer clearly due to the buildup of electric charges on the surface and in the thickness of the piezo layer, even when using a carbon coating.

Piezoresponse force microscopy

Piezoresponse force microscopy (PFM) was utilized to image domains, which were suspected based on the surface structures observed in AFM and SEM. The primary objective was to identify these domains and, if they were indeed present, to attempt their manipulation (switching) by applying a voltage to the sample. This process facilitated the measurement of the resulting change in the polarization state, as ferroelectric domains typically exhibit two non-zero spontaneous polarization states that can be reversed by the application of an external electrical field.

(a) 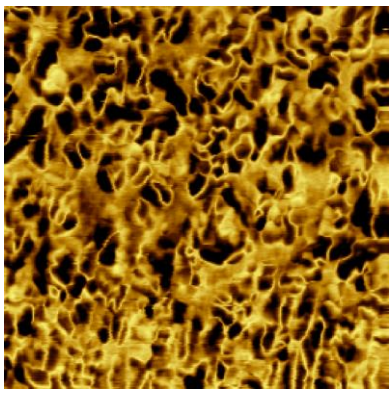 (b) 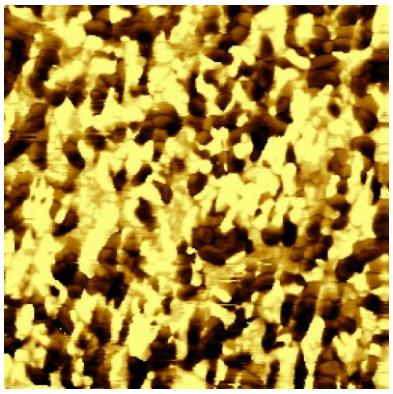

FIGURE 4.9. (1 × 1) μM^2 PFM OBSERVATIONS IN AMPLITUDE (A) AND PHASE (B) MODES FOR THE WAFER DEPOSITED AT 0.007 MBAR, 500°C, $LI_{1.1}NBO_{3.05}$ TARGET ON PT/TIN (P-4).

Clear and distinct ferroelectric domains with well-defined domain walls, observable as bright lines in the amplitude image, were identified in the highly polycrystalline layer, thereby validating the observations made through XRD and SEM. The phase image predominantly exhibited "bright" domains. Regrettably, the amplitude of the domains was not uniform due to the polycrystalline structure of the layer.

Efforts to switch these domains proved unsuccessful, even at voltage levels of up to ±10 V. Furthermore, the layer experienced degradation following the application of ±9 V. This degradation could be attributed to the Joule effect and/or surface oxidation, as evidenced by the presence of a hillock after the voltage application.

Summary

For growth of $LiNbO_3$ on Pt electrodes with TiN buffer layers, it's important to note that the appearance of the deposited layer is greatly influenced by specific deposition conditions, including the temperature, oxygen pressure, and the composition of the target material. In all deposition processes, we obtained highly oriented polycrystalline layers, and there were no instances of a low-Li parasitic phase in any of the samples. Table 4.5 presents a compilation of characterization results with variations in associated deposition conditions.

Wafer ID	Buffer layer	Growth conditions (Pressure, Target)	Main layer orientation	Texturation Degree, %	RC, °	Roughness, RMS 5x5 μm², nm
P-1	Pt (100 nm) / TiN (10 nm)	0.2 mbar, $LiNbO_3$	(0 0 6)	83	7.61	16.3
P-2	Pt (100 nm) / TiN (10 nm)	0.007 mbar, $LiNbO_3$	(0 0 6)	81	6.02	13.8
P-3	Pt (100 nm) / TiN (10 nm)	0.2 mbar, $Li_{1.1}NbO_{3.05}$	(0 0 6)	87	6.24	11.8
P-4	Pt (100 nm) / TiN (10 nm)	0.007 mbar, $Li_{1.1}NbO_{3.05}$	(0 0 6)	87	5.71	18.7
P-5	TiN (10 nm) / Pt (100 nm) / TiN (10 nm)	0.2 mbar, $LiNbO_3$	(0 1 2)	100	No data (signal is low)	13.7

TABLE 4.5. PRESENTATION OF THE SUMMARY THE CHARACTERIZATION FOR LAYERS GROWN ON PT/TIN/SI WAFERS WITH VARIATIONS IN ASSOCIATED DEPOSITION CONDITIONS.

Azimuth scans (φ scans) were executed, but no periodicity of signal was detected, indicating the absence of epitaxial layers, primarily due to the presence of a 500 nm amorphous SiO_2 layer within the stack, which led to the growth of polycrystalline structures. The predominant crystallographic orientation for most deposition conditions was (0 0 6) $LiNbO_3$. However, for growth directly on TiN, the primary crystallographic orientation was (0 1 2), and it was also not possible to perform RC fitting for this layer. Ultimately, the most favorable combination, achieving the highest degree of texture and the narrowest rocking curve, was observed in the layer grown on the Pt (100 nm)/TiN (10 nm) structure at 0.007 mbar and 500°C using the Li-rich target (P-4).

Regarding the surface characteristics, all of the AFM and SEM measurements consistently revealed the presence of crystal structures and large grains on the film surfaces.

These structures were identified as the primary contributors to the notably high surface roughness, with RMS roughness values exceeding 10 nm. With a film thickness of 200 nm, it is evident that the layers are indeed characterized by a high level of roughness. Importantly, there was no significant difference in surface roughness between the thin films deposited on Pt with a TiN underlayer under different conditions and the samples with a TiN/Pt/TiN multilayer configuration.

Piezoresponse force microscopy (PFM) was employed to visualize domains, which were suspected based on the surface structures observed in AFM and SEM. The results indeed revealed clear and distinct ferroelectric domains with well-defined domain walls, observable as bright lines in the amplitude image, thereby corroborating the observations made through XRD and SEM. The phase image predominantly exhibited "bright" domains. Unfortunately, the amplitude of the domains was not uniform due to the polycrystalline structure of the layer. Efforts to switch these domains were unsuccessful, and the layer underwent degradation with voltages applied lower than required for polarization changes. This degradation could be attributed to the Joule effect and/or surface oxidation.

Our findings for the growth on Pt/ TiN/ SiO_2/ Si structures (P-1 – P-4) align with the typical behavior of $LiNbO_3$ films, which tend to orient their *c*-axis perpendicular to the smooth substrate surface [18]. On the other hand, we demonstrated the growth of (0 1 2) $LiNbO_3$ on TiN/Pt/TiN/SiO_2/Si (P-5). Despite the low crystal quality of the film (impossible to measure the RC because the signal was low), this specific orientation had not been reported previously.

Unfortunately, the growth on Pt/TiN structures was not reported before, but it is possible to compare our results with the growth on Pt/TiO_2: prior it was reported about growth of textured $LiNbO_3$ layer oriented along (0 0 1) crystallographic plane (RC of 13.8°) at 575°C, but the presence of a secondary phase ($LiNb_3O_8$) and random cracks on the surface were observed [3]. In our case, we avoided the parasitic phases formation and cracks, possibly due to lower temperature of the deposition (500°). Also, the crystal quality of the layer deposited by us is better, since the FWHM of the RC is twice less (7.6° - 5.7°).

3.2 Growth using TiO_2 buffer layer

$LiNbO_3$ films were deposited on Pt electrodes with TiO_2 buffer layers. The goal was to obtain a layer with a (0 0 1) crystalline orientation, as the c-axis has the best piezoelectric properties. The stacks used to study the growth of $LiNbO_3$ on Pt/Si are shown in Figure 4.10.

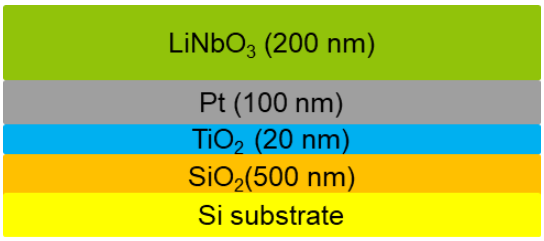

FIGURE 4.10. STACK EMPLOYED TO INVESTIGATE THE DEPOSITION OF $LiNbO_3$ USING TiO_2 BUFFER LAYER.

In summary, by combining various deposition conditions, it becomes possible to characterize the properties of the as-deposited thin films. Table 4.6 provides a summary of the various adjustments made to the deposition parameters for each sample.

Wafer ID	Buffer layer	Pressure (mbar)	Temperature (°C)	Target
P-6	Pt (100 nm) / TiO_2 (20 nm)	0.2	500	$LiNbO_3$
P-7	Pt (100 nm) / TiO_2 (20 nm)	0,2	500	$Li_{1.1}NbO_{3.05}$
P-8	Pt (100 nm) / TiO_2 (20 nm)	0,007	600	$Li_{1.1}NbO_{3.05}$
P-9	Pt (100 nm) / TiO_2 (20 nm)	0,007	500	$Li_{1.1}NbO_{3.05}$
P-10	Pt (100 nm) / TiO_2 (20 nm)	0,2	600	$Li_{1.1}NbO_{3.05}$

TABLE 4.6. PRESENTATION OF SAMPLES WITH VARIATIONS IN ASSOCIATED DEPOSITION CONDITIONS.

X-ray diffraction

In the diagram below, θ-2θ measurements with a 0.5° ω-offset are presented for all the wafers after deposition. The orientations of LiNbO3, TiO_2, Pt, and Si have been determined with reference to ICDD sheets: 00-020-0631 [22] for $LiNbO_3$, 00-021-1272 [18] for TiO_2, 00-004-0802 [14] for Pt, 00-026-1481 [23] for Si, as specified in Annex II. Symmetrical ω (rocking curve) measurements were carried out to assess the broadening of the diffraction peaks. This broadening of the peaks can be attributed to mosaicity, which serves as a measure of the misorientation of crystallites within the sample. Azimuth scans (φ scans) were conducted, but no epitaxial layers were observed due to the presence of a 500 nm amorphous SiO_2 layer in the stack, same as for layers grown on TiO_2.

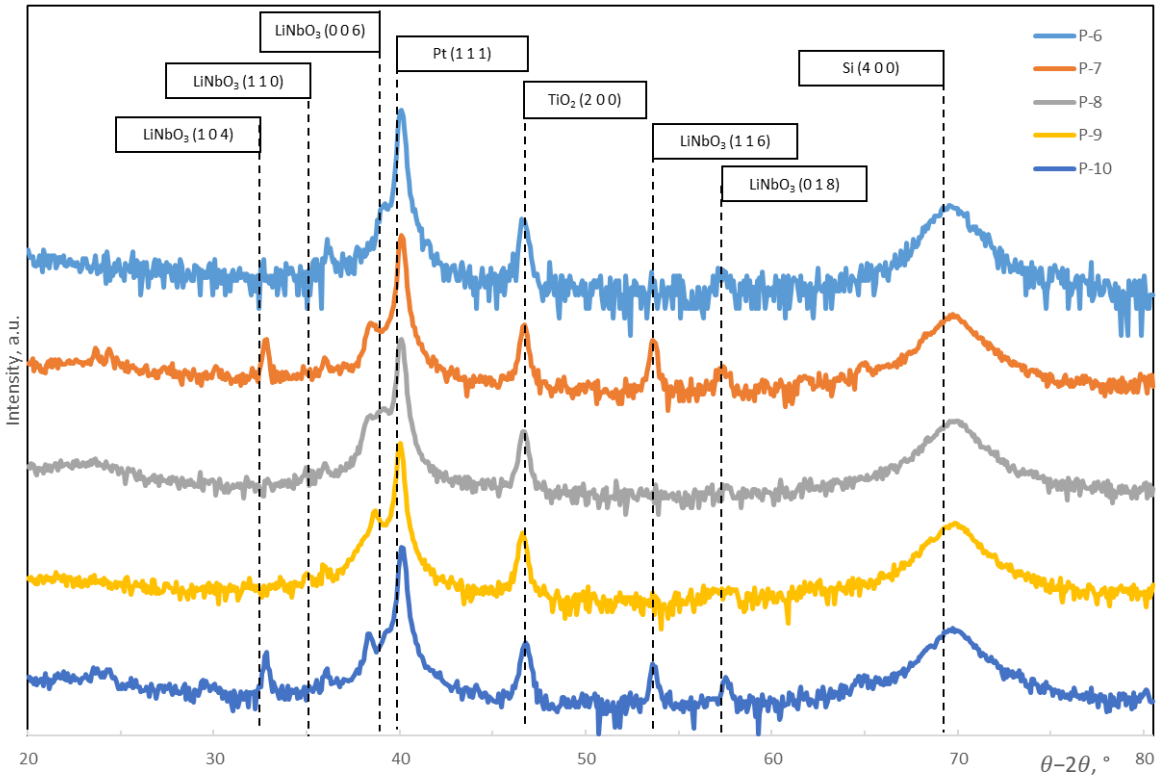

FIGURE 4.11. XRD Θ/2Θ SYMMETRICAL PATTERNS, WITH 0.5° Ω-OFFSET OF THE $LiNbO_3$ ON PLATINIZED SILICON HETEROSTRUCTURES WITH TiO_2 BUFFER.

The summary table presents XRD data for $LiNbO_3$ layers grown on Pt electrodes with TiO_2 buffer layers under various deposition conditions. The RC values for symmetrical measurements of layers are very high, ranging from 12.5° to higher than 20° depending on the sample. Azimuth scans (φ scans) were performed, but no signal was detected, indicating that there were no epitaxial layers.

Wafer ID	Pressure (mbar)	Temperature (°C)	Target	Main layer orientation	Texture Degree, %	RC, °
P-6	0.2	500	$LiNbO_3$	(0 0 6)	92	12.5
P-7	0.2	500	$Li_{1.1}NbO_{3.05}$	(0 0 6)	85	>20
P-8	0.007	600	$Li_{1.1}NbO_{3.05}$	(0 0 6)	99	13.9
P-9	0.007	500	$Li_{1.1}NbO_{3.05}$	(0 0 6)	99	14.2
P-10	0.2	600	$Li_{1.1}NbO_{3.05}$	(0 0 6)	90	>20

TABLE 4.7. PRESENTATION OF THE SUMMARY THE XRD RESULTS FOR LAYERS GROWN ON TiO_2/PT/SI WAFERS WITH VARIATIONS IN ASSOCIATED DEPOSITION CONDITIONS.

The predominant layer orientation for most deposition conditions was (0 0 6) $LiNbO_3$. Finally, the best combination of highest texture degree and lowest rocking curve was achieved for the layer grown on the Pt (100 nm)/TiO_2 (20 nm) structure at 0.007 mbar and 600 °C using the Li-rich target (P-8).

Atomic force microscopy

To explore the surface topography of $LiNbO_3$ thin films deposited on platinized silicon layers with titanium dioxide buffer layer, both AFM and SEM were used. The structural quality of the thin films deposited on Pt with a TiO_2 underlayer is comparable for all five samples. The effects of the deposition conditions on the film surface roughness are being explored. AFM images of the films using $Li_{1.1}NbO_{3.05}$ target are presented in Figures 4.12. and 4.13.

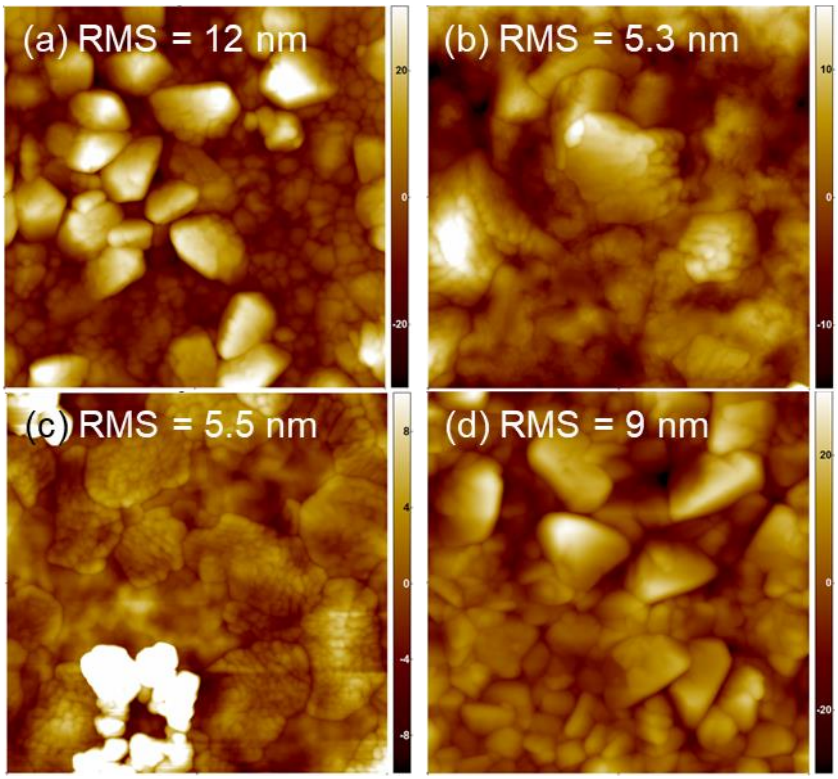

FIGURE 4.12. AFM MICROGRAPHS OF $LiNbO_3$ ON PT/TiO_2: A) P-7; (B) P-8; (C) P-9; (D) P-10. SCAN SIZE: (1 × 1) μM^2.

Figure 4.13. displays of AFM images obtained from 1 x 1 μm² scans of the deposited samples. In all these images, the presence of grain crystal structures on the film surfaces is clear, and these structures are the primary factors contributing to the observed surface roughness. Figure 4.14 presents AFM images of the deposited samples obtained from 5 x 5 μm² scans. Similar to the images acquired from 1 x 1 μm² scans, all of these images also clearly illustrate the presence of large grains on the film surfaces. These structures remain the primary contributors to the notably high surface roughness, with Root Mean Square (RMS) roughness values exceeding 10 nm.

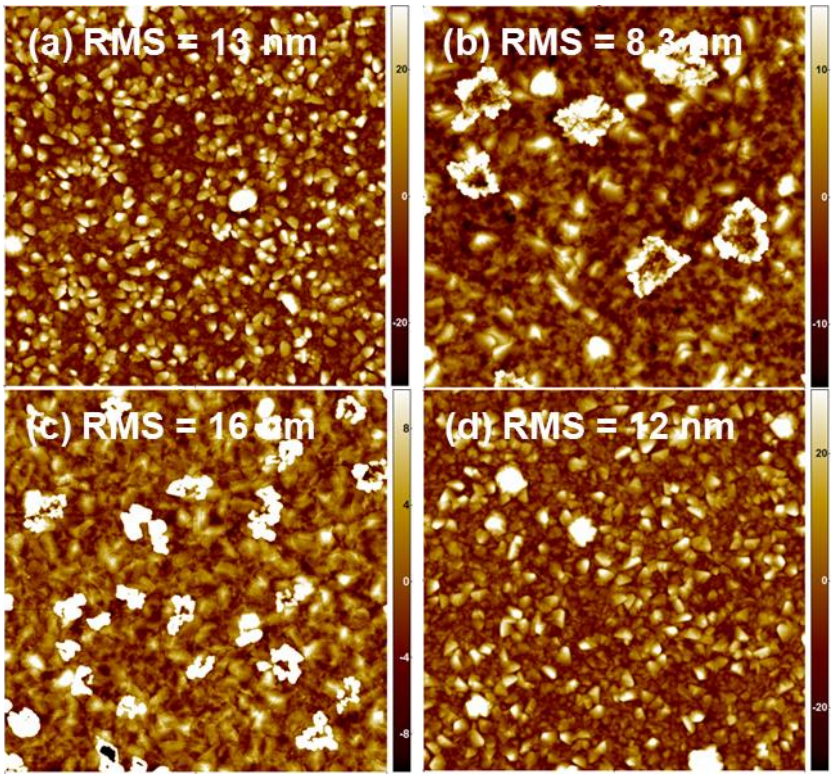

FIGURE 4.13. AFM MICROGRAPHS OF $LiNbO_3$ ON PT/TiO_2: A) P-7; (B) P-8; (C) P-9; (D) P-10. SCAN SIZE: (5 × 5) μM^2.

On the other hand, the layer deposited using a $LiNbO_3$ target exhibits lower roughness, and the surface characteristics differ. Figure 4.15 displays both (1 x 1) and (5 x 5) µm² AFM scans of the thin film deposited at 0.2 mbar and 500°C. These scans reveal the presence of crystal structures and some particles on the film surface. This is the main reason of the notably improved surface roughness, with RMS values lower than 4 nm. It's worth highlighting that this thin film displays the best surface roughness among the thin films deposited on silicon layer with Pt electrode and Ti-based underlayers.

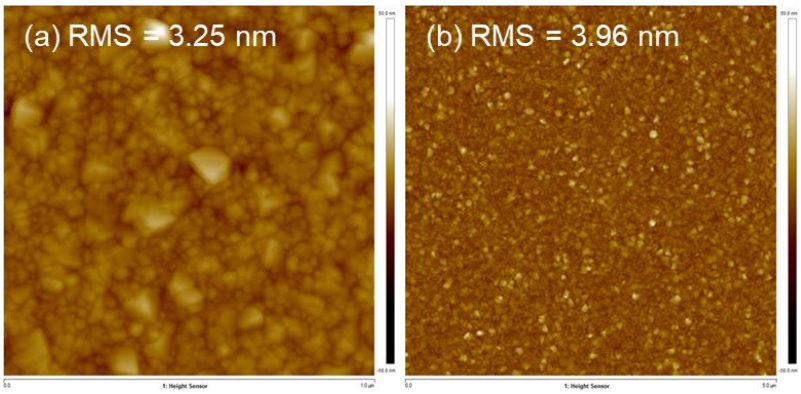

FIGURE 4.14. AFM MICROGRAPHS OF $LiNbO_3$ ON PT/TiO_2 (P-6). SCAN SIZES: (1 × 1) µM2 (A) AND (5 × 5) μM^2 (B).

ID	Buffer layer	Pressure (mbar)	Temperature (°C)	Target	RMS 1x1 µm², nm	RMS 5x5 µm², nm
P-6	Pt (100 nm) / TiO_2 (20 nm)	0.2	500	$LiNbO_3$	3.2	3.96
P-7	Pt (100 nm) / TiO_2 (20 nm)	0,2	500	$Li_{1.1}NbO_{3.05}$	12	13
P-8	Pt (100 nm) / TiO_2 (20 nm)	0,007	600	$Li_{1.1}NbO_{3.05}$	5.3	8.3
P-9	Pt (100 nm) / TiO_2 (20 nm)	0,007	500	$Li_{1.1}NbO_{3.05}$	5.5	16
P-10	Pt (100 nm) / TiO_2 (20 nm)	0,2	600	$Li_{1.1}NbO_{3.05}$	9	12

TABLE 4.8. PRESENTATION OF THE SUMMARY THE AFM MEASUREMENTS FOR LAYERS GROWN ON PT/TIO2/SI WAFERS WITH VARIATIONS IN ASSOCIATED DEPOSITION CONDITIONS.

Table 4.8. compiles the results related to the surface properties observed in the AFM scans. It offers an overview of how these surface properties are affected by various deposition conditions, including parameters such as oxygen pressure, and the quantity of Li in the target, specifically for depositions carried out on Pt/TiO_2 structures. It is worth noting that the RMS roughness values for almost all wafers deposited using Li-enhanced target exceed 10 nm. Given that the film thickness is 200 nm, it is evident that these layers exhibit a substantial level of roughness. On the other hand, thin film grown using a $LiNbO_3$ target display a significantly better surface state with RMS roughness lower than 4 nm.

Scanning electron microscopy

SEM observations are carried out to observe the layer deposited using a $LiNbO_3$ target (P-6) on the surface and in its thickness, particularly since this layer exhibits the lowest roughness. The surface is coated with a 7.7 nm layer of carbon, and the layer is initially observed from a top view. Subsequently, it is observed at a 15° tilt to observe in its thickness.

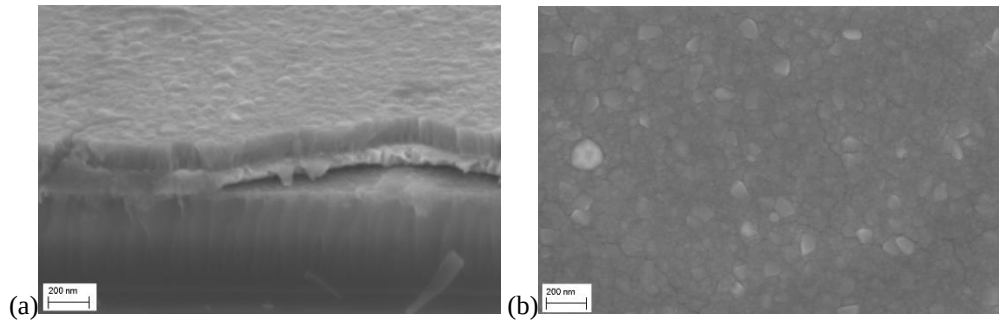

FIGURE 4.15. SEM OBSERVATION IN TOP-VIEW (A) AND IN CROSS-SECTION INCLINED AT 15° (B) OF P-6 WAFER.

Piezoresponse force microscopy

PFM was used to capture images of domains on the P-6 wafer, which were suspected based on the surface structures observed in AFM and SEM. The primary goal was to identify these domains and, if present, to try to switch them by applying a voltage to the sample.

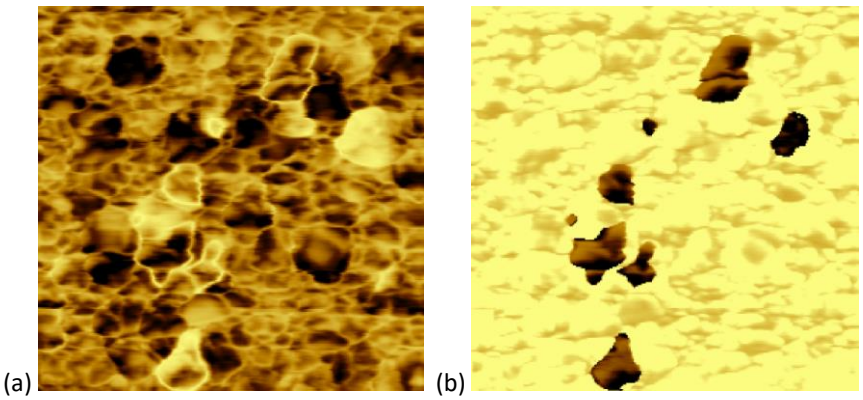

FIGURE 4.16. (1 × 1) μM^2 PFM OBSERVATIONS IN AMPLITUDE (A) AND PHASE (B) MODES FOR THE WAFER DEPOSITED AT 0.2 MBAR, 500°C, $LiNbO_3$ TARGET ON PT / TiO_2 (P-6).

Clear and distinct ferroelectric domains, with well-defined domain walls visible as bright lines in the amplitude image, were identified in the highly polycrystalline layer, confirming the observations made through XRD and SEM. The phase image predominantly displayed "bright" domains. Unfortunately, the amplitude of the domains was not uniform due to the polycrystalline structure of the layer.

Efforts to switch these domains were also unsuccessful, as observed in the wafers with a TiN buffer layer. The degradation experienced could be also attributed to the Joule effect and/or surface oxidation.

Summary

For growth of $LiNbO_3$ on Pt electrodes with TiO_2 buffer layers, it is important to note that the properties of the deposited layer are greatly influenced by specific deposition conditions. This includes factors such as temperature, oxygen pressure, and primarily, the composition of the target material. In all depositions, we achieved highly oriented polycrystalline layers, and no instances of a low-Li parasitic phase were observed in any of the samples. Table 4.9 provides a summary of characterization results with variations in associated deposition conditions.

In all the deposition processes, highly oriented polycrystalline layers were grown, and there were no low-Li parasitic phases observed in any of the samples. Although azimuth scans

(φ scans) were performed, no periodicity of the signal was detected, indicating the absence of epitaxial layers. This absence was primarily due to the presence of a 500 nm amorphous SiO_2 layer within the stack, resulting in the growth of polycrystalline structures. The predominant crystallographic orientation for all deposition conditions was (0 0 6) $LiNbO_3$.

ID	Pressure (mbar)	Temperature (°C)	Target	Main layer orientation	Texture Degree, %	RC, °	RMS 5x5 μm², nm
P-6	0.2	500	$LiNbO_3$	(0 0 6)	92	12.5	3.96
P-7	0,2	500	$Li_{1.1}NbO_{3.05}$	(0 0 6)	85	>20	13
P-8	0,007	600	$Li_{1.1}NbO_{3.05}$	(0 0 6)	99	13.9	8.3
P-9	0,007	500	$Li_{1.1}NbO_{3.05}$	(0 0 6)	99	14.2	16
P-10	0,2	600	$Li_{1.1}NbO_{3.05}$	(0 0 6)	90	>20	12

TABLE 4.9. PRESENTATION OF THE SUMMARY THE CHARACTERIZATIONS FOR LAYERS GROWN ON PT/TIO2/SI WAFERS WITH VARIATIONS IN ASSOCIATED DEPOSITION CONDITIONS.

Regarding the surface characteristics, all of the AFM and SEM measurements showed the presence of crystal structures and large grains on the film surfaces. These structures were identified as the primary contributors to the high surface roughness, with RMS roughness values of most of the layers exceeding 10 nm. With a film thickness of 200 nm, it is evident that the layers exhibit a high level of roughness. However, the layer deposited using a $LiNbO_3$ target displayed significantly lower roughness, and its surface characteristics differed considerably.

Piezoresponse force microscopy (PFM) was used to visualize domains on the wafer, which were suspected based on the surface structures observed in AFM and SEM. The results showed clear and distinct ferroelectric domains with well-defined walls. Unfortunately, efforts to switch these domains were unsuccessful, and the layer degradated with voltages applied lower than required for polarization changes. This degradation could be attributed to the Joule effect and/or surface oxidation.

Lithium niobate thin films deposited by us on $Pt/TiO_2/SiO_2/Si$ structures match how $LiNbO_3$ films usually aligns c-axis perpendicular to the smooth substrate surface [18]. Earlier, there were reports of growing a textured $LiNbO_3$ layer aligned along the (0 0 1) crystallographic plane (with an RC of 13.8°) at 575°C. However, it was noted that there was the presence of a secondary phase ($LiNb_3O_8$) and random cracks on the surface. [3]. In our depositions, no formation of the parasitic phases and cracks was observed. Additionally, the crystal quality of the layers we deposited is a little bit better, with the lowest FWHM of the RC of 12.5°.

4. Conclusions on the study

In this study, we employed Pulsed Laser Deposition to produce $LiNbO_3$ thin films on platinized silicon using Ti-based buffer layers. Three structural configurations were created:

- $LiNbO_3$ / Pt / TiN / SiO_2 / Si
- $LiNbO_3$ / Pt / TiO_2 / SiO_2 / Si
- $LiNbO_3$ / TiN / Pt / TiN / SiO_2 / Si

The structural properties of the as-grown $LiNbO_3$ layers were assessed using XRD, which included the following aspects:

- Out-of-plane texture (growth orientation) and potential presence of secondary phases: Highly oriented polycrystalline layers were obtained, and no low-Li parasitic phase was observed in any of the samples. The predominant crystallographic orientation for almost all deposition conditions was (0 0 6) $LiNbO_3$. However, for growth directly on TiN, the primary crystallographic orientation was (0 1 2), which was not reported before.
- Crystallite Disorientation and Layer Quality: Rocking curve analysis (ω scan) was performed to evaluate the disorientation of crystallites within the layer and the overall layer quality for all the wafers.
- Azimuth Scans (φ scans) were conducted, but no epitaxial layers were identified, mainly due to the presence of a 500 nm amorphous SiO_2 layer within the stack.

The best combination of achieving the highest texture degree and the lowest rocking curve values was observed in the layer grown on the Pt (100 nm)/TiN (10 nm) structure at 0.007 mbar and 500 °C using the Li-rich target (P-4). For layers grown with TiO_2 buffer, the rocking curve values for symmetrical measurements were significantly high, ranging from 12.5°, indicating lower crystal quality in the thin films. Another notable combination of high texture degree and low rocking curve values was found in the layer grown on the Pt (100 nm)/TiO_2 (20 nm) structure at 0.007 mbar and 600 °C using the Li-rich target (P-8). However, depositions on platinized silicon are resulting lower crystal quality and rougher surface when compared to growth on monocrystalline sapphire substrates, due to the presence of an amorphous SiO_2 layer in the stack.

It's essential to note the marked difference in the surface characteristics identified in the AFM and SEM measurements. For all films except those deposited using the $LiNbO_3$ target on the Pt/TiO_2 structure, crystal structures and larger grains were consistently observed. This

greatly contributed to the surface being rough, with roughness values higher than 10 nm (for layers of 200 nm thick). However, the layer deposited using the $LiNbO_3$ target on the Pt/TiO_2 structure stands out, displaying notably lower roughness with different surface characteristics.

The utilization of Piezoresponse Force Microscopy (PFM) allowed for the visualization of domains on the wafers. Clear and distinct ferroelectric domains were identified within the highly polycrystalline layers, featuring well-defined domain walls that were observable in the amplitude image. However, it's worth noting that the amplitude of these domains was not uniform, likely due to the polycrystalline structure of the layer. Despite these observations, attempts to switch or manipulate these domains were unsuccessful. The degradation experienced in these layers could be attributed to the Joule effect and/or surface oxidation, as indicated by the presence of hillocks after voltage application.

Integrating such layers into a bulk acoustic device (by simply depositing one more electrode on the top of the structure) could enable the analysis of resonance frequency and coupling coefficient. Also, FBAR device could be fabricated. However, there is still a need for optimizations. Firstly, additional experiments on depositions directly on TiN are required to confirm the growth on (0 1 2) $LiNbO_3$ and enhance the quality of the layer. For growth on Pt/TiN and Pt/TiO_2 structures, optimizations are necessary to improve the layer quality, facilitate domain switching without degrading the thin film, and gather information about the coercive field.

The optimizations to enhance quality could involve:

- Further refining the growth conditions, using 500°C as a reference. Also, two combinations of pressure and target could be used as references: 0.2 mbar, $LiNbO_3$ target for Pt/TiO_2 and 0.007mbar, $Li_{1.1}NbO_{3.05}$ target for Pt/TiN;
- Using targets with even more lithium compared to niobium. Shibata et al. got their best results with Li/Nb ratio 2.0, while ours were 1.1 and 1 [24].
- Exploring techniques such as rapid laser annealing for improvement of specific points of the thin film where there will devices done is also possible. From the other side annealing of full wafer, due to Pt later, could be not successful;
- Other materials like ZnO could be used as buffer layer to further promote c-axis growth of $LiNbO_3$ [3], [9].

4. Bibliography

[1] J. Rahn et al. , "Li self-diffusion in lithium niobate single crystals at low temperatures," *Physical chemistry chemical physics : PCCP,* vol. 14, pp. 2427-33, 2012.

[2] L. C. Sauze et al., "Homo-epitaxial growth of LiNbO3 thin films by Pulsed Laser deposition," *Journal of Crystal Growth,* vol. 601, p. 126950, 2023.

[3] L. Sauze, "Elaboration par PLD de couches de LiNbO3 sur substrats monocristallins," in *Élaboration et caractérisation de couches minces de LiNbO3 obtenues par pulvérisation cathodique et ablation laser pulsée,* Grenoble, Ecole Doctorale Polytechnique Hauts-de-France, 2022, pp. 117-127.

[4] Volk T and Wöhlecke M, Lithium Niobate: Defects, Photorefraction and Ferroelectric Switching, Berlin: Berlin: Springer, 2008.

[5] J. Rahn et al., "Li Diffusion in (110) Oriented LiNbO3 Single Crystals," *Defect and Diffusion Forum,* vol. 333, pp. 33-38, 2013.

[6] M. Graça et al., "Structural and dielectric characterization of LiNbO3 nano-size powders obtained by Pechini method," *Journal of Sol-Gel Science and Technology,* vol. 64, pp. 78-85, 2012.

[7] Perentzis et al., "Thermally activated ionic conduction in LiNbO3 electrolyte thin films," *Materials Science and Engineering: B,* vol. 108, no. 1-2, pp. 174-178, 2004.

[8] D. K. Fork & G. B. Anderson, "Epitaxial MgO on GaAs(111) as a buffer layer for z-cut epitaxial lithium niobate," *Applied Physics Letter,* vol. 63, no. 8, p. 1029–1031, 1993.

[9] S. Kilburger et al., "Properties of LiNbO3 based heterostructures grown by pulsed-laser deposition for optical waveguiding application," *Thin Solid Films,* vol. 518, no. 16, pp. 4654-4657, 2010.

[10] Shimizu, M et al., "Preparation and Optical Waveguide Properties of LiNbO3 Thin Films by RF Magnetron Sputtering," *Japanese Journal of Applied Physics,* vol. 32, no. 9, p. 4111–4114, 1993.

[11] Junhui He & Zhizhen Ye , "Highly C-axis oriented LiNbO3 thin film on amorphous SiO2 buffer layer and its growth mechanism," *Chinese Science Bulletin,* vol. 48, p. 2290–2294, 2003.

[12] E. Cha et al., "2D MoS2 as an efficient protective layer for lithium metal anodes in high-performance Li–S batteries," *Nature Nanotechnology,* vol. 13, no. 4, pp. 337-344, 2018.

[13] Li Zhang et al., "Microdisk resonators with lithium-niobate film on silicon substrate," *Optics Express,* vol. 27, no. 23, pp. 33662-33669, 2019.

[14] ICDD, "00-004-0802," 2021 International Centre for Diffraction Data, 1954.

[15] R. K. Kirby, "Platinum — A thermal expansion reference material," *Int J Thermophys,* vol. 12, p. 679–685, 1991.

[16] ICDD, "00-038-1420," 2021 International Centre for Diffraction Data, 1988.

[17] Z. H. Cen et al., "Temperature effect on titanium nitride nanometer thin film in air," *J. Phys. D: Appl. Phys,* vol. 50, no. 7, pp. 1-6, 2017.

[18] ICDD, "00-021-1272," 2020 International Centre for Diffraction Data, 1971.

[19] K.V.K. Rao et al., "Thermal Expansion of Rutile and Anatase," *J. Am. Ceram.,* vol. 50, pp. 124-126, 1970.

[20] Wang et al., "Effects of oxygen pressure on the c-axis oriented growth of LiNbO3 thin film SiO2/Si substrate by pulsed laser deposition," *Journal of Materials Science Letters ,* vol. 3, pp. 225-227, 2003.

[21] Z. Vakulov, D. Khakhulin, A. Geldash, R. V. Tominov, V. S. Klimin, V. A. Smirnov, and O. A. Ageev, "Impact of laser pulse repetition frequency on nucleation and growth of LiNbO3 thin films," *Journal of Advanced Dielectrics*, vol. 12, no. 2, p. 2160019, 2022.

[22] ICDD, "00-020-0631," 2020 International Centre for Diffraction Data, 1970.

[23] ICDD, "00-026-1481," 2021 International Centre for Diffraction Data, 1976.

[24] H. Matsunaga, H. Ohno, Y. Okamoto, and Y. Nakajima, "Heteroepitaxial growth of LiNbO3 single crystal films by ion plating method," *Journal of Crystal Growth*, vol. 99, no. 1–4, p. 630–633, 1990.

General conclusion and perspectives

This thesis was undertaken to advance the deposition process for thin layers of lithium niobate, specifically for applications in acoustic filtering. Due to its piezoelectric properties, $LiNbO_3$ has key features that make it well-suited for developing filters to meet the changing needs of advancing 5G technology.

However, achieving a single-phased and stoichiometric lithium thin film niobate through conventional deposition techniques presents notable challenges. To enhance filter performance, the deposited layer must meet strict criteria, including high crystallinity, with pure $LiNbO_3$ phase, and minimal surface roughness. Pulsed Laser Deposition was selected as the preferred method for $LiNbO_3$ deposition. Throughout this study, the focus was on growing thin films of lithium niobate with well-defined physicochemical properties, aiming for their potential use in acoustic wave devices.

The substrate material plays a foundational role for $LiNbO_3$ layer growth because it determines the possibilities for different applications from the one hand and has its own properties on the other. In our studies we obtained three kinds of thin films on different substrates (Figure 5.1):

- Epitaxial monocrystalline on $LiNbO_3$ of (1 1 0), (1 0 4), and (0 0 6) crystallographic orientations (Figure 5.1, a);
- Heteroepitaxial polycrystalline single-phased on Al_2O_3 with main crystallographic orientations: (0 0 1), (1 1 0), (1 0 0), (1 0 1), (0 1 2), (1 1 3), and (2 2 3) (Figure 5.1, b);
- Highly oriented polycrystalline layers on platinized silicon with (0 0 6) and (0 1 2) main crystallographic orientations(Figure 5.1, c);

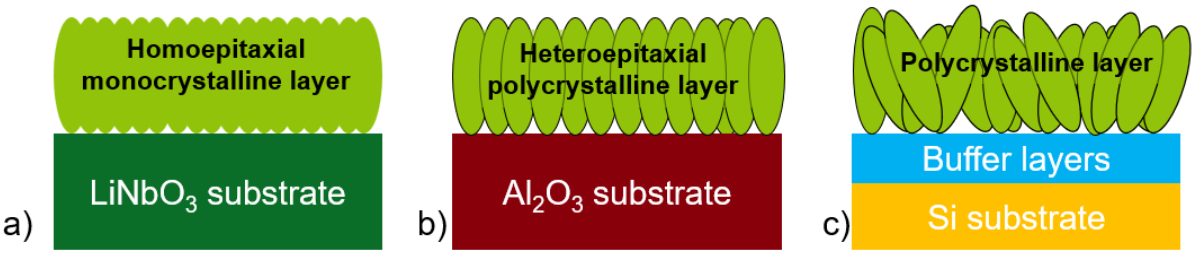

FIGURE 5.1 SCHEME OF THE DIFFERENT THIN FILMS GROWN.

The influence of deposition conditions, such as substrate, temperature, oxygen pressure, and target composition, on the microstructural properties of the layers was systematically analyzed.

The initial part of this research, discussed in chapter two, concentrated on characterizing thin films of $LiNbO_3$ grown on $LiNbO_3$ substrates. The goal was to achieve homoepitaxial growth with various crystallographic orientations. To manage film crystallinity and chemical composition, several growth parameters were explored, including substrate temperature, oxygen pressure, and target composition.

Various combinations of these parameters were tested to understand their impact on thin film growth. The results were summarized in a scheme for homoepitaxial growth, based on the following conclusions:

These parameters were applied in various combinations to highlight their effect on thin film growth. Finally, it is possible to summarize the effect of all deposition conditions for homoepitaxial growth into a scheme (Figure 5.1). This diagram is based on these conclusions:

- Oxygen pressure ranged from 0.2 to 0.007 mbar, resulting in negligible changes in surface roughness. However, at low pressure (0.007 mbar), deposited wafers, likely due to the resputtering during growth, were consisting from a mix of $LiNbO_3$ and a low-lithium phase. Depositions at 0.2 mbar consistently produced homoepitaxial monocrystalline layers.
- The substrate temperature ranged from 500 to 600°C. At 0.2 mbar pressure, homoepitaxial monocrystalline layers formed having similar crystal quality. With higher temperature, there was a slight increase in surface roughness due to more frequent formation of nanocrystalline grains on the surface, which is correlated with a bigger thickness of the final layer.
- Amount of lithium (Li) atoms in the plasma plume was varied by utilizing two different targets: $LiNbO_3$ and $Li_{1.1}NbO_{3.05}$. The utilization of the Li-enriched target resulted in an improvement of surface morphology, reducing the roughness.

As a result of this research, homoepitaxial monocrystalline layers with single phases were obtained: (1 1 0) for the X-cut substrate, (1 0 4) for the Y+128°-cut (previously not reported), and (0 0 6) for the Z-cut. Additionally, the surface roughness remained relatively small, ranging from 1 to 3 nm for layers with a thickness of 100 nm. In conclusion, the optimal

combination of deposition parameters appears to be 0.2 mbar for improved crystal quality, 600°C for enhanced deposition efficiency, and a Li-enriched target to decrease roughness.

In the next part of this research, discussed in chapter three, we look at $LiNbO_3$ layers deposited on monocrystalline sapphire substrates.

It's worth noting that, in most of our depositions, we used 4-inch substrates, which are bigger than what was typically reported before. By variating Al_2O_3 substrates orientations, heteroepitaxial single-phased polycrystalline $LiNbO_3$ layers with diverse main crystallographic orientations were grown, including (0 0 1), (1 1 0), (1 0 0), (1 0 1), (0 1 2), (1 1 3), and (2 2 3). AFM and SEM observations showed no signs of cracks in the layers for all the wafers. However, the presence of grains on the layers was identified. These grains constitute the primary source of surface roughness in the samples.

The growth of (1 0 1), (1 1 3), and (2 2 3) layers of $LiNbO_3$ using PLD on sapphire substrates had not been reported previously.

Different combinations of substrate temperature, oxygen pressure, and the composition of the target material were utilized to highlight their effect on thin film deposition (in the same way as for homoepitaxial growth) and for *c*-sapphire it is possible to conclude (for this comparison our reference conditions will be 0.2 mbar, 500°C, $LiNbO_3$ target):

- During depositions conducted at a pressure of 0.2 mbar, a consistent result was the formation of heteroepitaxial polycrystalline layers with good crystal quality (up to a symmetrical rocking curve of 0.87°). Reducing the pressure further improves crystal quality (symmetrical rocking curve of 0.78°), but it also raises the roughness of the layer unless other parameters are adjusted.
- Substrate temperature was very important factor and it ranged in most of the processes from 500 to 600°C. The process involving a gradual reduction of the substrate temperature to 200° after an initial stage at 600°C (to establish a seed layer) resulted in the growth of the combinations of low-Li subphase $LiNb_3O_8$ and $LiNbO_3$. Increasing the temperature without adjusting other parameters resulted only in higher film roughness without changes in crystallinity.
- Amount of lithium (Li) atoms in the plasma plume was varied in the same way as for homoepitaxial growth. Utilization of the Li-enriched target without changing other parameters led only to decrease in crystal structure.

- The most favorable combination of both low roughness (RMS of 0.8 nm) and good crystalline quality (symmetrical and asymmetrical Rocking Curve values of 0.99° and 1.41°, respectively) on Z-cut Al_2O_3 substrates was achieved using $Li_{1.1}NbO_{3.05}$ target, at 0.007mbar and 600°C.

During the growth process on *a*-sapphire substrates, we observed a competition in growth between the (0 0 6) and (1 1 0) orientations. Obtaining of the (1 1 0) main layer orientation, was only possible with $Li_{1.1}NbO_{3.05}$ target and the most favorable combination of low roughness (with a RMS of 4.96 nm) and excellent crystalline quality (RC of 0.43°), was achieved using for the growth at 0.2 mbar and 500°C.

For the growth on *r*-sapphire substrates, a variety of main crystallographic orientations were achieved, including (1 1 0), (1 0 0), (1 0 1), and (0 1 2). These variations indicate that by adjusting the deposition conditions on (0 1 2) Al_2O_3, it is possible to control the orientation of polycrystalline epitaxial thin films grown.

SAW devices were fabricated and tested on layers grown on *c*- and *a*-sapphire wafers using a process that involved lithography, wet etching, and stripping. Regrettably, the resulting structures did not demonstrate the expected piezoelectric response and transfer characteristics. This is probably due to the low thickness of the piezoelectric layer deposited, about 100 nanometers, even before lithography.

Controlling the growth orientation along various crystal planes is important to meet the requirements of various applications. For optical applications, layers oriented along the c-axis are predominantly utilized and represent the primary orientation achieved in thin layer growth growth [1], [2]. (1 1 0) and (1 0 0) oriented layers find application in surface acoustic wave devices. Additionally, more complex orientations, such as (1 0 1), (0 1 2), (1 1 3), and (2 2 3), can be also employed for SAW resonators.

In the final section, presented in the fourth chapter, our research focused on the growth of $LiNbO_3$ on silicon substrates, incorporating various buffer layers, including combinations of Pt with TiN and TiO_2. The choice of buffer layer substrates was guided by their compatibility with RF applications, especially those involving bulk acoustic waves, the possible application of these buffer layers as bottom electrodes for BAW devices.

Highly oriented polycrystalline layers were obtained, and no low-Li parasitic phase was observed. The predominant crystallographic orientation of the layer grown on most of the buffers was (0 0 6) and for growth on TiN, it was (0 1 2).

The optimal crystal properties were observed in the layer grown on the Pt/TiN structure at 0.007 mbar and 500°C using the Li-rich target. This can be attributed to several factors in combination:

- First, at the temperature of 500°C differences in CTE coefficients between $LiNbO_3$, Pt and TiN was lower than for 600°C, leading to reduced thermal stress.
- Low pressure caused an increase of the kinetic energy of atoms in plasma plume. This additional energy could serve as a source of an energy for crystals formation.
- Additional Li in the plasma plume was probably the most important factor, as these atoms could compensate for resputtering and diffusion within the film.

On the other side, the layer deposited using the $LiNbO_3$ target on the Pt/TiO_2 structure stood out, having lower roughness. This can also be clarified by:

- Possibly most important factor is similar structure of the molecules in TiO_2 and SiO_2 layers, resulting in lower stress between these layers. This influence reduces the roughness of the Pt layer, making it lower, and consequently causing the decrease of roughness of the $LiNbO_3$ layer. Unfortunately, it was not possible to check the roughness of Pt prior the deposition for all the wafers, so this is only hypothesis.
- The lowest roughness of the layer was observed after the deposition at 0.2 mbar, 500°C using the $LiNbO_3$ target. These deposition conditions can be explained by also reduced thermal stress at 500°C, and absence of resputtering at this pressure so there was no need of additional Li atoms. On the other hand, since, possibly, stress inside the buffer layer was lower compared to usage of Pt/TiN structure (reducing amount of defects in these layers), diffusion within the film could be also lower.

Within these highly polycrystalline layers, clear and distinct ferroelectric domains were identified, featuring well-defined domain walls. However, the amplitude of these domains was not uniform, due to the polycrystalline nature of the layer. Despite these observations, attempts to switch or manipulate these domains proved unsuccessful. The observed degradation in these layers could be attributed to the Joule effect and/or surface oxidation.

In conclusion, considering the possibility of post-deposition surface polishing or roughness reduction, the more important is crystal quality. It needs to be further improved allow

these structures to be used in BAW devices. In our study, optimal properties were observed in the layer grown on the Pt/TiN structure at 0.007 mbar and 500°C using the Li-rich target. Hypothetically, it is possible to further improve the deposition recipe by utilization of the target with even more lithium compared to niobium, since Shibata et al. got their best results with Li/Nb ratio 2.0 [3], while our was 1.1. Another potential variation in the deposition parameters involve using 0.007 mbar and 500°C as the reference for both temperature and pressure. Modifications to the substrate can also be beneficial and may include:

- Adding a sacrificial support layer beneath the buffer during deposition to reduce the stress during the process. This support layer can be later removed, leaving the structure suspended. By adding an electrode only on top of the structure, an FBAR (Film Bulk Acoustic Resonator) can be obtained.
- Including additional layers between the Si wafer based on their lattice constants and thermal expansion coefficients. This can not only reduce stress in the structure but also create a multilayer structure with alternating layers possessing different acoustic impedances, serving as a Bragg mirror. Utilizing such a stack and placing an electrode on the top of the structure allows the creation of a Solidly Mounted Resonator (SMR). ZnO is commonly employed for the low-impedance layers of the Bragg reflector, and given its ability to promote c-axis growth of $LiNbO_3$ [4], it can be very good choice.

Adjustments to deposition parameters are necessary to align with the specific substrate chosen. Finally, it is possible to make some conclusions on the possible effects of the deposition parameters for all types of substrates:

- Oxygen pressure is a critical parameter in the growth process. A decreased pressure (0.007 mbar) can result in the formation of the low-Li phase due to resputtering, for instance, in the case of homoepitaxial growth. On the other side, it enhances the energy of the atoms, leading to improved crystal quality. The higher pressure (0.2 mbar) results in the homoepitaxial monocrystalline layers for growth on $LiNbO_3$ substrates, and good crystalline quality on the other substrates, but careful adjustments are needed to control layer roughness.
- Substrate temperature also influences the crystal quality, surface roughness, and thickness of the deposited layers. These effects depend on the specific substrate and require careful adjustment of temperature along with other deposition parameters. In

general, raising the temperature results in a slight increases in roughness (which can be compensated by higher amount of Li in target and adjusting pressure) and thickness of the layers, and can also leads to higher structure quality.

- The amount of Li in the target also influences crystal structure and surface morphology, on different substrates and can be utilized to adjust the effect of other deposition parameters. Increasing the Li/Nb ratio can compensate resputtering and diffusion of Li atoms in the substrate, so preventing low-Li phases formation, and decreasing the misorientation of the crystals in case of polycrystalline films.

Finally, while there have been demonstrations of the growth of both homo- and heteroepitaxial, highly oriented polycrystalline layers, there is still potential for general enhancements in the PLD process and recipes applied:

- Depositing thicker layers is necessary for making effective acoustic devices. Due to the low thickness of the piezoelectric layer deposited, about 100 nanometers, it was not possible to achieve any piezoelectric response and transfer characteristics. Previous successful studies utilized a 300-nanometer-thick $LiNbO_3$ layer for SAW devices [5].
- Modifications in deposition conditions are possible. Primarily, temperature and pressure can be further adjusted, and detailed references for such variations are provided for each substrate.
- Increasing the amount of Li in the target is an option. There's a potential for further improving the deposition process by using a target with even more lithium compared to niobium. Shibata et al. achieved their best results with a Li/Nb ratio of 2.0 [3], while ours were 1.0 and 1.1.
- Changes in equipment can also be beneficial. For instance, installing to the platform in-situ characterization tools like Reflection High-Energy Electron Diffraction (RHEED) has the potential to provide real-time monitoring of layer growth within the deposition chamber.
- For the homo- and heteroepitaxial growth, annealing processes could potentially enhance crystal quality and reduce surface roughness, contributing to improved overall performance of the layer [2]. Utilizing techniques such as rapid laser annealing for improvement of specific points of the thin film where there will devices done is also possible.

- For the growth on monocrystalline substrates (Al_2O_3 and $LiNbO_3$) preannealing the wafer before deposition and using a lower frequency of the laser (for example, 15 Hz) could result in a higher quality layer (works performed by Lee and Balestrino can be an example [6], [7]).
- Adding more buffer layers from materials like MgO or ZnO can enhance the quality of the layers deposited. Combining them with other metals high impedance layers, which often consist of Molybdenum (M) and Tungsten (W) can result into SMR devices fabrication. The selection of such materials requires further research and since it can be based on lattice constants and thermal expansion coefficient (CTE), with the ideal scenario involving the use of an underlayer that is both conductive, limits lithium atom diffusion, and maintains CTE compatibility between the substrate and the layer.

Bibliography

[1] L. Sauze, «Elaboration par PLD de couches de LiNbO3 sur substrats monocristallins,» chez *Élaboration et caractérisation de couches minces de LiNbO3 obtenues par pulvérisation cathodique et ablation laser pulsée*, Grenoble, Ecole Doctorale Polytechnique Hauts-de-France, 2022, pp. 117-127.

[2] A. Bartasyte, T. Baron, S. Oliveri, S. Margueron, P. Boulet, «Toward High-Quality Epitaxial LiNbO3 and LiTaO3 Thin Films for Acoustic and Optical Applications,» *Adv. Mater. Interfaces*, vol. 4, 2017.

[3] Yoshihiko Shibata et al., «Epitaxial growth and surface acoustic wave properties of lithium niobate films grown by pulsed laser deposition,» *Journal of Applied Physics*, vol. 77, 1995.

[4] S. Kilburger et al., «Properties of LiNbO3 based heterostructures grown by pulsed-laser deposition for optical waveguiding application,» *Thin Solid Films*, vol. 518, n° %116, pp. 4654-4657, 2010.

[5] V. Edon, D. Rèmiens, S. Saada, «Structural, electrical and piezoelectric properties of LiNbO3 thin films for surface acoustic wave resonators applications,» *Applied Surface Science*, vol. 256, n° %15, pp. 1455-1460, 2009.

[6] G.H. Lee et al, «Effect of deposition flux on surface roughness of LiNbO3 thin film,» *Materials Science and Engineering*, n° %195, pp. 137-140, 2002.

[7] G. Balestrino et al., «Epitaxial LiNbO3 thin films grown by pulsed laser deposition for optical waveguides,» *Appl. Phys. Lett*, vol. 78, n° %19, p. 1204–1206, 2001.

[8] H. Matsunaga, H. Ohno, Y. Okamoto, and Y. Nakajima, «Heteroepitaxial growth of LiNbO3 single crystal films by ion plating method,» *Journal of Crystal Growth*, vol. 99, n° %11–4, p. 630–633, 1990.

[9] G.-H. Lee, «Role of substrate step bunches on the growth behavior of LiNbO3 hin film on a-Al2O3 substrate,» *Materials Science and Engineering B* , n° %1138, p. 41–45, 2007.

[10] Gim et al, «Growth of LiNbO3 films on single crystal sapphire substrates using pulsed laser deposition,» *Integrated Ferroelectrics*, vol. 25, n° %11-4, pp. 91-102, 2006.

Annexes

Annex I: Methodology

This Annex is dedicated to detailing the experimental procedures and techniques employed in the research. The Pulsed Laser Deposition technique was implemented using the Solmates 8 in.-wafer-based SIP800 platform. The physicochemical properties of the synthesized layers underwent thorough analysis using various characterization techniques, including X-ray diffraction, atomic force microscopy, scanning electron microscopy, and secondary ion mass spectrometry.

Pulsed Laser Deposition tool

During the deposition process, laser ablation was conducted using a KrF excimer laser with a wavelength of 248 nm, operating at a frequency of 100 Hz and delivering an energy of 450 mJ. Importantly, a fixed distance of 55 mm between the target and substrate was maintained throughout the entire deposition process.

The Pulsed Laser Deposition technique was executed utilizing the Solmates 8 in.-wafer-based SIP800 platform. The table below provides clarification of the deposition conditions for $LiNbO_3$ layers.

Laser	KrF excimer (λ = 248 nm)
Laser Energy (mJ)	450
Fluency (J/cm^{-2})	2.1
Spot Size (mm^2)	9.2
Frequency (Hz)	100
Focus (mm)	55
Pressure (mbar)	0.2; 0.007
Temperature (°C)	500; 600
Target	$LiNbO_3$; $Li_{1.1}NbO_{3.05}$

Transparency measurement

Transparency is delineated as the degree of optical clarity attainable when the refractive index maintains uniformity throughout the material in the direction of observation. This property was evaluated by passing light through the specimens and discerning the intensity of transmitted light in relation to the incident light.

The assessments were conducted utilizing an Agilent spectrophotometer, specifically the Cary7000 model, equipped with a Universal Measurement Accessory (UMA). The UMA facilitates the measurement of direct transmission and specular (mirror-like) reflectance off the surface of a sample at a predefined angle. To ensure positional stability during data collection, a high-resolution optical encoder was employed, preventing any displacement between the sample and detector. The measurement angle was consistently set at 90° (perpendicular configuration), and the wavelength span ranged from 250 to 2000 nm.

Time-of-Flight Secondary Ion Mass Spectrometry analysis

We conducted an analysis employing Time-of-Flight Secondary Ion Mass Spectrometry (TOF-SIMS), utilizing an ion gun with the capacity for deep sample ablation.

The table below provides clarification of the measurement conditions for $LiNbO_3$ layers.

Spectrometer	IONTOF TOF SIMS V mass spectrometer
Sputter beam	Cs^+ 1 keV ~ 80 nA
Raster size	200 µm x 200 µm
Primary beam	Bi_3^+ 25 keV ~0.3 pA
Field of View	60 µm x 60 µm

The TOF-SIMS depth profiles were generated using a TOF SIMS V mass spectrometer provided by IONTOF. The experimental parameters included the utilization of an analysis beam comprising Bi3+ ions with an energy level of 25 keV and a current ranging from approximately 0.3 to 0.5 picoamperes. The field of view was set at 60 µm × 60 µm, with data acquisition involving the capture of one shot per pixel, resulting in a total of 128 x 128 pixels. Sputtering was performed using Cs+ ions with an energy of 1 keV and a current of approximately 80

nanoamperes, resulting in sputter craters measuring 200 µm × 200 µm. Positive secondary ions, including MCs^+ and MCs_2^+ clusters, were detected with a cycle time of 100 microseconds. The analytical procedure was executed in an interlaced mode, comprising one frame of analysis followed by 30 frames of sputtering, with a 1-second pause interspersed between them.

It is crucial to emphasize that due to the absence of reference samples, quantification and depth calibration of the obtained profiles were not feasible. However, comparative assessments of the data were still possible by normalizing it against signals from the substrate. Additionally, reference standards prepared at 0.2 millibars and 500°C were utilized for comparative purposes.

X-ray diffraction analysis

X-ray diffraction (XRD) is a non-destructive characterization technique grounded in Bragg's law, enabling the analysis of crystalline samples in both powder and solid states. Diffracted signals emerge exclusively from crystal planes that satisfy the Bragg equation, allowing for the characterization of specific planes based on the analysis configuration. It is crucial to note that an amorphous layer lacking distinct crystal planes will not exhibit diffraction patterns.

In XRD analysis, a beam of X-rays is emitted from a source, typically composed of a copper cathode. Prior to reaching the sample, the X-ray beam undergoes adjustments through various optical components to configure and adapt the analysis to the specific characteristics of the examined samples. For instance, Soller slits ensure a consistent irradiated surface on the sample by controlling the divergence of the X-ray beam. Additionally, a filter is employed to selectively allow the passage of the Kα line of copper, effectively eliminating fluorescence background. Subsequently, a detector receives the diffracted information for further analysis.

In the assessment of the crystalline structure quality of deposited layers, a specialized methodology was developed, employing two distinct XRD tools. Specifically, the XRD3 JV/BRUKER, DELTA-XM was utilized for high-resolution scans (HR-XRD) in measurements conducted on homoepitaxial layers, particularly for obtaining Reciprocal Space Maps (RSMs). Simultaneously, the Panalytical XperPro diffractometer was employed for all other deposited thin films.

Bragg-Brentano configuration

The Bragg-Brentano analysis, θ/2θ scan, symmetric scan, or Qz-scan are techniques employed for phase identification and assessing the degree of grain texture perpendicular to the substrate, excluding the planar direction. In this configuration, both the X-ray source and the detector move simultaneously.

The interpretation of this analysis is multifaceted. It allows for the determination of the crystalline phases constituting the layer through the diffraction angle 2θ, and an approximate quantification can be derived from the integrated intensities. For each phase, the degree of texture in the plane can be calculated using both experimental and theoretical integrated intensities. A more in-depth analysis of a diffraction peak can provide an estimate of the stress in the layer. A tensile layer will exhibit a larger diffraction peak, while a compressive layer will display a smaller peak compared to the theoretical value.

Rocking Curve Analysis

Rocking Curve Analysis (ω-scan) is employed to determine the disorientation of grains relative to an axis perpendicular to the substrate, specifically the Q_x axis. This analysis is centered on the diffraction angle of the plane under examination, resulting in a single peak after the Rocking Curve (RC) analysis. The Full Width at Half Maximum (FWHM) of this peak is utilized to interpret the crystalline quality of the layer by assessing the disorientation of crystallites along an axis of preferential growth.

In this configuration, the X-ray source is fixed at the Bragg angle corresponding to the family of planes being analyzed, and the detector is in motion. The obtained rocking curve provides valuable information about the distribution of orientations within the crystalline structure, aiding in the characterization of the layer's overall crystalline quality and the alignment of crystallites along a specific growth axis.

Other configurations

Various configurations and analyses were selected based on the inherent characteristics of the samples

- High-Resolution X-ray Diffraction (HR-XRD) was performed using the XRD3 JV/BRUKER DELTA-XM system with monochromators. This technique was applied

to homoepitaxial layers, specifically for the acquisition of Reciprocal Space Maps (RSMs).

- Grazing Incidence X-ray Diffraction (GI-XRD) involved XRD in grazing incidence, enabling the investigation of thin layers of the sample. This measurements were performed utilizing the XRD3 JV/BRUKER DELTA-XM system.
- In-Plane Analysis (IP) was employed to determine growth directions within the plane of the sample. When combined with symmetrical analyses (out of the plane), this approach provided insights into the fiber texture of a layer.
- φ-Scans were utilized to identify crystallites rotating relative to the diffraction plane. In this technique, the 2θ position was fixed for a plane not perpendicular to the analyzed plane, while the angle φ was in motion.

These diverse configurations present a range of analytical methodologies, each customized to address specific characteristics and requirements inherent in the samples under investigation.

Atomic force microscopy

Atomic force microscopy (AFM) analysis involves the integration of a microscope and a probe to generate an image of a sample's surface. The probe is systematically moved across a designated surface, and the disparity in force between the surface and the probe is gauged by monitoring the deflection of a light beam reflected on the latter. This measurement process is both expeditious and non-destructive, making it applicable to samples with either insulating or conductive properties. The probe, employed to traverse the sample's surface, comprises a tip affixed to a cantilever, wherein the cantilever functions as the force sensor. The deformations of the cantilever are precisely quantified in this analytical process.

The examination produces various critical parameters, among which RMS Roughness (Root Mean Square) stands out. This parameter signifies the root mean square of the heights within the profile and is frequently supplied as an indicator of surface roughness.

Scanning electron microscopy

Scanning electron microscopy (SEM) is an imaging analysis method employed for the characterization of surface relief. Additionally, it facilitates the examination of material layer

stacks. To achieve the latter, sample cutting and preparation are essential to enable the observation of cross-sections. In such instances, this technique proves valuable in approximating layer thicknesses.

The layers were examined using a ZEISS^{TM}-MERLIN scanning electron microscope. To prevent charge accumulation, a 7.7 nm carbon coating was applied to the samples. During the analysis, observations were conducted at a low acceleration voltage (2 kV) in secondary electron mode to further mitigate the risk of charge accumulation.

Piezoresponse Force Microscopy

Piezoresponse Force Microscopy (PFM) enables the mapping of ferroelectric domains by leveraging the converse piezoelectric effect in conjunction with an atomic force microscope. PFM experiments were conducted using an NT-MDT NTEGRA AFM system, augmented with a HF2LI system from Zurich Instruments for Dual Frequency Frequency Tracking. This approach enhances the signal-to-noise ratio compared to single-frequency PFM by operating at the contact resonance frequency.

A PPP-EFM tip, coated with a PtIr layer to impart conductivity, was employed. The voltage applied to the sample was set to the resonance frequency (f_0~340 kHz) and modulated by a low-frequency signal (f_m=1.5 kHz). The PFM signal was acquired at f_0-f_m, with an amplitude of 500 mV.

The Dual-Resonance Frequency Tracking (DRFT) system facilitated tracking of the resonance frequency, ensuring that any shifts due to tip-sample interactions did not affect the PFM signal. This approach minimizes perturbations and maintains the stability of the resonance frequency during the experiment.

Annex II: ICDD datasets

$LiNbO_3$ 00-020-0631

00-020-0631 Jul 9. 2020 4:16 PM (RX1005)

Status Primary **Quality Mark:** Star **Environment:** Ambient **Temp:** 298.0 K (Assigned by ICDD editor)
Chemical Formula: Li Nb O3 **Empirical Formula:** Li Nb O3 **Weight %:** Li4.69 Nb62.84 O32.46
Atomic %: Li20.00 Nb20.00 O60.00 **Compound Name:** Lithium Niobium Oxide **Entry Date:** 09/01/1970

Radiation: CuKα1 (1.5405 Å) **Internal Standard:** W **Intensity:** Diffractometer - Peak **I/Ic:** 8

Crystal System: Rhombohedral **SPGR:** R3c (161)
Author's Unit Cell [a: 5.1494 Å **c:** 13.862 Å **Volume:** 318.32 Å³ **Z:** 6.00 **MolVol:** 53.05 **c/a:** 2.692]
Calculated Density: 4.627 g/cm³ **Color:** Colorless **SS/FOM:** F(30) = 55.5(0.0169, 32)

Space Group: R3c (161) **Molecular Weight:** 147.84 g/mol
Crystal Data [a: 5.149 Å **b:** 5.149 Å **c:** 13.862 Å **α:** 90.00° **β:** 90.00° **γ:** 120.00° **XtlCell Vol:** 318.32 Å³
XtlCell Z: 6.00 **c/a:** 2.692 **a/b:** 1.000 **c/b:** 2.692]
Reduced Cell [a: 5.149 Å **b:** 5.149 Å **c:** 5.494 Å **α:** 62.06° **β:** 62.06° **γ:** 60.00° **RedCell Vol:** 106.11 Å³]

nωβ: =>2.00

Atomic parameters are cross-referenced from PDF entry 04-002-3091 **AC Space Group:** R3cH (161)
AC Unit Cell [a: 5.1497 Å **b:** 5.1497 Å **c:** 13.861 Å **α:** 90° **β:** 90° **γ:** 120°]

Space Group Symmetry Operators:

Seq	Operator	Seq	Operator	Seq	Operator
1	x,y,z	3	-x+y,-x,z	5	x,x-y,z+1/2
2	-y,x-y,z	4	-y,-x,z+1/2	6	-x+y,y,z+1/2

Atomic Coordinates:

Atom	Num	Wyckoff	Symmetry	x	y	z	SOF	IDP	AET
O	1	18b	1	0.03763	0.32347	0.1028	1.0		4-a
Nb	2	6a	3.	0.0	0.0	0.0	1.0		6-a
Li	3	6a	3.	0.0	0.0	0.21956	1.0		6-a

Crystal (Symmetry Allowed): Non-centrosymmetric - Pyro / Piezo (p), Piezo (2nd Harm.)

Subfiles: Ceramic (Ferroelectric), Common Phase, Inorganic, NBS Pattern **Pearson Symbol:** hR10.00

Cross-Ref PDF #'s: 04-002-1194 (Alternate), 04-002-3091 (Alternate), 04-002-5019 (Alternate), 04-002-5061 (Alternate), 04-002-5230 (Alternate), 04-005-7246 (Alternate), 04-006-0844 (Alternate), 04-006-2274 (Alternate), 04-006-2858 (Alternate), 04-006-3266 (Alternate), 04-006-3695 (Alternate), 04-006-8180 (Alternate), 04-006-9899 (Alternate), 04-007-2804 (Alternate), 04-007-2805 (Alternate), 04-007-9413 (Alternate), 04-007-9421 (Alternate), 04-007-9464 (Alternate), 04-008-2374 (Alternate), 04-008-4937 (Alternate), 04-009-2213 (Alternate), 04-009-2214 (Alternate), 04-009-3435 (Alternate), 04-009-3436 (Alternate), 04-009-3437 (Alternate), 04-009-5524 (Alternate), 04-009-5525 (Alternate), 04-009-5526 (Primary), 04-009-5527 (Alternate), 04-009-8334 (Alternate), 04-009-8480 (Alternate), 04-009-8537 (Alternate)

References:

Type	DOI	Reference
Primary Reference		Natl. Bur. Stand. (U. S.) Monogr. 25 1968, 6, 22.
Crystal Structure		Crystal Structure Source: LPF.

Database Comments: Analysis: Impurities 0.001-0.01% each: Ba, Na, Mo. Sample Preparation: Sample recrystallized at NBS by W.S. Brower. It was pulled from a melt and then annealed in oxygen at 1100 C for 10 hours. Sample Source or Locality: The "Li Nb O3" was obtained from CIBA, Rare Metals Division, Summit, New Jersey. Unit Cell Data Source: Powder Diffraction.

d-Spacings (60) - Li Nb O3 - 00-020-0631 (Stick, Fixed Slit Intensity) - Cu Kα1 1.54056 Å

2θ (°)	d (Å)	I	h	k	l	*	2θ (°)	d (Å)	I	h	k	l	*
23.68114	**3.754000**	100	0	1	2		71.16441	1.323800	4	1	0	10	
32.66687	**2.739000**	40	1	0	4		73.51295	1.287200	2	2	2	0	
34.79771	**2.576000**	20	1	1	0		76.05315	1.250400	4	3	0	6	
38.93964	2.311000	4	0	0	6		76.78472	1.240300	2	2	2	3	
40.05839	2.249000	10	1	1	3		77.39029	1.232100	2	1	3	1	
42.52672	2.124000	10	2	0	2		78.47223	1.217800	4	3	1	2	
48.48469	1.876000	16	0	2	4		79.23347	1.208000	6	1	2	8	
53.21001	1.720000	20	1	1	6		81.71282	1.177500	2	0	2	10	
54.79272	1.674000	2	2	1	1		82.76322	1.165200	2	1	3	4	
56.10188	1.638000	12	1	2	2		83.63128	1.155300	2	0	0	12	
56.97325	1.615000	6	0	1	8		86.00431	1.129400	2	3	1	5	
61.11937	1.515000	10	2	1	4		86.46128	1.124600	4	2	2	6	
62.39764	1.487000	10	3	0	0		88.81320	1.100800	2	0	4	2	
64.62618	1.441000	2	1	2	5		92.00169	1.070800	4	2	1	10	
68.52536	1.368200	4	2	0	8		93.04629	1.061500	2	4	0	4	

00-020-0631 Jul 9. 2020 4:16 PM (RX1005)

2θ (°)	d (Å)	I	h	k	l	*	2θ (°)	d (Å)	I	h	k	l	*
93.92132	1.053900	4	1	1	12		124.89868	0.868800	2	4	0	10	
99.09086	1.012300	2	2	3	2		126.21011	0.863700	2	0	5	4	
99.81425	1.006900	4	3	1	8		127.24409	0.859800	3	2	2	12	
102.46889	0.987900	2	2	2	9		127.64935	0.858300	2	3	3	0	
103.41893	0.981400	4	3	2	4		128.91991	0.853700	2	1	2	14	
104.61983	0.973400	2	4	1	0		129.85857	0.850400	2	1	0	16	
105.65384	0.966700	2	0	1	14		132.60835	0.841200	1	2	4	1	
107.96994	0.952300	2	4	1	3		134.06512	0.836600	1	4	2	2	
110.47938	0.937600	2	0	4	8		138.72465	0.823100	2	3	2	10	
113.17347	0.922800	2	1	3	10		140.27571	0.819000	2	2	4	4	
115.23952	0.912100	1	3	0	12		145.07254	0.807500	2	0	2	16	
116.67135	0.905000	2	2	0	14		145.61878	0.806300	1	4	2	5	
118.39121	0.896800	4	4	1	6		146.45744	0.804500	1	3	3	6	
121.09566	0.884600	1	5	0	2		151.01251	0.795600	2	1	5	2	
121.90687	0.881100	2	2	3	8		152.50349	0.793000	2	5	0	8	

$LiNb_3O_8$ 04-013-9445

04-013-9445 Mav 18. 2022 10:39 AM (RX1005)

Status Primary **Quality Mark:** Star **Environment:** Ambient **Temp:** 293.0 K **Chemical Formula:** Li Nb3 O8
Empirical Formula: Li Nb3 O8 **Weight %:** Li1.68 Nb67.38 O30.94 **Atomic %:** Li8.33 Nb25.00 O66.67
Compound Name: Lithium Niobium Oxide **Entry Date:** 09/01/2010 **Modification Date:** 09/01/2011
Modifications: Reflections

Radiation: CuK?1 (1.5406 ?) **d-Spacing:** Calculated **Intensity:** Calculated - Peak

Crystal System: Monoclinic **SPGR:** P21/a (14)
Author's Unit Cell [a: 15.262(2) ? **b:** 5.033(1) ? **c:** 7.457(1) ? **?:** 107.34(1)? **Volume:** 546.77 ?? **Z:** 4.00
MolVol: 136.69 **c/a:** 0.489 **a/b:** 3.032 **c/b:** 1.482] **Calculated Density:** 5.025 g/cm?
Structural Density: 5.02 g/cm? **Color:** Colorless **SS/FOM:** F(30) = 102.1(0.0070, 42) **R-factor:** 0.036 **I/Ic:** 2.83
I/Ic - CW ND: 0.2

Space Group: P21/n (14) **Molecular Wt:** 413.65 g/mol
Crystal Data [a: 14.856 ? **b:** 5.033 ? **c:** 7.457 ? **?:** 90.00? **?:** 101.29? **?:** 90.00? **XtlCell Vol:** 546.77 ??
XtlCell Z: 4.00 **c/a:** 0.502 **a/b:** 2.952 **c/b:** 1.482]
Reduced Cell [a: 5.033 ? **b:** 7.457 ? **c:** 14.856 ? **?:** 101.29? **?:** 90.00? **?:** 90.00? **RedCell Vol:** 546.77 ??
]

AC Space Group: P121/a1 (14)
AC Unit Cell [a: 15.262(2) ? **b:** 5.033(1) ? **c:** 7.457(1) ? **?:** 90? **?:** 107.34(1)? **?:** 90?]
Space Group Symmetry Operators:

Seq	Operator	Seq	Operator	Seq	Operator	Seq	Operator
1	x,y,z	2	-x,-y,-z	3	-x+1/2,y+1/2,-z	4	x+1/2,-y+1/2,z

ADP Type: B
Atomic Coordinates:

Atom	Num	Wyckoff	Symmetry	x	y	z	SOF	Biso	AET
Nb	1	4e	1	0.16852	0.26959	0.00831	1.0	0.402	
Nb	2	4e	1	0.07508	0.75486	0.24924	1.0	0.433	
Nb	3	4e	1	0.16458	0.25757	0.51674	1.0	0.396	
Li	4	4e	1	0.4201	0.2673	0.2597	1.0	2.27	
O	5	4e	1	0.2817	0.4326	0.0846	1.0	0.84	
O	6	4e	1	0.1558	0.4	0.7354	1.0	0.77	
O	7	4e	1	0.2157	0.5886	0.4148	1.0	0.92	
O	8	4e	1	0.0389	0.1077	0.8551	1.0	0.75	
O	9	4e	1	0.0989	0.9402	0.5005	1.0	0.58	
O	10	4e	1	0.0485	0.4387	0.3528	1.0	0.62	
O	11	4e	1	0.1006	0.5796	0.0375	1.0	0.71	
O	12	4e	1	0.1551	0.0855	0.2225	1.0	0.72	

Crystal (Symmetry Allowed): Centrosymmetric

Subfiles: Inorganic **Pearson Symbol:** mP48.00 **LPF Prototype Structure (Formula Order):** Li Nb3 O8,mP48,14
LPF Prototype Structure (Alpha Order): Li Nb3 O8,mP48,14 **ANX:** AB3X8 **Wyckoff Sequence:** e12

Cross-Ref PDF #'s: 00-026-1176 (Alternate), 04-011-2140 (Alternate) **Former PDF Numbers:** 01-075-2154

References:

Type	DOI	Reference
Primary Reference Structure	10.3891/acta.chem.scand.25-3337	Calculated from LPF using POWD-12++. Lundberg M. "The Crystal Structure of LiNb3O8". Acta Chem. Scand. 1971, 25, 3337-3346.

Database Comments: ANX: AB3X8. Habit: needle-like. LPF Collection Code: 1815729. Sample Preparation: STARTINGMATERIALS: Li Nb O3, Nb2 O5. COMPOUND PREPARATION: heated at 1273 K for 48 h. CRUCIBLE: platinum crucible. Temperature of Data Collection: 293 K. Wyckoff Sequence: e12. Unit Cell Data Source: Powder Diffraction.

d-spacings (198) - Li Nb3 O8 - 04-013-9445 (Stick, Fixed Slit Intensity) - X-ray (Cu K?1 1.54056 ?)

2? (?)	d (?)	I	h	k	l	*	2? (?)	d (?)	I	h	k	l	*
12.140	7.28419	102	2	0	0		23.879	3.72340	138	4	0	-1	
14.566	6.07603	196	2	0	-1		24.323	3.65635	256	2	0	-2	
18.637	4.75711	2	1	1	0		24.420	3.64210	263	4	0	0	
19.852	4.46858	123	2	0	1		24.999	3.55905	102	0	0	2	
21.442	4.14073	275m	1	1	-1		25.467	3.49466	7	3	1	0	
21.442	4.14073	275m	2	1	0		25.858	3.44266	2	3	1	-1	
21.607	**4.10950**	353	0	1	1		26.655	3.34157	57	2	1	1	
22.926	3.87596	74	2	1	-1		29.375	3.03801	62	4	0	-2	
23.462	3.78849	2	1	1	1		29.824	2.99331	31m	1	1	-2	

04-013-9445 Mav 18. 2022 10:39 AM (RX1005)

2? (?)	d (?)	I	h	k	l	*	2? (?)	d (?)	I	h	k	l	*
29.824	2.99331	31m	4	1	-1		56.891	1.61715	6m	2	3	-1	
30.187	**2.95815**	1000	2	1	-2		57.259	1.60763	15m	6	1	-4	
30.266	**2.95058**	990	4	1	0		57.259	1.60763	15m	7	2	-2	
30.702	2.90968	59m	0	1	2		57.416	1.60360	13m	2	2	3	
30.702	2.90968	59m	4	0	1		57.416	1.60360	13m	9	1	-1	
31.055	2.87735	173	2	0	2		58.125	1.58570	7	3	3	0	
31.780	2.81339	4	3	1	-2		58.325	1.58076	2	3	3	-1	
32.835	2.72538	1	1	1	2		58.444	1.57781	1	6	2	-3	
34.454	2.60091	20m	4	1	-2		58.738	1.57062	6	2	3	1	
34.454	2.60091	20m	5	1	-1		58.847	1.56797	8	8	1	1	
35.292	2.54108	7	6	0	-1		59.273	1.55770	1	5	2	2	
35.648	2.51650	206m	0	2	0		59.901	1.54286	4m	2	1	4	
35.648	2.51650	206m	4	1	1		59.901	1.54286	4m	9	1	0	
35.921	2.49795	225	2	1	2		60.684	1.52482	156m	2	3	-2	
36.121	2.48462	35m	1	2	0		60.684	1.52482	156m	4	3	0	
36.121	2.48462	35m	2	0	-3		60.927	1.51933	24m	8	2	-1	
36.992	2.42806	27	6	0	0		60.927	1.51933	24m	10	0	-1	
37.791	2.37856	9m	1	2	-1		61.078	1.51593	10	10	0	-2	
37.791	2.37856	9m	2	2	0		61.620	1.50388	2	3	3	-2	
38.104	2.35972	86	6	0	-2		62.004	1.49550	1m	2	2	-4	
38.592	2.33102	16	4	0	-3		62.004	1.49550	1m	3	2	-4	
38.696	2.32498	30	2	2	-1		62.259	1.48997	3m	1	3	2	
39.033	2.30568	2	1	2	1		62.259	1.48997	3m	6	0	3	
39.702	2.26836	22	6	1	-1		62.519	1.48440	11m	2	0	-5	
40.454	2.22793	25	2	1	-3		62.519	1.48440	11m	4	0	-5	
40.594	2.22055	68	3	2	-1		62.770	1.47907	38	4	2	-4	
40.779	2.21093	75	1	1	-3		62.949	1.47529	38	8	2	0	
40.900	2.20462	62	5	1	1		63.268	1.46862	5m	4	3	-2	
41.133	2.19271	19m	2	2	1		63.268	1.46862	5m	5	3	-1	
41.133	2.19271	19m	3	1	-3		63.497	1.46388	3	3	1	4	
41.247	2.18688	7	6	1	0		64.031	1.45295	145m	0	2	4	
42.066	2.14617	24	0	1	3		64.031	1.45295	145m	4	3	1	
42.746	2.11361	2m	4	1	-3		64.211	1.44931	190m	2	3	2	
42.746	2.11361	2m	6	0	1		64.211	1.44931	190m	6	2	2	
43.363	2.08496	41m	1	2	-2		64.500	1.44352	14	4	2	3	
43.363	2.08496	41m	4	2	-1		64.744	1.43867	17	4	0	4	
43.627	2.07297	83	2	2	-2		65.272	1.42829	10m	6	0	-5	
43.684	2.07036	84	4	2	0		65.272	1.42829	10m	6	1	3	
44.034	2.05475	25m	0	2	2		65.506	1.42376	6m	2	1	-5	
44.034	2.05475	25m	3	2	1		65.506	1.42376	6m	4	1	-5	
44.320	2.04211	25m	1	1	3		65.939	1.41545	2	8	2	-3	
44.320	2.04211	25m	4	1	2		66.108	1.41224	2	1	2	4	
44.707	2.02534	3	6	0	-3		66.402	1.40670	8	6	2	-4	
45.178	2.00532	1	5	1	-3		66.794	1.39939	12m	3	3	2	
45.291	2.00060	2	7	1	-1		66.794	1.39939	12m	10	1	0	
45.597	1.98786	2	1	2	2		66.890	1.39762	12	8	1	2	
46.566	1.94874	35	6	1	1		67.284	1.39039	6	2	3	-3	
46.840	1.93798	24m	4	2	-2		67.677	1.38327	83m	3	3	-3	
46.840	1.93798	24m	5	2	-1		67.677	1.38327	83m	4	1	4	
47.228	1.92293	12m	2	1	3		68.223	1.37352	5m	6	1	-5	
47.228	1.92293	12m	7	1	0		68.223	1.37352	5m	9	1	-4	
47.743	1.90338	26m	4	2	1		68.430	1.36987	21m	0	1	5	
47.743	1.90338	26m	5	2	0		68.430	1.36987	21m	0	3	3	
47.988	1.89424	111	2	2	2		68.841	1.36269	6m	2	2	4	
48.405	1.87892	38	6	1	-3		68.841	1.36269	6m	9	2	0	
48.881	1.86170	2m	2	0	-4		69.212	1.35629	1	7	2	-4	
48.881	1.86170	2m	8	0	-2		69.559	1.35038	7m	7	2	2	
49.347	1.84523	1	5	1	2		69.559	1.35038	7m	10	0	1	
49.657	1.83443	8	5	2	-2		70.082	1.34157	8m	1	3	3	
49.838	1.82818	51	4	0	-4		70.082	1.34157	8m	4	3	2	
50.047	1.82105	49	8	0	0		70.184	1.33987	8	10	0	-4	
51.298	1.77953	116	0	0	4		70.585	1.33324	7m	7	1	-5	
51.451	1.77459	115	6	0	2		70.585	1.33324	7m	11	1	-2	
51.655	1.76806	30	2	2	-3		70.762	1.33034	7m	7	3	-1	
51.837	1.76228	11	4	0	3		70.762	1.33034	7m	8	0	-5	
52.025	1.75634	4	5	2	1		70.838	1.32909	7m	1	1	5	
52.355	1.74607	69m	2	1	-4		70.838	1.32909	7m	11	1	-1	
52.355	1.74607	69m	8	1	-2		71.101	1.32483	2m	2	0	5	
53.166	1.72133	277m	1	1	-4		71.101	1.32483	2m	7	1	3	
53.166	1.72133	277m	6	2	-2		71.775	1.31404	7	6	3	1	
53.266	1.71833	201	4	1	-4		72.283	1.30604	4m	2	3	3	
53.465	1.71241	182m	4	2	-3		72.283	1.30604	4m	7	3	0	
53.465	1.71241	182m	8	1	0		72.409	1.30408	1m	5	1	4	
54.006	1.69650	9	6	0	-4		72.409	1.30408	1m	10	1	1	
54.660	1.67774	10	0	1	4		72.643	1.30046	18m	8	2	-4	
54.807	1.67360	11m	1	2	3		72.643	1.30046	18m	10	2	-1	
54.807	1.67360	11m	6	1	2		72.768	1.29853	16	10	2	-2	
55.176	1.66327	2	4	1	3		73.013	1.29477	2	10	1	-4	
55.655	1.65009	3m	5	2	-3		73.196	1.29199	11	6	3	-3	
55.655	1.65009	3m	8	0	1		73.582	1.28617	5m	8	1	-5	
55.738	1.64782	3	7	2	-1		73.582	1.28617	5m	9	1	2	
56.292	1.63293	19m	0	3	1		73.915	1.28119	2m	2	1	5	
56.292	1.63293	19m	2	3	0		73.915	1.28119	2m	5	3	2	
56.747	1.62090	14m	2	0	4		74.094	1.27854	9m	2	2	-5	
56.747	1.62090	14m	8	1	-3		74.094	1.27854	9m	4	2	-5	
56.891	1.61715	6m	1	1	4		74.474	1.27295	1	8	0	3	

04-013-9445 Mav 18. 2022 10:39 AM (RX1005)

2? (?)	d (?)	I	h	k	l	*	2? (?)	d (?)	I	h	k	l	*
74.639	1.27054	4	12	0	-2		75.495	1.25825	22m	0	4	0	
74.913	1.26657	4	6	0	4		75.495	1.25825	22m	8	3	-1	
75.316	1.26080	9m	10	2	0		75.680	1.25564	13	10	2	-3	
75.316	1.26080	9m	12	0	-1		75.826	1.25358	4	1	4	0	

Li_3NbO_4 04-009-6335

04-009-6335 May 18. 2022 10:37 AM (RX1005)

Status Primary **Quality Mark:** Star **Environment:** Ambient **Temp:** 298.0 K (Assigned by ICDD editor)
Chemical Formula: Li3 Nb O4 **Empirical Formula:** Li3 Nb O4 **Weight %:** Li11.72 Nb52.28 O36.01
Atomic %: Li37.50 Nb12.50 O50.00 **Compound Name:** Lithium Niobium Oxide **Alternate Name:** trilithium niobate
Entry Date: 09/01/2006 **Modification Date:** 09/01/2011 **Modifications:** Reflections

Radiation: CuK?1 (1.5406 ?) **d-Spacing:** Calculated **Intensity:** Calculated - Peak

Crystal System: Cubic **SPGR:** I-43m (217)
Author's Unit Cell [a: 8.412(2) ? **Volume:** 595.25 ?? **Z:** 8.00 **MolVol:** 74.41] **Calculated Density:** 3.966 g/cm?
Structural Density: 3.97 g/cm? **Color:** Colorless **SS/FOM:** F(30) = 999.9(0.0001, 30) **R-factor:** 0.031 **I/Ic:** 5.59
I/Ic - CW ND: 0.59

Space Group: I-43m (217) **Molecular Wt:** 177.73 g/mol
Crystal Data [a: 8.412 ? **b:** 8.412 ? **c:** 8.412 ? **?:** 90.00? **?:** 90.00? **?:** 90.00? **XtlCell Vol:** 595.25 ??
XtlCell Z: 8.00 **a/b:** 1.000 **c/b:** 1.000]
Reduced Cell [a: 7.285 ? **b:** 7.285 ? **c:** 7.285 ? **?:** 109.47? **?:** 109.47? **?:** 109.47? **RedCell Vol:** 297.62 ??
]

AC Space Group: I-43m (217)
AC Unit Cell [a: 8.412(2) ? **b:** 8.412(2) ? **c:** 8.412(2) ? **?:** 90? **?:** 90? **?:** 90?]

Space Group Symmetry Operators:

Seq	Operator	Seq	Operator	Seq	Operator	Seq	Operator	Seq	Operator	Seq	Operator
1	x,y,z	5	y,x,z	9	y,-z,-x	13	-x,y,-z	17	-y,x,-z	21	-y,-z,x
2	z,x,y	6	z,y,x	10	x,-z,-y	14	-z,x,-y	18	-z,y,-x	22	-x,-z,y
3	y,z,x	7	x,-y,-z	11	y,-x,-z	15	-y,z,-x	19	-x,-y,z	23	-y,-x,z
4	x,z,y	8	z,-x,-y	12	z,-y,-x	16	-x,z,-y	20	-z,-x,y	24	-z,-y,x

ADP Type: U

Atomic Coordinates:

Atom	Num	Wyckoff	Symmetry	x	y	z	SOF	Uiso	AET
Nb	1	8c	.3m	0.14028	0.14028	0.14028	1.0	0.0074	6-a
O	2	8c	.3m	-0.109	-0.109	-0.109	1.0	0.0084	3#a
Li	3	24g	..m	0.3782	0.3782	0.1046	1.0	0.017	6-a
O	4	24g	..m	0.1247	0.1247	0.3601	1.0	0.0112	6-a

Crystal (Symmetry Allowed): Non-centrosymmetric - Piezo (2nd Harm.)

Subfiles: Ceramic (Microwave), Inorganic **Pearson Symbol:** cI64.00 **Prototype Structure (Alpha Order):** Li3 Nb O4
LPF Prototype Structure (Formula Order): Li3 Nb O4,cI64,217
LPF Prototype Structure (Alpha Order): Li3 Nb O4,cI64,217 **ANX:** AB3X4 **Wyckoff Sequence:** g2 c2

Cross-Ref PDF #'s: 00-050-0052 (Primary), 04-008-9517 (Alternate), 04-008-9627 (Alternate)
Former PDF Numbers: 01-082-1198

References:

Type	DOI	Reference
Primary Reference		Calculated from LPF using POWD-12++.
Structure	10.1107/S0108270193008890X	Ukei K., Suzuki H., Shishido T., Fukuda T. "Li3NbO4". Acta Crystallogr., Sect. C: Cryst. Struct. Commun. 1994, 50, 655.

Database Comments: ANX: AB3X4. LPF Collection Code: 1501718. Wyckoff Sequence: g2 c2. Unit Cell Data Source: Single Crystal.

d-spacings (52) - Li3 Nb O4 - 04-009-6335 (Stick, Fixed Slit Intensity) - X-ray (Cu K?1 1.54056 ?)

2? (?)	d (?)	I	h	k	l	*	2? (?)	d (?)	I	h	k	l	*
14.881	**5.948180**	882	1	1	0		60.205	1.535810	248	5	2	1	
21.105	4.206000	33	2	0	0		62.395	1.487050	195	4	4	0	
25.923	**3.434180**	1000	2	1	1		64.543	1.442650	72	5	3	0	
30.021	2.974090	2	2	2	0		66.654	1.402000	13	6	0	0	
33.664	2.660110	334	3	1	0		68.731	1.364610	91	6	1	1	
36.988	2.428340	61	2	2	2		70.780	1.330050	2	6	2	0	
40.073	2.248200	161	3	2	1		72.802	1.298000	20	5	4	1	
42.972	**2.103000**	455	4	0	0		74.803	1.268160	21	6	2	2	
45.722	1.982730	208	3	3	0		76.786	1.240280	27	6	3	1	
48.348	1.880980	11	4	2	0		78.752	1.214170	46	4	4	4	
50.871	1.793440	11	3	3	2		80.705	1.189640	34	7	1	0	
53.307	1.717090	34	4	2	2		82.648	1.166530	14	6	4	0	
55.668	1.649730	134	4	3	1		84.581	1.144730	72	5	5	2	

04-009-6335 Mav 18. 2022 10:37 AM (RX1005)

2? (?)	d (?)	I	h	k	l	*	2? (?)	d (?)	I	h	k	l	*
86.509	1.124100	10	6	4	2		114.121	0.917824	4	8	4	2	
88.433	1.104550	33	7	3	0		116.245	0.907089	75	9	2	1	
92.276	1.068330	47	6	5	1		118.408	0.896722	5	6	6	4	
94.202	1.051500	16	8	0	0		120.616	0.886703	18	8	5	1	
96.131	1.035450	37	7	4	1		125.195	0.867632	31	9	3	2	
98.069	1.020100	9	8	2	0		127.583	0.858546	29	8	4	4	
100.013	1.005430	14	6	5	3		130.049	0.849740	22	7	7	0	
101.972	0.991364	17	8	2	2		132.608	0.841200	8	10	0	0	
103.944	0.977875	54	7	4	3		135.278	0.832912	8	10	1	1	
105.933	0.964923	7	6	6	2		138.079	0.824864	17	8	6	2	
107.942	0.952471	1	7	5	2		141.041	0.817046	2	9	5	0	
109.974	0.940490	39	8	4	0		144.208	0.809445	5	10	2	2	
112.032	0.928950	8	8	3	3		147.638	0.802053	75	9	5	2	

Al_2O_3 00-046-1212

00-046-1212 Jul 9. 2020 10:25 AM (RX1005)

Status Primary **Quality Mark:** Star **Environment:** Ambient **Temp:** 298.0 K (Assigned by ICDD editor) **Phase:** α
Chemical Formula: Al2 O3 **Empirical Formula:** Al2 O3 **Weight %:** Al52.93 O47.07 **Atomic %:** Al40.00 O60.00
Compound Name: Aluminum Oxide **Mineral Name:** Corundum, syn **Alternate Name:** α-Al2 O3
Entry Date: 09/01/1996 **Modification Date:** 09/01/2008 **Modifications:** I/Ic

Radiation: CuKα1 (1.5406 Å) **d-Spacing:** Diffractometer **Cutoff:** 4.40 Å **Intensity:** Diffractometer - Peak **I/Ic:** 1

Crystal System: Rhombohedral **SPGR:** R-3c (167)
Author's Unit Cell [a: 4.7587(1) Å **c:** 12.9929(3) Å **Volume:** 254.81 Å³ **Z:** 6.00 **MolVol:** 42.47 **c/a:** 2.730]
Calculated Density: 3.987 g/cm³ **SS/FOM:** F(25) = 357.3(0.0028, 25)

Space Group: R-3c (167) **Molecular Weight:** 101.96 g/mol
Crystal Data [a: 4.759 Å **b:** 4.759 Å **c:** 12.993 Å **α:** 90.00° **β:** 90.00° **γ:** 120.00° **XtlCell Vol:** 254.81 Å³
XtlCell Z: 6.00 **c/a:** 2.730 **a/b:** 1.000 **c/b:** 2.730]
Reduced Cell [a: 4.759 Å **b:** 4.759 Å **c:** 5.129 Å **α:** 62.36° **β:** 62.36° **γ:** 60.00° **RedCell Vol:** 84.94 Å³]

εα: =1.7604 **nωβ:** =1.7686 **Sign:** =-

Atomic parameters are cross-referenced from PDF entry 04-007-4873 **AC Space Group:** R-3cH (167)
AC Unit Cell [a: 4.75932(2) Å **b:** 4.75932(2) Å **c:** 12.99250(8) Å **α:** 90° **β:** 90° **γ:** 120°]

Space Group Symmetry Operators:

Seq	Operator	Seq	Operator	Seq	Operator	Seq	Operator
1	x,y,z	4	y,-x+y,-z	7	-y,-x,z+1/2	10	-x,-x+y,-z+1/2
2	-x,-y,-z	5	-x+y,-x,z	8	y,x,-z+1/2	11	-x+y,y,z+1/2
3	-y,x-y,z	6	x-y,x,-z	9	x,x-y,z+1/2	12	x-y,-y,-z+1/2

ADP Type: B

Atomic Coordinates:

Atom	Num	Wyckoff	Symmetry	x	y	z	SOF	Biso	AET
Al	1	12c	3.	0.0	0.0	0.35228	1.0	0.45	6-a
O	2	18e	.2	0.3062	0.0	0.25	1.0	0.45	4-a

Crystal (Symmetry Allowed): Centrosymmetric

Subfiles: Cement and Hydration Product, Common Phase, Forensic, Inorganic, Metal & Alloy, Mineral Related (Mineral, Synthetic), Pharmaceutical (Excipient), Superconducting Material

Mineral Classification: Corundum (supergroup), corundum (group) **Pearson Symbol:** hR10.00
Prototype Structure [Formula Order]: Al2 O3 **Prototype Structure [Alpha Order]:** Al2 O3
LPF Prototype Structure [Formula Order]: Al2 O3,hR30,167
LPF Prototype Structure [Alpha Order]: Al2 O3,hR30,167

Cross-Ref PDF #'s: 04-002-3621 (Alternate), 04-002-5941 (Alternate), 04-002-8135 (Alternate), 04-003-2497 (Alternate), 04-003-5819 (Alternate), 04-004-2852 (Primary), 04-004-5100 (Alternate), 04-004-5285 (Alternate), 04-004-5434 (Alternate), 04-004-8977 (Alternate), 04-005-4213 (Alternate), 04-005-4311 (Alternate), 04-005-4497 (Alternate), 04-005-4503 (Alternate), 04-005-4505 (Alternate), 04-006-2060 (Alternate), 04-006-3495 (Alternate), 04-006-9359 (Alternate), 04-006-9730 (Alternate), 04-007-1400 (Alternate), 04-007-4873 (Alternate), 04-007-5143 (Alternate), 04-007-9625 (Alternate), 04-007-9768 (Alternate), 04-007-9769 (Alternate), 04-007-9906 (Alternate), 04-010-6476 (Alternate), 04-010-6477 (Alternate)

References:

Type	DOI	Reference
Primary Reference		Huang, T., Parrish, W., Masciocchi, N., Wang, P. Adv. X-Ray Anal. 1990, 33, 295.
Crystal Structure		Crystal Structure Source: LPF.
Structure		Acta Crystallogr., Sect. B: Struct. Sci. 1993, 49, 973.

Database Comments: General Comments: Unit cell computed from dobs. Sample Source or Locality: The sample is an alumina plate as received from ICDD.

d-Spacings (25) - Al2 O3 - 00-046-1212 (Stick, Fixed Slit Intensity) - Cu Kα1 1.54056 Å

2θ (°)	d (Å)	I	h	k	l	*	2θ (°)	d (Å)	I	h	k	l	*
25.57794	3.479750	45	0	1	2		57.49573	**1.601560**	89	1	1	6	
35.15192	**2.550850**	100	1	0	4		59.73881	1.546670	1	2	1	1	
37.77599	2.379470	21	1	1	0		61.11669	1.515060	2	1	2	2	
41.67497	2.165420	2	0	0	6		61.29812	1.511010	14	0	1	8	
43.35504	**2.085320**	66	1	1	3		66.51865	1.404520	23	2	1	4	
46.17491	1.964320	1	2	0	2		68.21199	1.373720	27	3	0	0	
52.54896	1.740070	34	0	2	4		70.41808	1.335990	1	1	2	5	

Page 1 / 2

00-046-1212 Jul 9. 2020 10:25 AM (RX1005)

2θ (°)	d (Å)	I	h	k	l	*	2θ (°)	d (Å)	I	h	k	l	*
74.29668	1.275550	2	2	0	8		84.35624	1.147210	3	2	2	3	
76.86901	1.239150	29	1	0	10		85.14012	1.138640	<1	1	3	1	
77.22381	1.234340	12	1	1	9		86.35989	1.125660	2	3	1	2	
80.41913	1.193150	1	2	1	7		86.50058	1.124190	3	1	2	8	
80.69788	1.189730	2	2	2	0		88.99411	1.099030	9	0	2	10	
83.21484	1.160020	1	3	0	6								

Si 00-026-1481

00-026-1481 Sep 24. 2021 11:07 AM (RX1005)

Status Alternate **Quality Mark:** Star **Environment:** Ambient **Temp:** 298.0 K (Assigned by ICDD editor)
Chemical Formula: Si **Empirical Formula:** Si **Weight %:** Si100.00 **Atomic %:** Si100.00
Compound Name: Silicon **CAS Number:** 7440-21-3 **Entry Date:** 09/01/1976

Radiation: CuKα1 (1.5406 Å) **I/Ic:** 4.7

Crystal System: Cubic **SPGR:** Fd-3m (227)
Author's Unit Cell [a: 5.4309 Å **Volume:** 160.18 Å³ **Z:** 8.00 **MolVol:** 20.02] **Calculated Density:** 2.329 g/cm³
SS/FOM: F(11) = 173.5(0.0049, 13)

Space Group: Fd-3m (227) **Molecular Wt:** 28.09 g/mol
Crystal Data [a: 5.431 Å **b:** 5.431 Å **c:** 5.431 Å **α:** 90.00° **β:** 90.00° **γ:** 90.00° **XtlCell Vol:** 160.18 Å³
XtlCell Z: 8.00 **a/b:** 1.000 **c/b:** 1.000]
Reduced Cell [a: 3.840 Å **b:** 3.840 Å **c:** 3.840 Å **α:** 60.00° **β:** 60.00° **γ:** 60.00° **RedCell Vol:** 40.05 Å³]

Atomic parameters are cross-referenced from PDF entry 04-012-7888 **AC Space Group:** Fd-3m (227)
AC Unit Cell [a: 5.4317(6) Å **b:** 5.4317(6) Å **c:** 5.4317(6) Å **α:** 90° **β:** 90° **γ:** 90°]

Space Group Symmetry Operators:

Seq	Operator	Seq	Operator	Seq	Operator	Seq	Operator	Seq	Operator
1	x,y,z	11	z,-x+1/4,-y+1/4	21	-y+1/4,z,-x+1/4	31	-x+1/4,-z+1/4,y	41	z,y,x
2	-x,-y,-z	12	-z,x+3/4,y+3/4	22	y+3/4,-z,x+3/4	32	x+3/4,z+3/4,-y	42	-z,-y,-x
3	x,-y+1/4,-z+1/4	13	-z+1/4,x,-y+1/4	23	-y+1/4,-z+1/4,x	33	y,x,z	43	z,-y+1/4,-x+1/4
4	-x,y+3/4,z+3/4	14	z+3/4,-x,y+3/4	24	y+3/4,z+3/4,-x	34	-y,-x,-z	44	-z,y+3/4,x+3/4
5	-x+1/4,y,-z+1/4	15	-z+1/4,-x+1/4,y	25	x,z,y	35	y,-x+1/4,-z+1/4	45	-z+1/4,y,-x+1/4
6	x+3/4,-y,z+3/4	16	z+3/4,x+3/4,-y	26	-x,-z,-y	36	-y,x+3/4,z+3/4	46	z+3/4,-y,x+3/4
7	-x+1/4,-y+1/4,z	17	y,z,x	27	x,-z+1/4,-y+1/4	37	-y+1/4,x,-z+1/4	47	-z+1/4,-y+1/4,x
8	x+3/4,y+3/4,-z	18	-y,-z,-x	28	-x,z+3/4,y+3/4	38	y+3/4,-x,z+3/4	48	z+3/4,y+3/4,-x
9	z,x,y	19	y,-z+1/4,-x+1/4	29	-x+1/4,z,-y+1/4	39	-y+1/4,-x+1/4,z		
10	-z,-x,-y	20	-y,z+3/4,x+3/4	30	x+3/4,-z,y+3/4	40	y+3/4,x+3/4,-z		

Origin: O2

Atomic Coordinates:

Atom	Num	Wyckoff	Symmetry	x	y	z	SOF	IDP	AET
Si	1	8a	-43m	0.125	0.125	0.125	1.0		

Crystal (Symmetry Allowed): Centrosymmetric

Subfiles: Ceramic (Semiconductor), Common Phase, Forensic, Inorganic, Metal & Alloy, NBS Pattern
Pearson Symbol: cF8.00 **Prototype Structure [Alpha Order]:** C
LPF Prototype Structure [Formula Order]: C,cF8,227 **LPF Prototype Structure [Alpha Order]:** C,cF8,227

Cross-Ref PDF #'s: 00-001-0787 (Deleted), 00-001-0791 (Deleted), 00-002-0561 (Deleted), 00-003-0529 (Deleted), 00-005-0565 (Alternate), 00-027-1402 (Primary), 01-070-5680 (Alternate), 01-071-3770 (Alternate), 01-071-4631 (Alternate), 01-073-6978 (Alternate), 01-075-0589 (Alternate), 01-077-2108 (Alternate), 01-077-2109 (Alternate), 01-077-2110 (Alternate), 01-077-2111 (Alternate), 01-085-4375 (Alternate), 01-085-8586 (Alternate), 01-086-4266 (Alternate), 01-089-2749 (Alternate), 01-089-2955 (Alternate), 03-065-1060 (Alternate), 04-001-7247 (Primary), 04-002-0118 (Alternate), 04-002-0891 (Alternate), 04-002-2831 (Alternate), 04-003-1456 (Alternate), 04-003-3352 (Alternate), 04-003-3353 (Alternate), 04-003-4734 (Alternate), 04-004-5099 (Alternate), 04-004-6896 (Alternate), 04-005-9699 (Alternate), 04-006-2527 (Alternate), 04-006-2591 (Alternate), 04-006-4528 (Alternate), 04-006-6436 (Alternate), 04-007-5232 (Alternate), 04-007-8736 (Alternate), 04-010-2410 (Alternate), 04-012-0806 (Alternate), 04-012-7888 (Alternate), 04-013-4795 (Alternate), 04-014-0211 (Alternate), 04-014-0247 (Alternate), 04-014-8844 (Alternate), 04-016-4861 (Alternate), 04-016-5305 (Alternate)

References:

Type	DOI	Reference
Primary Reference		Natl. Bur. Stand. (U. S.) Monogr. 25 1976, 13, 35.
Crystal Structure		Crystal Structure Source: LPF.

Database Comments: Additional Patterns: See PDF 00-027-1402. To replace 00-005-0565. Unit Cell Data Source: Powder Diffraction.

d-spacings (11) - Si - 00-026-1481 (Stick, Fixed Slit Intensity) - Cu Kα1 1.54056 Å

2θ (°)	d (Å)	I	h	k	l	*	2θ (°)	d (Å)	I	h	k	l	*	2θ (°)	d (Å)	I	h	k	l	*
28.447	**3.1350**	100	1	1	1		76.377	1.2459	11	3	3	1		114.087	0.9180	7	5	3	1	
47.300	**1.9202**	55	2	2	0		88.016	1.1087	12	4	2	2		127.541	0.8587	8	6	2	0	
56.117	**1.6376**	30	3	1	1		94.960	1.0451	6	5	1	1		136.890	0.8282	3	5	3	3	
69.136	1.3576	6	4	0	0		106.699	0.9601	3	4	4	0								

Pt 00-004-0802

00-004-0802 Sep 24. 2021 11:04 AM (RX1005)

Status Primary **Quality Mark:** Star **Environment:** Ambient **Temp:** 299.0 K **Chemical Formula:** Pt
Empirical Formula: Pt **Weight %:** Pt100.00 **Atomic %:** Pt100.00 **Compound Name:** Platinum
Mineral Name: Platinum, syn **CAS Number:** 7440-06-4 **Entry Date:** 09/01/1954

Radiation: CuKα1 (1.5406 Å) **Filter:** Ni Beta **Intensity:** Diffractometer - Peak

Crystal System: Cubic **SPGR:** Fm-3m (225)
Author's Unit Cell [a: 3.9231 Å **Volume:** 60.38 Å³ **Z:** 4.00 **MolVol:** 15.10] **Calculated Density:** 21.461 g/cm³
Measured Density: 21.37 g/cm³ **Color:** Light gray metallic **SS/FOM:** F(9) = 143.2(0.0070, 9)

Space Group: Fm-3m (225) **Molecular Wt:** 195.09 g/mol
Crystal Data [a: 3.923 Å **b:** 3.923 Å **c:** 3.923 Å **α:** 90.00° **β:** 90.00° **γ:** 90.00° **XtlCell Vol:** 60.38 Å³
XtlCell Z: 4.00 **a/b:** 1.000 **c/b:** 1.000]
Reduced Cell [a: 2.774 Å **b:** 2.774 Å **c:** 2.774 Å **α:** 60.00° **β:** 60.00° **γ:** 60.00° **RedCell Vol:** 15.09 Å³]

Atomic parameters are cross-referenced from PDF entry 04-011-9016 **AC Space Group:** Fm-3m (225)
AC Unit Cell [a: 3.924(1) Å **b:** 3.924(1) Å **c:** 3.924(1) Å **α:** 90° **β:** 90° **γ:** 90°]

Space Group Symmetry Operators:

Seq	Operator	Seq	Operator	Seq	Operator	Seq	Operator	Seq	Operator	Seq	Operator
1	x,y,z	9	y,x,z	17	y,-z,-x	25	-x,y,-z	33	-y,x,-z	41	-y,-z,x
2	-x,-y,-z	10	-y,-x,-z	18	-y,z,x	26	x,-y,z	34	y,-x,z	42	y,z,-x
3	z,x,y	11	z,y,x	19	x,-z,-y	27	-z,x,-y	35	-z,y,-x	43	-x,-z,y
4	-z,-x,-y	12	-z,-y,-x	20	-x,z,y	28	z,-x,y	36	z,-y,x	44	x,z,-y
5	y,z,x	13	x,-y,-z	21	y,-x,-z	29	-y,z,-x	37	-x,-y,z	45	-y,-x,z
6	-y,-z,-x	14	-x,y,z	22	-y,x,z	30	y,-z,x	38	x,y,-z	46	y,x,-z
7	x,z,y	15	z,-x,-y	23	z,-y,-x	31	-x,z,-y	39	-z,-x,y	47	-z,-y,x
8	-x,-z,-y	16	-z,x,y	24	-z,y,x	32	x,-z,y	40	z,x,-y	48	z,y,-x

Atomic Coordinates:

Atom	Num	Wyckoff	Symmetry	x	y	z	SOF	IDP	AET
Pt	1	4a	m-3m	0.0	0.0	0.0	1.0		

Crystal (Symmetry Allowed): Centrosymmetric

Subfiles: Ceramic (Semiconductor), Common Phase, Educational Pattern, Forensic, Inorganic, Metal & Alloy, Mineral Related (Mineral, Synthetic), NBS Pattern

Mineral Classification: Gold (supergroup), 1C-disordered (group) **Pearson Symbol:** cF4.00
Prototype Structure [Formula Order]: Cu **Prototype Structure [Alpha Order]:** Cu
LPF Prototype Structure [Formula Order]: Cu,cF4,225 **LPF Prototype Structure [Alpha Order]:** Cu,cF4,225
ANX: N

Cross-Ref PDF #'s: 04-001-0112 (Primary), 04-001-0489 (Alternate), 04-001-0537 (Alternate), 04-001-0839 (Alternate), 04-001-1793 (Alternate), 04-002-0887 (Alternate), 04-002-2613 (Alternate), 04-002-9729 (Alternate), 04-002-9895 (Alternate), 04-003-2557 (Alternate), 04-003-6500 (Alternate), 04-003-7036 (Alternate), 04-003-7149 (Alternate), 04-004-4405 (Alternate), 04-004-4514 (Alternate), 04-004-6287 (Alternate), 04-004-6358 (Alternate), 04-004-6364 (Alternate), 04-004-8457 (Alternate), 04-004-8733 (Alternate), 04-007-2989 (Alternate), 04-011-7822 (Alternate), 04-011-9016 (Alternate)

References:

Type	DOI	Reference
Primary Reference		Swanson, Tatge. Natl. Bur. Stand. (U. S.), Circ. 539 1953, I, 31.
Crystal Structure		Crystal Structure Source: LPF.

Database Comments: ANX: N. Opaque Optical Data: Opaque mineral optical data on specimen from unspecified locality: RR2Re=70.3, Disp.=16, VHN50=122-129, Color values=.318, .324, 70.7, Ref.: IMA Commission on Ore Microscopy QDF. Sample Preparation: Sample prepared at NBS, Gaithersburg, Maryland, USA, and estimated to be more than 99.99% pure. Temperature of Data Collection: 299 K. Unit Cell Data Source: Powder Diffraction.

d-spacings (9) - Pt - 00-004-0802 (Stick, Fixed Slit Intensity) - Cu Kα1 1.54056 Å

2θ (°)	d (Å)	I	h	k	l	*	2θ (°)	d (Å)	I	h	k	l	*	2θ (°)	d (Å)	I	h	k	l	*
39.763	**2.2650**	100	1	1	1		81.286	**1.1826**	33	3	1	1		117.711	0.9000	22	3	3	1	
46.243	**1.9616**	53	2	0	0		85.712	1.1325	12	2	2	2		122.807	0.8773	20	4	2	0	
67.454	1.3873	31	2	2	0		103.508	0.9808	6	4	0	0		148.261	0.8008	29	4	2	2	

SiO_2 00-046-1045

00-046-1045 Sep 24, 2021 11:09 AM (RX1005)

Status Primary **Quality Mark:** Star **Environment:** Ambient **Temp:** 296.0 K **Chemical Formula:** Si O2
Empirical Formula: O2 Si **Weight %:** O53.26 Si46.74 **Atomic %:** O66.67 Si33.33 **Compound Name:** Silicon Oxide
Mineral Name: Quartz, syn **Entry Date:** 09/01/1996

Radiation: CuKα1 (1.5406 Å) **Filter:** Ge Mono **Internal Standard:** Si **d-Spacing:** Diffractometer
Intensity: Diffractometer - Integrated **I/Ic:** 3.41

Crystal System: Hexagonal **SPGR:** P3221 (154)
Author's Unit Cell [a: 4.91344(4) Å **c:** 5.40524(8) Å **Volume:** 113.01 Å³ **Z:** 3.00 **MolVol:** 37.67 **c/a:** 1.100
] Calculated Density: 2.649 g/cm³ **Measured Density:** 2.66 g/cm³ **Color:** White
SS/FOM: F(30) = 538.7(0.0018, 31)

Space Group: P3221 (154) **Molecular Wt:** 60.08 g/mol
Crystal Data [a: 4.913 Å **b:** 4.913 Å **c:** 5.405 Å **α:** 90.00° **β:** 90.00° **γ:** 120.00° **XtlCell Vol:** 113.01 Å³
XtlCell Z: 3.00 **c/a:** 1.100 **a/b:** 1.000 **c/b:** 1.100]
Reduced Cell [a: 4.913 Å **b:** 4.913 Å **c:** 5.405 Å **α:** 90.00° **β:** 90.00° **γ:** 120.00° **RedCell Vol:** 113.01 Å³]

nωβ: =1.544 **εγ:** =1.553 **Sign:** =+

Atomic parameters are cross-referenced from PDF entry 04-012-0490 **AC Space Group:** P3221 (154)
AC Unit Cell [a: 4.91427(12) Å **b:** 4.91427(12) Å **c:** 5.4058(2) Å **α:** 90° **β:** 90° **γ:** 120°]
Space Group Symmetry Operators:

Seq	Operator	Seq	Operator	Seq	Operator
1	x,y,z	3	-x+y,-x,z+1/3	5	-x,-x+y,-z+2/3
2	-y,x-y,z+2/3	4	y,x,-z	6	x-y,-y,-z+1/3

ADP Type: U
Atomic Coordinates:

Atom	Num	Wyckoff	Symmetry	x	y	z	SOF	Uiso	AET
Si	1	3a	.2.	0.4723	0.0	0.66666	1.0	0.00754	
O	2	6c	1	0.416	0.2658	0.7881	1.0	0.01747	

Anisotropic Displacement Parameters:

Atom	Num	Uani11	Uani22	Uani33	Uani12	Uani13	Uani23
Si	1	0.0075	0.0095	0.0063	0.00475	-0.002	-4.0E-5
O	2	0.026	0.02	0.0124	0.016	-0.003	-5.0E-5

Crystal (Symmetry Allowed): Non-centrosymmetric

Subfiles: Cement and Hydration Product, Common Phase, Forensic, Inorganic, Metal & Alloy, Mineral Related (Mineral, Synthetic), Pharmaceutical (Excipient)
Mineral Classification: Quartz (supergroup), Class Member **Pearson Symbol:** hP9.00
Prototype Structure [Formula Order]: Si O2 **Prototype Structure [Alpha Order]:** O2 Si
LPF Prototype Structure [Formula Order]: Si O2,hP9,152 **LPF Prototype Structure [Alpha Order]:** O2 Si,hP9,152

Cross-Ref PDF #'s: 00-033-1161 (Alternate), 01-085-0335 (Alternate), 04-005-4494 (Alternate), 04-012-0490 (Alternate)

References:

Type	DOI	Reference
Primary Reference		Kern, A., Eysel, W., Mineralogisch-Petrograph. Inst., Univ. Heidelberg, Germany. ICDD Grant-in-Aid 1993.
Crystal Structure		Crystal Structure Source: LPF.
Optical Data		Swanson, Fuyat. Natl. Bur. Stand. (U. S.), Circ. 539 1954, 3, 24.
Structure		Z. Kristallogr. 1992, 198, 177.

Database Comments: Additional Patterns: To replace 00-033-1161. See PDF 01-085-0335. General Comments: Low temperature quartz. 2θ determination based on profile fit method. Temperature of Data Collection: 296(1) K. Unit Cell Data Source: Powder Diffraction.

d-spacings (58) - Si O2 - 00-046-1045 (Stick, Fixed Slit Intensity) - Cu Kα1 1.54056 Å

2θ (°)	d (Å)	I	h	k	l	*	2θ (°)	d (Å)	I	h	k	l	*	2θ (°)	d (Å)	I	h	k	l	*
20.859	**4.254990**	16	1	0	0		50.621	1.801740	<1	0	0	3		68.142	1.374960	7	2	0	3	
26.639	**3.343470**	100	1	0	1		54.873	1.671730	4	2	0	2		68.316	1.371880	5	3	0	1	
36.543	2.456870	9	1	1	0		55.323	1.659190	2	1	0	3		73.466	1.287910	2	1	0	4	
39.464	2.281490	8	1	0	2		57.234	1.608270	<1	2	1	0		75.658	1.255950	3	3	0	2	
40.299	2.236130	4	1	1	1		59.958	1.541530	9	2	1	1		77.673	1.228320	1	2	2	0	
42.449	2.127710	6	2	0	0		64.034	1.452890	2	1	1	3		79.882	1.199820	2	2	1	3	
45.792	1.979860	4	2	0	1		65.784	1.418410	<1	3	0	0		80.044	1.197790	<1	2	2	1	
50.138	**1.817960**	13	1	1	2		67.742	1.382100	6	2	1	2		81.171	1.183990	2	1	1	4	

00-046-1045 Sep 24, 2021 11:09 AM (RX1005)

2θ (°)	d (Å)	I	h	k	l	*	2θ (°)	d (Å)	I	h	k	l	*	2θ (°)	d (Å)	I	h	k	l	*
81.489	1.180170	2	3	1	0		103.873	0.978345	<1	3	0	4		122.600	0.878167	<1	4	1	2	
83.838	1.152980	1	3	1	1		104.199	0.976174	<1	3	2	0		127.245	0.859796	<1	3	0	5	
84.955	1.140650	<1	2	0	4		106.589	0.960785	<1	3	2	1		131.197	0.845837	<1	1	1	6	
87.437	1.114550	<1	3	0	3		112.110	0.928526	<1	4	1	0		132.750	0.840746	<1	5	0	1	
90.828	1.081550	2	3	1	2		114.057	0.918159	<1	3	2	2		134.286	0.835918	<1	4	0	4	
92.785	1.063800	<1	4	0	0		114.463	0.916060	2	4	0	3		136.417	0.829560	1	2	0	6	
94.648	1.047720	1	1	0	5		114.635	0.915176	2	4	1	1		137.888	0.825393	2	4	1	3	
95.115	1.043800	<1	4	0	1		115.881	0.908890	<1	2	2	4		140.310	0.818911	<1	3	3	0	
96.234	1.034610	1	2	1	4		117.532	0.900851	<1	0	0	6		143.242	0.811682	3	5	0	2	
98.747	1.014900	1	2	2	3		118.308	0.897188	<1	2	1	5		144.110	0.809668	<1	3	3	1	
102.228	0.989576	<1	1	1	5		120.119	0.888910	1	3	1	4								
102.563	0.987246	<1	3	1	3		121.848	0.881352	<1	1	0	6								

\

00-038-1420 Sep 24, 2021 11:02 AM (RX1005)

d-spacings (10) - Ti N - 00-038-1420 (Stick, Fixed Slit Intensity) - Cu Kα1 1.54056 Å

2θ (°)	d (Å)	I	h	k	l	*	2θ (°)	d (Å)	I	h	k	l	*	2θ (°)	d (Å)	I	h	k	l	*
36.662	**2.449170**	72	1	1	1		77.962	1.224490	12	2	2	2		125.672	0.865770	12	4	2	2	
42.596	**2.120710**	100	2	0	0		93.169	1.060420	5	4	0	0		141.312	0.816367	7	5	1	1	
61.812	**1.499670**	45	2	2	0		104.673	0.973049	6	3	3	1								
74.068	1.278920	19	3	1	1		108.607	0.948481	14	4	2	0								

TiO_2 00-021-1272

00-021-1272 Jul 9. 2020 10:34 AM (RX1005)

Status Primary **Quality Mark:** Star **Environment:** Ambient **Temp:** 298.0 K **Chemical Formula:** Ti O2
Empirical Formula: O2 Ti **Weight %:** O40.06 Ti59.94 **Atomic %:** O66.67 Ti33.33
Compound Name: Titanium Oxide **Mineral Name:** Anatase, syn **Entry Date:** 09/01/1971

I/Ic: 3.3

Crystal System: Tetragonal **SPGR:** I41/amd (141)
Author's Unit Cell [a: 3.7852 Å **c:** 9.5139 Å **Volume:** 136.31 Å³ **Z:** 4.00 **MolVol:** 34.08 **c/a:** 2.513]
Calculated Density: 3.892 g/cm³ **Color:** Colorless **SS/FOM:** F(30) = 74.2(0.0116, 35)

Space Group: I41/amd (141) **Molecular Weight:** 79.86 g/mol
Crystal Data [a: 3.785 Å **b:** 3.785 Å **c:** 9.514 Å **α:** 90.00° **β:** 90.00° **γ:** 90.00° **XtlCell Vol:** 136.31 Å³
XtlCell Z: 4.00 **c/a:** 2.514 **a/b:** 1.000 **c/b:** 2.514]
Reduced Cell [a: 3.785 Å **b:** 3.785 Å **c:** 5.458 Å **α:** 110.29° **β:** 110.29° **γ:** 90.00° **RedCell Vol:** 68.16 Å³]

Atomic parameters are cross-referenced from PDF entry 04-007-0701 **AC Space Group:** I41/amd (141)
AC Unit Cell [a: 3.7845 Å **b:** 3.7845 Å **c:** 9.5143 Å **α:** 90° **β:** 90° **γ:** 90°]
Space Group Symmetry Operators:

Seq	Operator	Seq	Operator	Seq	Operator	Seq	Operator
1	x,y,z	5	-x,y,z	9	y+1/2,x+1/2,-z+1/2	13	-y+1/2,x+1/2,-z+1/2
2	-x+1/2,-y+1/2,z+1/2	6	x+1/2,-y+1/2,z+1/2	10	-y,-x,-z	14	y,-x,-z
3	x+1/2,y,-z+3/4	7	-x+1/2,y,-z+3/4	11	y,x+1/2,z+1/4	15	-y,x+1/2,z+1/4
4	-x,-y+1/2,-z+1/4	8	x,-y+1/2,-z+1/4	12	-y+1/2,-x,z+3/4	16	y+1/2,-x,z+3/4

ADP Type: U **Origin:** O1
Atomic Coordinates:

Atom	Num	Wyckoff	Symmetry	x	y	z	SOF	Uiso	AET
Ti	1	4a	-4m2	0.0	0.0	0.0	1.0	0.0058	6-a
O	2	8e	2mm.	0.0	0.0	0.20806	1.0	0.0072	3#b

Anisotropic Displacement Parameters:

Atom	Num	Uani11	Uani22	Uani33	Uani12	Uani13	Uani23
Ti	1	0.0052	0.0052	0.007	0.0	0.0	0.0
O	2	0.0117	0.0027	0.0072	0.0	0.0	0.0

Crystal (Symmetry Allowed): Centrosymmetric

Subfiles: Common Phase, Educational Pattern, Forensic, Inorganic, Metal & Alloy, Mineral Related (Mineral, Synthetic), NBS Pattern, Pharmaceutical (Excipient), Pigment/Dye

Pearson Symbol: tI12.00 **Prototype Structure [Formula Order]:** Ti O2 **Prototype Structure [Alpha Order]:** O2 Ti
LPF Prototype Structure [Formula Order]: Ti O2,tI12,141 **LPF Prototype Structure [Alpha Order]:** O2 Ti,tI12,141

Cross-Ref PDF #'s: 00-001-0562 (Deleted), 01-071-1166 (Alternate), 04-001-7641 (Alternate), 04-002-2678 (Alternate), 04-002-2750 (Alternate), 04-002-2751 (Alternate), 04-002-8296 (Alternate), 04-006-1918 (Alternate), 04-006-9240 (Alternate), 04-007-0701 (Alternate)

References:

Type	DOI	Reference
Primary Reference		Natl. Bur. Stand. (U. S.) Monogr. 25 1969, 7, 82.
Crystal Structure		Crystal Structure Source: LPF.

Database Comments: Additional Patterns: See PDF 01-071-1166. Validated by calculated pattern. General Comments: Anatase and another polymorph, brookite (orthorhombic), are converted to rutile (tetragonal) by heating above 700 C. Pattern reviewed by Holzer, J., McCarthy, G., North Dakota State Univ, Fargo, North Dakota, USA, ICDD Grant-in-Aid (1990). Agrees well with experimental and calculated patterns. Sample Source or Locality: Sample obtained from National Lead Co., South Amboy, New Jersey, USA. Temperature of Data Collection: 298 K. Unit Cell Data Source: Powder Diffraction.

d-Spacings (39) - Ti O2 - 00-021-1272 (Stick, Fixed Slit Intensity) - Cu Kα1 1.54056 Å

2θ (°)	d (Å)	I	h	k	l	*	2θ (°)	d (Å)	I	h	k	l	*
25.28059	**3.520000**	100	1	0	1		68.76015	1.364100	6	1	1	6	
36.94594	2.431000	10	1	0	3		70.30871	1.337800	6	2	2	0	
37.80022	**2.378000**	20	0	0	4		74.02890	1.279500	<2	1	0	7	
38.57503	2.332000	10	1	1	2		75.02943	1.264900	10	2	1	5	
48.04869	**1.892000**	35	2	0	0		76.01733	1.250900	4	3	0	1	
53.88969	1.699900	20	1	0	5		80.72490	1.189400	<2	0	0	8	
55.06016	1.666500	20	2	1	1		82.13614	1.172500	2	3	0	3	
62.11896	1.493000	4	2	1	3		82.65939	1.166400	6	2	2	4	
62.68842	1.480800	14	2	0	4		83.14647	1.160800	4	3	1	2	

00-021-1272 Jul 9. 2020 10:34 AM (RX1005)

2θ (°)	d (Å)	I	h	k	l	*
93.21744	1.060000	2	2	1	7	
94.17833	1.051700	4	3	0	5	
95.13944	1.043600	4	3	2	1	
98.31523	1.018200	2	1	0	9	
99.80073	1.007000	2	2	0	8	
101.21747	0.996700	2	3	2	3	
107.44367	0.955500	4	3	1	6	
108.95853	0.946400	4	4	0	0	
112.83607	0.924600	<2	3	0	7	
113.85685	0.919200	2	3	2	5	
114.90411	0.913800	2	4	1	1	
118.43409	0.896600	4	2	1	9	
120.09892	0.889000	2	2	2	8	
121.71997	0.881900	<2	4	1	3	
122.33066	0.879300	2	4	0	4	
131.02899	0.846400	2	4	2	0	
135.99104	0.830800	<2	3	2	7	
137.38386	0.826800	4	4	1	5	
143.87846	0.810200	2	3	0	9	
150.02819	0.797400	4	4	2	4	
152.62189	0.792800	2	0	0	12	

Annex III: XRD characterizations

HRXRD RSMs

Z-cut

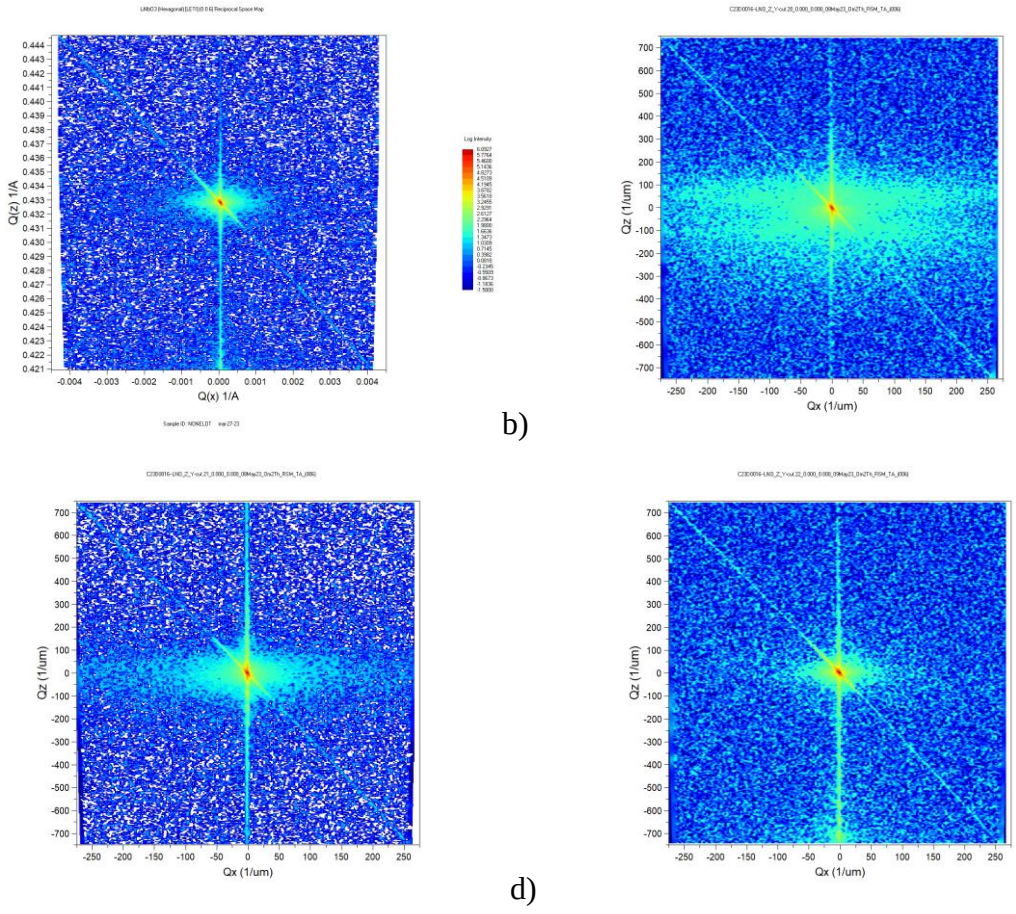

a) b)

c) d)

FIGURE 5.1 RECIPROCAL SPACE MAPS (RSMS) OF (A) Z-1, (B) Z-2, (C) Z-4 AND (D) Z-5 WAFERS

X-cut

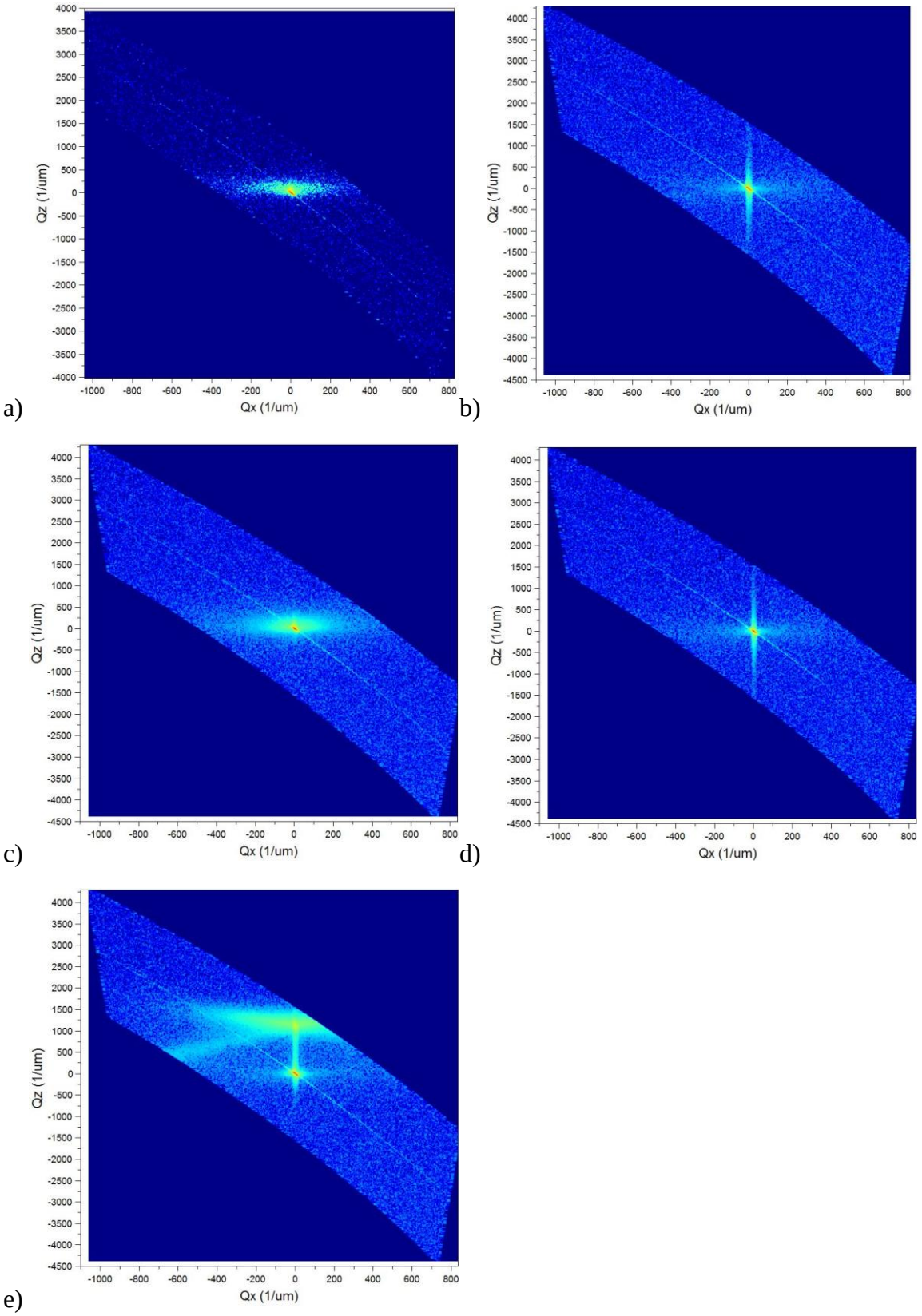

FIGURE 5.2 RECIPROCAL SPACE MAPS OF (A) X-1, (B) X-2, (C) X-3, (D) X-4 AND (E) X-5.

Y+128°-cuts

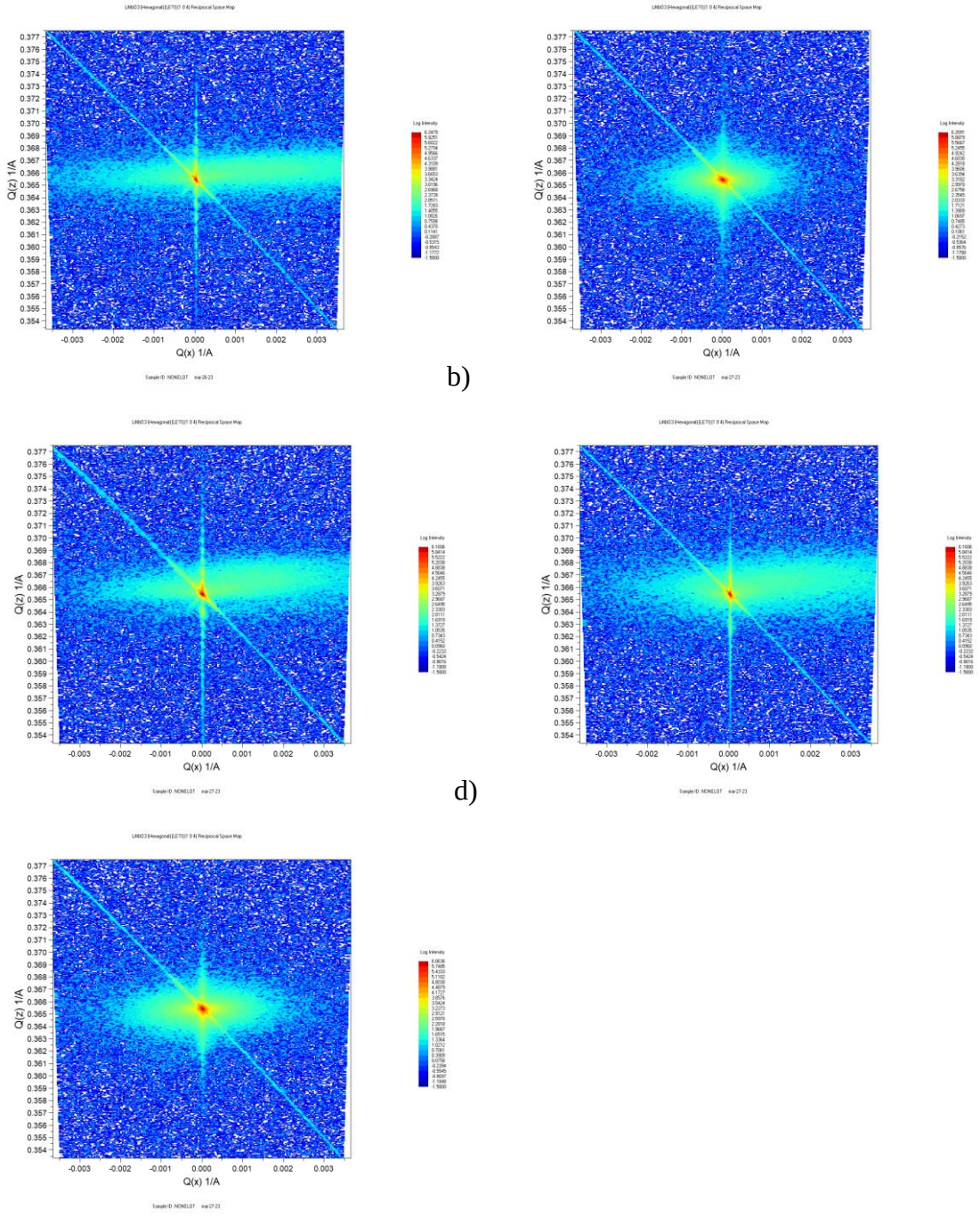

FIGURE 5.3 RECIPROCAL SPACE MAPS OF (A) Y-1, (B) Y-2, (C) Y-3, (D) Y-4 AND (E) Y-5.

Annex IV: AFM characterizations

Deposition on *c*-sapphire

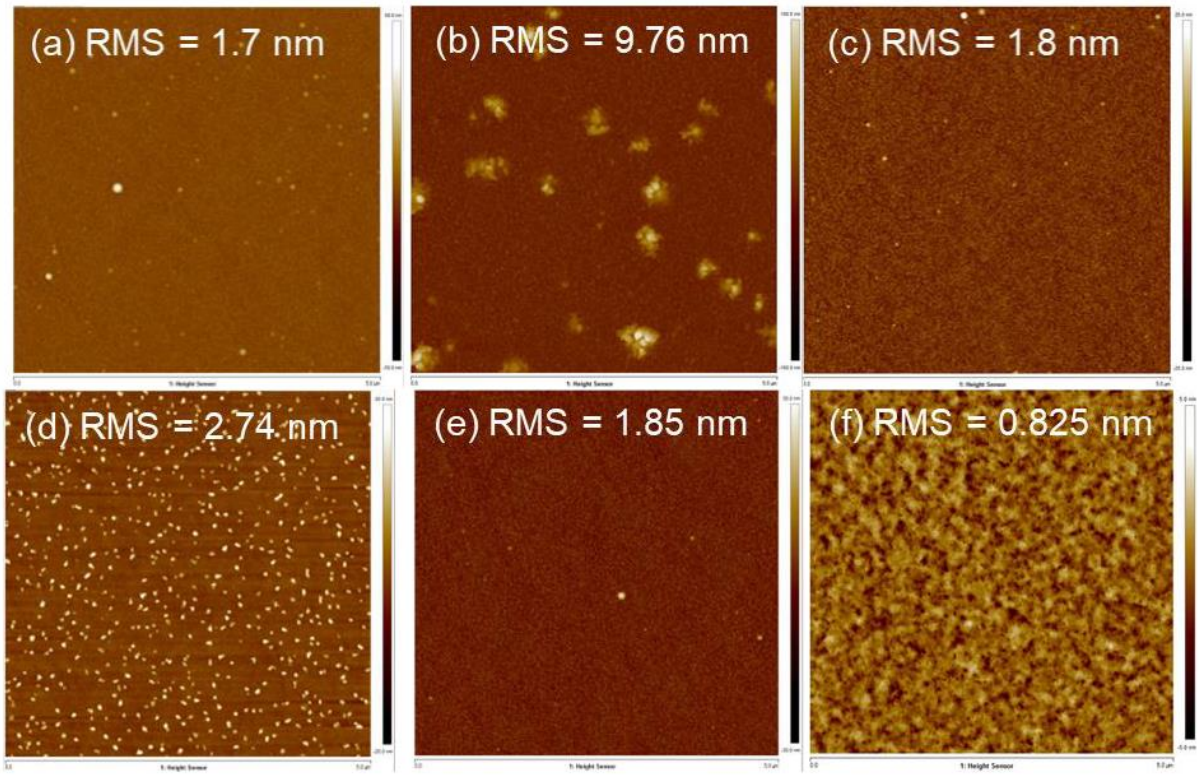

FIGURE 5.4 AFM MICROGRAPHS OF $LiNbO_3$ ON Z-CUT Al_2O_3 GROWN AT: (A) 0.2 MBAR, 500°C, $LiNbO_3$ TARGET; (B) 0.007 MBAR, 500°C, $LiNbO_3$ TARGET; (C) 0.2 MBAR, 600°C, $LiNbO_3$ TARGET; (D) 0.2 MBAR, 600°C, $Li_{1.1}NbO_{3.05}$ TARGET; (E) 0.007 MBAR, 500°C, $Li_{1.1}NbO_{3.05}$ TARGET; (F) (E) 0.007 MBAR, 600°C, $Li_{1.1}NbO_{3.05}$ TARGET;. SCAN SIZE: (5 × 5) μM^2.

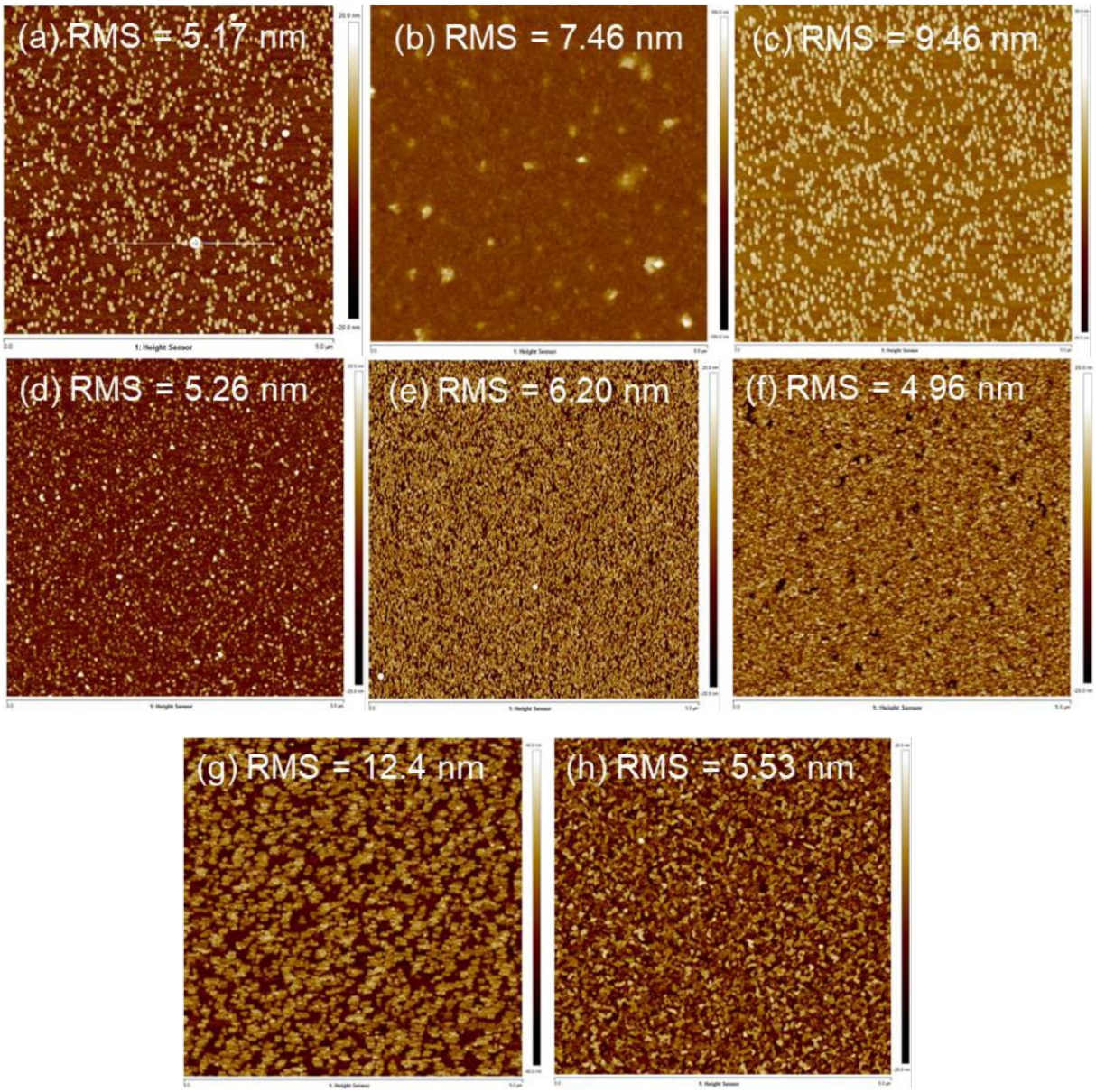

FIGURE 5.4 AFM MICROGRAPHS OF $LiNbO_3$ ON X-CUT Al_2O_3: : (A) A-1; (B) A-2; (C) A-3; (D) A-4; (E) A-5; (F) A-6; (G) A-7; (H) A-8;. SCAN SIZE: (5 × 5) μM^2.